EXPERIMENTAL INVESTIGATION INTO THE FATIGUE LIFE OF HYBRID JOINTS UNDER FULLY REVERSED FLEXURE LOADING

Project Report:

Structural Response of Hybrid Ship Connections Subject To Fatigue Loads

by

Dominique Corriveau, Graduate Research Assistant,

Vincent Caccese, PhD. P.E, Professor and Principal Investigator

Senthil S. Vel, Associate Professor and Co-Principal Investigator

Prepared for:

Office of Naval Research

800 N Quincy St.

Arlington VA. 22217-5660

Grant No. N00014-05-1-0735

Dr. Roshdy G.S. Barsoum,

Program Manager

University of Maine

Department of Mechanical Engineering

Orono, ME 04469-5711

June 2008

Report No. C-2004-015-RPT-01

ABSTRACT

Glass Reinforced Polymers (GRP's) have a variety of properties that make them desirable for use in marine applications. For instance: high strength, low weight, corrosion resistance, inherent complex forming abilities, and low electromagnetic signature characteristics can be exceedingly advantageous in such areas. The U.S. Navy currently has an objective to investigate the use of lightweight materials to enhance naval capabilities, and GRP's have been of particular interest. Composite/metal hybrid systems offer a potential solution to many of the complications encountered in the construction of naval vessels, such as the weight of materials that are currently used and difficulty of forming them. Prevention of structural failures in a ship is essential if human injury, casualties and economic loss are to be avoided. Fatigue of connections is a major concern in an ocean environment. The overall objective of this research is to develop and demonstrate methods for fatigue testing various common and novel steel/composite hybrid connections and to evaluate their suitability for their desired applications. Fatigue of hybrid connections subject to out-of-plane loading is highly variable and there is a lack of data reported in the literature. The intention of this effort is to provide additional baseline data for this type of connection. Testing and analysis techniques were successfully developed and employed. It was determined that separate analyses of the individual components of a hybrid joint (e.g. the composite plate and the steel T-section) are insufficient to determine the effects of fatigue loading on a given joint due to the effects of joining methods on the strength. Fatigue testing of a full joint configuration is necessary to adequately evaluate its response to fatigue loading. Further testing beyond what is presented in this report is recommended.

ACKNOWLEDGEMENTS

The authors gratefully acknowledge funding for this project through the Office of Naval Research under grant number N00014-05-1-0735. Dr. Roshdy G..S. Barsoum of ONR is the cognizant program officer. His support and encouragement is greatly appreciated. The authors would also like to thank the assistance of the project team at the University of Maine including undergraduate students Jacob Folz, Brendan Owen, and Radek Glaser.

TABLE OF CONTENTS

LIST OF TABLES

LIST OF FIGURES

1. Introduction

Prevention of structural failures in a ship is essential if human injury, casualties and economic loss are to be avoided. Fatigue of connections is a major concern in an ocean environment. A ship must be able to survive when exposed to loading which occurs dynamically and repeatedly. Structural failures due to fatigue can initiate at connections and/or interfaces. In hybrid structures that combine metals and composites, this is in part due to the stiffness mismatch between the connection material constituents, which can give rise to stress concentrations that significantly influence fatigue life. The structural response of the interfaces of the materials can be complex. An accurate appraisal of structural integrity depends on a thorough investigation into the mechanics of the connections and interfaces of the vessels, as well as a sound estimate of the dynamic loads that induce failure. A report by Bonanni et al. (2000) presents examples of numerous types of connections used, and discusses the importance of connection design in naval ship construction. It is essential to evaluate the fatigue life of hybrid joints to insure that newly emerging hybrid ship designs will have a high degree of structural integrity. Additional, in-depth research on the fatigue of metal-to-composite connections is needed, and understanding the nonlinear connection mechanics, the interactions between the two materials, and the response under severe environmental conditions is essential. The fatigue characterization of various hybrid joints is therefore the objective of the current research.

This research project builds on the past ONR funded efforts at the University of Maine that focused on hybrid ship construction methods and hybrid connections. These efforts included the Advanced Hull Form Inshore Demonstrator (AHFID) and Modular Advanced Composite Hull Form (MACH) projects. These efforts focused on response of structural connections, including hybrid and laser welded types. In the MACH concept, the connections relied mostly upon their out-of-plane response. A lack of data on fatigue analysis of hybrid connections subject to out-of-plane loads was reported, which provided the impetus for this study where primarily structural response due to out-of-plane dynamic stresses are evaluated. Using the MACH project as a conceptual starting point, fatigue analysis of various possible joint configurations is performed.

It is envisioned that the emerging hybrid joint fatigue data, composite construction technology, and fabrication techniques presented under this effort will have applicability beyond the current project. The development of this hybrid system focuses primarily on the performance of the connections between the metal and composite so as to insure their resilience to fatigue loading, with attention given to connections designed for out-of-plane resistance.

1.1 Research Background

The U.S. Navy currently has an objective to develop high-speed ships to combat existing threats and to enhance the future naval capabilities. Stealth, speed, and low weight have become important concerns in current naval ship designs (Black, 2003). Speed for such vessels can be increased by reduction in weight and in innovative complex shaping of the hull-form. However, as with most large structures, the cost of these vessels is a major driver in their design. This presents a problem because conventional hull construction techniques have limited the ability to build and maintain the complex shapes required for high-speed military support vessels in a cost effective manner. Reasons for this include the difficulty of forming metal into complex shapes. The lightweight characteristics and inherent forming abilities of composite materials quickly identified them as good candidates to assist in overcoming these problems. To further assist in cost reduction, lower cost material systems such as Glass Reinforced Polymers (GRP's) are often preferred as opposed to more expensive carbon fiber systems for ship hull construction. Although the original direction for use of new materials focused on composites alone, it was quickly determined that GRP composites lack the stiffness and connectablity required in the medium to long length modern ships. The lower natural frequencies resulting from the reduced stiffness influence the design of sensitive equipment and instrumentation that must go onboard. Alm (1983) estimated that a 50m naval ship would be 2.4 times less stiff than its steel counterpart. Makinen et al. (1988) reported similar findings, stating that the deflections would be 3 times greater. In an article by Boyd et al. (2004a), they reported that an all-composite ship greater than 150 meters is currently unfeasible. Barsoum (2003) came to the same conclusion, and stated that GRP's used by themselves lack the stiffness and in-plane strength required for the larger

ship hull structures. The use of hybrid structures composed of GRP and steel are expected to solve these problems, because they combine the benefits of traditional steel construction while using low-density composites in weight critical areas. Such structures are being used in a widening range of engineering disciplines. Barsoum (2003) describes the development of hybrid hulls where non-magnetic stainless steel is used in combination with composites to create hybrid hull-forms with low electromagnetic signatures. Two innovative structural types were presented, one of which involved a ship mid-section made of steel with a composite bow and stern. In this case the hybrid connection interface carries predominately in-plane loads. The other structural type entailed a metallic skeleton and composite outer shell. If this second structural system is employed, the composite/metal interface is between the metal skeleton and the outer panels allowing for a readily quantifiable metal-to-metal interface between the equipment and structural frame. The feasibility of one approach over the other is dependent upon cost, watertight integrity, structural integrity and environmental durability of the connections. Development of robust connection methodologies and cost effective manufacturing of the composite/metal interfaces are imperative if widespread use of hybrid construction for hulls and other structural components is to advance. This is especially true for naval vessels where the environment is harsh and forces are large and dynamic in nature.

From 2000 to 2004, the office of Naval Research (ONR) funded the development of a high speed craft called the Navtek Sea Flyer. This vessel, shown in Figure 1.1, uses an underwater body to enhance performance and sea keeping. The large underwater body used in the Sea Flyer vessel was studied under the MACH program for its potential as a structural component. The University of Maine teamed with Navatek of Honolulu, HI, and ATS of Sanford, Maine on this program. These collaborators undertook a mission to develop fast, efficient surface vessels that use additional underwater bodies attached to a more traditional hull-form. They worked in conjunction with the Navy laboratory at Carderock, MD (NSWCCD) and NRL on this effort, the end goal of which was to deploy ships where more payload and/or higher speeds could be achieved at little or no additional power consumption and with excellent sea keeping ability. Figure 1.2 shows

Figure 1.1 – Navatek's Sea Flyer

one example vessel called the MIDFOIL where a hydrofoil and a parabolic lifting body shape are combined with a catamaran hull to achieve additional buoyancy and dynamic lift which greatly improves the performance and sea-keeping of the vessel. Sea trials on the Sea Flyer, MIDFOIL, and similar vessels have shown that this method may be advantageous for fast military support craft and commercial vessels such as ferries. Recent efforts under the MACH project have shown that the addition of underwater bodies on non-optimized structures can improve speed, reduce fuel consumption, and increase payload. These efforts have also demonstrated that hybrid construction has the potential to bring about high structural efficiency.

Similar to the second innovative structural type described in the previous section, the method proposed for construction of a hybrid version of an underwater lifting body was to use a skin made of composite materials attached to a metal framework. Figure 1.3 shows a schematic of this concept and a photograph of a 4-panel test section with hybrid connections in the UMaine Hybrid Structures Laboratory. The skin design was GRP hat-stiffened and used a doubler type bolted joint hybrid connection to attach the GRP panels to a steel frame. Detailing this connection to have adequate strength, fatigue resistance and watertight integrity was essential. Concepts from this previous research were carried

over to the present project and provided an excellent starting point for the current research.

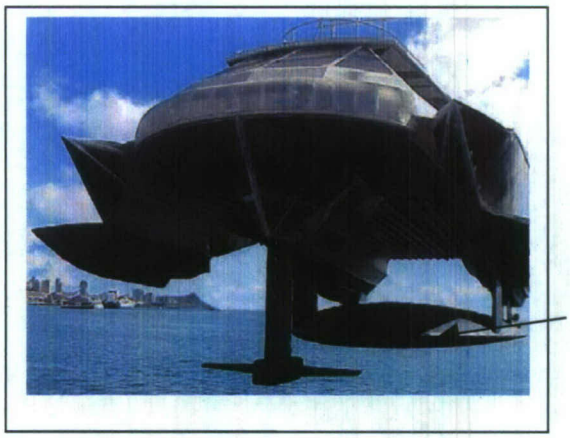

Figure 1.2 – MIDFOIL Craft with Parabolic Underwater Lifting Body.

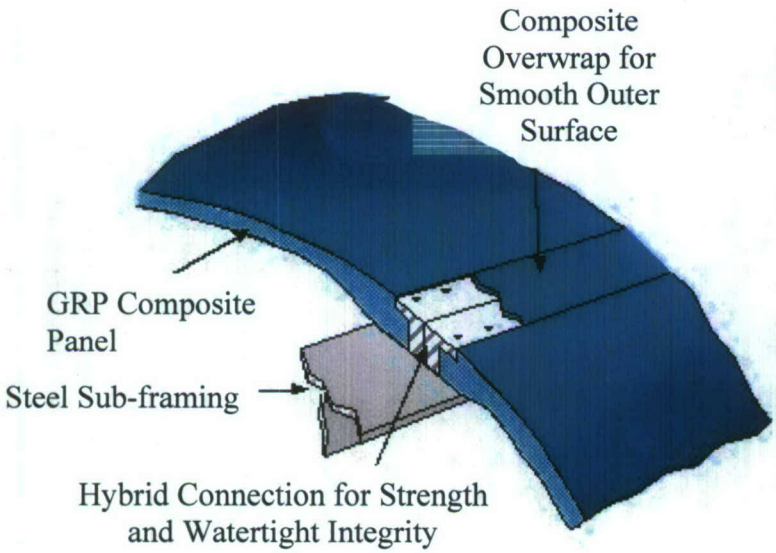

Four panel large scale test section with hybrid steel-GRP bolted joints fabricated as part of the MACH program

Figure 1.3 – Hybrid Structure Constructed Using GRP Composite Skin Over Metal Substructure

1.2 Objectives

The focus of this research is the fatigue response of metallic to composite connections, namely hybrid connections, which are an essential detail of hybrid ship structures. The primary goal of the experimental study is to produce some fatigue response data which can be used to develop, analyze and quantify the fatigue performance of hybrid composite/metallic structural systems and hybrid connection concepts for application to naval ship hulls. The emerging concepts used are to be part of a robust efficient system with high structural integrity, with the developed technology being demonstrated at the joint component level. This work highlights the development of connection concepts for out-of-plane response, and fatigue testing of various hybrid structural connection details.

The specific research objectives of the current effort are to:

1) Experimentally study the out-of-plane fatigue response of metal-GRP bolted hybrid connections.
2) Develop robust hybrid connection design and manufacturing concepts for out-of-plane joining of composite to metallic structures.
3) Develop methodologies and criteria for experimental/numerical verification of fatigue resistance and structural integrity.
4) Compare structural performance and response to existing databases.
5) Suggest modifications to improve existing designs and future research tasks.
6) Develop methodologies to assess panel material and connection integrity.

1.3 Scope of Work

A literature review of previous work relating to the present research is presented in the remainder of this section. A preliminary finite element analysis (FEA) performed prior to experimentation is presented in Section 2 of this report for the purposes of obtaining realistic values of relative shear and moment forces seen by the joints of interest to this study. Details of the analysis are outlined and the relevance of the results to the experimental research is discussed. Section 3 outlines the vacuum assisted resin transfer molding (VARTM) fabrication processes used to obtain the E-glass/vinyl ester composite materials used in testing and the resulting material properties. Section 4 describes the various tests performed for the research. Cyclic tests to failure, intermediate cyclic tests, fatigue tests, and residual strength tests were performed on both clamped and standard bolted joint configurations. The procedures used are thoroughly explained. Results of all tests are presented and discussed in Section 5.

1.4 Literature Review

The potential areas of application of GRP composite materials have proven to be many. A vast variety of fields have been impacted by the emergence and improvement of GRP's, the marine industry being no exception. The range of uses for GRP composites in the marine industry is large and continues to grow. Reasons for this include the high strength and low weight properties of composite materials, their corrosion resistance, and their inherent complex forming abilities. In some cases their low electromagnetic signature characteristics prove to be advantageous as well, such as in military applications. However, their implementation must be done with caution, especially when subjected to repetitive stresses as in a ship. The lightweight characteristics of GRP's are one of the main reasons for their study for marine applications. If composite structures can completely replace the steel components of a ship, for instance, significant weight reductions may result.

Connections are a critical area in a structure, especially with regard to composites. Consequently, the joining of GRP's has been a particular area of interest. Herszberg et al. (2005) investigated damage assessment methods for composite ship joints, specifically

the detection of disbonds and determination of critical disbond sizes in GRP using embedded optical fibers. Disbonds in T-joints (see Figure 1.4) that would potentially be used for a connection between GRP bulkhead and a GRP hull were studied.

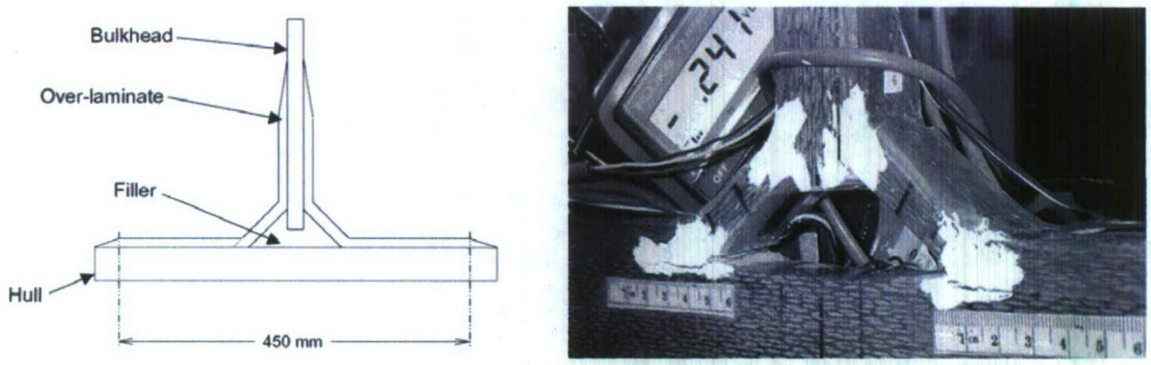

Figure 1.4 – Typical T-Joints Used by Hertzberg et al. (2005)

1.4.1 Fatigue of Bolted Connections

Much research has been done with composite bolted connections, especially with regard to in-plane response. One good example of this can be found in a report by Bonanni et al. (2000). Work on bolted connections undergoing out-of-plane response was performed at the University of Maine. Since the complete replacement of steel with GRP's is often not feasible, especially in large vessel applications, Kabche et al. (2007b) investigated watertight methods of joining composite material to steel. The specific applications in mind for this research were modular panel sections for use on an advanced hull form structure where removability was desired. Consequently, bolted joints subject to out-of-plane loads were the primary object of study. Large scale testing of four stiffened panel sections, as seen in Figure 1.5, was performed. Using a watertight hydrostatic test tank, a uniform design pressure of 12 psi was applied to the panel assembly. This value was determined through fluid mechanics calculations as well as finite element analysis. The style of hybrid joint used to connect the composite panels to the steel I-beams was a bolted joint using a doubler plate (see Figure 1.6b). This joint style proved to be

successful for the application in that the hybrid panel assembly withstood three times the design load (36 psi) without leaking after the stiffeners had delaminated.

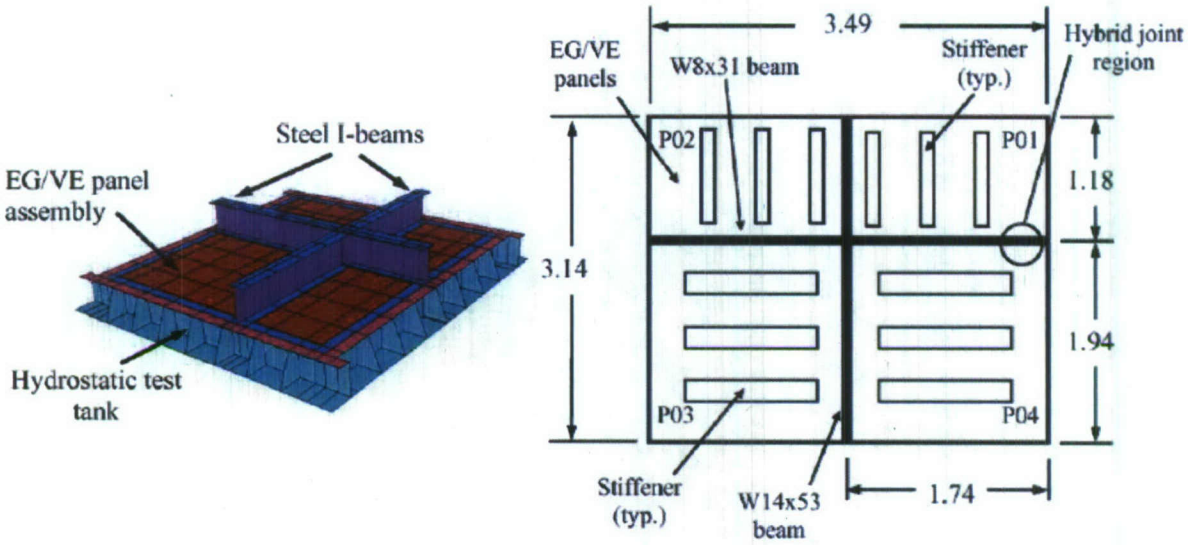

Figure 1.5 – Four-Panel Assembly Tested by Kabche et al. (2007b)

Kabche et al. proceeded to perform further testing on different joint styles intended for the same application (2007). Figure 1.6 depicts four of the types of joints used: a standard bolted joint using pultruding bolts, a bolted joint with a doubler plate using tapered bolts, a standard bolted joint using tapered bolts, and an adhesive joint.

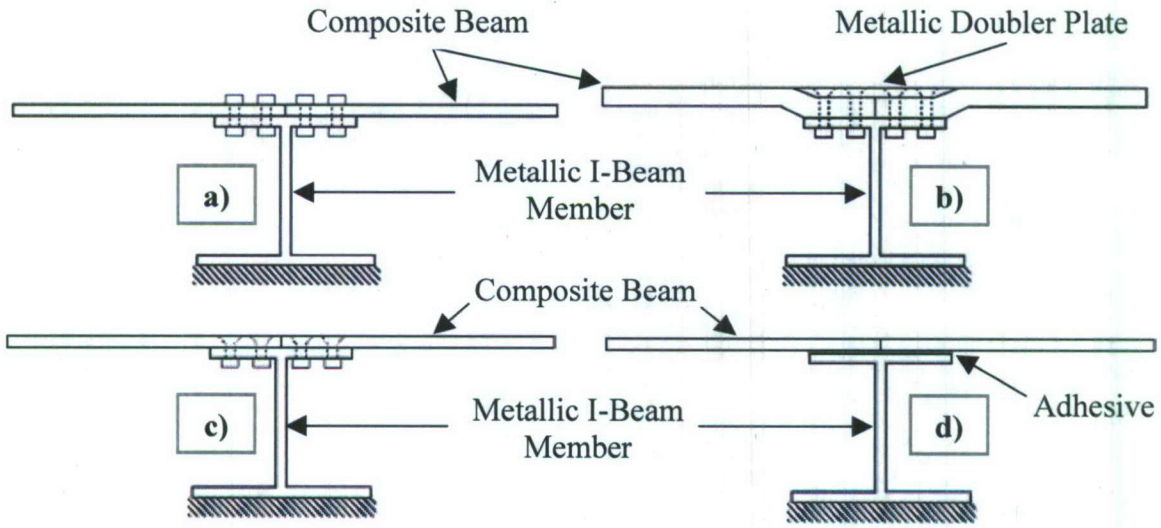

Figure 1.6 – Joint Configurations Analyzed by Kabche et al. (2007a)

Flexural loading was applied to the test specimens since it is one of the dominant types of loading a submerged panel in a hull form structure would experience. Other types of loading were left for future study. The cyclic response, load vs. displacement envelopes, failure modes, damage and ultimate loads, and initial joint rotational stiffness were all observed. It was found that the joint style employing the doubler plate (Figure 1.6b) was most successful in creating a watertight connection and reducing creep effects. Kabche et al. (2007a) suggested repeating similar tests to investigate variability in joint performance. It was also suggested to further develop fabrication techniques, run in-plane tension and compression tests on the same joint styles, run fatigue tests on the same joint styles, and investigate possibilities for creating weldable hybrid joints for the same application.

1.4.2 Adhesive Connections

An alternative approach of joining GRP's to steel is using solely adhesives. This has been the object of much study. Standards such as the Standard Guide for Preparation of Metal Surfaces for Adhesive Bonding (ASTM Standard D 2651) currently exist, and various studies have been performed on joining for marine applications using only adhesives. Adhesive joint strength depends on many factors, most importantly including the chemical and mechanical properties of the adhesive and adherends, the surface preparation, and the bond line thickness. Environmental influences such as temperature and humidity also play an important role in adhesive response. Additionally, fitup is important to adhesive joint response, and in ship structures thin bond lines may be economically unfeasible. Hashim and Knox (2004) studied the use of adhesives for thick-adherend applications. Different limitations encountered when using adhesives were discussed, as well as strategies for overcoming these difficulties. Three case studies were performed investigating the effects of tapering on the strength of double-lap steel and joints, the effects of tensile loading on adhesive joints consisting of steel stiffeners bonded to various composite laminates, and the effects of high temperatures on the strength of joints consisting of steel stiffeners bonded to a GRP laminate. While it was concluded that relevant design tools could help to overcome difficulties associated with the use of adhesives, such as the optimization of joint geometries, adhesion compatibility,

and creep resistance in high-temperature applications, it was still clear that success with adhesive joints requires much care and can be a detailed and drawn out process. Davies et al. (2004) investigated adhesively bonding composite stiffeners fabricated separately from a panel to replace the process of overlaminating composite stiffeners currently in practice. The practice of overlamination described involved bonding a foam stiffener "former" to the composite panel, and then manually overlaminating it with fiber-reinforced composite layers. This somewhat complicated process and associated debonding were avoided in the technique of adhesively bonding the pre-fabricated stiffeners. Multiple adhesives were tested, and the resulting panels ended up being stiffer than those produced by overlamination. Nonetheless, it was conceded that there were serious limitations in the use of adhesives alone. One such limitation was that room temperature curing is usually required and post curing not applied because of the size requirements of many marine structures. Post curing expedites the cross-linking and curing process with the addition of heat, resulting in stiffer panels much more quickly. Another limitation is that the dimensional variability of marine structures often results in larger bond line thicknesses as opposed to the tighter tolerances in aerospace applications. Boone et al. (2003) studied the use of adhesives in an E-glass/vinyl ester composite-to-aluminum hybrid joint application. Six adhesives along with 3 surface preparation methods were evaluated. An FEA analysis of the joint used was performed, as well as four point flexure testing. It was found that failure progressed slowly in some of the adhesives, but always drastically in others due to their ductility after they had cured. It was also found that failure occurred prematurely in some of the adhesives under environmental conditions (150F, 98-99% relative humidity). Wacker et al. (2004) looked specifically at the requirements for adhesive bonding in marine structures. Multiple aspects of the design of adhesive joints were discussed, including: specification, design methods, the use of test samples to determine properties, approval processes, and stress and deformation assessments. Experiments were then performed to determine whether the design process had been successful. It was concluded that for adhesive bonding to be performed more confidently, improvements in the theoretical analysis approaches would have to be made, as theoretical values did not adequately represent experimental values. Additionally, manufacturing requirements that were stressed for successful adhesive

bonding, including personnel qualification and production facilities, seemed rather strenuous and beyond what reality often allows. The use of adhesives clearly presents many limitations and difficulties. Quality control is an issue due to the complexity of the bonding process, and there is much room for human error. If the joint depends solely on successful adhesion, any small mistake could potentially cause complete failure. Beyond the requirements for successful bonding just discussed, adhesives also typically have low peel strength. Low peel strength can be a significant disadvantage, especially when out-of-plane loading is involved in the joint's application. For these reasons, it is risky to use only adhesives in the joining process. Mechanical fasteners present an alternative, but they have practical disadvantages such as high stress concentrations and the immense amount of material and labor required to implement bolted connections for larger vessels.

1.4.3 Weldable Connections

Methods of embedding steel into GRP components for developing a weldable connection show promise for use in hybrid connections. This is potentially very advantageous because an embedded joint combines mechanical interlock with adhesion, eliminating the more serious drawbacks that characterize adhesive-only joining methods. However, the heat input from welding may present a problem due to composites' low tolerance of high temperatures. Wright et al. (2000) studied the feasibility of incorporating the GRP's for use in transverse ship bulkheads for the purpose of weight reduction. Symmetric and asymmetric versions of two different methods of joining GRP composite sandwich panels with steel were obtained (see Figure 1.7), the idea being that the steel part of the hybrid bulkhead could then be welded to a steel ship hull. In the first method, a steel insert was laminated into the composite panels. In the second, steel "tuning forks" were bonded over the composite sandwich panel. Finite element analysis predicted that the symmetric configurations of the joints would be superior to asymmetric, the bonded "tuning fork" configuration superior to the embedded steel configuration. Static and fatigue tension and compression tests were performed on the "tuning fork" joints and showed the connections to be satisfactory.

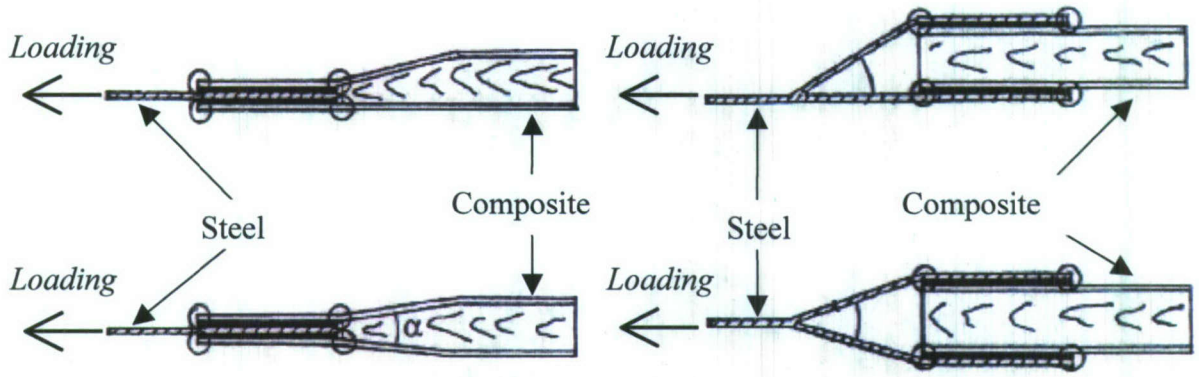

Figure 1.7 – Joint Configurations Analyzed by Wright et al. (2000)

Due to the weight and stiffness differences between steel and GRP's, it is often of greater interest to retain the steel substructures of ships and attempt to replace the superstructures instead. Replacing steel superstructures with composite could prove to be especially advantageous to the stability of a ship, in that the mass above the waterline could be reduced. Also, since steel bulkheads are required to maintain the stiffness required in larger vessels, incorporation of composite bulkheads is especially inadvisable in these applications. Consequently, much investigation has been made into joining GRP composite panels to steel sub structures and bulkheads. The adhesion of stainless steel to GRP's for the application of embedded joints was considered by Melograna and Grenestedt (2002a). In this case, the steel inserts were laminated into fiberglass layup during fabrication. Many different methods of adhesion were investigated, including preparation techniques, the use of additives, various kinds of adhesives, and various cure times. Once the specimens were finished, transverse tensile tests were performed to compare the various adhesion methods to each other. It was found that although some more complicated and expensive preparation techniques resulted in slightly better connections, the simple and cost effective method of grit-blasting followed by acetone cleansing performed very well. Cao and Grenestedt (2003) and Clifford et al. (2002) also performed a study on a particular hybrid joint intended for welding (See Figure 1.8). The joint studied was a balsa-core sandwich structure joint with an embedded steel insert all laid up and infused via the Vacuum Assisted Resin Transfer Molding (VARTM) process. The adhesion in this case is the adhesion of the resin to the steel. Mechanical interlock is also important, as the steel is embedded into the GRP. Once built, flexural and four-point bending tests were performed on the joint. It was found that the joint did not perform

particularly well under flexural loading, but modifications were made to the joint throughout the study that significantly improved its performance. A relationship between surface roughness of the steel and the toughness of the joint was also determined.

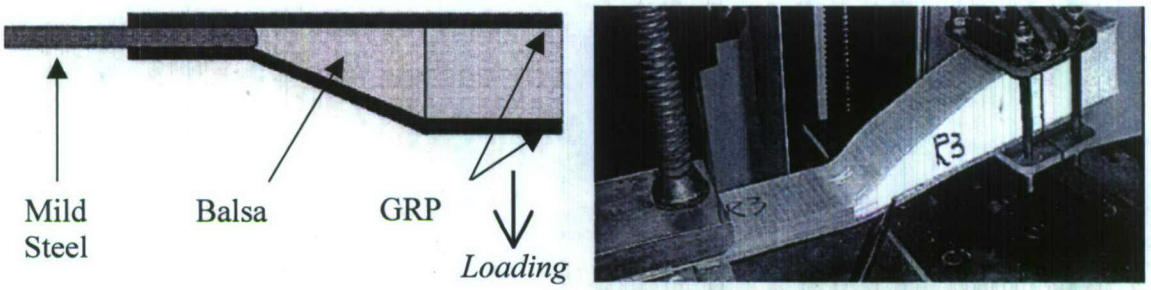

Figure 1.8 – Joint Configurations Analyzed by Clifford et al. (2002) & Cao and Grenestedt (2003)

Boyd et al. (2004b) examined a very similar joint to those just mentioned. The joint used in this particular investigation was one modeled after a joint from a helicopter hangar used by the French Navy. The hangar has composite walls and a steel insert on the bottom for the purposes of welding to the steel deck. Static tests on the welded hybrid joint were run in compression to imitate the actual conditions seen by the joint on the ship. Material properties such as the ultimate compressive strength were determined with static tests. It was determined that a fatigue analysis of the joint would be necessary, with acceleration due to wave motions as the prime generator of cyclic loading. The test that most accurately represented the loading conditions of the joint was an axial zero-compression test because the force from the weight of the hangar as the ship rose and sank with waves would be the main factor in fatigue of the joint. It was found that the data produced from the fatigue tests fit a Weibull cumulative density function well. In order to improve the strength and mechanical interlock properties of embedded hybrid joints, Melograna and Grenestedt (2002b) investigated the effect of perforations in the steel on the strength of such joints. Joints were manufactured in which steel inserts with a hole pattern patented by Unden and Ridder (1985) were laminated into the GRP.

Tensile tests were performed, and it was found that the use of perforations significantly aided the strength of the joints. There were multiple reasons for this, including reduction in stiffness mismatch in the elastic properties of the steel and composite attributed to the progressively widening hole pattern in the steel. Additionally, the holes provided significant mechanical interlock whereas embedded joints without holes rely strictly on the adhesion between the insert and the composite for strength. It was found that by using an optimized hole pattern and adequately preparing the surface, failure could be moved from delamination at the steel and composite interface to the composite itself just beyond the end of the insert. While the tensile tests showed that perforations can damatically improve the strength of an embedded hybrid joint, fatigue tests were not performed, and the effect of perforations on the fatigue life of such a joint remains unknown. It is suggested by Melograna and Grenestedt (2002b) that further research be done in this area.

1.4.4 Fatigue of Steel Connections

Extensive research has been performed on the fatigue life of steel connections, and there are a variety of approaches when it comes to determining their fatigue characteristics. Kendrick (2005) and Fricke and Kahl (2005) outline some approaches that have been used:

1. *S-N* curves (used for crack initiation)
    a. Nominal stress approach
        i. Fatigue characteristics of specific joint details
        ii. Abbreviated joint classification
    b. Hot spot-stress approach
    c. Notch-stress approach
    d. Mesh-insensitive approach
2. Fracture mechanics (used for crack propagation)

The *S-N* curve approach is the aspect of characterization focused on in this research, and deals with the crack initiation phase of fatigue. In general, this approach involves creating predictive curves for the fatigue life of a connection or component based on the

stress level (S) and the number of cycles (N). The fatigue response is predicted by the expression,

$$N \cdot S^m = A \qquad \text{(Eq. 1.1)}$$

where N is the number of cycles, S is the stress level at the location where the joint or material fails at the given N number of cycles, and m and A are constants which are arrived at through statistical analysis. These curves are then linearized by taking the logarithms of both sides as follows:

$$\log(N) + m\log(S) = \log(A) \qquad \text{(Eq. 1.2)}$$

and then used to predict the fatigue life of similar joints. Approaches a-d listed under the *S-N* methods in the previous list then takes this general expression and modifies it by a procedure specific to the approach being used. The reason for the multiple approaches within the *S-N* method is the amount of variability and that the peak stresses that initiate fatigue often occur at regions of mathematical stress singularities. In the vast majority of real-world applications, there is a great deal of variability in the loads applied to a particular connection, and they are often a function of time. Loading conditions may change from axial to transverse to shear or any combination, which can also make it more difficult to quantify the stress level for fatigue characterization. For this reason, statistical methods (such as Miner's Rule) are often used to categorize the load levels. Miners rule, as described by Kendrick (2005), essentially states that failure will occur when the following equation is true,

$$\sum \frac{n_i}{N_i} = 1 \qquad \text{(Eq. 1.3)}$$

where N_i is the number of cycles to failure for a constant stress amplitude S_i, and n_i is the number of cycles actually endured at S_i by a given component. For example, it is assumed that a certain component undergoes cyclic loading at stress levels, S_1, S_2, and S_3. The fatigue life curve developed with constant amplitude tests predicts that the number of cycles to failure at the various stress levels are N_1 (e.g. 10), N_2 (e.g. 100), and N_3 (e.g. 1000), respectively. If the number of cycles applied to the component at S_1 (n_1) is 9, and the number of cycles applied at S_2 (n_2) is 1, then Miner's rule would predict that the number of cycles at S_3 (n_3) needed for the component to fail would have to be 90 because,

$$\frac{n_1}{N_1}+\frac{n_2}{N_2}+\frac{n_3}{N_3}=1 \qquad \text{or} \qquad \frac{9}{10}+\frac{1}{100}+\frac{90}{1000}=1$$

Miner's rule, therefore, attempts to provide a means by which to quantify the load history of a component by using the constant amplitude data. Regardless of how developed the statistical approaches may be, however, constant amplitude fatigue tests can never truly model variable loading with complete accuracy, especially with continually changing load paths. Geometric factors also play a large part in complicating stress level selection as well. Identical connections types that have different weld radii, chamfer instead of a fillet welds, partial instead of full penetration welds, or even similar geometries that were created with different welding methods, for instance, can have completely different fatigue characteristics. These examples should make it very clear why choosing the stress level to characterize a joint can be a difficult task, and why there are so many different justifiable methods for doing so.

Nominal stress approaches use the far-field stress, S_{nom}, at the potential site of cracking for the S in Equation 1.1. The specific nominal stress approach takes data compiled from the fatigue testing of specific joint details and generates the constants m and A for each detail. This method does not directly take into account the different geometric effects (due to different weld styles or other such factors) which may exist within a particular detail, because it is assumed that these effects are characterized by the detail-specific curves. Munse et al. (1983) used this method of characterization, and performed an exhaustive review of the information available on the fatigue of welded joints, providing the *S-N* data for 53 different welded joint configurations. A sample of the weld details Munse et al. evaluated can be seen in Figure 1.9 and compared to the joint used in the present research seen in Figure 1.10. The *S-N* data for these joints are given in Table 1.1 and graphed in Figure 1.11.

Table 1.1 – *S-N* Data for Munse et al. (1983) Joint Details

Detail	*m*	$Log_{10}\tilde{A}$ (ksi)
5	3.278	9.65
12	4.398	14.12
13	4.229	12.12
14A	*Data scatter makes evaluation questionable*	
32B	3.533	9.71
42	7.358	16.98

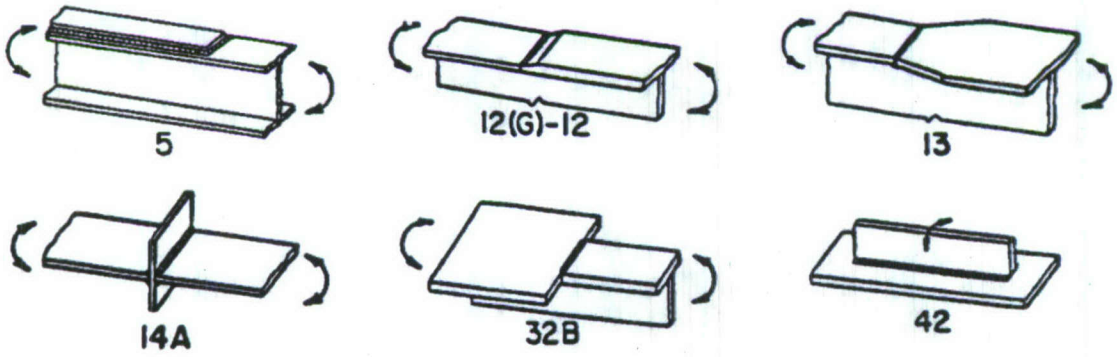

Figure 1.9 – Sample of Welded Joint Configurations Studied by Munse et al. (1983)

Figure 1.10 – Joint Under Evaluation in Present Research

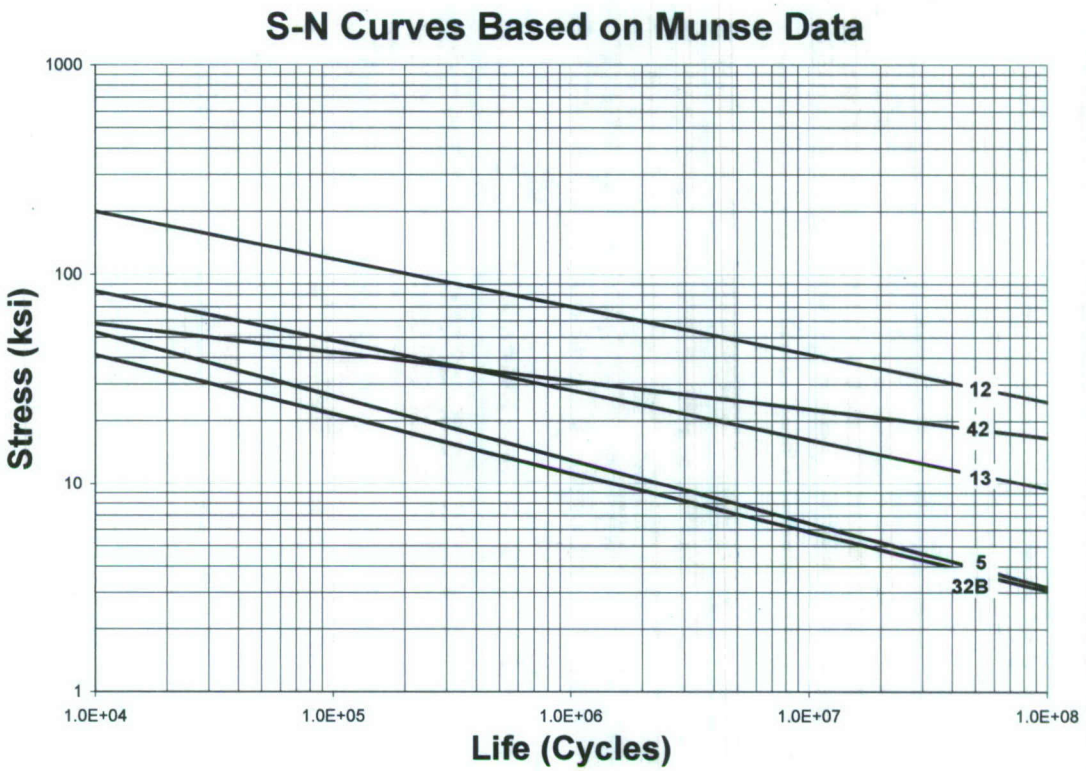

Figure 1.11 – Munse et al. (1983) Weld Detail Fatigue Curves

Mansour et al. (1996) presented the abbreviated joint classification approach, which is an adaptation of the nominal stress approach just discussed, with the welded joint fatigue curves as given in Table 1.2 developed by the British. The categories used for these curves are broader than those seen with the Munse et al. (1983) data. With the specific nominal stress approach, good predictions depend on the accuracy of the assumption that the joint detail used for prediction is exactly the same as the joint being predicted. The abbreviated nominal stress approach takes for granted that there may be geometric differences or even minor differences in the joint details of the joints being compared. The curves are therefore necessarily more conservative, but the likelihood of a detail failing before predicted is much smaller. Each of the categories presented by Mansour et al. (1996) were extensively evaluated, and Equations 1.1 and 1.2 are again used, replacing S with S_{nom}. The m and A values for these joints are found in Table 1.2 and the S-N curves are graphed in Figure 1.12. A table of brief descriptions of the various categories is found in Table 1.3. Gurney (1976) further discusses the British design rules and how they are to be used. More detail is provided on the joint classifications, and

graphic representations are also included. It is explained that the stress quoted in the fatigue curves is irrespective of any stress concentrations due to the weld profile, as the classifications take these into account. The stress levels used are the total combined stresses resulting from both shear and bending effects. Fricke (2002) describes a type of fatigue classification that employs curves like those developed by the British. The FAT class of a particular component is the nominal stress level in MPa for which it fails at 2 million cycles. For instance, if a component has a fatigue class FAT 90, it means that the component will fail at two million cycles when subjected to a stress level of 90 MPa. Fatigue curves like those developed by the British are useful for this versatile classification method, because the stress level for the FAT classification of a particular joint category can be picked off the graph by finding the point at which the joint category's curve intersects with the 2 million cycle line. The type of research performed in this project best fits the nominal stress approach that has been described. For this reason, the data from Munse et al. and Mansour et al. are very beneficial for comparison purposes.

Table 1.2 – British Standard Joint Classification (Mansour et al., 1996)

Class	*m*	Design Curve (A_0)	
		MPa	ksi
B	4.0	1.01×10^{15}	4.47×10^{11}
C	3.5	4.23×10^{13}	4.91×10^{10}
D	3.0	1.52×10^{12}	4.64×10^{9}
E	3.0	1.04×10^{12}	3.17×10^{9}
F	3.0	6.30×10^{11}	1.92×10^{9}
F2	3.0	4.30×10^{11}	1.31×10^{9}
G	3.0	2.50×10^{11}	7.63×10^{8}
W	3.0	1.60×10^{11}	2.88×10^{8}

Table 1.3 – *S-N* Data for British Standard Joint Details (Mansour et al., 1996)

Class	Description
B	• Plain steel in the as-rolled condition, or with cleaned surfaces, but with no flame cut edges or re-entrant corners • Full penetration butt welds, parallel to the direction of applied stress, with the weld overfill dressed flush with the surface and finish-machined in the direction of stress, and with the weld proved free from significant defects by non-destructive examination
C	• Butt or fillet welds, parallel to the direction of applied stress, with the welds made by an automatic submerged or open arc process and with no stop-start positions within the length • Transverse butt welds with the weld overfill dressed flush with the surface and with the weld proved free from significant defects by non-destructive examination
D	• Transverse butt welds with the welds made in the shop either manually or by an automatic process other than submerged arc, provided all runs are made in the flat position
E	• Transverse butt welds that are not class C or D
F	• Load-carrying fillet welds with the joint made with full penetration welds with any undercutting at the corners of the member dressed out by local grinding
F2	• Load-carrying fillet welds with the joint made with partial penetration or fillet welds with any undercutting at the corners of the member dressed out by local grinding (***The standard bolted joints under evaluation in the present research fall into his category***)
G	• Parent metal at the ends of load-carrying fillet welds which are essentially parallel to the direction of applied stress
W	• Weld metal in load-carrying joints made with fillet or partial penetration welds, with the welds either transverse or parallel to the direction of applied stress (based on nominal shear stress on the minimum weld throat area)

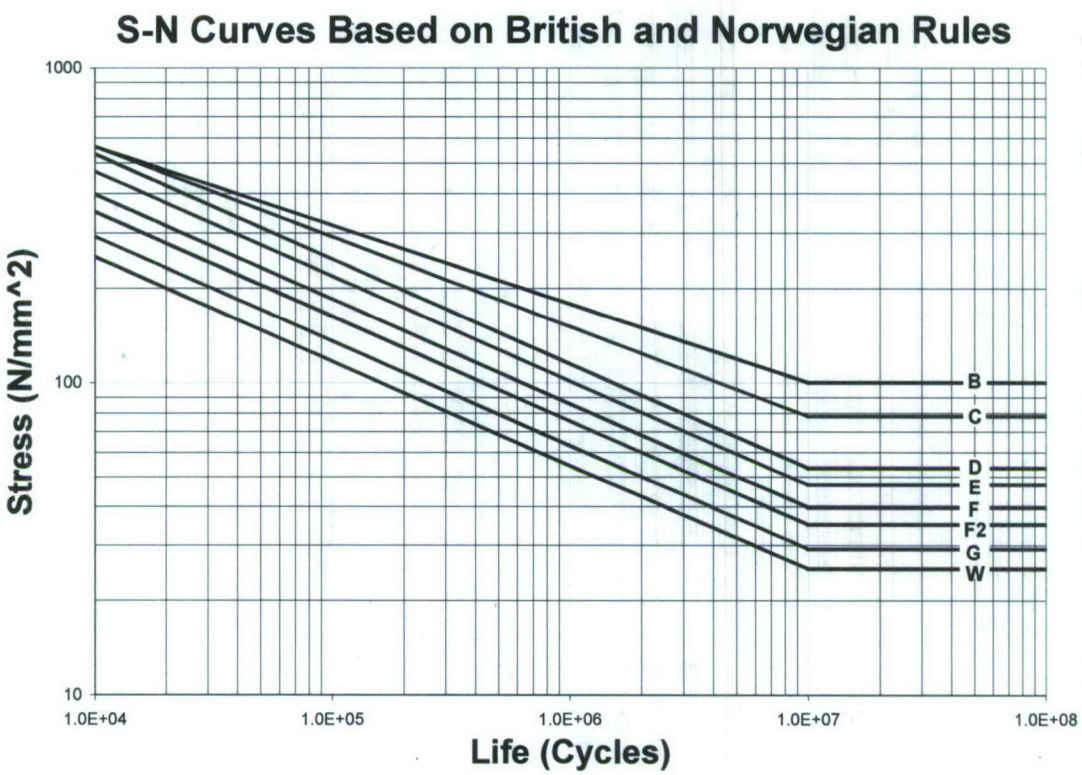

Figure 1.12 – British Standard Weld Detail Fatigue Curves (Mansour et al., 1996)

The hot spot-stress approach as described by Fricke (2002) and Fricke and Kahl (2005) uses finite element analysis to determine the location in a joint where the fatigue stress is the highest. This stress is referred to as the hot spot-stress (S_{hs}). Successful prediction with this method requires the FEA representation of the joint and geometries to be accurate. Problems may occur while determining S_{hs}, the difficulty being that it is usually a mesh-dependent mathematical singularity and will increase as the mesh size decreases. Techniques for overcoming these difficulties include extrapolation, e.g. using reference points at 0.4t/1.0t, 0.4t/0.9t/1.4t, or 0.5t/1.5t to extrapolate the stress at the hot spot, as well as refining the mesh around the hot spot and taking the stress at a pre-determined distance as the hot spot stress. Once the hot spot-stress is determined, it can also be related to the nominal stress with a geometric stress-concentration factor K_g as seen in Equation 1.4. The hot spot-stress approach then sets the S in Equations 1.1 and 1.2 to S_{hs} to obtain prediction curves.

$$S_{hs} = K_g \cdot S_{nom} \qquad \text{(Eq. 1.4)}$$

Another approach is the notch-stress approach, which takes the fatigue data and S_{nom} for smooth material specimens without notches, and then applies multiple stress concentration factors to account for the notches that exist in reality. The various stress concentration factors used attempt to account for gross geometry, weld geometry, eccentricity tolerance, angular mismatch, and un-symmetrical stiffeners idealized as beams. For example, Kendrick (2005) presents the following notch stress equations,

$$S_{notch} = K_g \cdot K_w \cdot S_{nom} \quad \text{(Eq. 1.5)}$$

where K_g is the stress concentration factor due to the gross geometry of the joint detail and K_w is the stress concentration factor due to the weld geometry, and,

$$S_{notch} = K_g \cdot K_w \cdot K_{te} \cdot K_{t\alpha} \cdot K_n \cdot S_{nom} \quad \text{(Eq. 1.6)}$$

where as before K_g is the stress concentration factor due to the gross geometry of the joint detail, K_w is the stress concentration factor due to the weld geometry, K_{te} is a stress concentration factor for the eccentricity tolerance (used for plate connections), $K_{t\alpha}$ is a stress concentration factor for the angular mismatch (used for plate connections), and K_n is a concentration factor for un-symmetrical stiffeners on laterally loaded panels (used when S_{nom} is derived from simple beam analyses).

An additional approach described is the mesh-insensitive approach formulated by Dong (2003). The mesh-insensitive approach is essentially the hot spot-stress approach, but deals with singularities differently. The nodal forces are used to compute the stress at or near the singularity because they are much less sensitive to the mesh than FEA-calculated stresses. This is especially beneficial in cases where more course meshes are employed.

Maddox (2000) presented many areas in which improvements could be made to supplement available fatigue life evaluation and prediction techniques. The effect of various factors on the fatigue life of welded steel joints were discussed, such as the influence of residual stress, plate thickness, material tensile strength, welding processes, weld quality, loading conditions, and environmental conditions. It is suggested that these various effects be included in fatigue evaluation to procure more accurate predictions of fatigue life.

1.4.5 Fatigue of Laser Welded Connections

Future efforts on this project will entail fatigue of laser welded connections. Therefore, a brief summary is given here. Caccese et al. (2006) compared the effect of weld geometries on laser welded HSLA-65 steel cruciforms (see Figure 1.13). New welding techniques were employed, specifically a combined laser and gas-metal-arc welding (GMAW) procedure. Advantages of laser welding were discussed, such as the ease of process automation, high welding speed, high productivity, increased process reliability, low distortion in the finished part, and no requirement for filler metal. Additionally, it was indicated that full-penetration welds are possible on materials up to one inch thick. The high speeds possible for this kind of welding are evident in that the specimens fabricated for this study were welded at rates of 10-75 in/min, and the low and focused heat output may make laser welding the preferred method for weldable hybrid joints. If integrated into the application of weldable hybrid joints for use in naval ships, these types of weld speeds could provide a very promising alternative to significantly more arduous task of joining the components of hybrid joints for an entire ship with fasteners. A number of fatigue tests were run on laser-welded cruciforms of different weld geometries available with laser welding, as well as some conventionally welded specimens. It was found that if weld geometry is carefully controlled, the hybrid laser welded specimens performed better than the conventionally welded specimens and what the currently accepted fatigue life equations would predict.

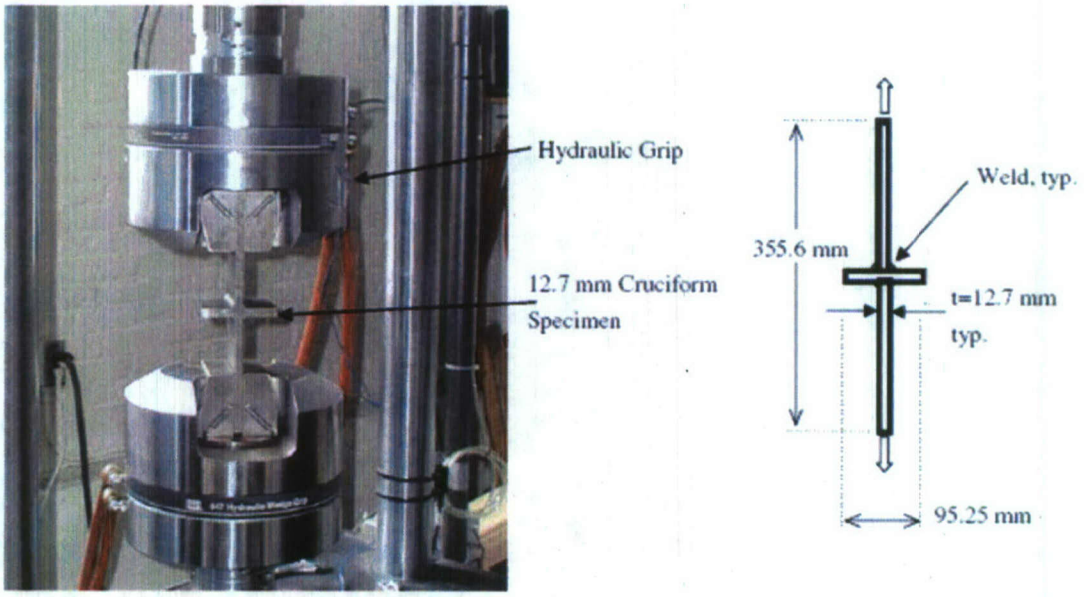

Figure 1.13 – Cruciform and Fatigue Test Fixture Used by Caccese et al. (2006)

1.4.6 Fatigue of Composite Materials

Some relevant research that has been performed on the fatigue life of composite materials will be described in this section. Van Paepegem and Degrieck (2001) proposed a one-dimensional fatigue damage model for glass fiber reinforced polymers. The following three stages of damage were described: 1) early microscopic cracks in the material, 2) gradual material degradation and reduction of stiffness, 3) accelerated fiber failure and unstable delamination growth. The damage model proposed was a coupled system of growth rate equations which was capable of keeping track of stress redistributions through the fatigue life of the specimen. Bending fatigue tests were performed and the damage model implemented into a finite element code for woven glass fiber reinforced epoxy specimens. Figure 1.14 depicts how the damage model represented experimental results. Van Paepegem and Degrieck proceeded to present a multi-dimensional damage model for fully reversed cyclic loading (2004).

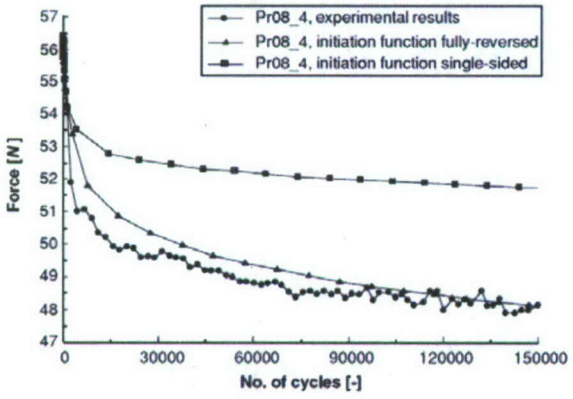

a) Damage initiation for fully-reversed bending with uncoupled and coupled growth rate equations.

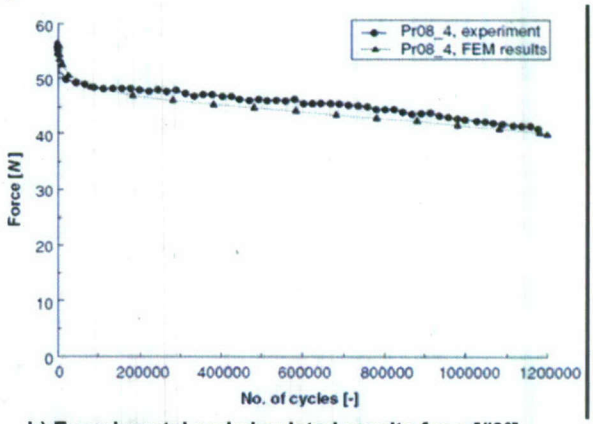

b) Experimental and simulated results for a $[\#0°]_8$ specimen with u_{max} = 19.5 mm and R_d = -1.0.

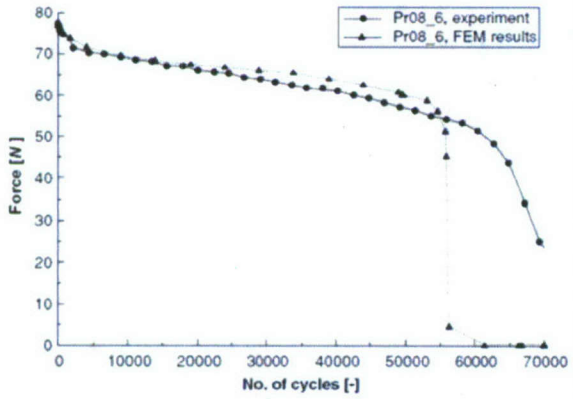

c) Experimental and simulated results for a $[\#0°]_8$ specimen with u_{max} = 27.0 mm and Rd = -1.0.

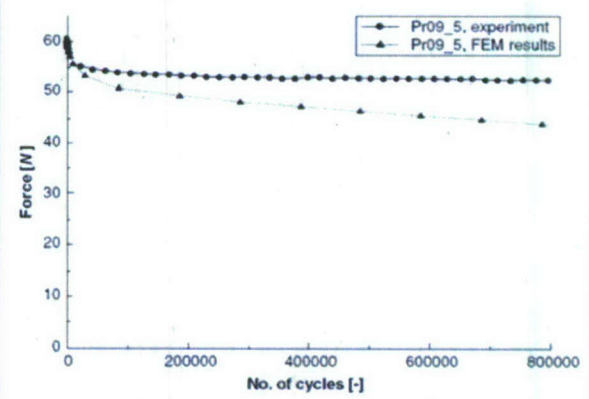

d) Experimental and simulated results for fully-reversed bending of a $[\#0°]_8$ specimen with u_{max} = 21.8 mm and Rd = -1.0.

Figure 1.14 – Results of Model Presented by Van Paepegem and Degrieck (2001)

Fully reversed loading was considered to be the most harmful to fiber reinforced composites, hence the choice of bending fatigue over axial tension/compression tests. Differential damage growth rate equations were coupled to represent the interaction between different damage modes. These coupled equations were in turn able to simulate the bending force over the force-cycle history in a specimen subjected to this bending fatigue tests. Implementing the coupled growth rate equations into finite element simulations provided reliable predictions of the evolution of damage state variables, in-plane stresses, and stiffness degradation (see Figure 1.15).

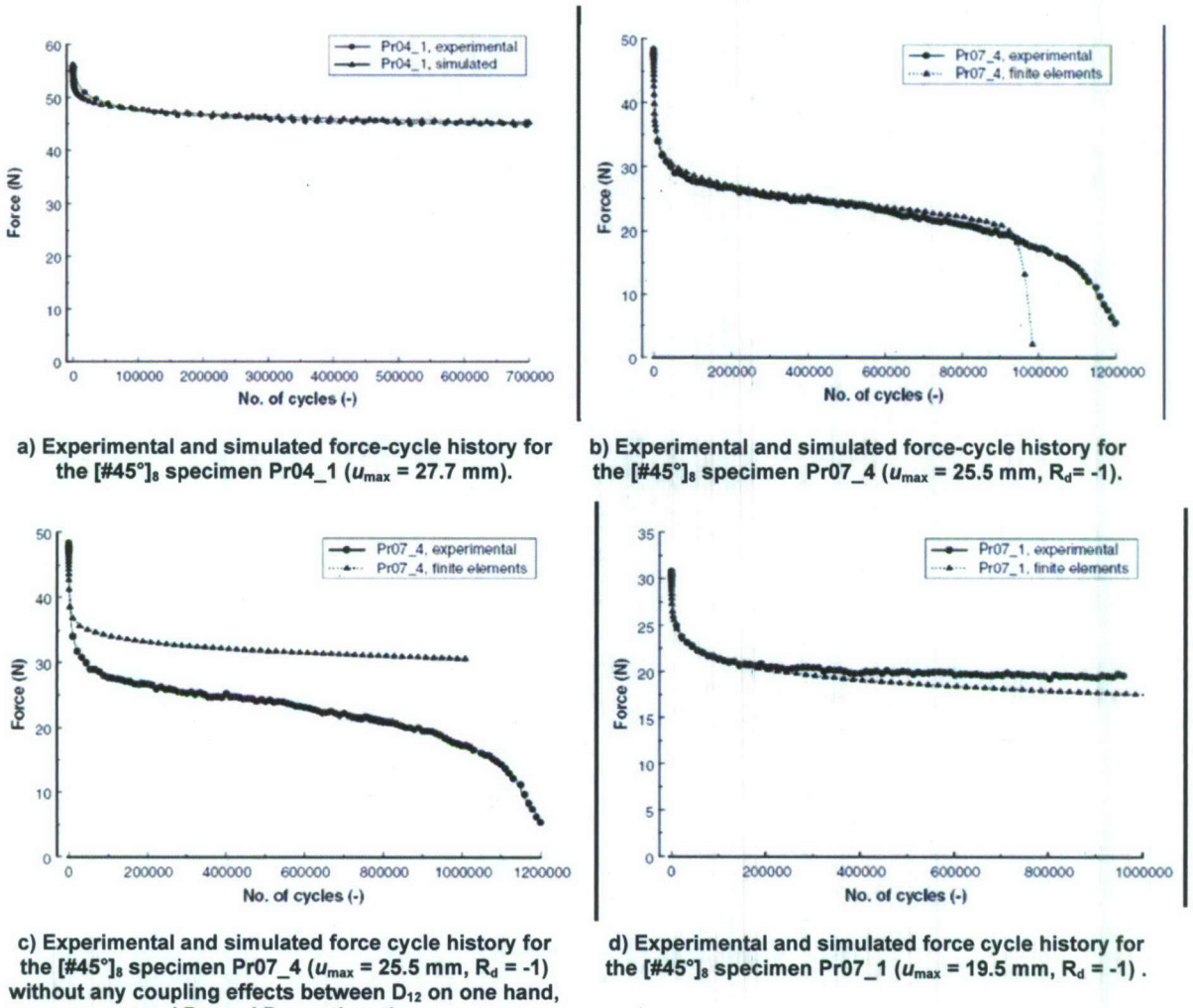

a) Experimental and simulated force-cycle history for the $[\#45°]_8$ specimen Pr04_1 (u_{max} = 27.7 mm).

b) Experimental and simulated force-cycle history for the $[\#45°]_8$ specimen Pr07_4 (u_{max} = 25.5 mm, R_d= -1).

c) Experimental and simulated force cycle history for the $[\#45°]_8$ specimen Pr07_4 (u_{max} = 25.5 mm, R_d = -1) without any coupling effects between D_{12} on one hand, and D_{11} and D_{22} on the other.

d) Experimental and simulated force cycle history for the $[\#45°]_8$ specimen Pr07_1 (u_{max} = 19.5 mm, R_d = -1) .

Figure 1.15 – Results of Model Presented by Van Paepegem and Degrieck (2004)

Mouritz (2006) presented a simple model for estimating the fatigue life of 3D composites that exhibit linear fatigue life S-log(N) curves. It was found that the lack of published fatigue data seriously limited the applicability of the model, as well as a more comprehensive verification of it, and more research was called for. The model,

$$S_{3D} = \frac{\sigma_{3D}}{\sigma_{2D}}\left(\sigma_{2D} + m \log N\right) \qquad \text{(Eq. 1.7)}$$

was proposed, where σ_{3D} and σ_{2D} are the strength values of the 3D composite and the 2D laminate, and m is the experimentally determined slope of the fatigue-life curve for the 2D laminate. The value of m is assumed to be the same for the slope of the S–log(N) curve of the 3D composite. Equation 1.7 was applied to various sets of fatigue data for carbon-epoxy laminates currently available under tension-tension fatigue, cyclic compression fatigue, and flexural fatigue. The flexural fatigue graph presented can be seen in Figure 1.16. This data is of carbon/epoxy laminates with z-binder fibers, or pins, in the through-thickness direction of the laminates.

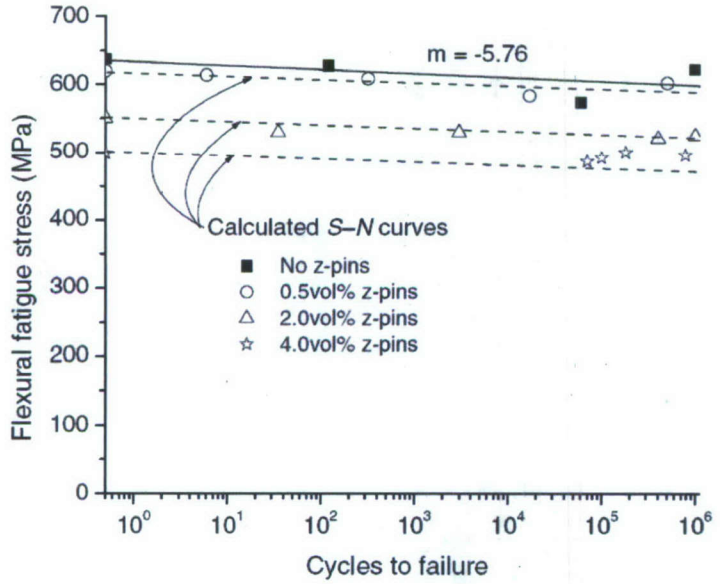

Figure 1.16 – Flexural Fatigue Data Presented by Mouritz (2006)

Mahfuz et al. (2000) used a concept referred to as fatigue modulus to develop fatigue life prediction models for thick-section S2-glass/vinyl ester composites. Fatigue modulus is the slope of a stress-strain curve at a given cycle, n. Three prediction models were developed, each including more parameters than the previous model. The models were of the form,

$$N_f = [B(1\text{-}r)]^{1/C} \qquad \text{(Eq. 1.8)}$$

where N_f is the predicted cycles to failure, r is the stress level (applied stress/ultimate stress), and B and C are material properties. In the first model, B and C were taken to be constant with respect to the stress level, r, and thickness, t. In the second model, they were functions of the stress level but not the thickness. In the third model, B and C were taken to be functions of both stress level and thickness. Flexural fatigue tests were performed at various stress levels on specimens of various thicknesses to evaluate the accuracy of the predictions of the three fatigue life models. The tables and graphs of this data can be found in Figure 1.17 and Table 1.3. The experimentation verified that for accurate prediction of fatigue life in thick-section composites, the thickness of the specimens must be taken into account (as in the third model). The fatigue modulus was found to be a function of cycle number, applied stress, and thickness. The resulting expressions for B and C were determined to be,

$$B = \left(-1.8e12t^2 + 2.2e12t - 6.4e11\right) \times 10^{r\left(-208t^2 + 246t - 63\right)} \qquad \text{(Eq. 1.9)}$$

$$C = -\left(-32r^2 + 37.2r - 13\right) + \left(11r^2 - 12r + 5.7\right) \qquad \text{(Eq. 1.10)}$$

and the values of N_f calculated with these expressions for B and C were within 10% of the experimental values.

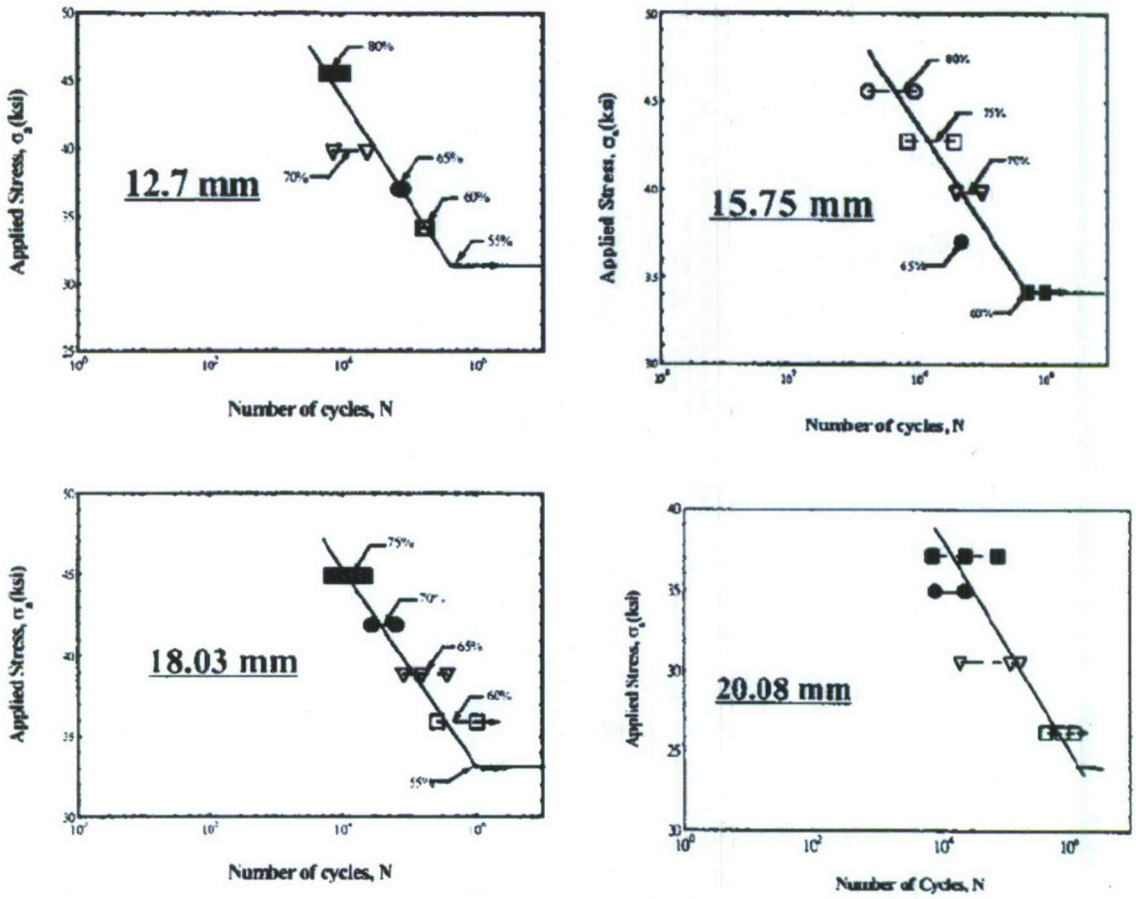

Figure 1.17 – Mahfuz et al. (2000) Fatigue Graphs

Table 1.2 – Mahfuz et al. (2000) Fatigue Data

Thickness	Applied stress level	Specimen ID	Cycles to failure	Thickness	Applied stress level	Specimen ID	Cycles to failure
12.7 mm (0.50 in.)	80%	20LFS5	5,862	15.75 mm (0.62 in.)	80%	25LFS5	1,759
		20LFS13	10,432			25LFS11	8,905
	70%	20LFS3	7,454		75%	25LFS6	6,709
		20LFS10	23,422			25LFS12	35,974
	65%	20LFS6	77,964		70%	25LFS4	96,266
		20LFS11	68,234			25LFS13	38,432
	60%	20LFS7	157,002		65%	25LFS3	47,002
		20LFS9	174,210			25LFS8	46,502
	55%	20LFS4	Run-out		60%	25LFS9	529,107
		20LFS8	456,782			25LFS10	Run-out
Thickness	**Applied stress level**	**Specimen ID**	**Cycles to failure**	**Thickness**	**Applied stress level**	**Specimen ID**	**Cycles to failure**
18.03 mm (0.71 in.)	75%	30LFS4	11,616	20.08 mm (0.82 in.)	85%	P2SP6	22,347
		30LFS11	6,865			P2SP8	6,791
		30LFS15	20,841			P2SP10	7,513
	70%	30LFS3	27,010			P1SP14	73,326
		30LFS12	63,239		80%	P1SP10	21,468
	65%	30LFS6	80,418			P1SP11	23,583
		30LFS13	153,234			P2SP3	18,617
		30LFS14	361,126		70%	P1SP8	116,339
	60%	30LFS5	253,962			P1SP6	166,988
		30LFS10	Run-out			P1SP9	421,810
	55%	30LFS7	Run-out		60%	P2SP4	437,294
		30LFS9	Run-out			P1SP12	779,005
						P1SP13	Run-out
						P2SP7	Run-out
					55%	P2SP1	Run-out
						P2SP5	Run-out

Shah, Khan and Mouritz (1996) investigated the effects of stitching on the fatigue life of GRP laminates. E-glass/vinyl ester laminates were stitched and then tested in zero-to-tension loading. It was found that while there was no significant change in the strength, the fatigue resistance was significantly reduced by stitching, especially at low cyclic stresses. A graph of the fatigue data from this study is found in Figure 1.18.

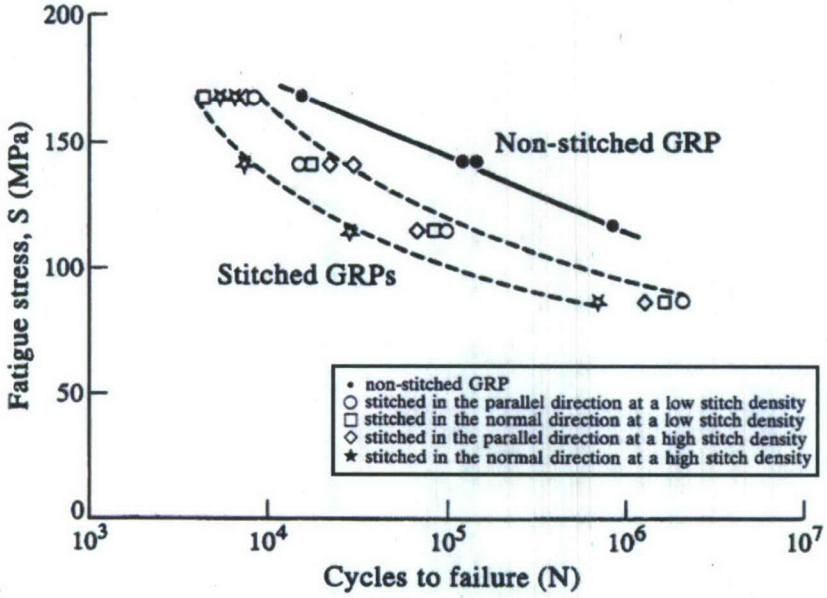

Figure 1.18 – Fatigue Data for Stitched Composites (Shah Khan and Mouritz, 1996)

Shivakumar et al. (2005) and Chen et al. (2006) proposed and compared three different total fatigue life models for composite laminates. The focus was on delamination and the delamination growth rate. The models are meant to predict the delamination growth rate in all three domains of which the fatigue life is composed: The subcritical growth region, the G dominate region, and the unstable region (Figure 1.19).

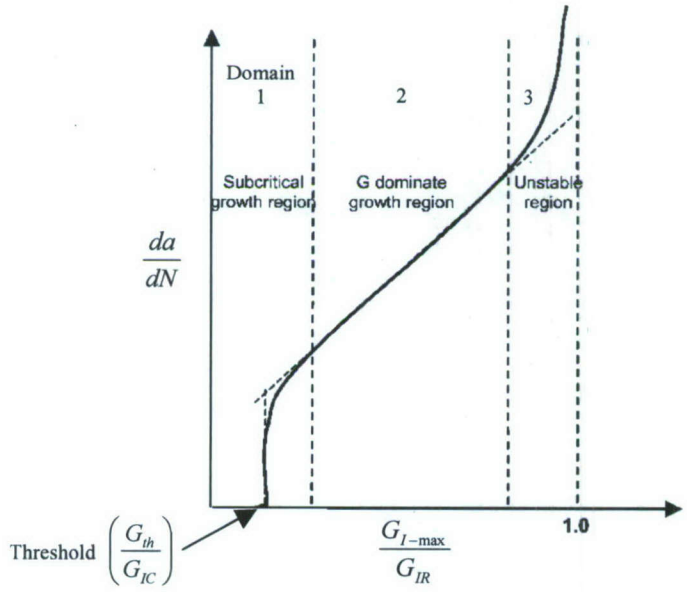

Figure 1.19 – Shivakumar et al. (2005) and Chen et al. (2006) Delamination Domains

The equations presented for the three models are as follows,

$$\frac{da}{dN} = A\left(\frac{G_{I-\max}}{G_{IR}}\right)^{m} \frac{\left(1-\left(\frac{G_{Ith}}{G_{I-\max}}\right)^{D_1}\right)}{\left(1-\left(\frac{G_{I-\max}}{G_{IR}}\right)^{D_2}\right)} \qquad \text{(Eq. 1.11)}$$

$$\frac{da}{dN} = 10^{\left[A_1\left(\frac{G_{I-\max}}{G_{IC}}\right)+m_1\right]} \frac{\left[1-\left(\frac{G_{Ith}}{G_{I-\max}}\right)^{D_1}\right]}{\left[1-\left(\frac{G_{I-\max}}{G_C}\right)^{D_2}\right]} \qquad \text{(Eq. 1.12)}$$

$$\frac{da}{dN} = A_c\left(\frac{G_{I-\max}}{G_{IC}}\right)^{m_c} \frac{\left[1-\left(\frac{G_{Ith}}{G_{I-\max}}\right)^{D_1}\right]}{\left[1-\left(\frac{G_{I-\max}}{G_C}\right)^{D_2}\right]} \qquad \text{(Eq. 1.13)}$$

where $\frac{da}{dN}$ is the delamination growth rate, G_C is the critical energy release rate, G_{IC} is the opening Mode I interlaminar fracture toughness, $G_{I\text{-max}}$ is the maximum cyclic mode I energy release rate, G_{IR} is the opening Mode I interlaminar fracture toughness resistance, G_{Ith} is the threshold value of mode I energy release rate, and D_1, D_2, A, A_1, A_c, m, m_1, and m_c are material constants determined by fitting the equations they are contained in to experimental data. Equation 1.11 belongs to the first total fatigue life model. This model is referred to as Method 1, or equation with G_{IR} normalization. Equation 1.12 belongs to Method 2, or log-linear equation with G_{IC} normalization. Equation 1.13 is from the third model, Method 3. This is also called the log-log equation with G_{IC} normalization. Of the three models, Method 1 was the most successful for predicting the fatigue life under both typical and aggressive loading. Tang et al. (2000) developed a fatigue model for E-glass/vinyl ester composites subjected to tension-tension loading. The model was experimentally verified through experiments at four stress levels, three environments (air, freshwater, and saltwater), and two test frequencies (2Hz and 10Hz). The model was a

cumulative damage model for which the change in modulus was used to determine the state of damage. Similarly to the approach of Shivakumar et al. (2005) and Chen et al. (2006), the cumulative damage was taken to consist of three domiains: initial damage growth, a more linear mid-section, and then damage growth near the end of the growth cycle. However, since the experiments performed did not indicate an initial growth region, this domain and the associated equation were not included in the model. Through integration of the damage rate equation, the predictive fatigue model was obtained as

$$\log \sigma_{\max} = m \log N_f + C \qquad \text{(Eq. 1.14)}$$

where m and C are determined experimentally. It was mentioned that C was a function of frequency. The slopes of the fatigue curves for the three different environmental conditions can be seen in Figure 1.20.

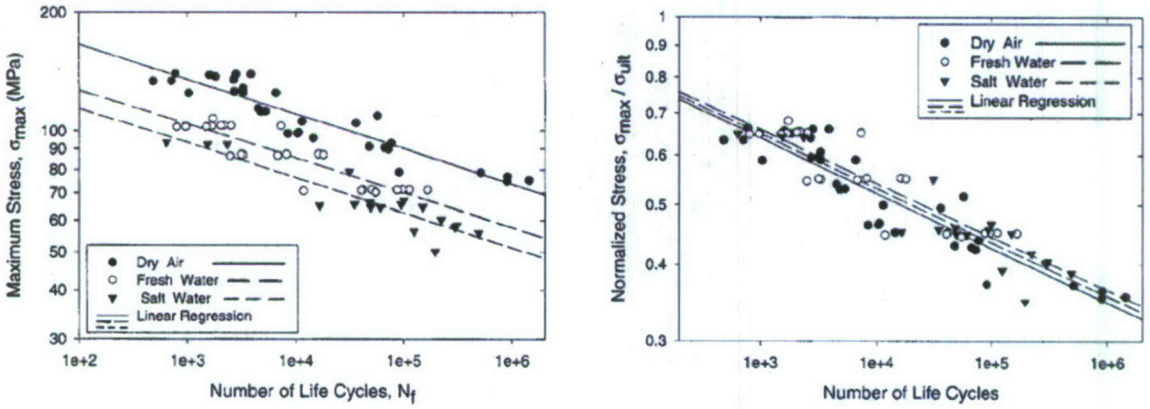

Figure 1.20 – Standard and Normalized *S-N* Curves of Tang et al. (2000) 10Hz Tests

It was determined that the similarity of the linear constants and m values resulting from the data of the three environments validated combining them to create one generalized curve. This curve can be seen in Figure 1.21. The *S-N* equation generated form this generalized data is,

$$S_{\max}^{11.40} N_f = \frac{13.11}{1 + \frac{8}{f}} \qquad \text{(Eq. 1.15)}$$

where N_f is the number of cycles to failure, $S_{\max}$ is the normalized maximum stress ($\sigma_{\max}$/ σ_{ult}), and f is the frequency.

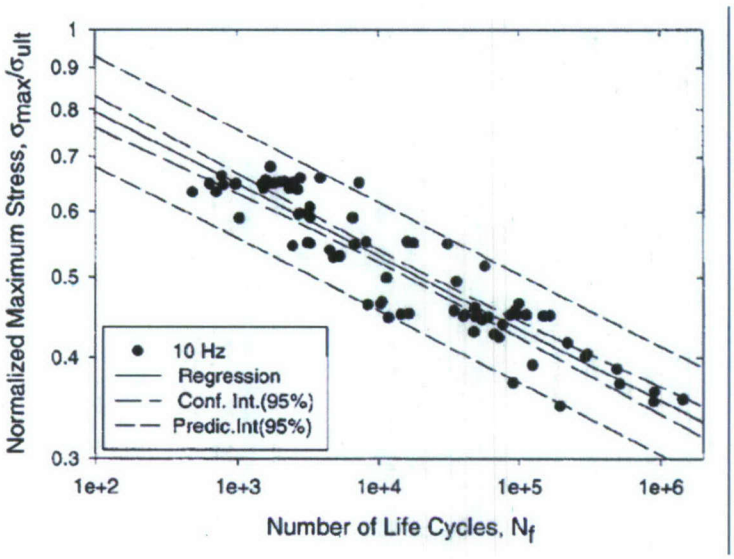

Figure 1.21 – General Normalized *S-N* Curve of Tang et al. (2000) 10Hz Tests

Kim and Zhang (2001) also used fatigue damage for life prediction in E-glass/vinyl ester composites. Damage rate equations are used to obtain the following equation for fatigue life,

$$N = \frac{\sigma_u^{-\beta}}{\alpha(\beta - 1)}\left[\left(\frac{\sigma_{\max}}{\sigma_u}\right)^{1-\beta} - 1\right] \qquad \text{(Eq. 1.16)}$$

where α and β are determined experimentally. The experimental data from the tests performed along with this predictive curve can be seen in Figure 1.22.

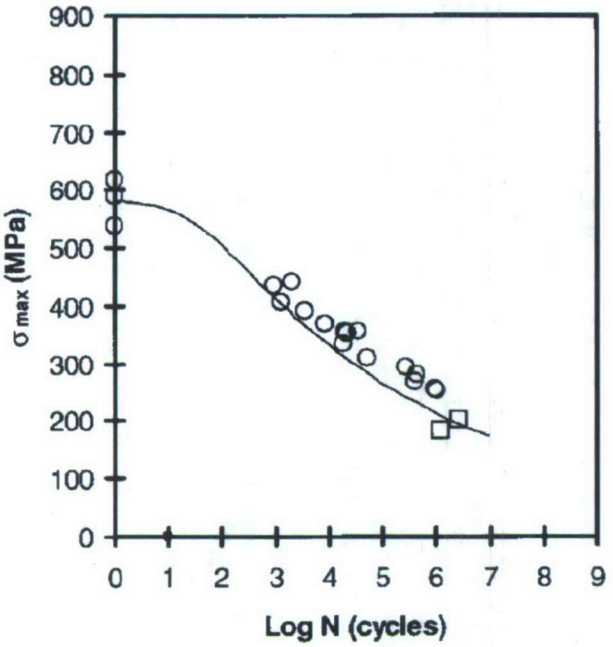

Figure 1.22 – Experimental Data and Predictive Curve from Kim and Zhang (2001)

As can be clearly seen, much of the available literature on topics relevant to the current research warrants the fatigue testing of different hybrid joint connections. There is much research that can be done, especially in the areas of more novel connection techniques such as laser-weldable hybrid joints composed of perforated steel inserts and E-glass reinforced composites. Many concepts that have shown much promise in static tests are in need of fatigue life characterization. Fatigue data is available for the various materials that compose hybrid joints. It would be beneficial to perform similar experimentation on full hybrid joints and compare the resulting data to that available for the individual components. This would make it possible to evaluate the effects of the interactions between the different components, and would also make the implementation of novel joining techniques into practical applications more viable.

2. Finite Element Analysis of Representative Ship Hull Plating

Flexure fatigue testing for out of plane loads on hybrid connections is the primary object of this research. Flexure fatigue loading of a built-in type of connection consists of a combination of bending moment and shear force acting through the connection. The first step in the experimental effort is to determine the types and relative magnitude of shaer and moment loading to be used during the tests. This should be based upon loads potentially experienced in the joints of such a vessel. The most efficient method to test the fatigue life of these hybrid connections is to model a smaller sub-component section of the panel that represents a location with the more extreme loading experienced. A model of the joint to be tested, shown in Figure 2.1, is similar to those shown in Figure 1.6. In order for this to be sufficiently accomplished, several parameters must be determined, especially the lever arm, L, which controls the ratio of shear force to moment. To accurately represent the fatigue loading it is essential to quantify this ratio, which can also be thought of as the moment arm of the joint. This knowledge is needed before meaningful testing can begin since this ratio may control the failure mode. High values of shear relative to moment will cause a predominance of delamination failures at the plane of maximum shear. In the converse case, high tension and compression stresses at the outer fibers will cause degradation governed by matrix cracking and fiber breakage. A preliminary finite element analysis was undertaken to obtain realistic and appropriate values for the moment arm, or moment to shear ratio.

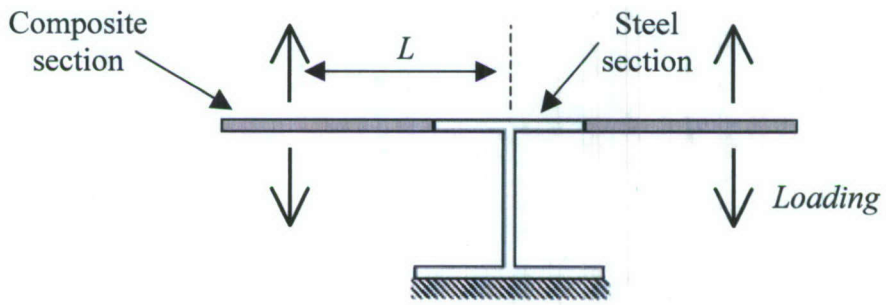

Figure 2.1 – Joint Model

The types of connections used by Kabche et al. (2007b) are those of interest for fatigue analysis in this research. For this reason, the panels analyzed in that study are replicated here. They studied the hybrid connections in the lifting body of a ship with an advanced hull form. Lifting bodies like the one pictured in Figure 2.2 provide enhanced sea-keeping through reduction in motions and higher lift-to-drag ratios. It is desirable to use stiffened E-glass composite panels joined to steel sub-structures for the skin of these lifting bodies. Kabche et al. (2007b) chose to analyze the panels on the underside of the lifting body. These panels were to be bolted to the steel framework of lifting body so as to be easily removable in order to access equipment housed within. The four-panel testing region studied can be seen in Figure 2.3.

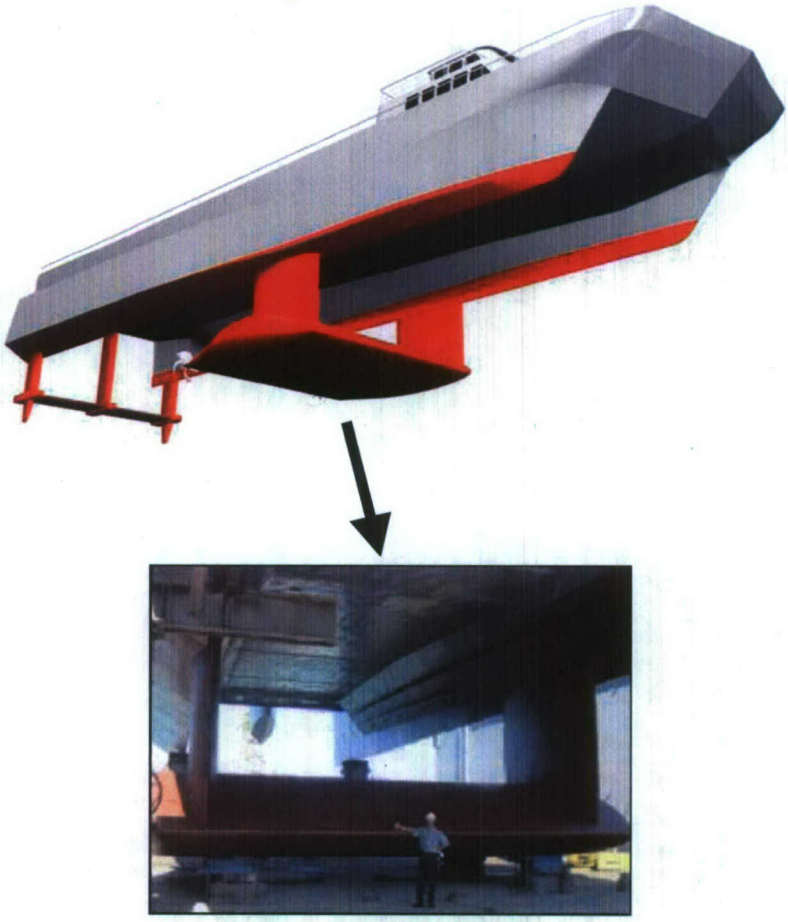

Figure 2.2 – Reconditioned Surface Effect Ship (SES-200) with Underwater Lifting Body

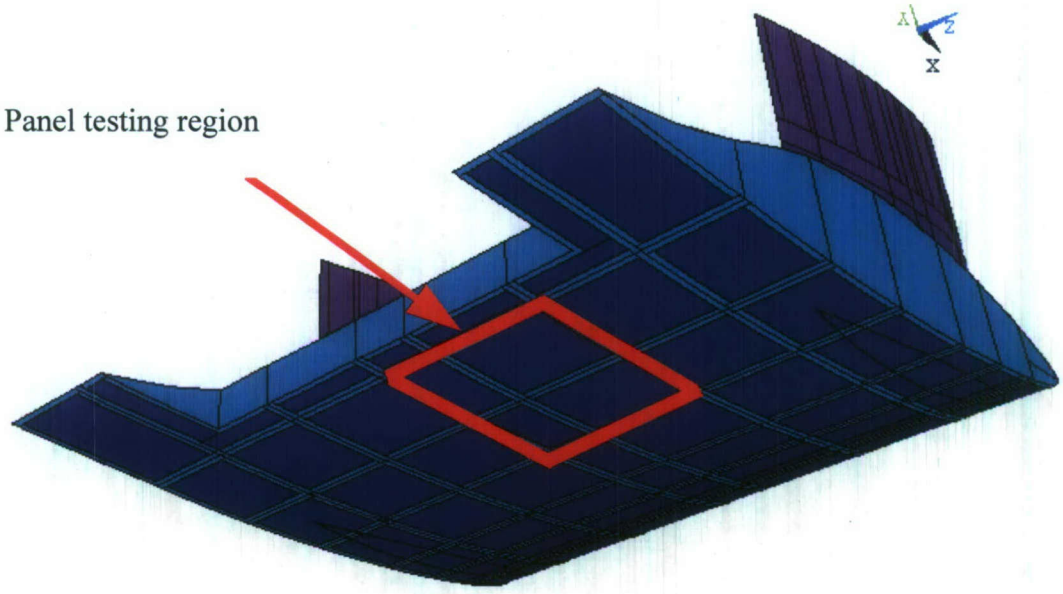

Figure 2.3 – Hybrid Lifting Body Showing Region Selected For Panel Testing

Implementing some concepts and results from preceding studies, an introductory finite element analysis was performed on similar yet simplified panels to investigate and determine the moment arm values. The moment arm values at which the load and moment were at a maximum would be taken and applied to the smaller panel section actually used in the fatigue testing. The representative joint should be applicable for other ships with similar panel sizes. The determination of realistic values for the relative shear and moment forces was the practical motivation which led to the preliminary finite element analysis

Using the ANSYS finite element software, two analyses were performed; one of a simplified flat 6-ft x 6-ft panel section and the other of a similar 10-ft x10-ft section. The basic geometry of the plate used for analysis is shown in Figure 2.4. The two plates analyzed were square with dimensions a=b=6-ft and a=b=10-ft, respectively. Three equidistant stiffeners were placed across the plate. Those used in the 6-ft x6-ft plate had

a length l_s of 4-ft, while those used in the 10'x10' plate had an l_s of 8-ft. The pressure of 12 psi applied to the panels was based upon a design analysis described in Thompson et al. (2005). Three boundary condition cases were evaluated in both analyses by varying the rigidity of the stiffeners as follows:

1. Stiffened composite plate: simply supported at boundary
2. Stiffened composite plate: clamped at boundary
3. Stiffened hybrid plate (steel border): clamped at boundary

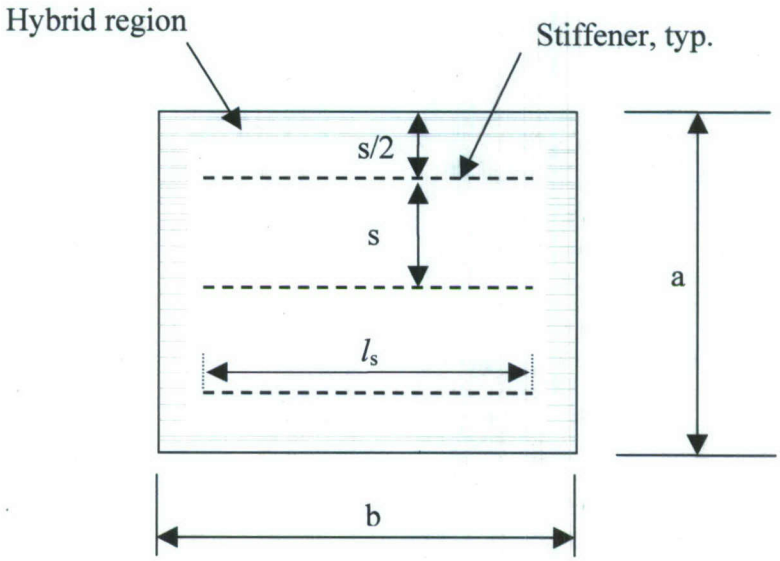

Figure 2.4 – Plate Geometry Used in the Finite Element Study

In the clamped and simply supported cases, the plate extended fully to the boundary. In the hybrid case, a steel border 0.75-in thick and six inches wide surrounded the composite to model the hybrid region. The outer boundary of the steel border was clamped. These details caused this analysis to be stiffer than the other two cases. The represented stiffness of the hybrid connection used a method similar to Kabche et al. (2007b). In that case, the hybrid region consisted of a composite panel sandwiched between the flange of a W14x53 beam and a 0.25-in doubler plate. Since the stiffness of the steel significantly surpasses that of the composite material, this hybrid region in this case was approximated as a 0.75-in steel flange portion alone.

The plates were constructed with SHELL93 8-node shell elements, with an element size of 1inx1in determined as satisfactory through a convergence study. The ANSYS shell layup function was employed to create the elements, using the layup pattern and material properties of the plates being fabricated for testing in conjunction with the analysis described in Section 3. It was found that for the target plate thickness of 0.75-in, 21 layers of the fiberglass fabric were needed. Since the fabric being used was bidirectional knit fabric (2 perpendicular unidirectional layers knit together), this was entered into the shell layup function as 42 unidirectional layers of appropriate thickness (0.0179-in). The layup configuration was as close to quasi-isotropic as possible with 21 bidirectional layers. The layup configuration is denoted as follows:

$$\left|(\pm 45/0/90/\mu\, 45/90/0)_2\,(\pm 45/0/90)\overline{(90/0)}\right|_S$$

The lamina properties were based on those determined in tests previously performed on the coupons of materials being used for this research (Kabche et al., 2006). Those properties were integrated into a composite material properties program named COMPRO®. These values, stored in COMPRO®, were designated as the properties for the individual lamina in the ANSYS shell layup function. The properties can be found in Table 2.1. The stiffeners were approximated as BEAM189 3-node beam elements for simplicity and compatibility with the 8-node shell elements, and were assumed to have tapered ends that stop short of the boundary as shown in Figure 2.4.

Table 2.1 – Lamina Properties

Lamina Properties (psi)	
E_1	5.500×10^6
E_2	1.531×10^6
E_3	1.531×10^6
G_{12}	4.629×10^5
G_{13}	4.629×10^5
G_{23}	3.274×10^5

A study of the effect of the relative rigidity was performed by varying the bending rigidity of the stiffeners (EI), while keeping all other parameters constant. This provided a simple but effective method of evaluating the influence of stiffeners on force distribution. The plate rigidity was calculated by COMPRO®. This was done by entering the layup configuration into the program, the lamina properties already existing. Through standard composite material theory, COMPRO® then calculated D_x as one of the laminate properties. The value calculated was 1.054×10^5 lb-in for the 0.75-in. thick laminate of the layup described. This rigidity was then used along with the stiffener rigidity (lb-in^2) to obtain a relative stiffener to plate rigidity (in) that could be varied. Since the plates were not scalable, the stiffener length to plate length ratio changing, the data obtained in this study was not normalized or non-dimensionalized.

Figures 2.5 and 2.6 show the results of the displacement at the central node for the three boundary condition cases. It is observed that stiffeners have little influence on the overall response until a relative stiffener to plate rigidity ratio of about 9.5-in. A sensitive region follows where an increase in relative rigidity causes a substantial reduction in displacement. In both the 6-ft x 6-ft and 10-ft x10-ft cases, relative rigidities above 9500-in improve the overall stiffness very little. However, while 6-ft x 6-ft plate has essentially reached the fully effective state at a relative rigidity of 950-in, the displacement for the 10-ft x10-ft plate seems to level out more towards the relative rigidity of 9500-in. Figures 2.7 and 2.8 depict the nodal contour results for the transverse displacement with the relative rigidity set to 950in in the 6-ft x 6-ft and 10-ft x 10-ft plates, respectively.

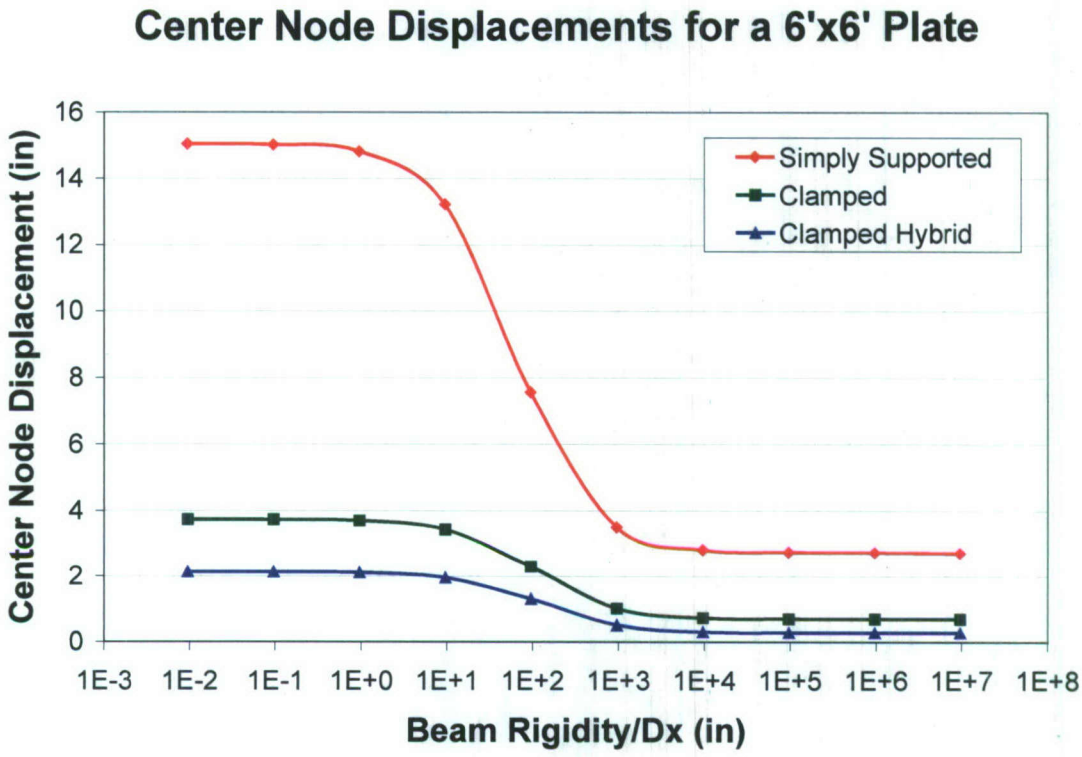

Figure 2.5 – 6'x6' Plate Center Node Displacement vs. Relative Rigidity

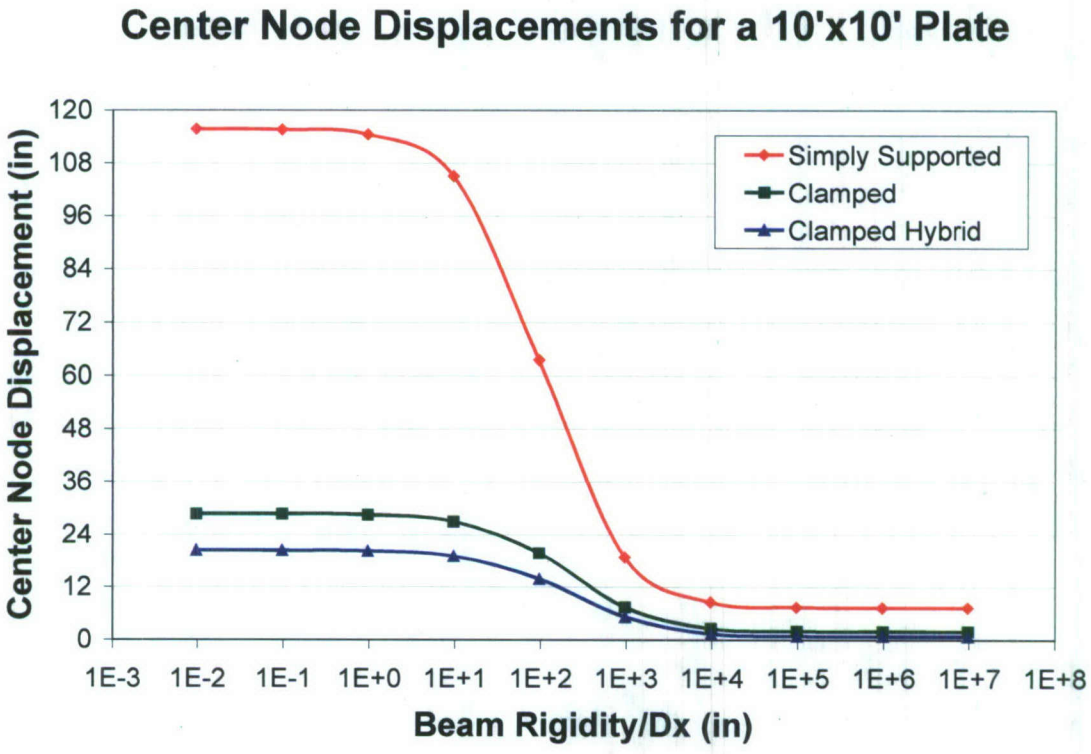

Figure 2.6 – 10'x10' Plate Center Node Displacement vs. Relative Rigidity

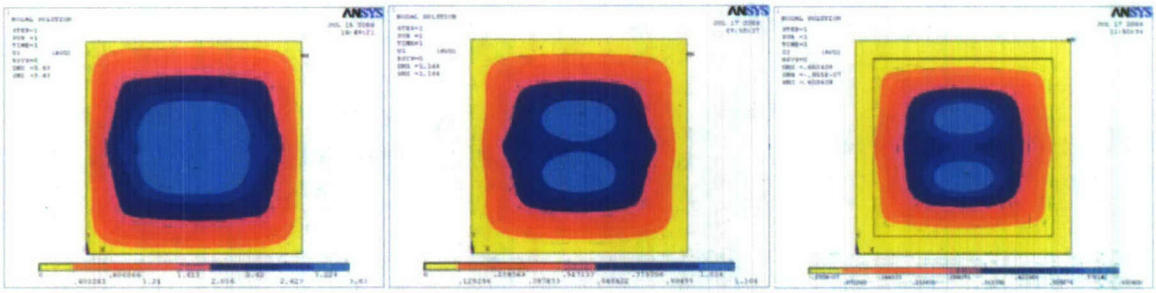

Figure 2.7 – 6'x6' Stiffened Plate Displacement Contour Plots (Left: simply supported composite, Center: clamped composite, Right: clamped hybrid)

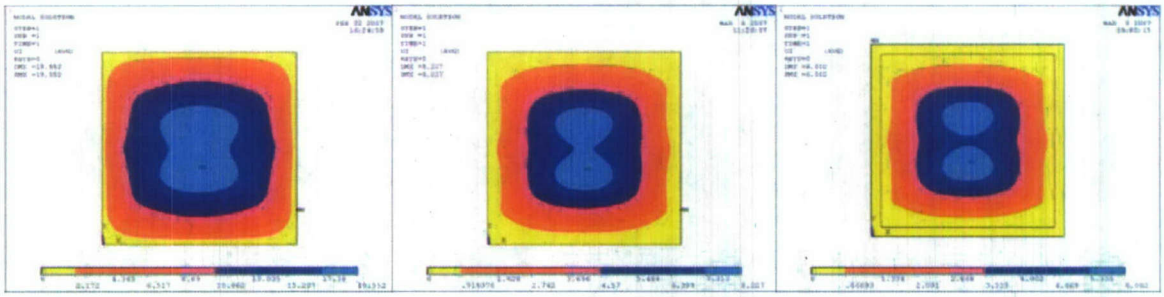

Figure 2.8 – 10'x10' Stiffened Plate Displacement Contour Plots (Left: simply supported composite, Center: clamped composite, Right: clamped hybrid)

Following the center node displacement evaluation, analyses of the load and moment reactions at the left and bottom edges (see Figure 2.9) were performed. The resulting values are graphed for various boundary conditions and relative rigidities in Figures 2.10a-j and 2.11a-j. Figures 2.9 a-j are the results for the 6-ft x 6-ft plates, and 2.10a-j are those for the 10-ft x10-ft plates. For both the 6-ft and 10-ft cases, the force reactions of both the left and bottom edges are shown first. This is done for the simply supported case, the clamped case, and finally the clamped hybrid case. After the force reactions are shown, the moment reactions are presented. This is done in a similar fashion to the force reactions, with the left and bottom edges represented. However, since the simply supported case does not resist moments, only the data for the clamped and clamped hybrid cases are available. In all graphs, regardless of the case, there are 10 data series.

Each of these represents a relative rigidity. The rigidity of the beams was varied for the analysis, which of course, also varied the beam-to-plate relative rigidity ratio. These rigidities were arbitrarily selected to represent a full spectrum, even though the upper and lower end cases may not even be possible to physically reproduce. The lowest relative rigidity was 9.5×10^{-3} in and the highest was 9.5×10^{6} in. The effect of the stiffeners is clearly represented in the graphs. The stiffeners are perpendicular to the left edge of the plate, and for all cases, they transmit a greater amount of force to the corresponding locations on that edge as the rigidity is increased. This results in the peaks which are very apparent in the graphs of the left edge. In contrast, the stiffeners are parallel to the bottom edge, and the loads are distributed more equally to the bottom edge over the length of the stiffeners as the rigidity is increased. This is especially true for the moments and for the 10-ft x10-ft plate because it is larger and there is more space for the stiffener to flatten out the effect.

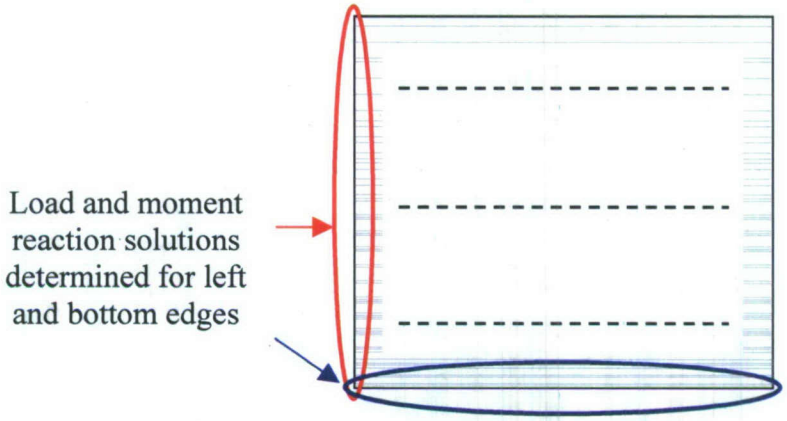

Figure 2.9 – Edges at which Load and Moment Reaction Solutions were Determined

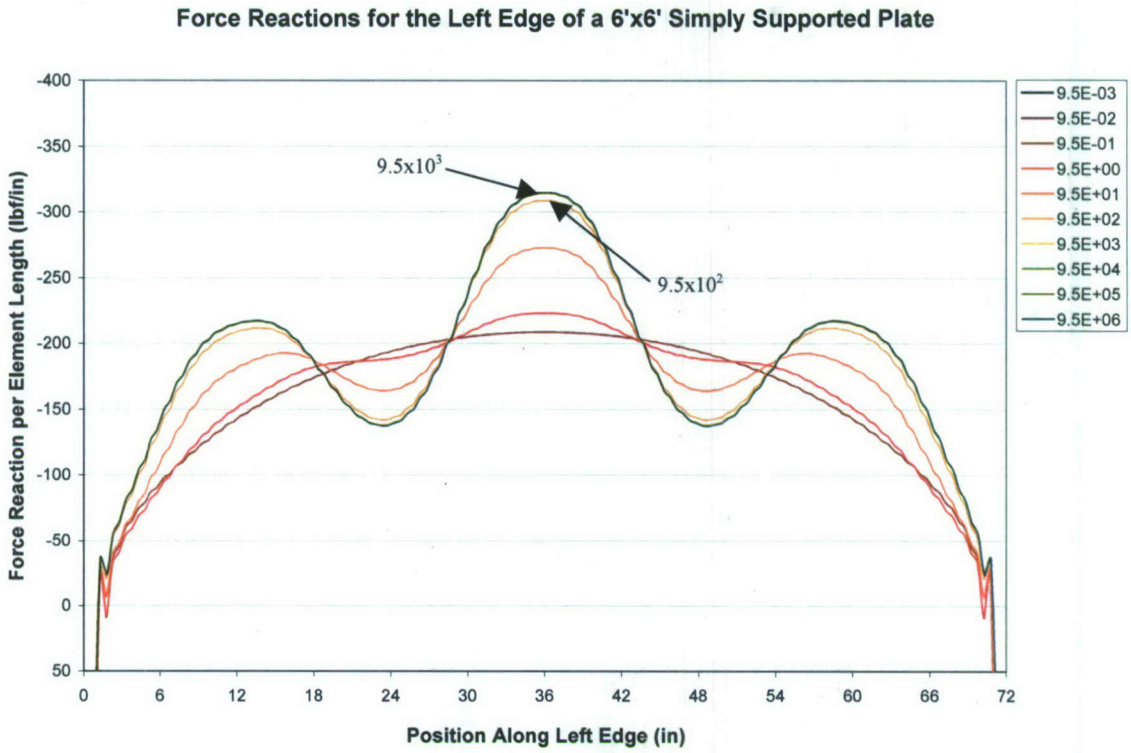

Figure 2.10a – 6'x6' Simply Supported Plate: Left Edge Force Reactions

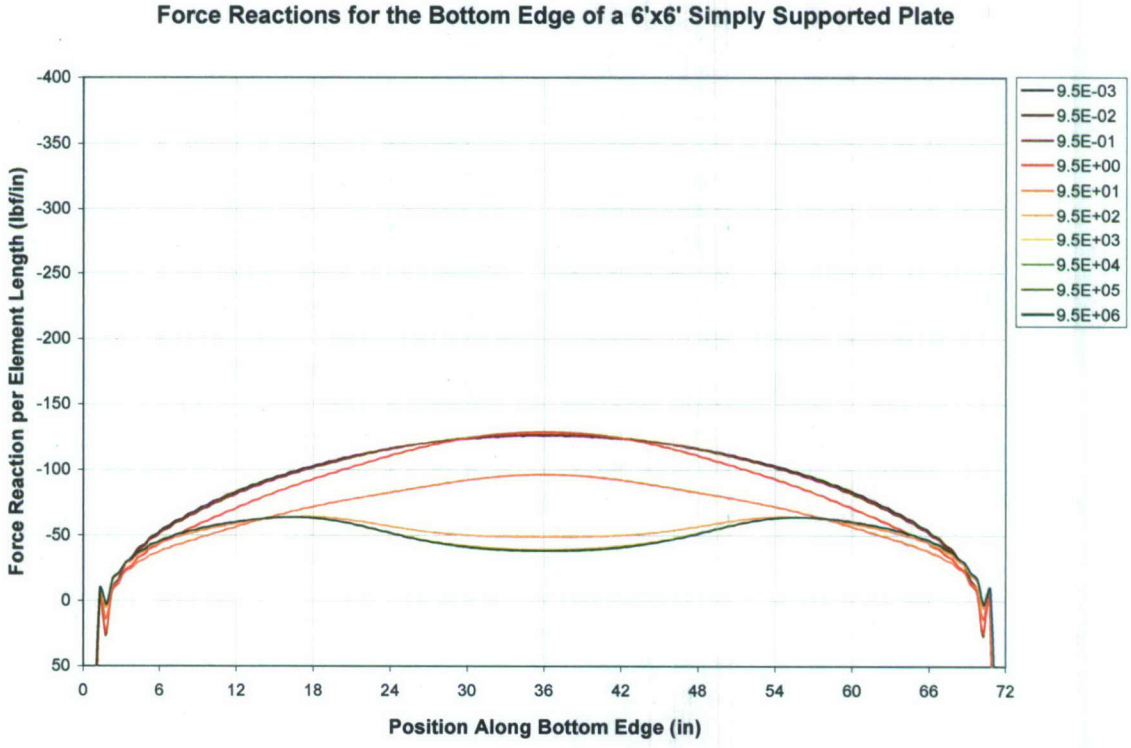

Figure 2.10b – 6'x6' Simply Supported Plate: Bottom Edge Force Reactions

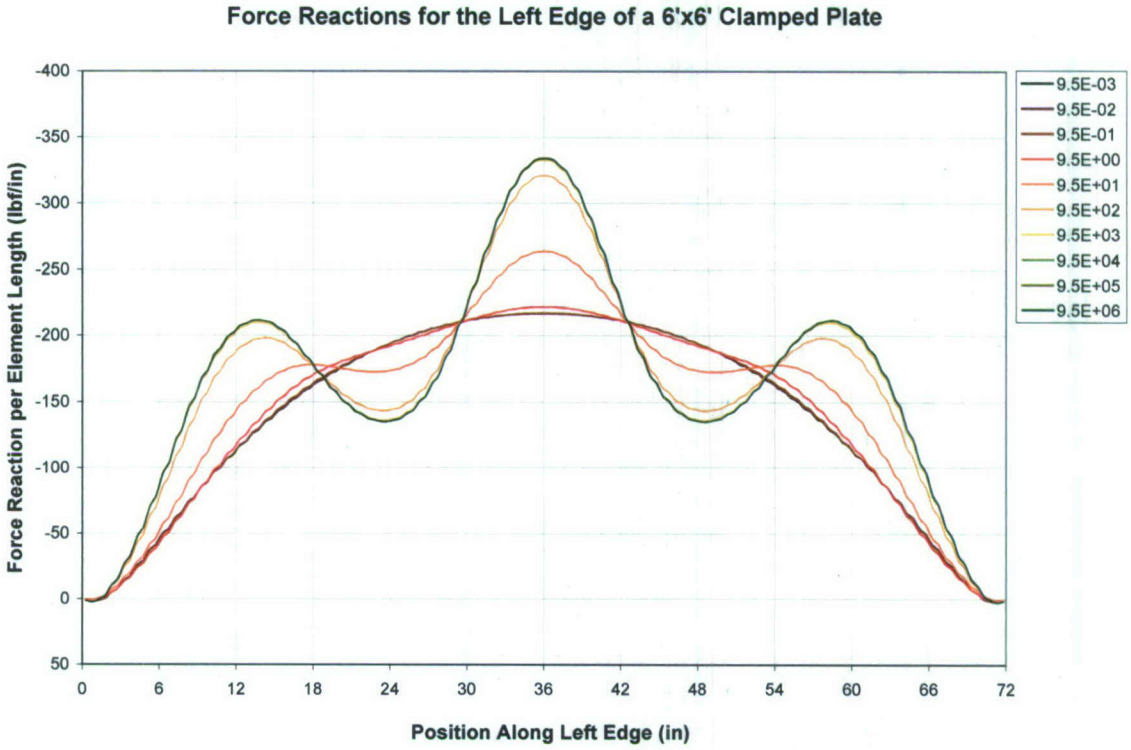

Figure 2.10c – 6'x6' Clamped Plate: Left Edge Force Reactions

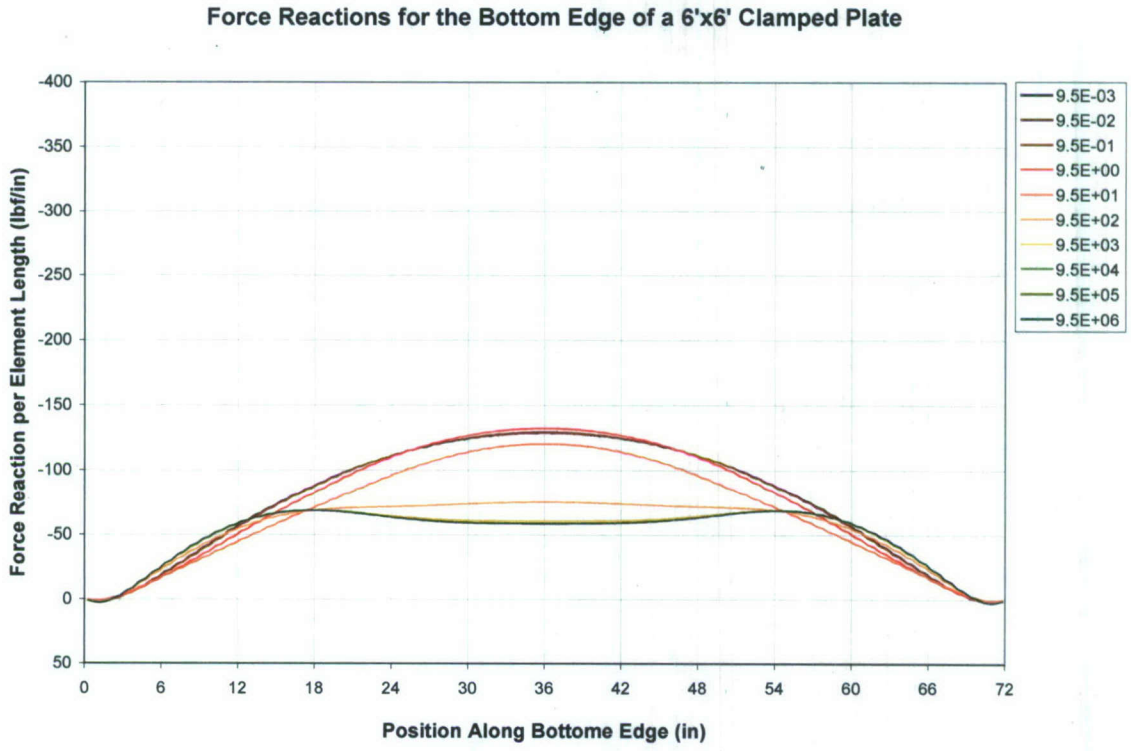

Figure 2.10d – 6'x6' Clamped Plate: Bottom Edge Force Reactions

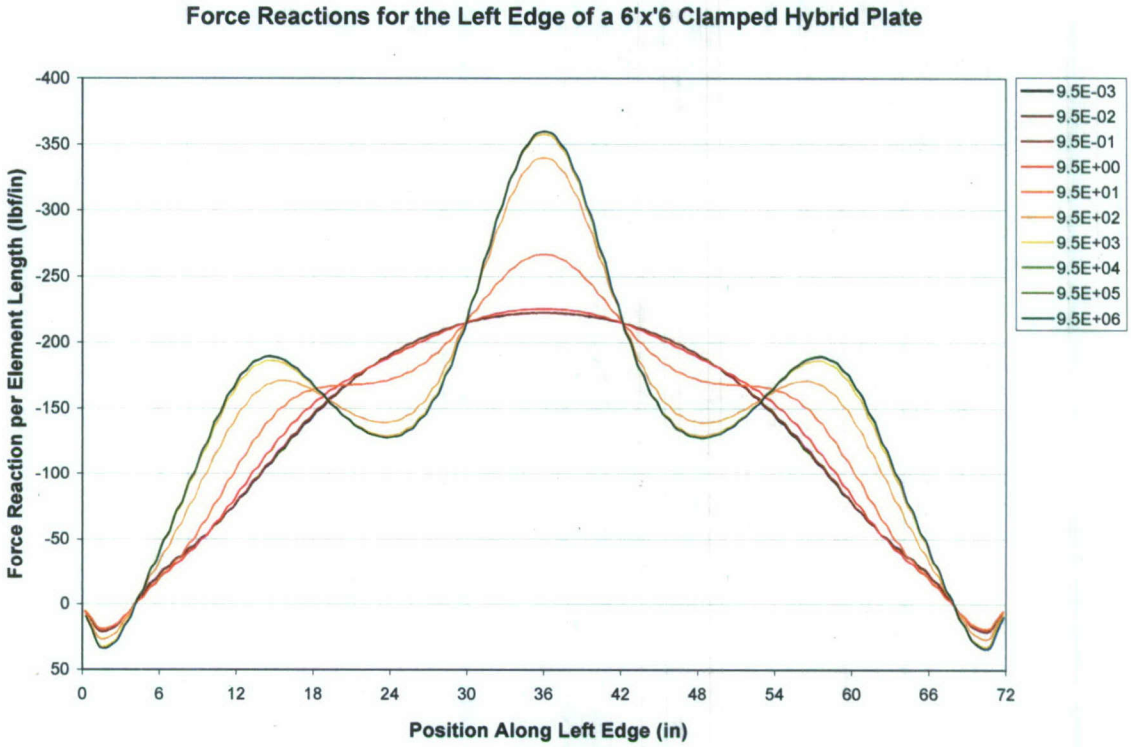

Figure 2.10e – 6'x6' Hybrid Plate: Left Edge Force Reactions

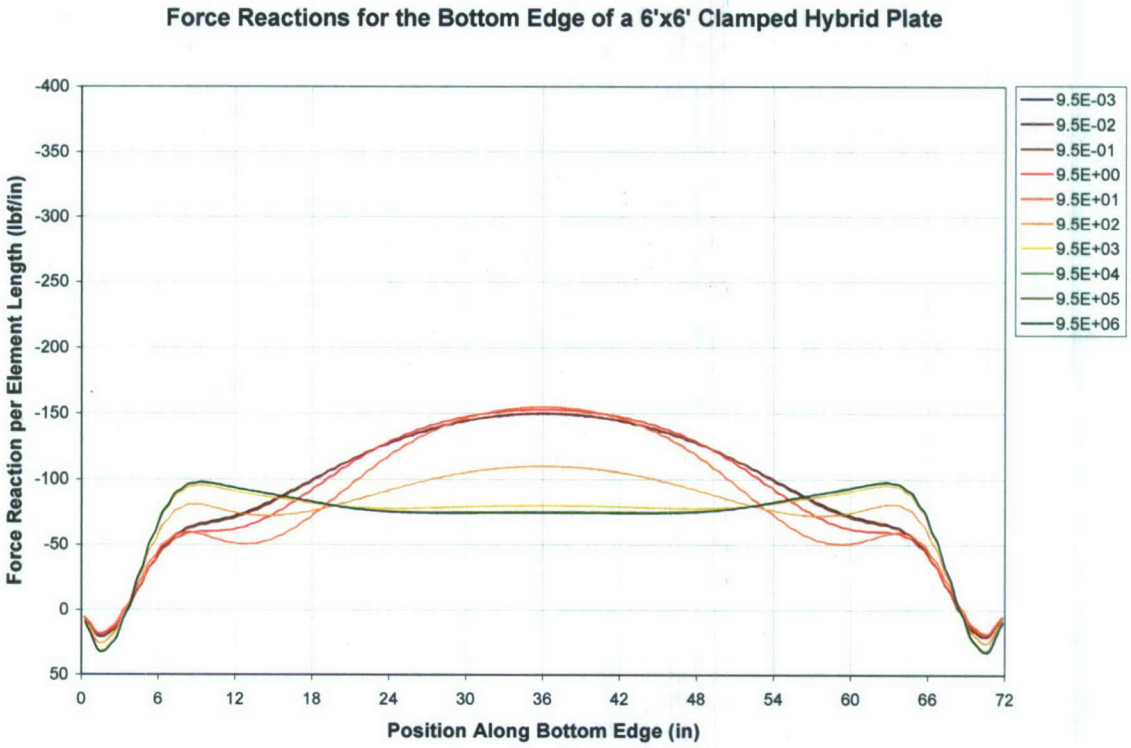

Figure 2.10f – 6'x6' Hybrid Plate: Bottom Edge Force Reactions

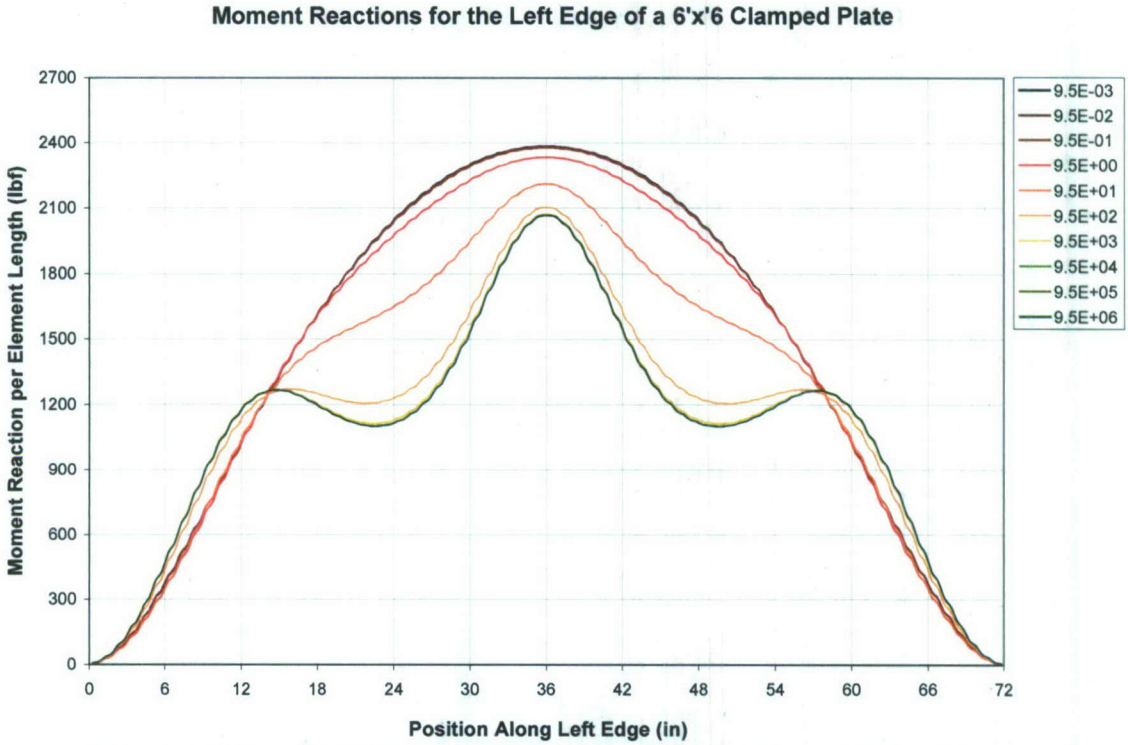

Figure 2.10g – 6'x6' Clamped Plate: Left Edge Moment Reactions

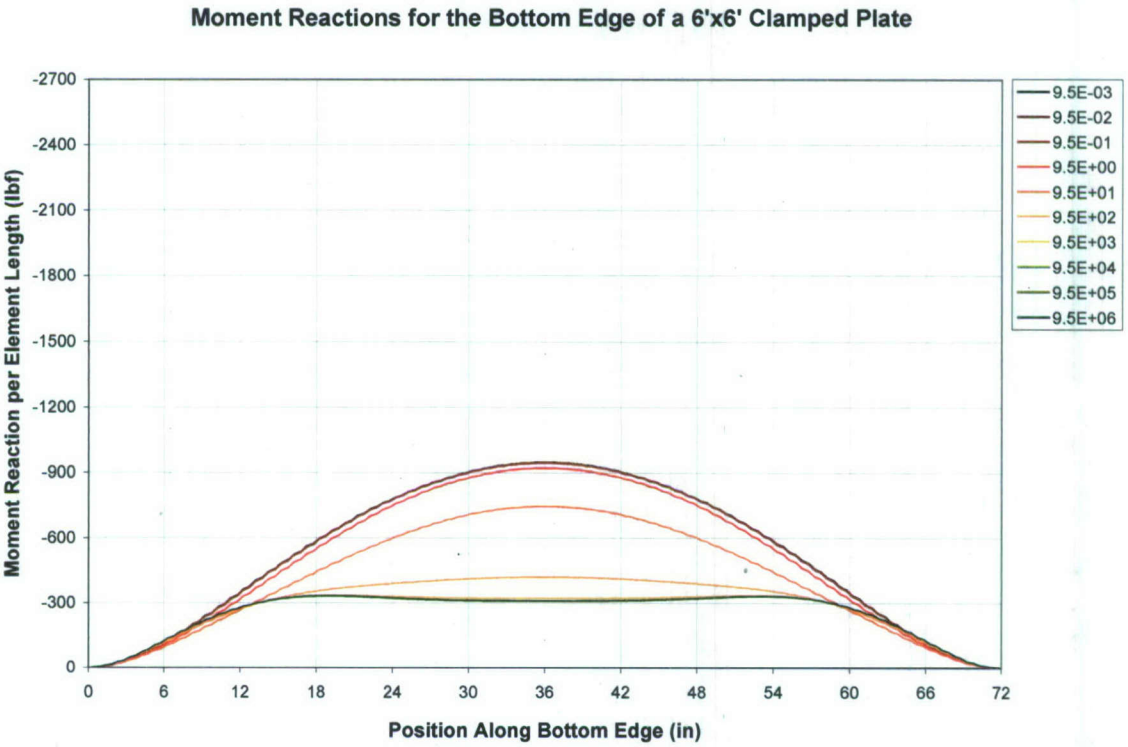

Figure 2.10h – 6'x6' Clamped Plate: Bottom Edge Moment Reactions

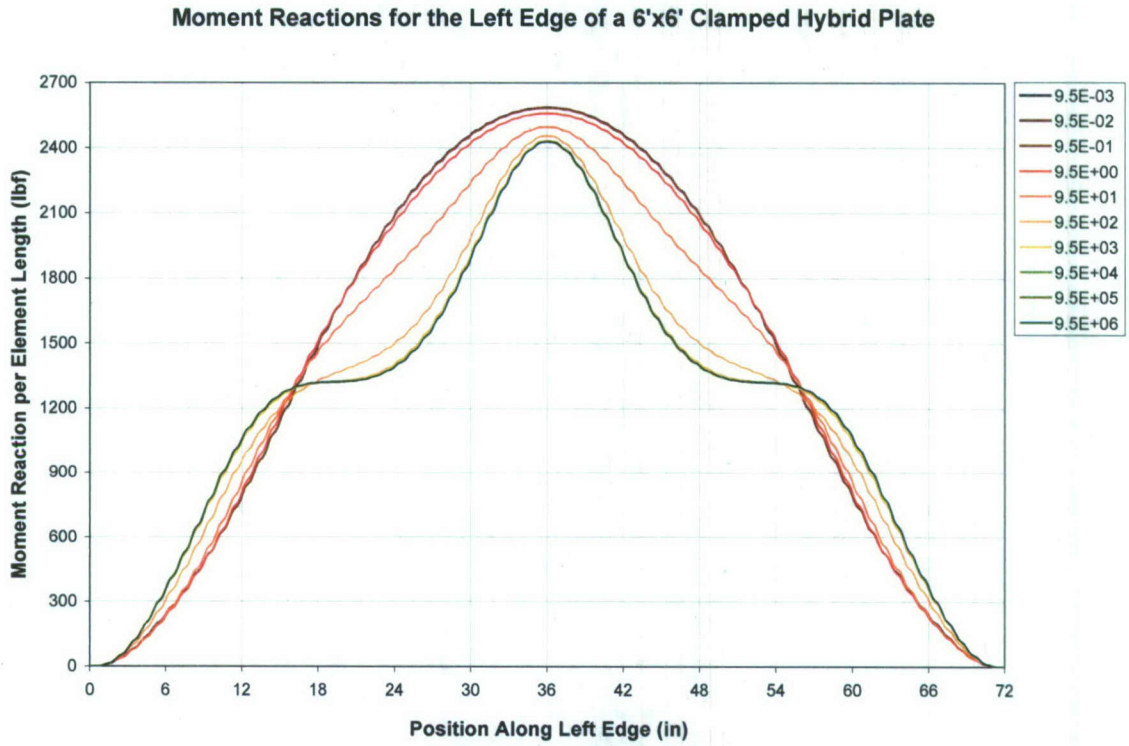

Figure 2. 10i – 6'x6' Hybrid Plate: Left Edge Moment Reactions

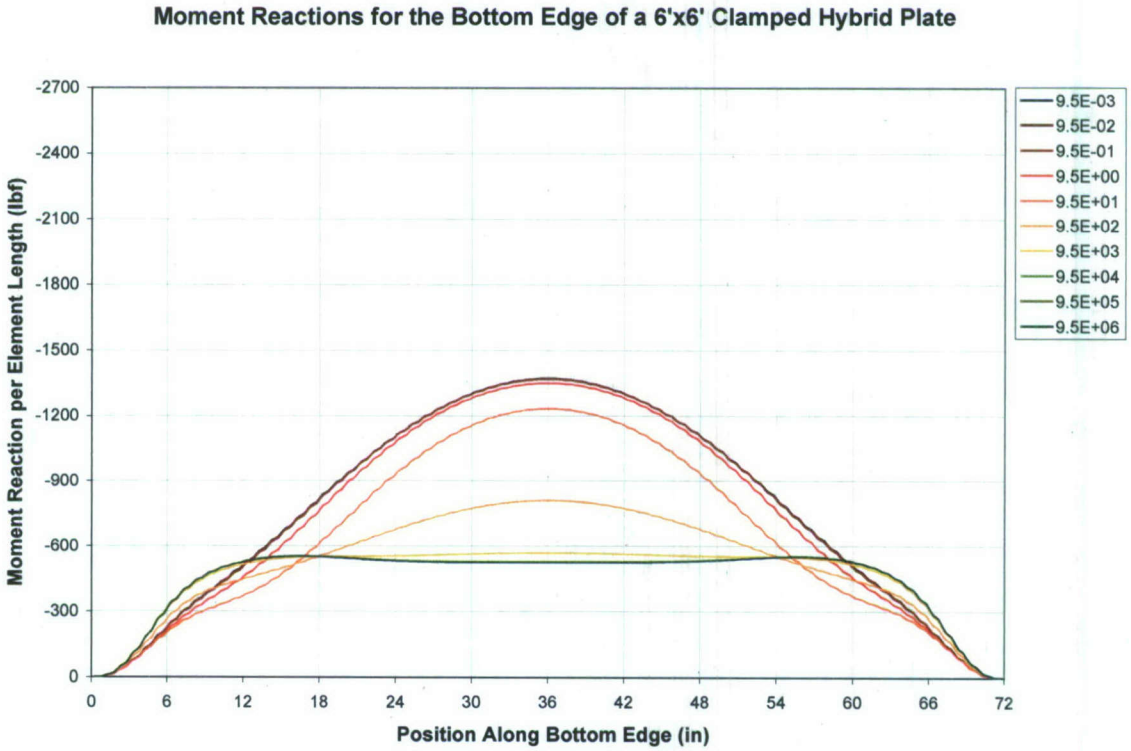

Figure 2. 10j – 6'x6' Hybrid Plate: Bottom Edge Moment Reactions

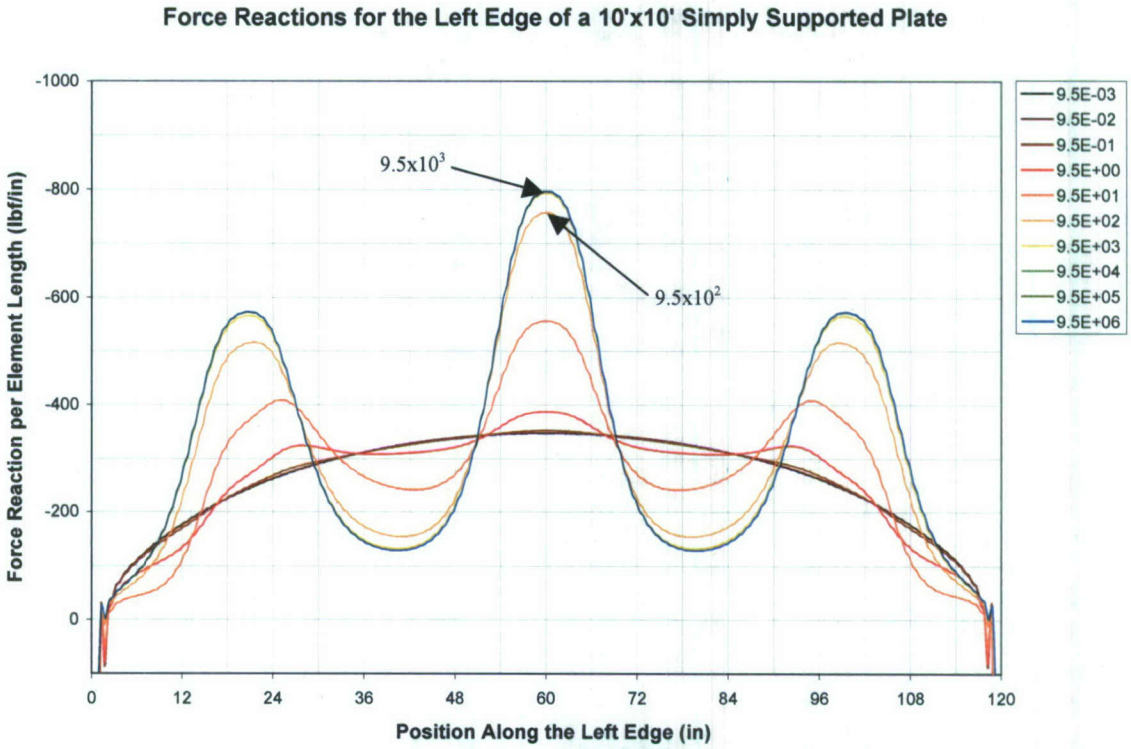

Figure 2.11a – 10'x10' Simply Supported Plate: Left Edge Force Reactions

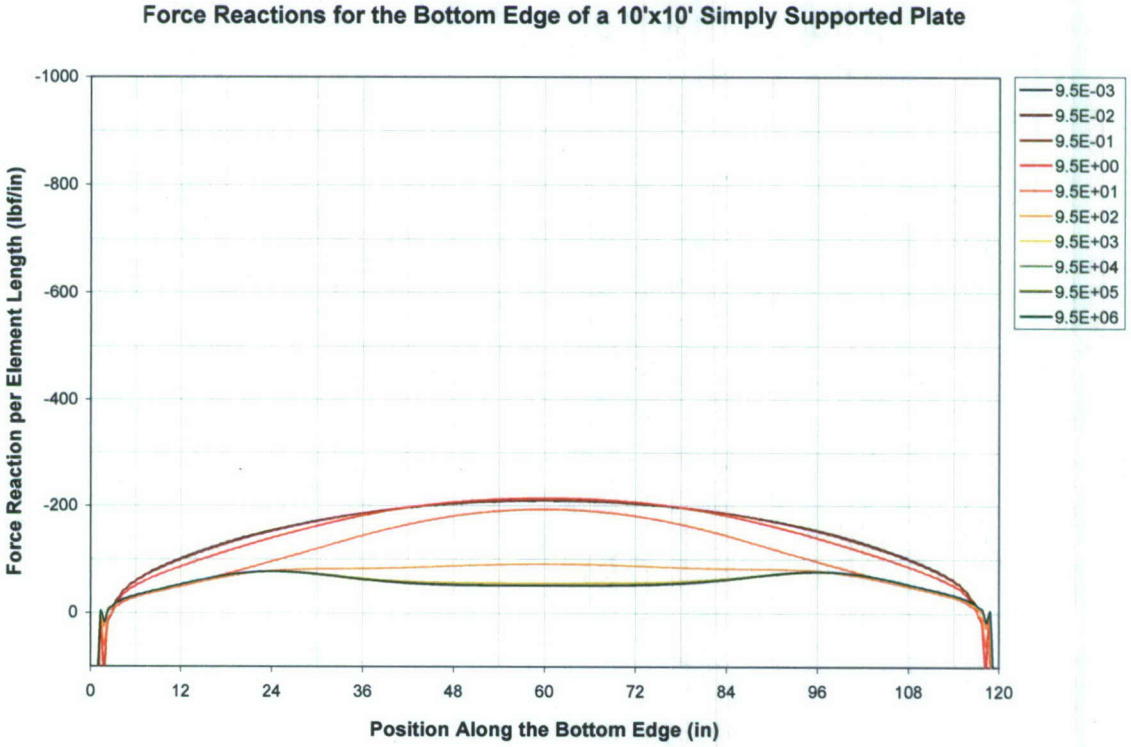

Figure 2.11b – 10'x10' Simply Supported Plate: Bottom Edge Force Reactions

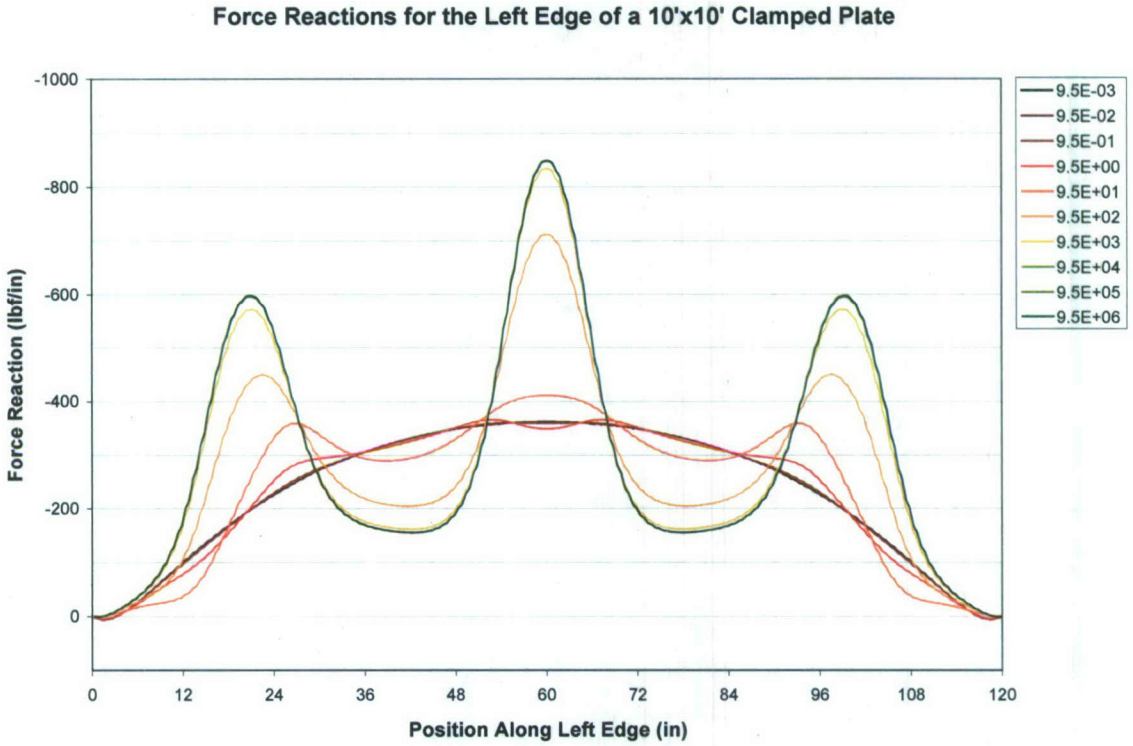

Figure 2.11c – 10'x10' Clamped Plate: Left Edge Force Reactions

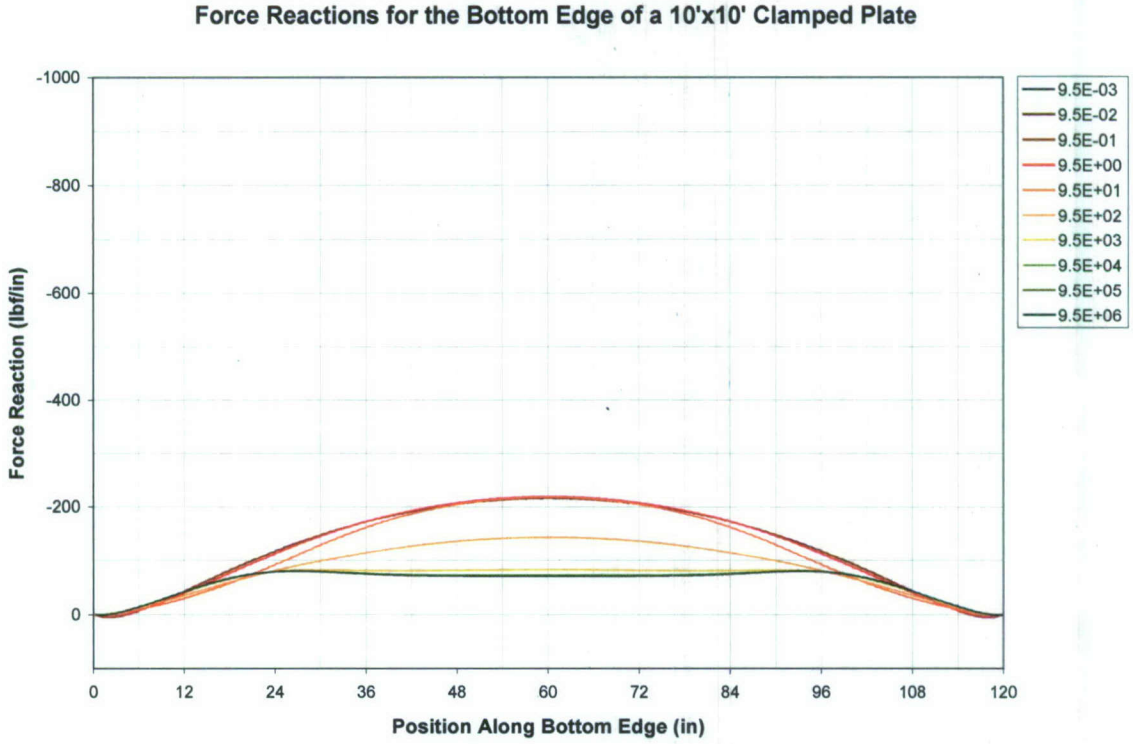

Figure 2.11d – 10'x10' Clamped Plate: Bottom Edge Force Reactions

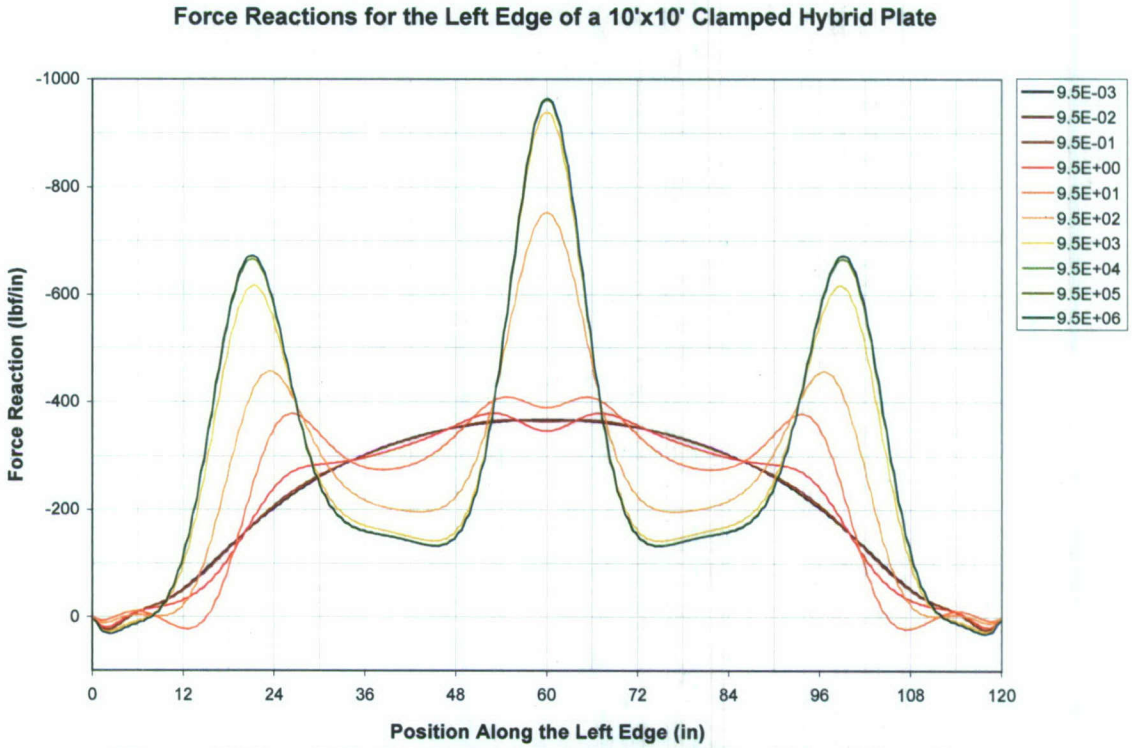

Figure 2.11e – 10'x10' Hybrid Plate: Left Edge Force Reactions

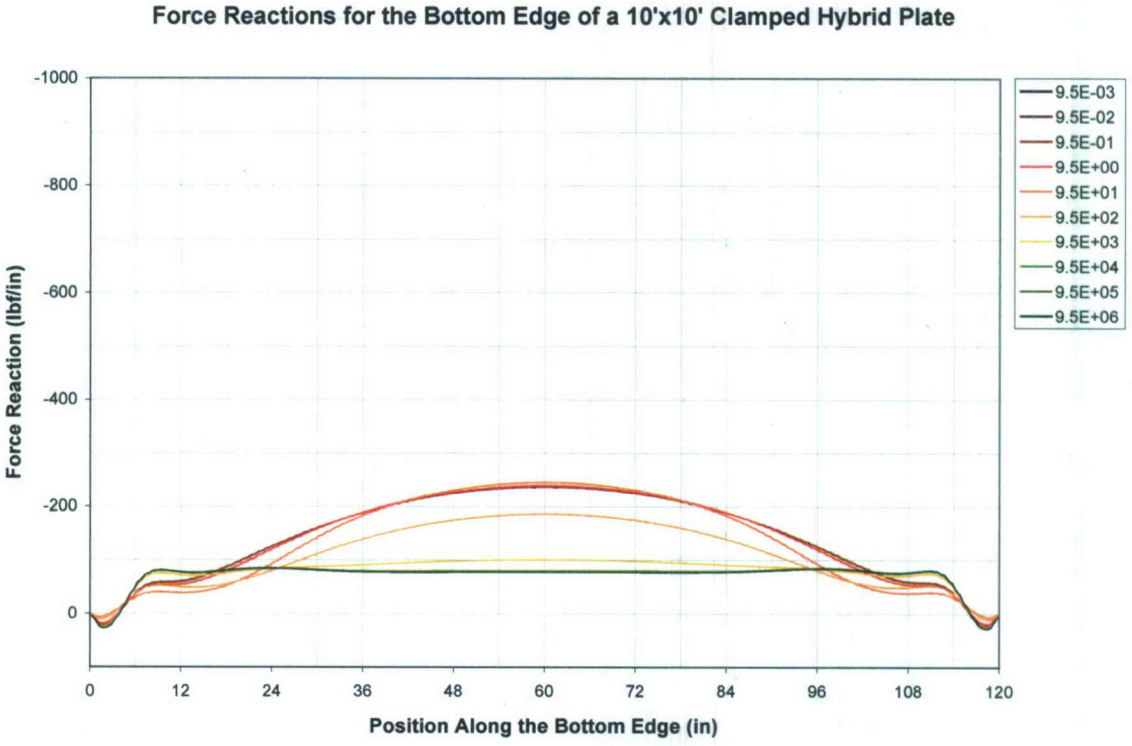

Figure 2.11f – 10'x10' Hybrid Plate: Bottom Edge Force Reactions

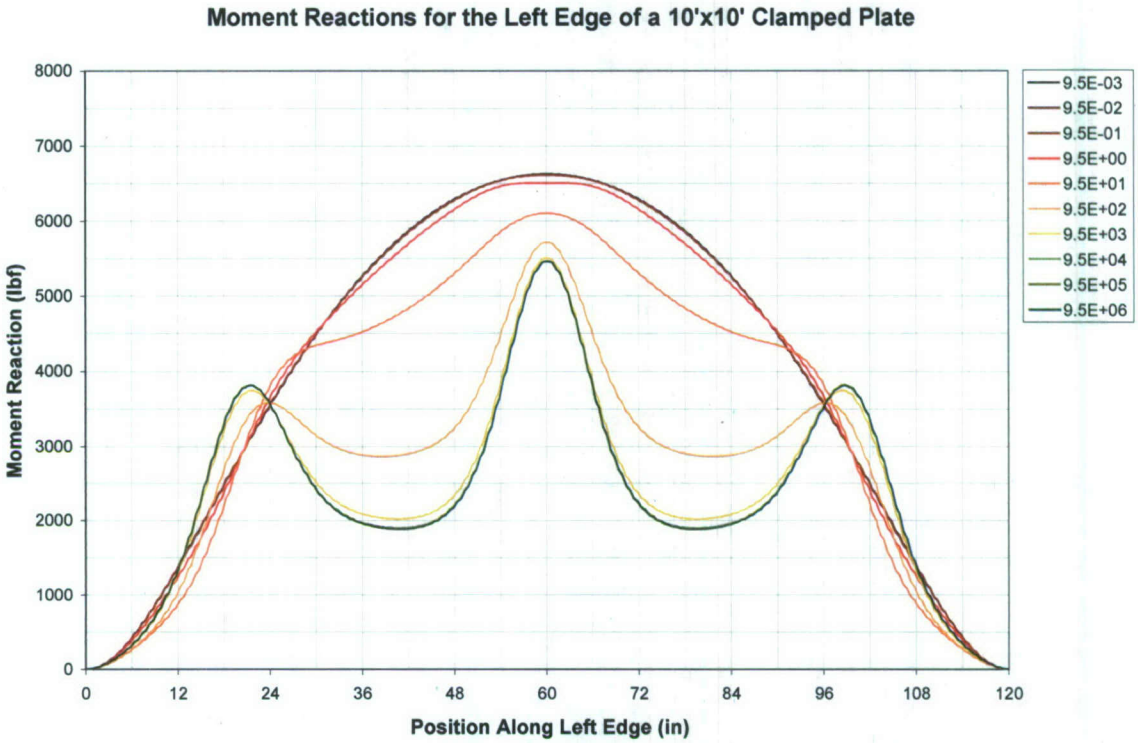

Figure 2.11g – 10'x10' Clamped Plate: Left Edge Moment Reactions

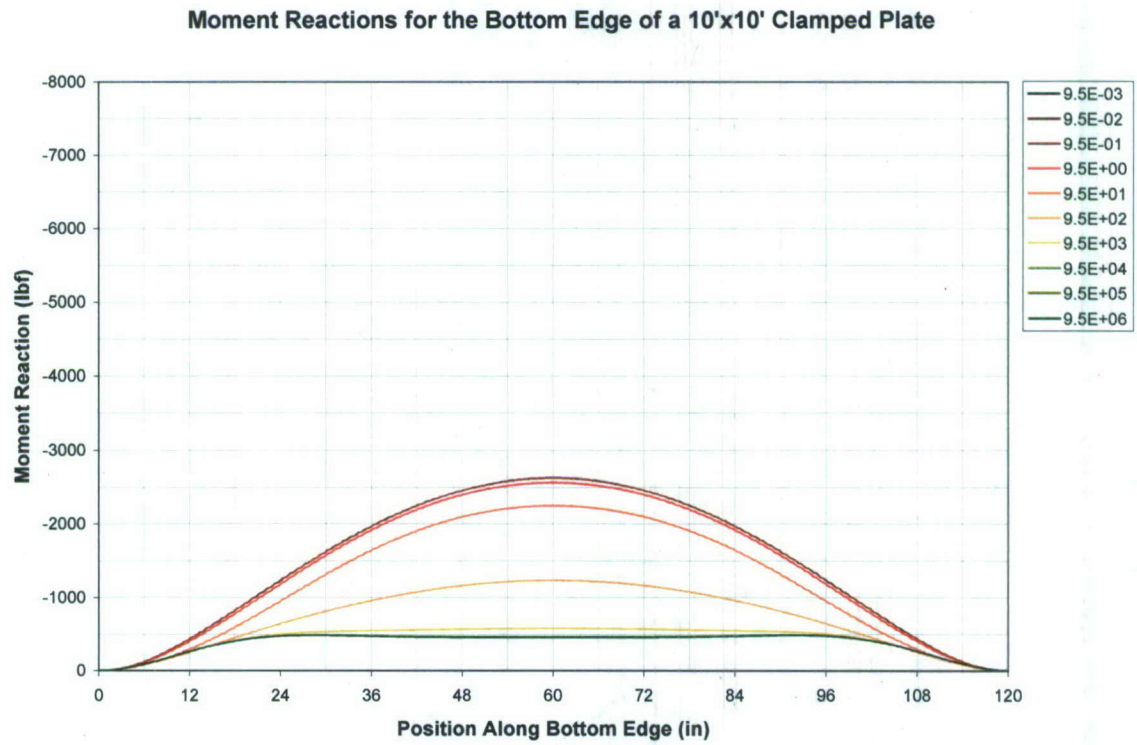

Figure 2.11h – 10'x10' Clamped Plate: Bottom Edge Moment Reactions

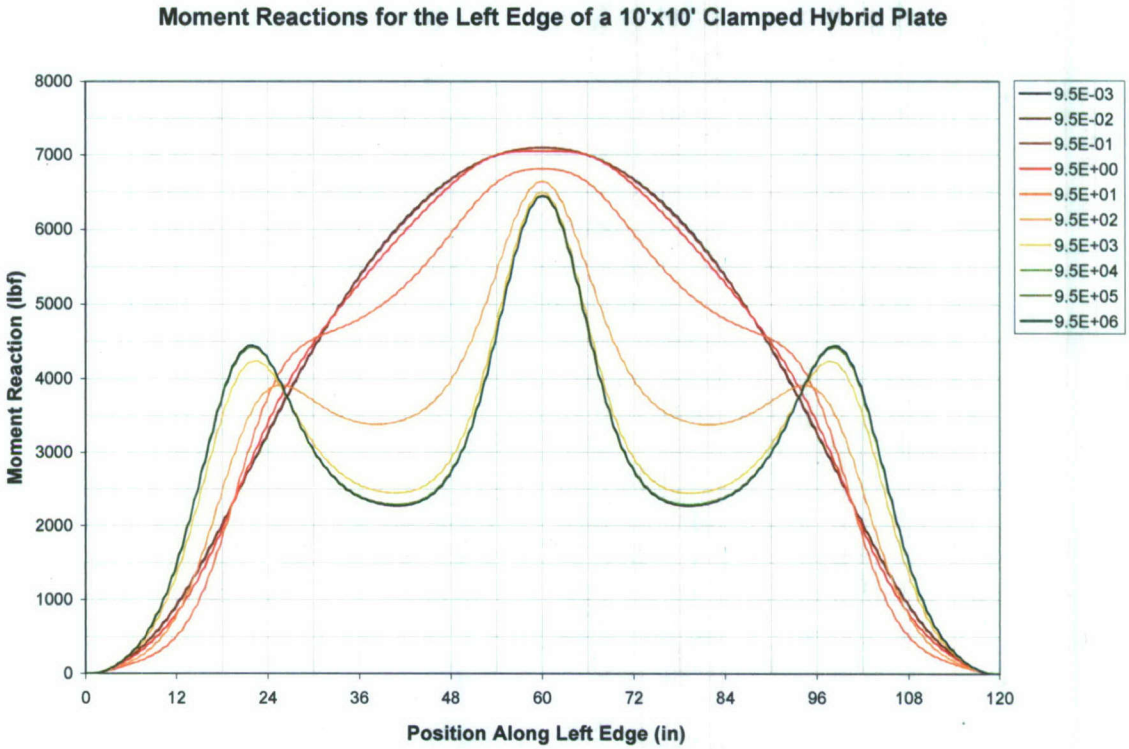

Figure 2.11i – 10'x10' Hybrid Plate: Left Edge Moment Reactions

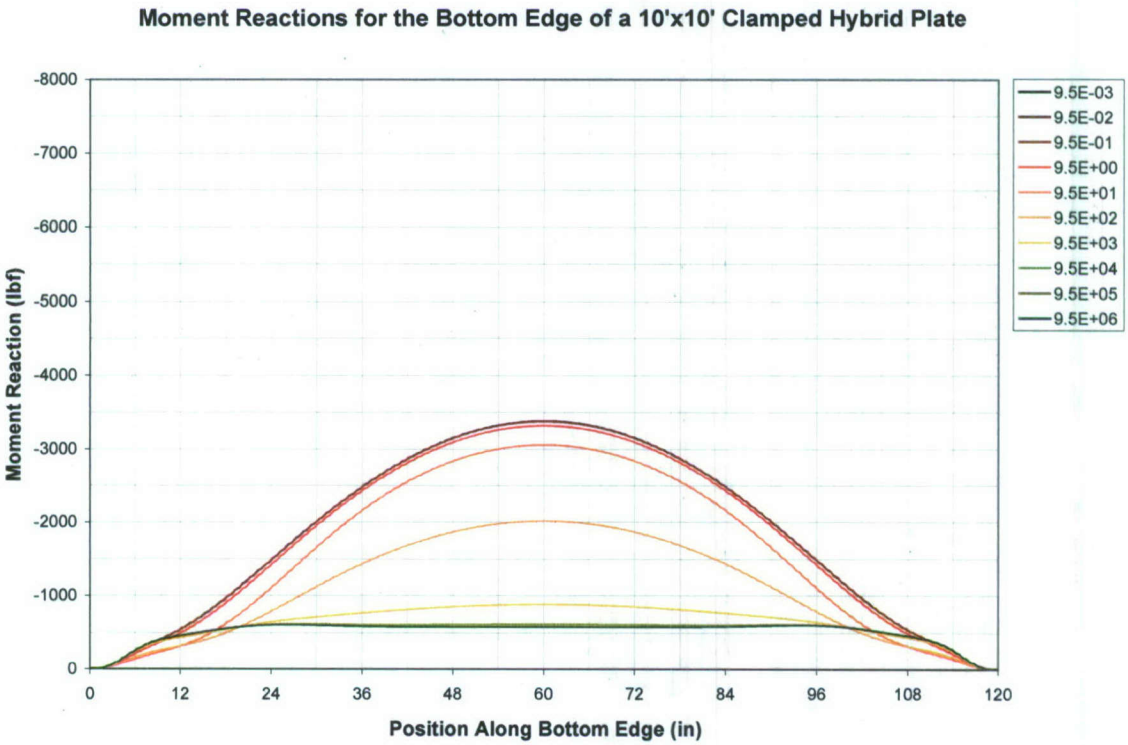

Figure 2.11j – 10'x10' Hybrid Plate: Bottom Edge Moment Reactions

Observation of the various graphs also reveals that the maximum magnitudes of the loads and moments experienced by the left (and right) side of the plate are always greater than those experienced by the bottom (top). For this reason, the values from the FEA analysis that were taken into consideration were the maximum values from the left hand side. The maximum value of the forces and the moments over the entire left hand edge of the plate for each relative rigidity for all cases are provided in Tables 2.2 and 2.3 for the 6'x6' plate and 10'x10' plate, respectively. They are also graphed in Figures 2.12-15. The center node displacement shows a sensitive transition region is apparent in these figures from relative rigidities of 9.5in to 950in with the stiffeners becoming fully effective between 950in and 9500in. It can be seen that the magnitude of the maximum force increases with the relative rigidity for the graphs of the left edge (see Figure 2.12) due to the transmission of the loads to the left edge by the stiffeners. This can also be tracked back in Figures 2.10a, 2.10c, 2.10e, 2.11a, 2.11c, and 2.11e. The maximum value for the force corresponds to the peaks seen at the center of the plates. Correspondingly, Figure 2.13 shows that the magnitude of the maximum value decreases as the relative rigidity increases for the bottom edge of the plates because the loads are being transmitted away from the bottom edge to the left edge. The moments, interestingly enough, do not exhibit the same behavior as the forces. For the bottom edges, the effect of the relative rigidity on the maximum moments closely resembles its effect on the maximum forces for the same reason—the load and corresponding moment are being transmitted away from the bottom edge as the stiffeners become more rigid. This results in the maximum values decreasing (see Figure 2.15). The left edge, however, is different. Even though peaks can still be seen as the relative rigidity increases (see Figures 2.10g, 2.10i, 2.11g, 2.11i) the maximum values actually decrease in magnitude. Figure 2.14 shows this very clearly. The reason for this is that even though the loads are being transmitted to the left edge, the distance from where this force is being applied to the left edge is decreasing as the stiffeners become more rigid and bring the loading closer. The sizeable gap between the clamped and clamped hybrid curves in Figures 2.12-15 is a result of the way that the two plates were designed. The steel border in the hybrid plate cuts into the composite, reducing the span of the composite. This makes the plate more stiff, and more load is transmitted through to the edge at the critical point.

Table 2.2 – 6'x6' Left Edge Maximum Force and Moment Reactions per Unit Length

Maximum Left Edge Force Reactions (lbf/in)				Maximum Left Edge Moment Reactions (lbf)		
Rel. Rigidity	SS	CI	Hy	Rel. Rigidity	CI	Hy
$9.5x10^{-3}$	-208.48	-216.60	-222.27	$9.5x10^{-3}$	2383.90	2585.60
$9.5x10^{-2}$	-208.48	-216.61	-222.26	$9.5x10^{-2}$	2383.30	2585.30
$9.5x10^{-1}$	-208.50	-216.86	-222.29	$9.5x10^{-1}$	2377.15	2582.35
9.5	-223.01	-221.40	-225.18	9.5	2332.75	2557.75
$9.5x10^{1}$	-272.67	-263.52	-266.37	$9.5x10^{1}$	2210.30	2495.65
$9.5x10^{2}$	-308.72	-320.65	-339.45	$9.5x10^{2}$	2101.70	2453.60
$9.5x10^{3}$	-314.22	-332.46	-357.19	$9.5x10^{3}$	2069.85	2431.05
$9.5x10^{4}$	-314.79	-333.72	-359.08	$9.5x10^{4}$	2065.90	2427.30
$9.5x10^{5}$	-314.84	-333.85	-359.27	$9.5x10^{5}$	2065.45	2426.85
$9.5x10^{6}$	-314.85	-333.86	-359.29	$9.5x10^{6}$	2065.45	2426.85

Table 2.3 – 10'x10' Left Edge Maximum Force and Moment Reactions per Unit Length

Maximum Left Edge Force Reactions (lbf/in)				Maximum Left Edge Moment Reactions (lbf)		
Rel. Rigidity	SS	CI	Hy	Rel. Rigidity	CI	Hy
$9.5x10^{-3}$	-347.39	-361.32	-367.01	$9.5x10^{-3}$	6626.65	7101.70
$9.5x10^{-2}$	-347.85	-361.03	-366.65	$9.5x10^{-2}$	6625.35	7101.55
$9.5x10^{-1}$	-352.17	-359.52	-365.93	$9.5x10^{-1}$	6612.70	7099.05
9.5	-386.92	-365.06	-378.39	9.5	6505.80	7053.55
$9.5x10^{1}$	-556.26	-410.52	-408.49	$9.5x10^{1}$	6103.15	6814.05
$9.5x10^{2}$	-757.09	-710.81	-751.39	$9.5x10^{2}$	5711.50	6639.80
$9.5x10^{3}$	-793.05	-833.25	-937.21	$9.5x10^{3}$	5499.55	6490.25
$9.5x10^{4}$	-796.12	-847.44	-959.91	$9.5x10^{4}$	5459.80	6445.45
$9.5x10^{5}$	-796.37	-848.87	-962.17	$9.5x10^{5}$	5455.50	6440.10
$9.5x10^{6}$	-796.43	-849.02	-962.36	$9.5x10^{6}$	5455.05	6439.60

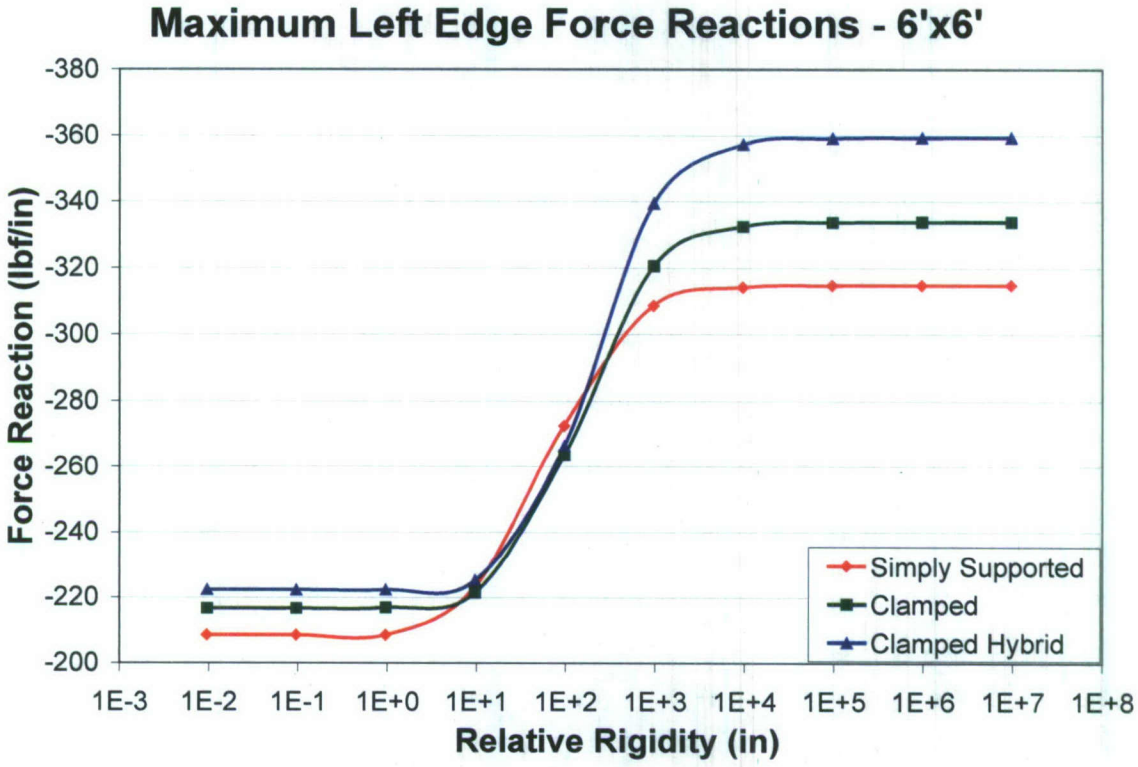

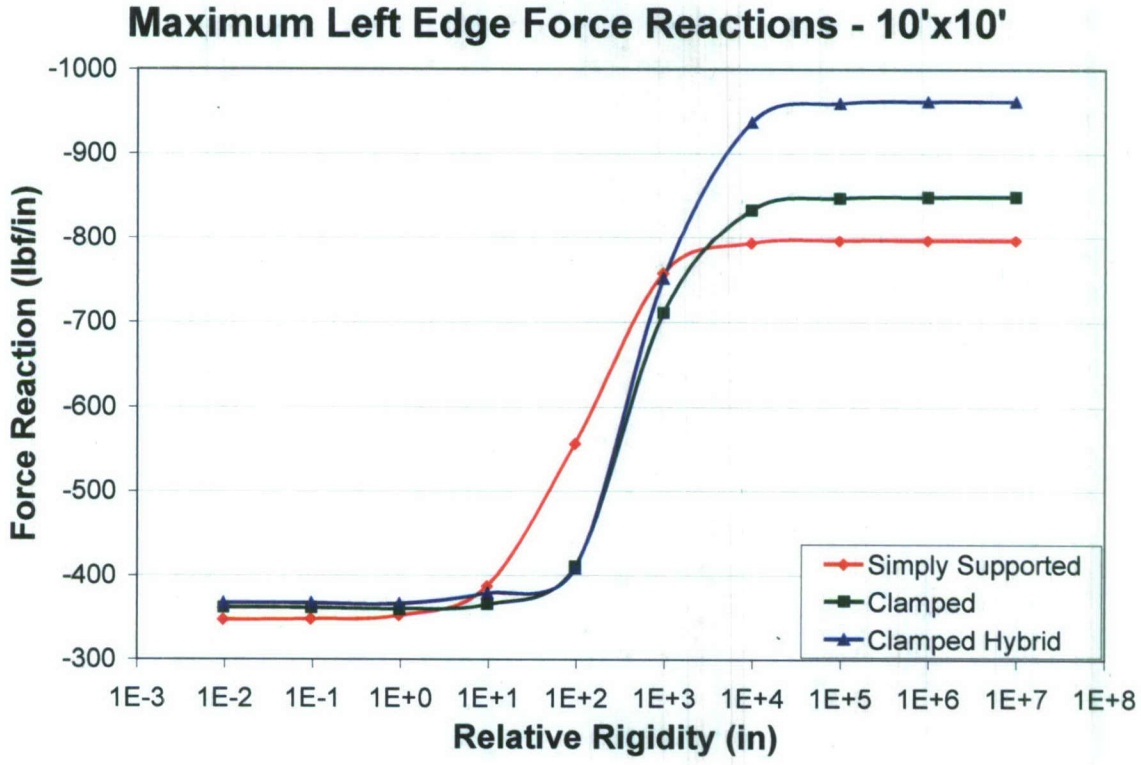

Figure 2.12 – Maximum Left Edge Force Reactions vs. Relative Rigidity

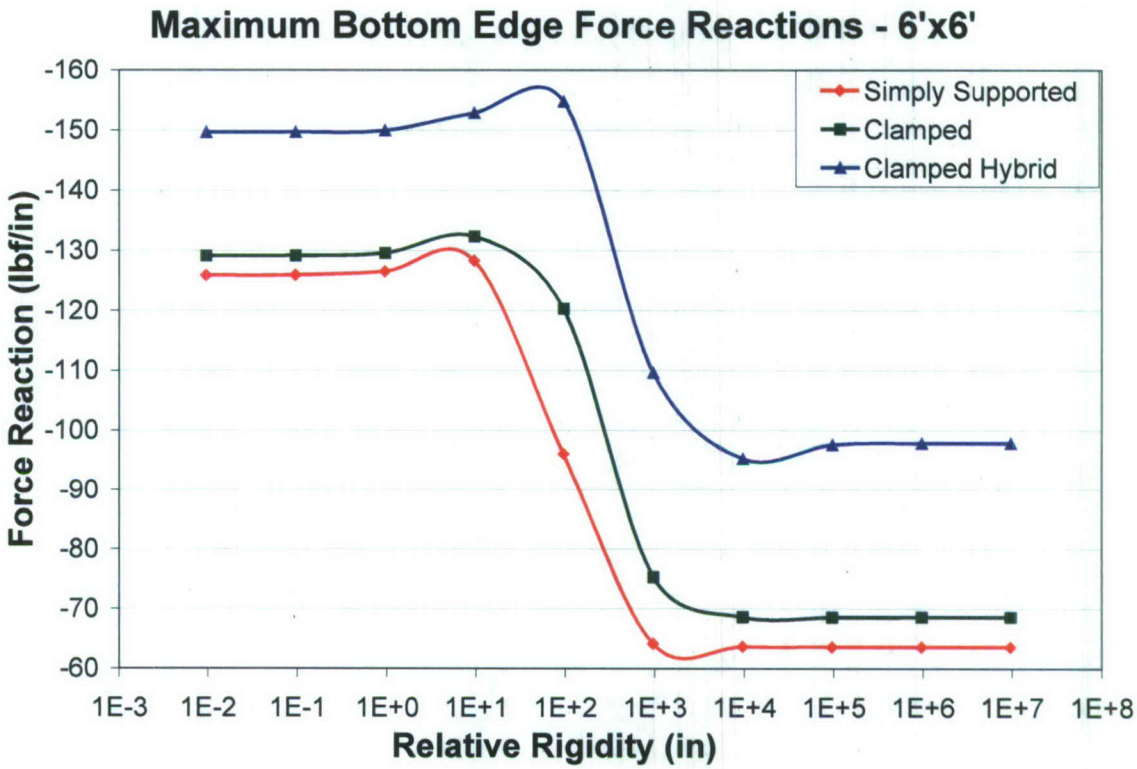

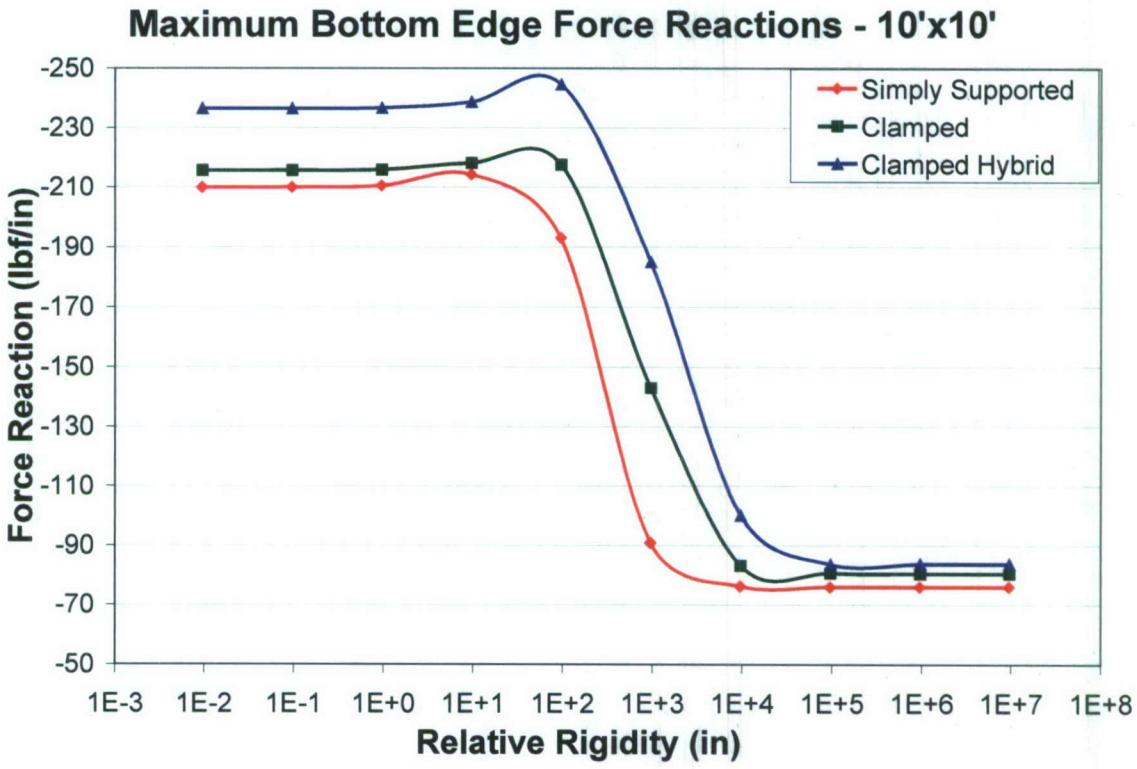

Figure 2.13 – Maximum Bottom Edge Force Reactions vs. Relative Rigidity

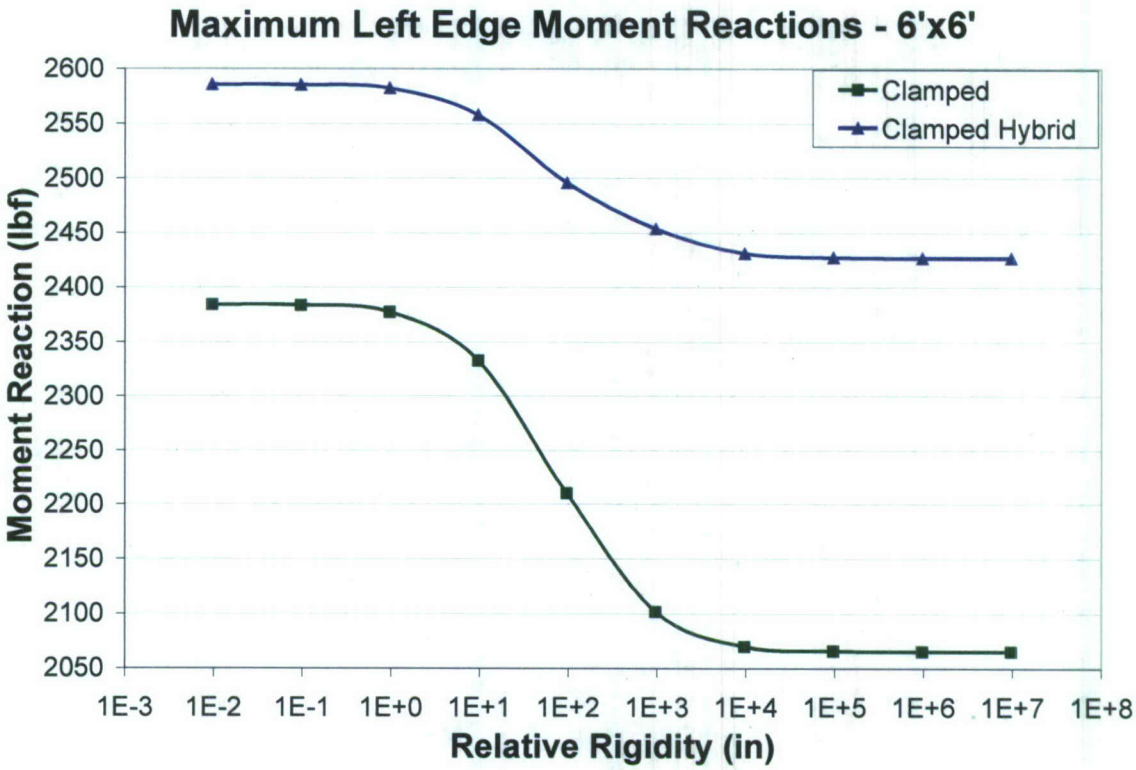

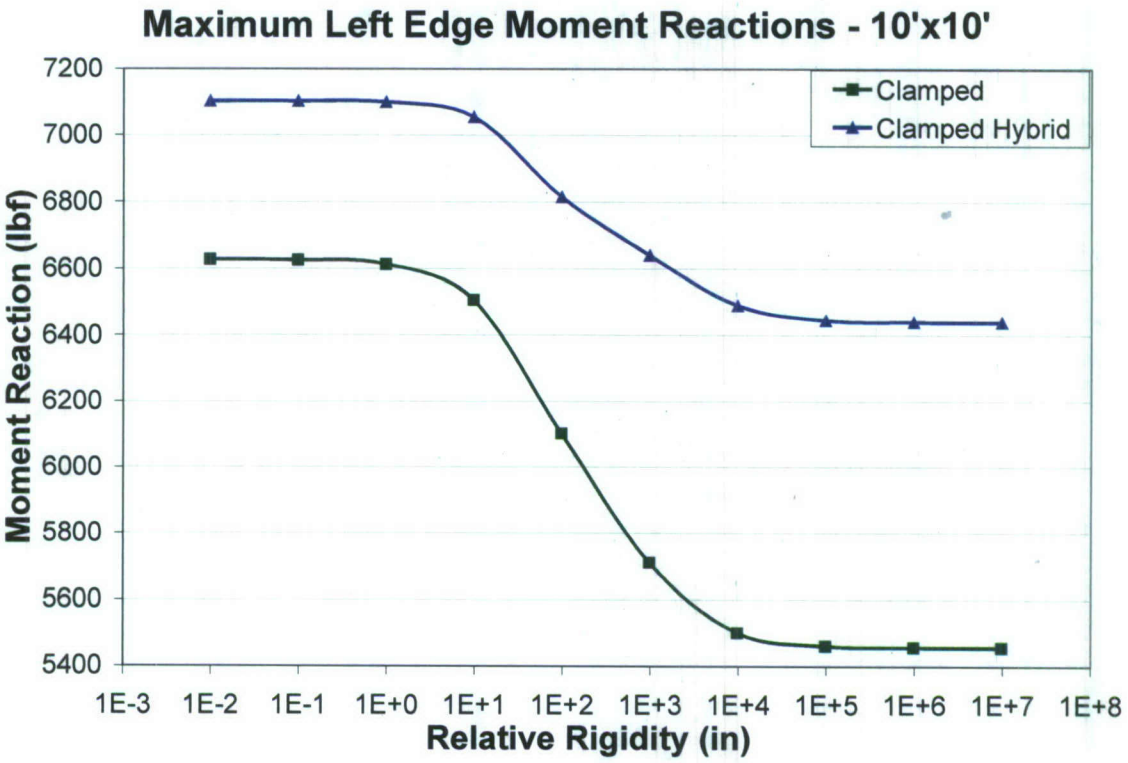

Figure 2.14 – Maximum Left Edge Moment Reactions vs. Relative Rigidity

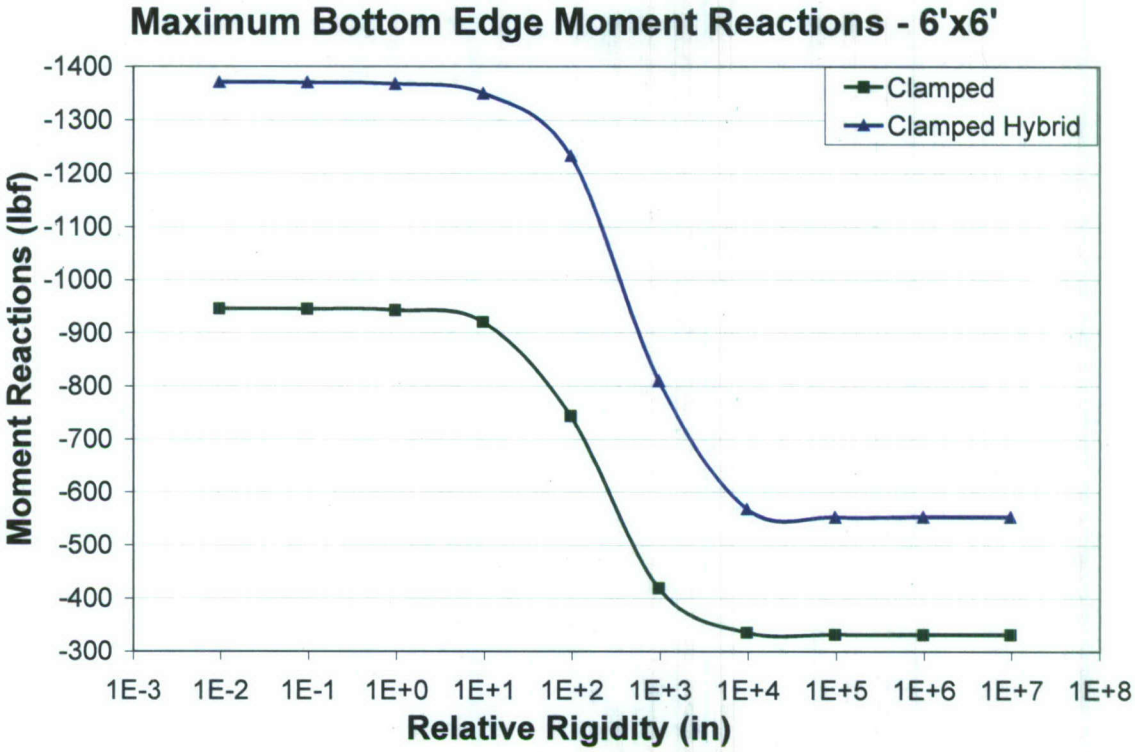

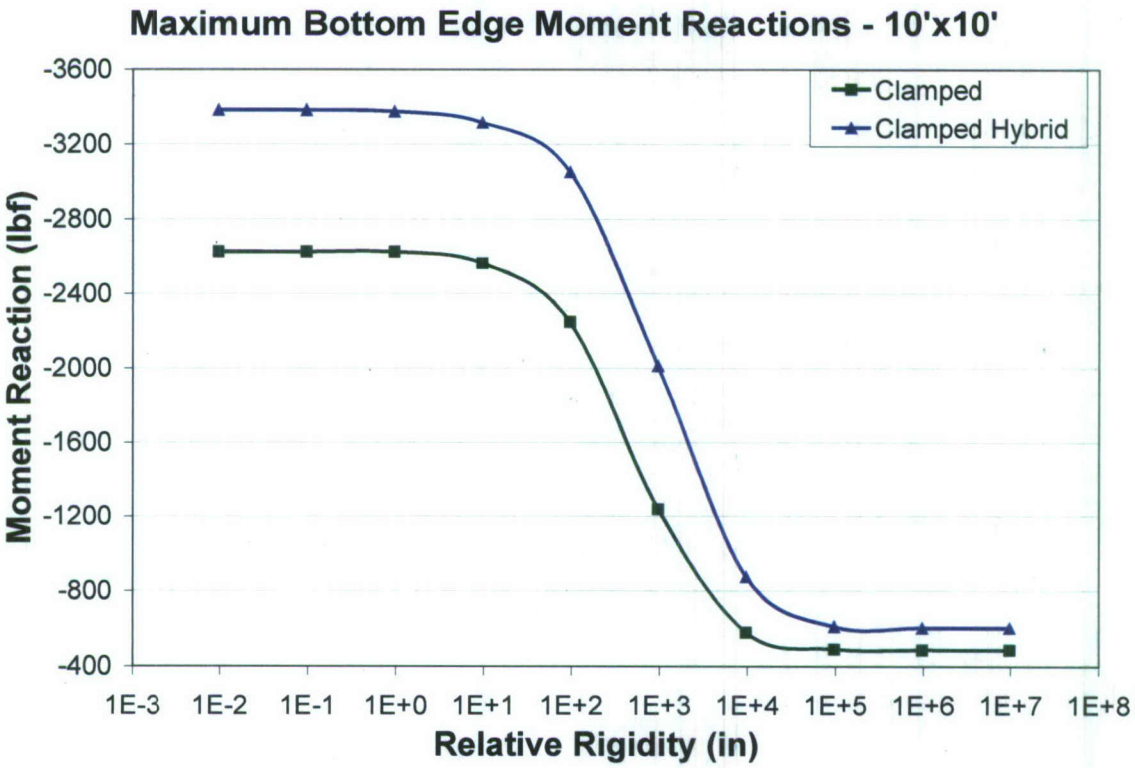

Figure 2.15 – Maximum Bottom Edge Moment Reactions vs. Relative Rigidity

This study clearly indicates that the fully effective relative rigidity is between $9.5x10^3$in and $9.5x10^4$in depending on the case. It was assumed that fully effective stiffeners would be used on the panels, and consequently the maximum force and moment values that are applicable to the tests are those that occurred at these relative rigidities. This narrowed the data from which to draw the test moment arm values from. The data for the stiffened plates with relative rigidity ratios of $9.5x10^3$in and $9.5x10^4$in is presented in Table 2.4. All things considered, the range of moment arms is fairly tight. Since the main goal of the FEA analysis is to determine the moment arm in the fatigue tests, what remains is to decide what value from the range calculated in the analysis will yield the most beneficial data from the tests. The tests to be performed are flexure fatigue tests for the out-of-plane loads in the panels. One reason for this is that the connections in the panel used by Kabche (2007b) were predominantly in bending, and that panel serves as a conceptual starting point for this research. Also, some of the advantages of bending fatigue over uni-axial fatigue for the testing of composites presented by Van Paepegem (2004) apply, including the elimination of buckling issues and decreased force and facility size requirements. Since shear stresses are usually lower than axial and bending stresses, it is appropriate to study the cases where the moment arm is greater. There is also practical motivation for a greater moment arm, because a moment arm at the lower end of the spectrum would bring the clamping mechanism in too close to the steel tee. For these reasons, a moment arm of 8.5in was chosen; a value at approximately the 87^{th} percentile of the range calculated in the analysis.

Table 2.4 – Maximum Load, Moment, and Moment Arm per Element Length

FEA results for load, moment, and moment arm (M/V)					
Plate Size	**Case**	**Relative Rigidity (in)**	**V (lbf/in)**	**M (lbf)**	**M/V (in)**
6x6	Clamped	$9.5x10^3$	320.65	2101.70	6.55
6x6	Clamped	$9.5x10^4$	332.46	2069.85	6.23
6x6	Hybrid	$9.5x10^3$	339.45	2453.60	7.23
6x6	Hybrid	$9.5x10^4$	357.19	2431.05	6.81
10x10	Clamped	$9.5x10^3$	710.81	5711.50	8.04
10x10	Clamped	$9.5x10^4$	833.25	5499.55	6.60
10x10	Hybrid	$9.5x10^3$	751.39	6639.80	8.84
10x10	Hybrid	$9.5x10^4$	937.21	6490.25	6.93

3. Materials and Test Article Fabrication

Test article fabrication was carried out in parallel with the Finite Element Analysis. The manufacturing process employed for specimen fabrication was the Vacuum Assisted Resin Transfer Molding (VARTM) process, and it was used with E-glass fiber knit fabric and epoxy vinyl-ester resin. This largely followed previous manufacturing that has been done at the University of Maine, and consequently many of the practices already in use were adopted.

3.1 Flow Media Test and Replacement

Before any specimens were actually manufactured, it was determined that a change in one of the materials used in the VARTM process would reduce the amount of time required for panel layup, as well as eliminate a potential source of process failure. The structural properties of E-glass/vinyl ester composites made with the VARTM process are heavily dependent on the fabrication processes, which will be discussed in detail later in this section. Fabrication processes used in previous projects performed at the UMaine Hybrid Structures Laboratory used one layer of aluminum screen sandwiched between two layers of soft plastic screen as the flow media. While this provided good flow and wet-out of the parts, the aluminum screen often punctured the vacuum bagging material, making the infusion process somewhat cumbersome. After an analysis of the different flow media currently available, it was decided that the panel infusion process could be improved by upgrading to a different type of polymer media. The flow media chosen was VIP infusion flow R750 from Richmond products, shown in Figure 3.1. It was desired that the flow rates of the old system and the new system be the same, since gel time is a vital factor in the infusion process.

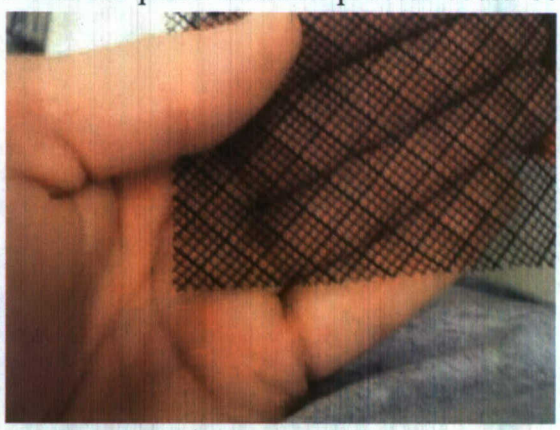

Figure 3.1 – Richmond Products VIP Infusion Flow R750 Flow Media

To determine whether the new flow media would generate a flow rate similar enough to the previous type to be an acceptable replacement, an experiment was conducted to compare the two (see Figure 3.2). This was done using four vacuum-bagged panels. Each panel was 12inx20in in size and used 3 layers of [0/90] E-glass fabric. The panels were overlain with flow media in configurations which can be summarized as follows:

Panel 1 – 2 layers of VIP Infusion Flow R750

Panel 2 – 1 layer of VIP Infusion Flow R750

Panel 3 – Soft plastic screen/aluminum screen/soft plastic screen

Panel 4 – Soft plastic screen/2 layers of aluminum screen/soft plastic screen

The experiment showed that the flow rate of the resin substitute (corn syrup) in Panels 2 and 3 with the two different flow media setups was virtually identical. For this reason, the older configuration of flow media was replaced with VIP Infusion Flow R750 for all of the infusions performed following the experiment. The advantages of the new type of flow media were primarily as follows:

1.) There was no aluminum screen: This had proved to be a major disadvantage in the past because of its propensity to puncture the vacuum bag.

2) There were fewer layers to cut: Due to the sandwich configuration, 3 layers of material in the older configuration were needed for every one in the new. This saved time and energy in infusion lay-up and preparation, and also reduced waste.

3) The material was easier to cut: Aluminum screen was more troublesome to cut than the softer plastic VIP Infusion Flow R750.

Figure 3.2 – Flow Media Test

3.2 Test Article Geometry and Naming Convention

Part of the research performed was the design and actual manufacture of the various test articles to be used. As already mentioned, the process used for this was the VARTM manufacturing process. A typical flexure fatigue test article is shown in Figure 3.3. It consists of a metallic T-shaped substructure representing the backbone of the metallic frame structure. The composite panels are joined to the metallic tee frame by various methods.

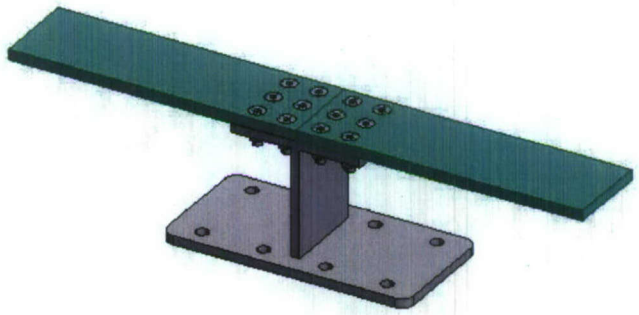

Figure 3.3 – Typical Composite Joint Test Article

The baseline hybrid connection test article had a length of 20 inches, width of 6.75 inches and a thickness of 0.75 inches. The different potential connection geometric configurations are shown in Figure 3.4.

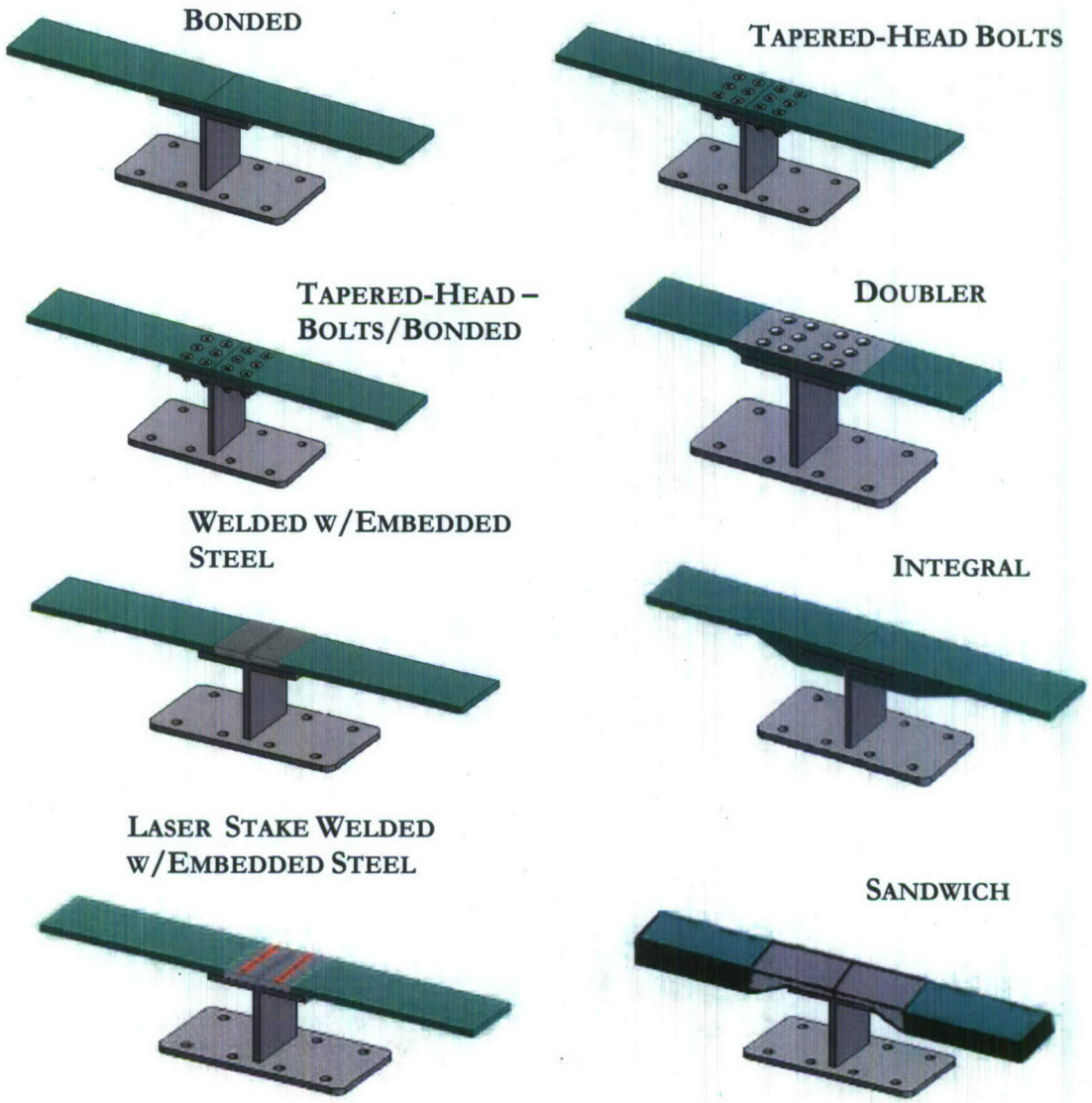

Figure 3.4 – Potential Hybrid Connection Configurations

The possible parameters considered in the joint configuration were: bolt type, bolt diameter, number of bolts, size of doubler plate, thickness of doubler plate, type of tee support, and whether the connection is a double cantilever beam or continuous beam. The specimens are to be designated according to the convention seen in Table 3.1. The

different types of hybrid connections under current investigation are presented in Table 3.2.

Table 3.1 – Test Article Naming Convention

TT-M#-JJ- NNN -H-SS-###	
TT	**Test Type:** **FC**– Constant Amplitude Fatigue Test; **FR**– Random Amplitude Fatigue Test; **C**- Cyclic Test
M#	**Metal Material:** **S**– Steel; **A**– Aluminum; **#: 1**– A36; **2**– HSLA65
JJ	**Joint Type:** **CL**– Clamped; **AB**– Adhesive Bond Only; **BT**– Bolted with Tapered Head; **BP**– Bolted with Protruding Head; **BA**– Bolted and Adhesively Bonded; **DS**– Bolt with Short Doubler; **EM**– Embedded Metal; **IJ**– Integral Joint; **SC**– Sandwich Connection
NNN	**Joiner Dimensions**: Bolt Diameter in Inches x100; Adhesive Thickness in Mils; Embedded Metal Thickness in Inches
SS	**Special Provisions:** **LW**– Laser Welded; **GW**– GMAW weld; **CP**– Continuous Panel; **FI**– Foam Insert; **SA**– SIA Adhesive: **LA**– Locktite Adhesive; nominal composite thickness*100 for bolted joint or clamped joint
###	**Specimen Number in Series**

Table 3.2 – Fatigue Test Article Summary (Near Term Tests)

Test Designation	Joint Style	Bolt Diam. (in)	Tee Support	Peak Load (kips)
FC-S1-BP-050-75-001	Bolted	0.50	Steel - A36	± 8
FC-S1-BP-050-75-002	Bolted	0.50	Steel - A36	± 7
FC-S1-BP-050-75-003	Bolted	0.50	Steel - A36	± 6
FC-S1-BP-050-75-004	Bolted	0.50	Steel - A36	± 5
FC-S1-BP-050-75-005	Bolted	0.50	Steel - A36	± 4
FC-S1-CL-000-75-001	Clamped	0.75	Stiffened	± 8
FC-S1-CL-000-75-002	Clamped	0.75	Stiffened	± 7
FC-S1-CL-000-75-003	Clamped	0.75	Stiffened	± 6.5
FC-S1-CL-000-75-004	Clamped	0.75	Stiffened	± 6
FC-S1-CL-000-75-005	Clamped	0.75	Stiffened	± 5

Connection Denomination	Bolt Type	Bolt D (in)	Tee Support	Doubler Size (in)	Doubler or Embedded Metal Thickness (in)	Notes
C-S-BP-050-075-001	None	-	Steel	--	--	---
C-S-CL-075-000-002	-	3/4	Steel - DH36	--	--	---
FC-S-BP-050-075-003	-	1/2	Steel-HSLA65	--	--	---
FC-S-BP-050-075-004	-	1/2	Steel-HSLA65	--	--	---

3.3 Materials and Test Article Fabrication

The composite material specimens used in the experimental testing described in this section are fabricated at the Hybrid Structures Laboratory of the Mechanical Engineering Department at the University of Maine. Standard VARTM procedures are taken and modified to best suit the type and size of the articles made. The procedure followed to fabricate the test articles is as follows, and is a description of the most complex type of test article used. Other simpler articles are fabricated using the same procedure with some of the steps removed. For instance, the test articles used in the clamped and bolted tests are obviously fabricated eliminating the steps pertaining to the steel inserts.

Step 1 – Clean Table: The VARTM Infusions are performed on a 4' by 8' glass table, and it is critical that the surface is clean—free from dust and especially fibers of any kind—before beginning. This assures good adhesion between the sealant tape and the table. Stray fibers between the two have proven to be a source of leakage that is difficult to stop. A damp rag is ideal for this. Chemicals are avoided if possible, as they may have unforeseen reactive effects later on.

Step 2 – Apply Sealant Tape: Once the table free of any dust or debris, the first layer of sealant tape (Fibre Glast #581-A Vacuum Bag Sealant Tape) is applied, with the paper backing left on the tape. The area enclosed must be large enough to enclose the fiberglass and bleeder material (Steps 7 & 12).

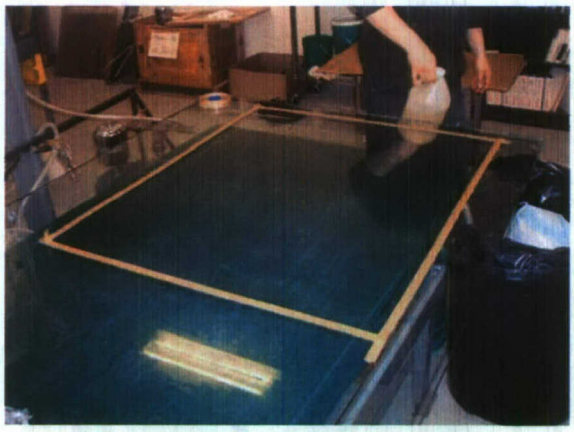

Figure 3.5 – Sealant Tape Application

Step 3 – Wax Enclosed Area: In order to allow the test article to easily release from the table once it is finished, it is important to wax the area inside the tape. Getting wax on the tape should be avoided. The wax is rubbed onto the table with a cloth. Partall Paste #2 wax, manufactured by Rexco, is used.

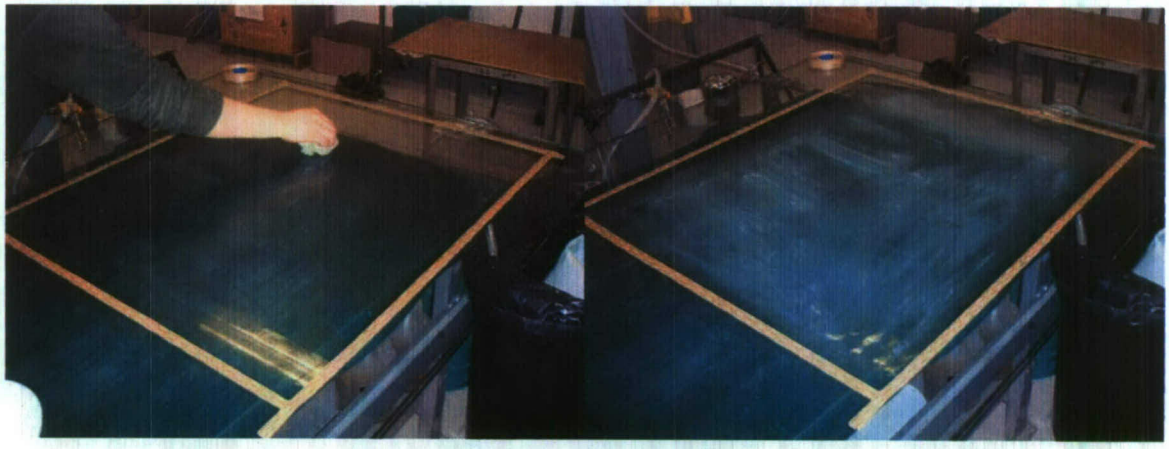

Figure 3.6 – Wax Application

Step 4 – Lay Down First Layer of Peel Ply: The peel ply, like the wax, aids in the release from the table once the test article is finished. The size of the peel ply is such that it essentially fills the inside of the tape boundary. It is advantageous to keep the peel ply within the waxed area. PFG Performance Fabrics code 52008 nylon peel ply is used.

Figure 3.7 – Bottom Layer of Peel Ply

Step 5 – Lay Down First Layer of Flow Media: Flow media assists the resin through the fiberglass by providing the resin with a low-resistance front. Were it not for the flow media, the resin would move much more slowly through the part. The flow media (VIP

infusion flow R750) is cut approximately 1in shorter than the size of the test article. This allows the rear of the resin front to catch up with the foremost parts of the front on the top and bottom due to the flow media.

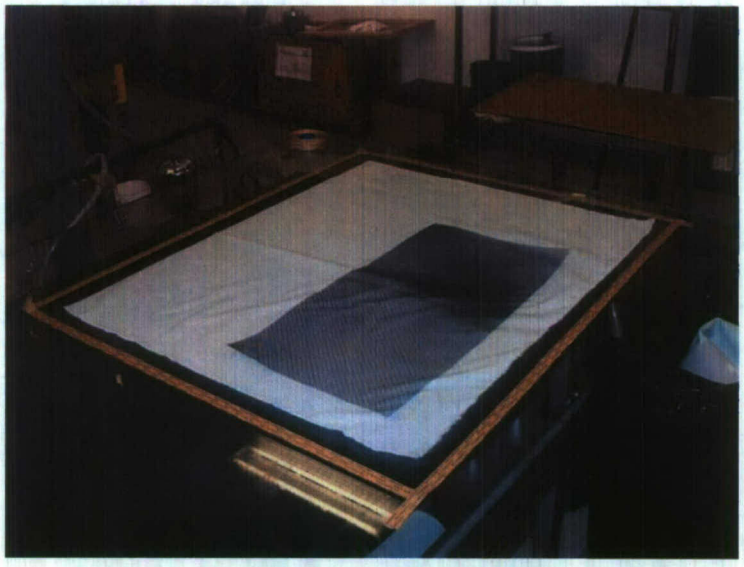

Figure 3.8 – Bottom Layer of Flow Media

Step 6 – Lay Down Second Layer of Peel Ply: A second layer of peel ply is placed down over the flow media to allow it be peeled off the test article once the infusion is complete.

Step 7 – Lay Down First Layers of Fiberglass: Layers of fiberglass fabric must be cut to the desired size. St Gobain (BTI) 24oz 0°-90° knit fabric and 24oz ±45° knit fabric is the type of fiberglass used. The 0° and 90° fibers are stitched together, as are the +45° and -45°. Layup configurations differ, and the fiberglass must be cut so as to have layers oriented correctly throughout the layup. As previously mentioned, the configuration used for the 0.75in thick test articles analyzed in this research is:

$$\left[(\pm 45/0/90/\mu\, 45/90/0)_2\,(\pm 45/0/90)\overline{(90/0)}\right]_S$$

For an embedded joint, the fiberglass must also be cut to encapsulate the insert as the following figures depict.

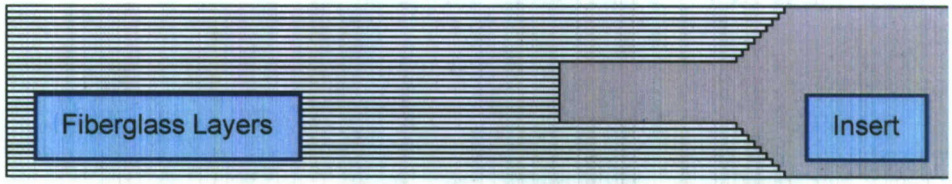

Figure 3.9 – Profile View of Fiberglass and Insert

Once the fabric has been cut correctly, it is laid down on top of the flow media. For an embedded joint of the type used, only the layers that fit beneath and around the insert are laid down.

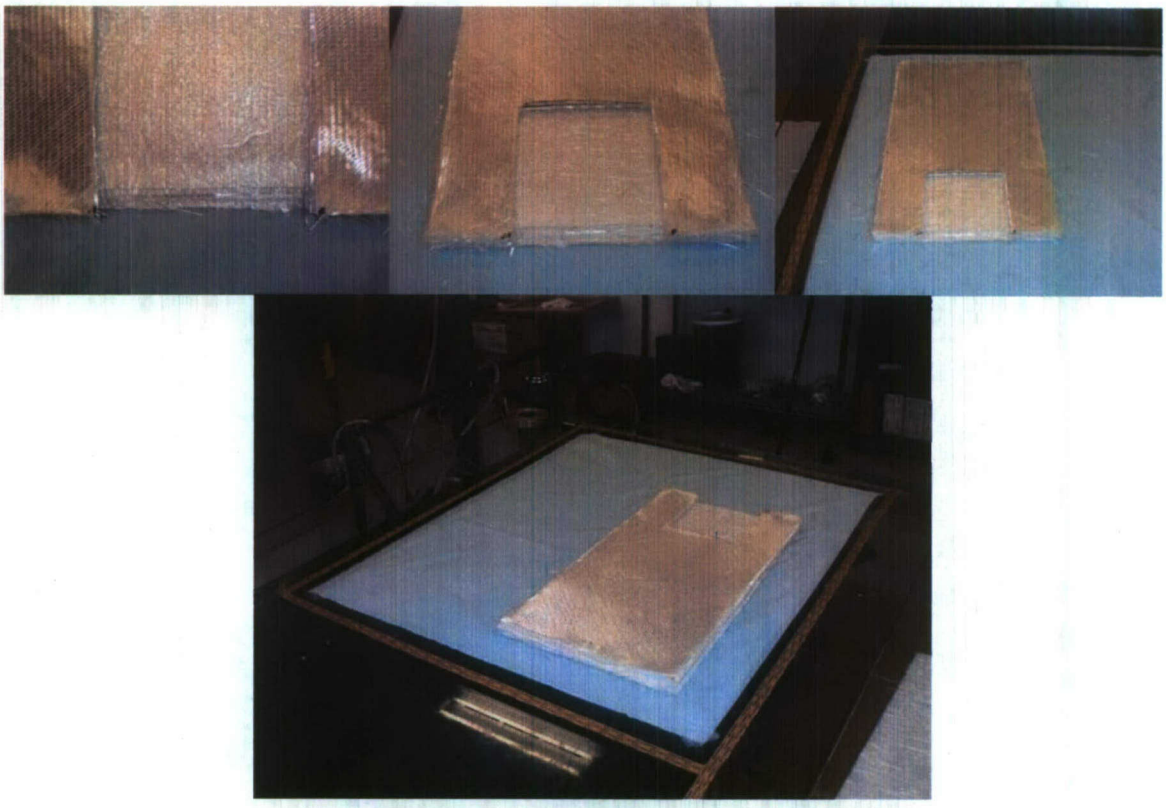

Figure 3.10 – Bottom and Surrounding Fiberglass Layers

Step 8 – Embed Insert: The steel insert is placed as it fits into the fiberglass. Once this is completed, perforations in the steel are filled with fiberglass to prevent dips in the finished test article due to the fiberglass voids the perforations create. The fiberglass used to fill the perforations is not packed tightly, however, as this creates a high resistance area for the resin during infusion.

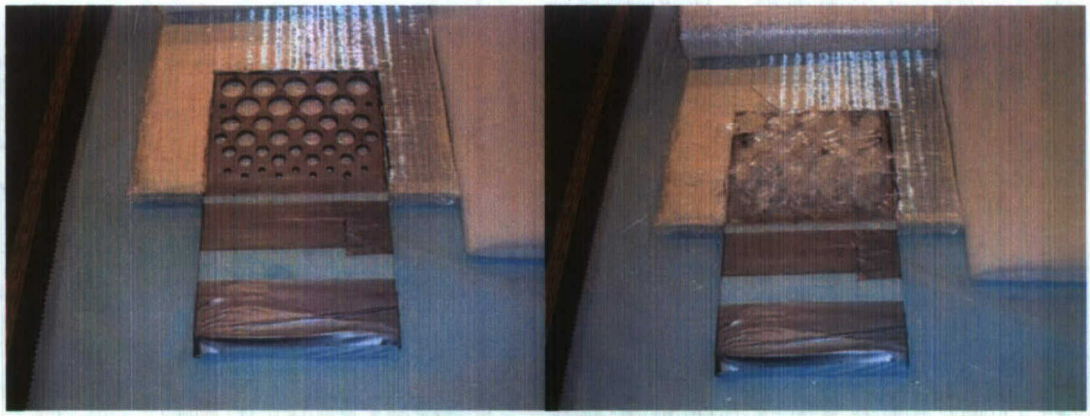

Figure 3.11 – Embedded Steel Insert

Step 9 – Lay Down Remaining Fiberglass Layers: The remaining top fiberglass layers are carefully laid down on top of the insert and other layers.

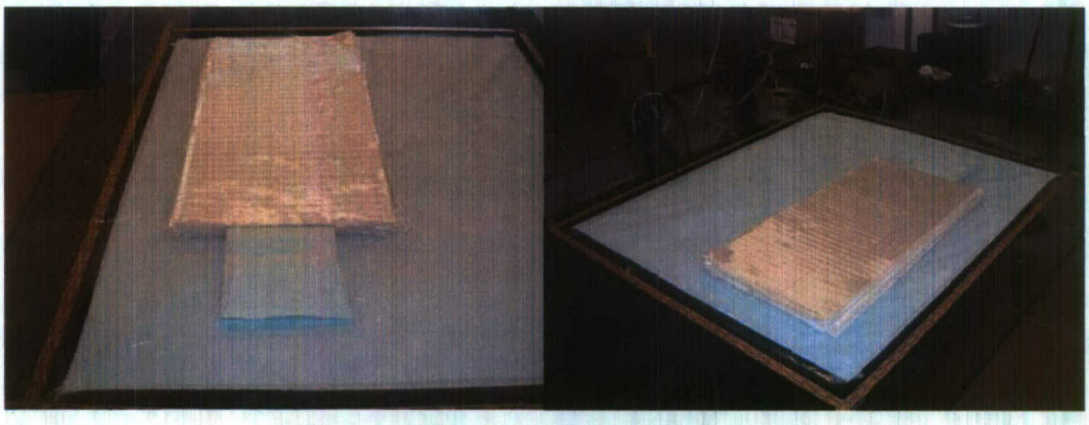

Figure 3.12 – Top Fiberglass Layers

Step 10 – Lay Down Third Layer of Peel Ply: Peel ply is laid down on top of the test article to prevent the top layer of flow media as well as the bagging film from being encapsulated. This layer of peel ply is cut large enough to at least lay down the sides of the part and make a border of about an inch around it on all sides.

Step 11 – Lay Down Second Layer of Flow Media: The top layer of peel ply, cut the same size as the bottom layer, is now laid on the test article.

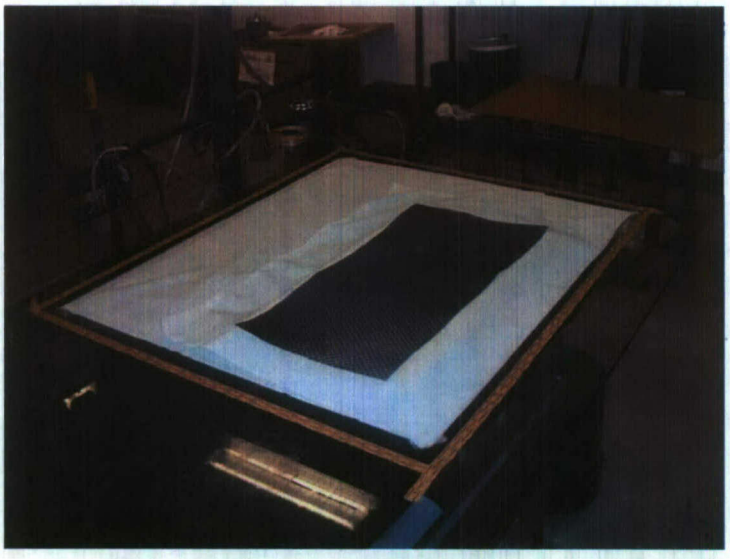

Figure 3.13 – Top Layer of Flow Media

Step 12 – Lay Down Bleeder Material: Bleeder material is used to enable better test article wet-out. It provides the resin with more time to pull through the test article before arriving at the vacuum hose. The bleeder should lay up on the part slightly to assure that there is no gap between it and the test article when vacuum is applied. The bleeder material should be folded over at least twice to get at least 4 layers. Airtech Airweave N4 bleeder material is used.

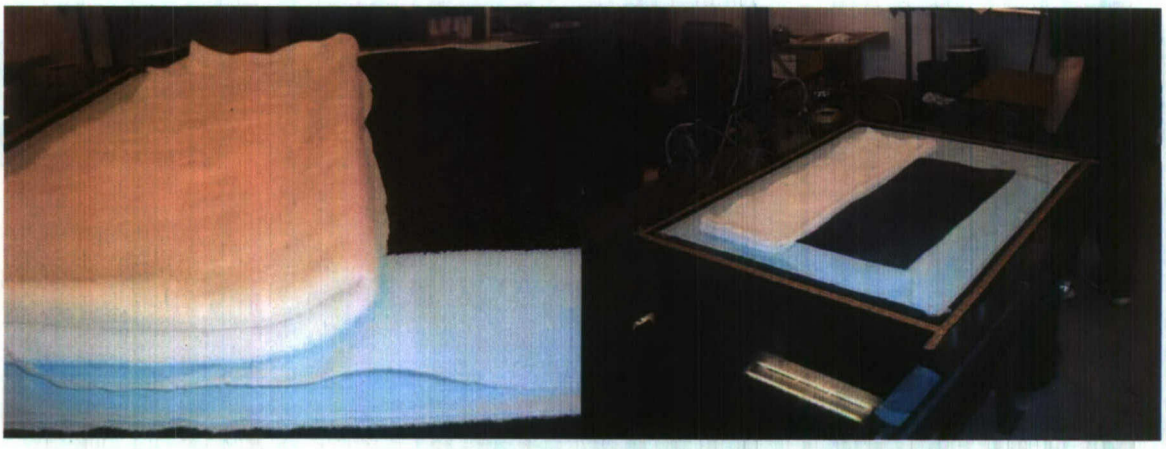

Figure 3.14 – Bleeder Material

Step 13 – Make Vacuum and Resin Hoses: The hoses are composed of two parts: plastic tubing and helical wire wrap. The wire wrap has the same outer diameter as the inner diameter of the plastic tubing (0.5in in this case) and it is taped inside the tubing.

For the resin hose, the plastic tubing goes off the side of the table into the bucket of resin. The exposed helical wrap should be stretched a little, and it should be approximately the length of the part. The plastic tubing must be long enough to reach from the edge of the part to the bottom of the resin bucket. The vacuum hose starts at the airtight vacuum pot which is connected to the vacuum pump. The tubing extends about six feet up from that point, and a tee is inserted so that there are two arms to come down to the table. Each end of the helical wire wrap is inserted into one of the tubing arms in the same way that it was for the resin hose. This creates a uniform vacuum.

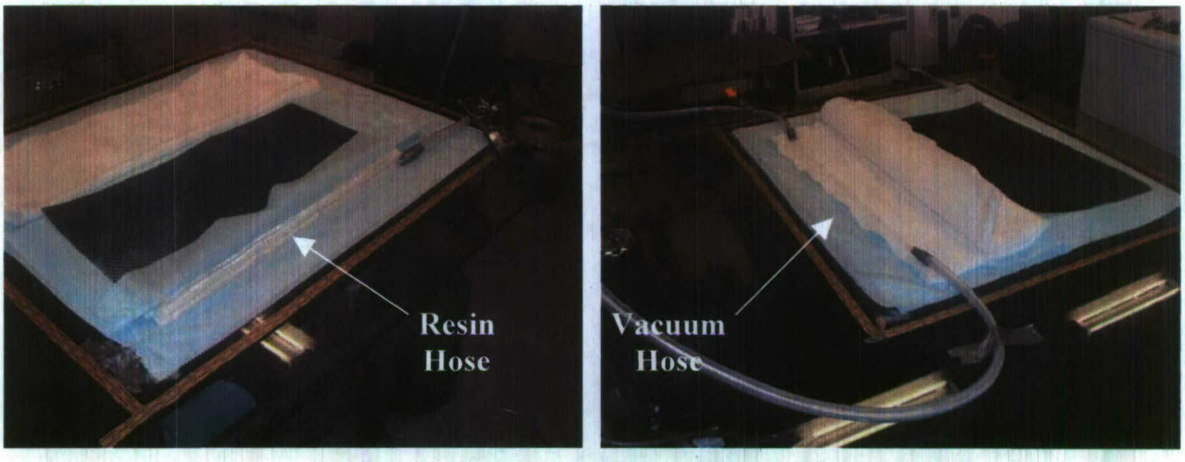

Figure 3.15 – Vacuum and Resin Hose

Step 14 – Lay Hoses in Panel: The helical wire wrap portion of the resin hose is placed over the top layer of peel ply up against the fiberglass. The vacuum hose is folded into the bleeder material near the rear.

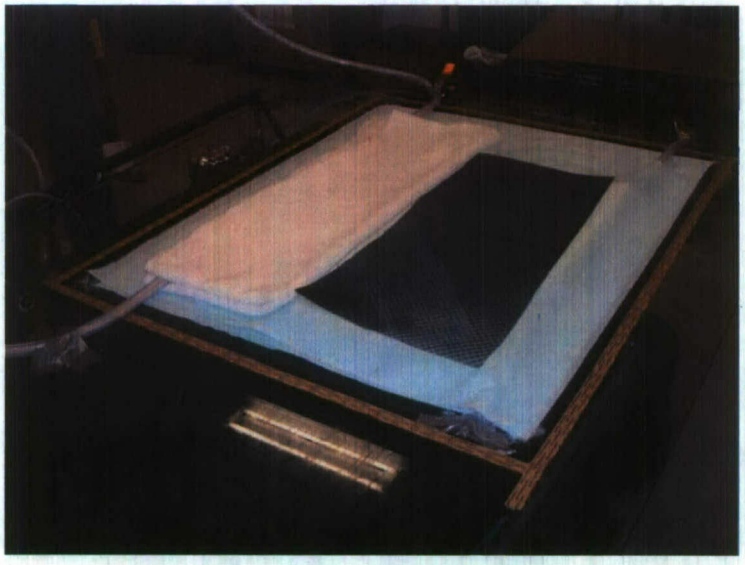

Figure 3.15 – Hoses in Place

Step 15 – Seal Hoses: Sealant tape is placed around the hoses as follows:

a. Tear open backing of the tape on the table below the hose

b. Wrap tape around hose and remove backing

c. Stick hose to the tape on the table

d. Fill side gaps to make a bell shape

e. Block any holes between table, hose, and filler tape

f. Lay a layer of tape over the setup to provide a smooth length of tape for the bagging film to adhere to the table. For instance, the bag will need extra slack to go from the table up the side of the test article. Flaps create the required slack. The first step in this process is simply to put them down.

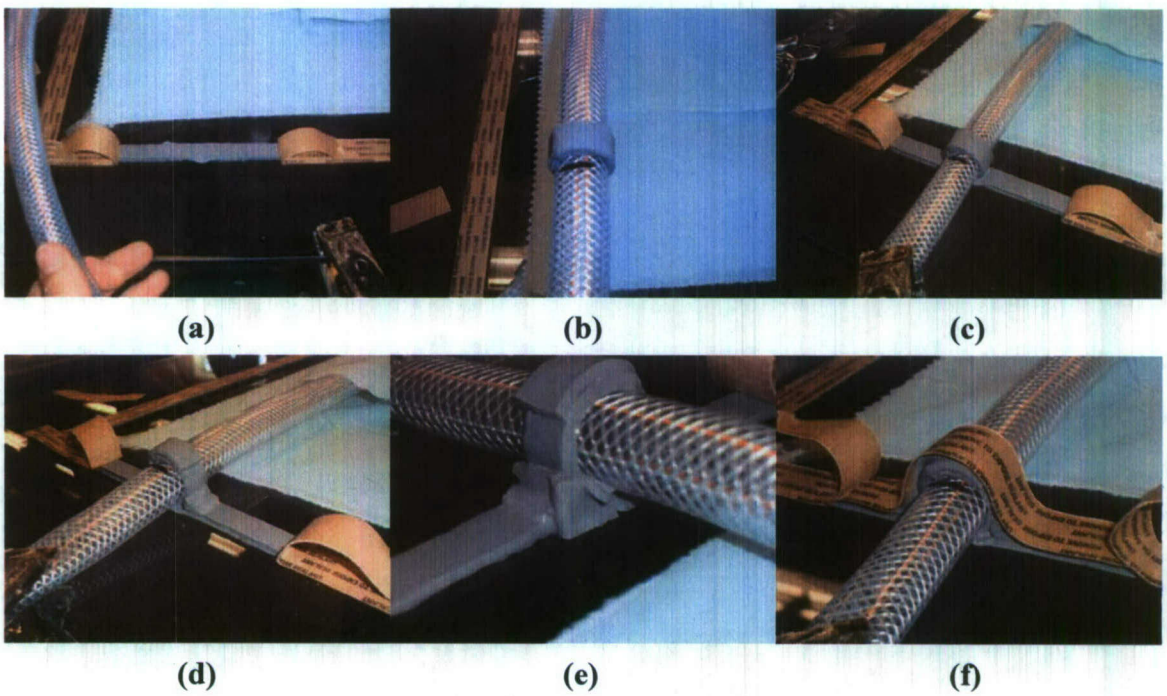

Figure 3.16 – Steps to Seal Hoses

Step 16 – Put Down Flaps: Flaps are placed to account for any change in thickness on

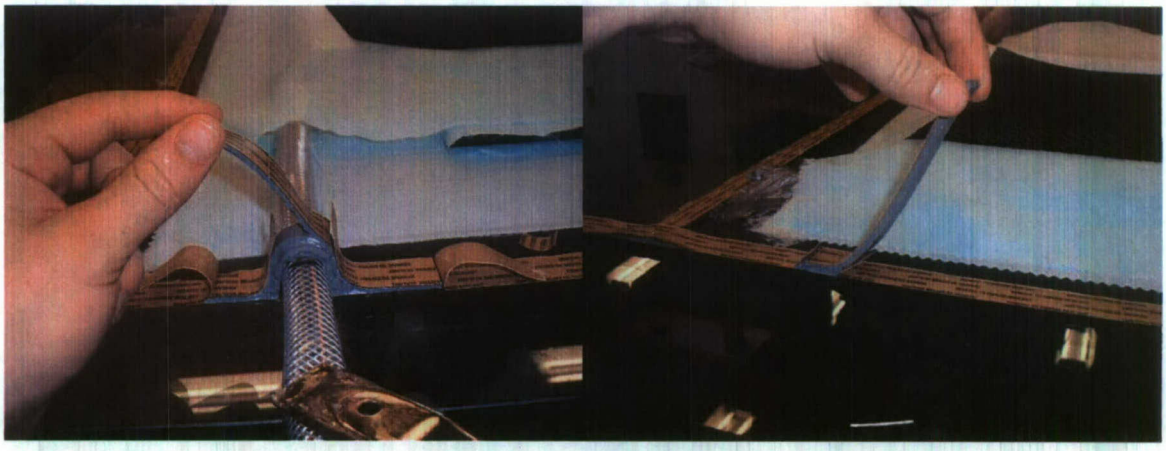

Figure 3.17 – Flaps

Step 17 – Begin Bagging: The vacuum bagging film is cut at least a foot longer and wider than the area marked out by the sealant tape. This ensures that the slack needed to fit around the shape of the panel will be there. A corner is picked to begin with, the paper backing on the sealant tape removed, and the bagging film is pressed into the exposed sealant tape. A line is drawn along where the tape is for guidance to remain straight as the bag is stuck down (do this on each side).

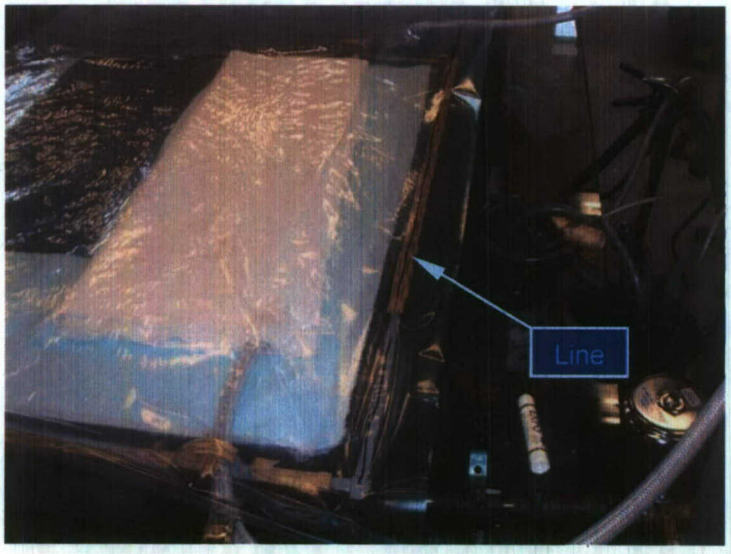

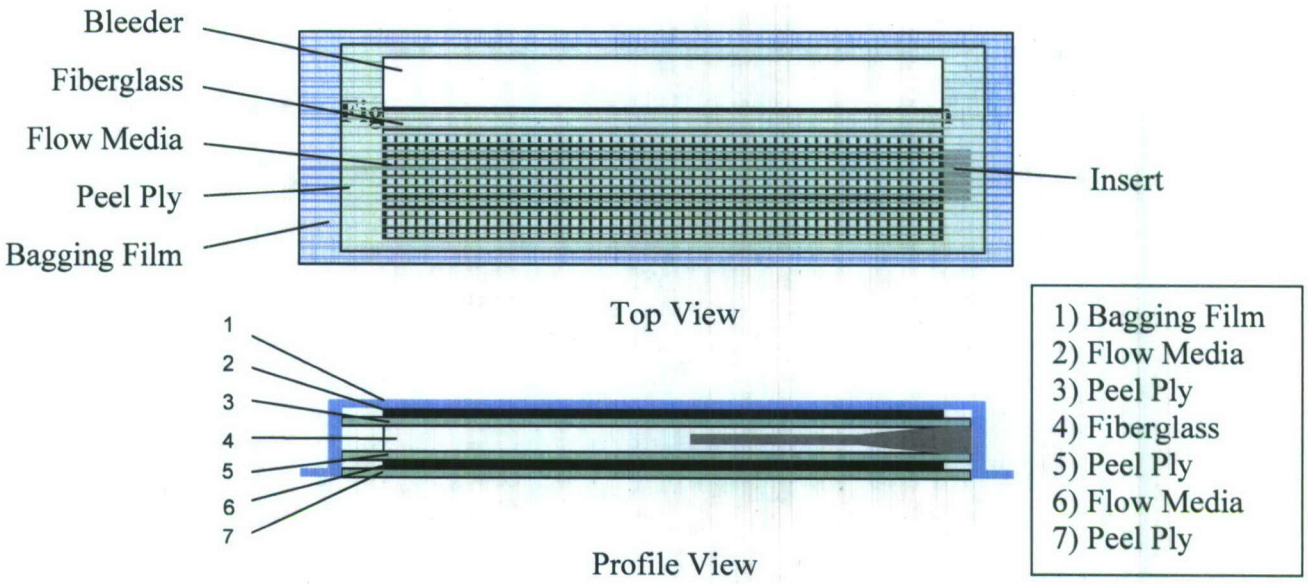

Figure 3.19 – Layers Involved in Layup

Step 18 – Adhere Bagging Film to Flaps: First the bagging film is adhered to the full length of the flap. Then, the flap is lifted, and the top folded over itself. Finally, the end of the flap is pressed into the tape against the table.

Figure 3.20 – Adhesion of Bagging Film to Flaps

Step 19 – Adhere Final Flap: Once the first three sides and most of the fourth are done, finishing with the final flap is the last step in the sealing process. The flap has to be of a variable height, because it is responsible for taking up whatever slack may remain in the bag. This flap is made extra long in case there is a significant amount of slack remaining in the bag. The first step is to lay the flap down near the final corner. The bag is adhered to the full length of the flap.

Figure 3.21 – Bagging Film Adhered to Long Flap

Next, the bagging film is adhered to the tape on the table. This is begun at the corner, and progresses back toward the end of the long flap. Once this is reached, the flap should make a bridge. The bridge is adhered to the tape on the table, starting at the ends, and working towards the middle. The Bridge meets itself and creates the final flap.

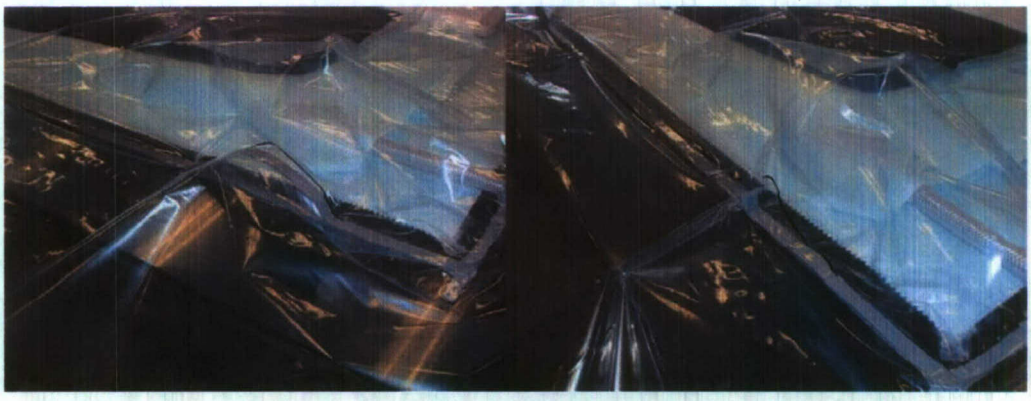

Figure 3.22 – Creation of Final Flap

Step 20 – Pull Vacuum and Inspect Layup for Leaks: The resin hose is clamped off, and the vacuum pump turned on to pull vacuum on the layup. Leaks can often be identified by a hissing sound they make as they pull air into the layup. The vacuum gage should also be observed, with any changes in magnitude noted. The bagging film should be pressed down all around (especially at flaps and hose inlets) to make sure everything is adequately sealed.

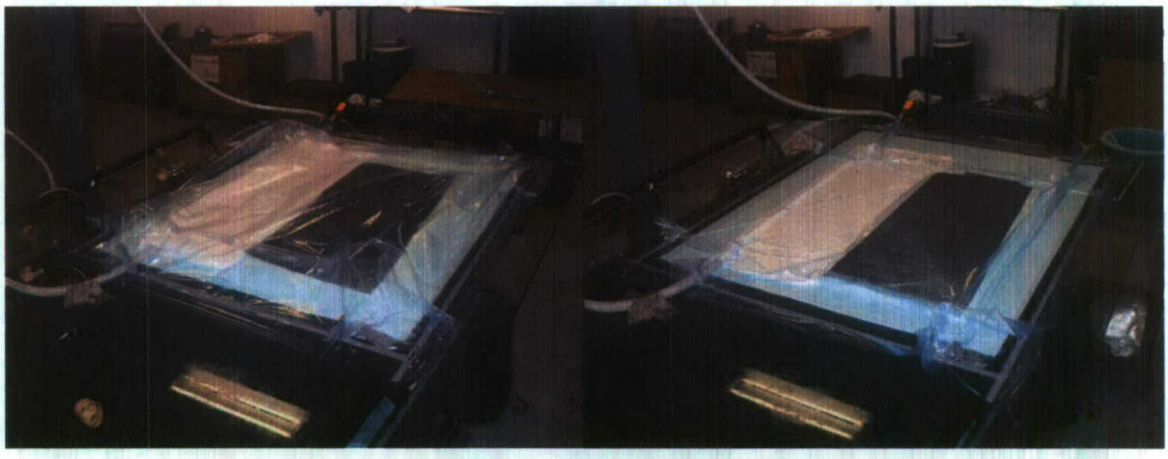

Figure 3.23 – Layup Before and After Vacuum is Applied

Step 21 – Begin Infusion: Once confidence in the integrity of the bagging film and seal is established, the infusion is begun. The end of the resin hose is placed into the catalyzed resin (Derakane 8084 epoxy vinyl ester resin), and the clamp keeping the hose shut removed. This allows the resin to be pulled through the test article.

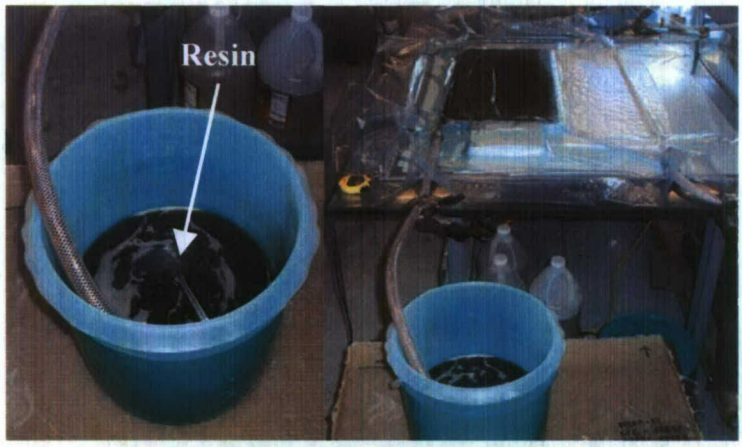

Figure 3.24 – Resin as Infusion Begins

Step 22 – Clamp Resin Hose: Once the resin has had ample time to pull through the test article, and the estimated gel time is approaching, the resin hose is clamped off.

Step 23 – Clamp Vacuum Hoses: Shortly after the resin hose is clamped off, the vacuum hoses are clamped off as well.

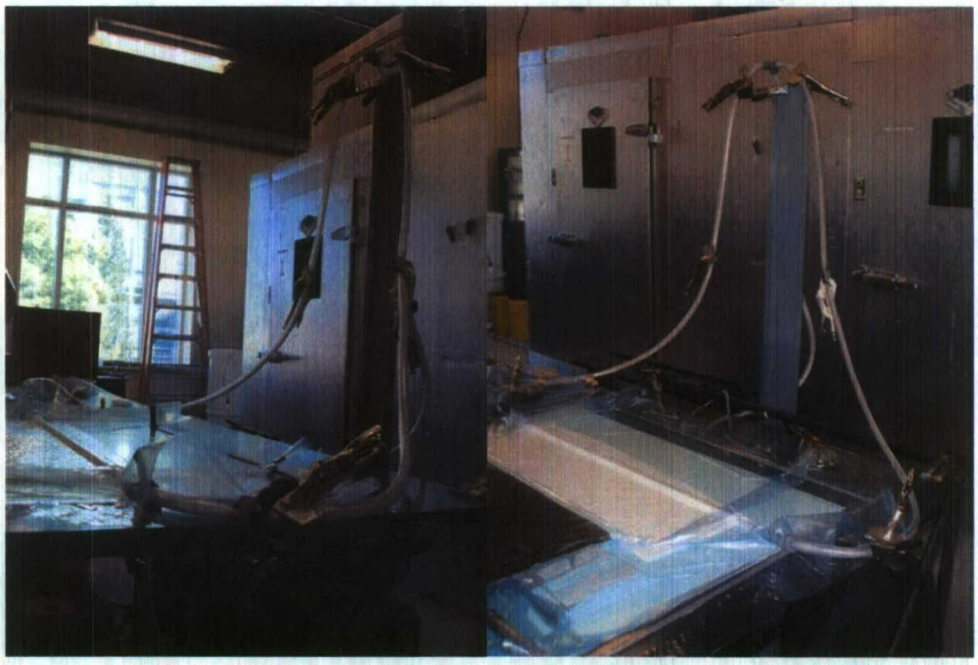

Figure 3.25 – Vacuum Hoses Clamped Off

Step 24 – Allow Test Article to Cure: The infusion is now finished, and the panel should be left to cure for at least 24 hours. Once the resin is completely cured, the lay-up can be torn up. Parts should be allowed to cure for several weeks afterwards.

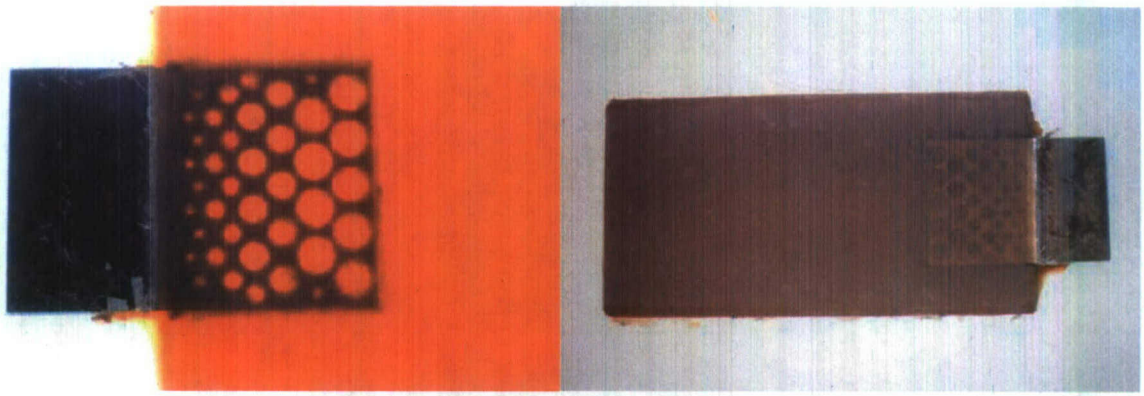

Figure 3.26 – Successfully Fabricated Test Article

3.4 Material Properties

Material testing has been performed on 0.25in quasi-isotropic coupons fabricated with the same resin and fabric as used here. The resulting values are representative of the current

panels. The average ultimate tensile and compressive strengths of the material are 39.27ksi and -40.37ksi, respectively. The fiber volume fraction of the material is on average 48.5. It should be stated that there is inherent variability in the fabrication and material properties of VARTM composites. Even within one panel, there may be variation in the fiber volume fraction, strength, or other properties. For this reason, it is necessary to rely on averages. It should be kept in mind, however, that any predictions made based on these average values should be conservative, and it should be expected that material properties will differ from component to component.

4. Experimental Fatigue Analysis of Hybrid Joints

The preliminary understanding of the loads and moments experienced by the joints of interest, as well as successful fabrication of test articles, made the experimental fatigue testing viable. Keeping in mind that the tests were to be modeled after the vessels studied in the MACH project, flexure fatigue was chosen as the testing method. This was deemed appropriate since the hull panels in small to mid-size hybrid vessels composed of a GRP composite over a steel skeleton are primarily exposed to out-of-plane loads. Also, due to the small amount of data available on flexure fatigue, this data should serve to expand the current knowledge base.

4.1 Flexure Fatigue Test Setup

The first step in performing fatigue tests was to obtain an appropriate test fixture. The fixture that was currently available in the UMaine Hybrid Structures Laboratory was far too massive to run satisfactory tests. Its excessive mass would have contributed to a significant waste of resources while hindering the ability to obtain precise test results. Its large size would have been both unnecessary and cumbersome for the smaller moment arms determined for and used in the tests. For these reasons, a new test fixture was designed specifically for the present research, as seen in Figures 4.1-2. This fixture is simple, and consists mainly of three parts. The first part is a steel tab 0.75in thick for the hydraulic grip on the actuator to clamp. It is bolted to the second part, the load transfer beam. This beam transfers the load applied by the actuator to the third part: the clamping mechanism, or grippers, which are also bolted to it. 0.75in bolts clamp the two rollers on each side of the clamping mechanism to the test article.

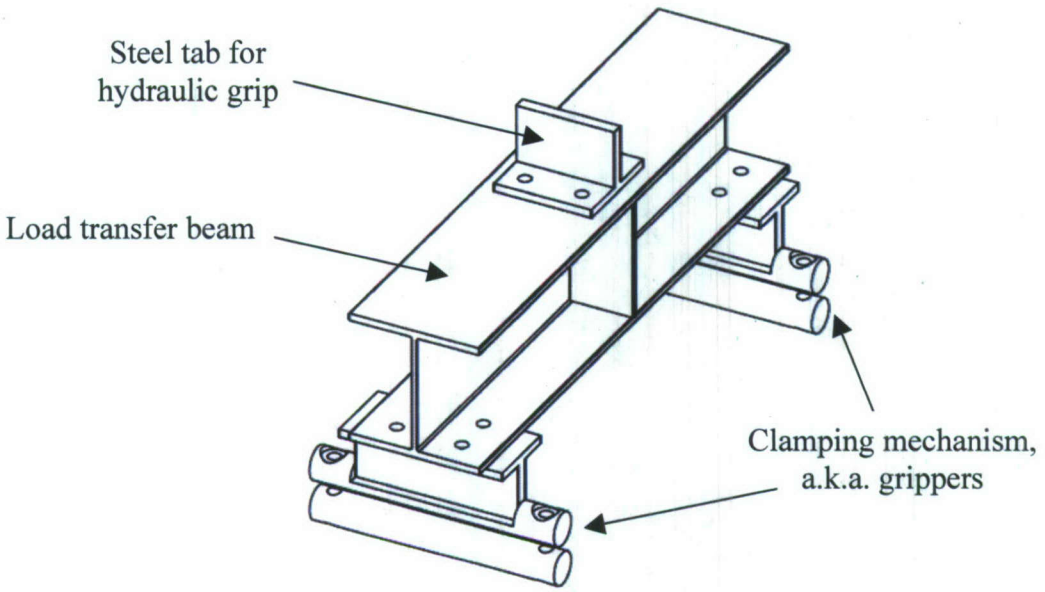

Figure 4.1 – Isometric View of Fixture Designed for Fatigue Tests

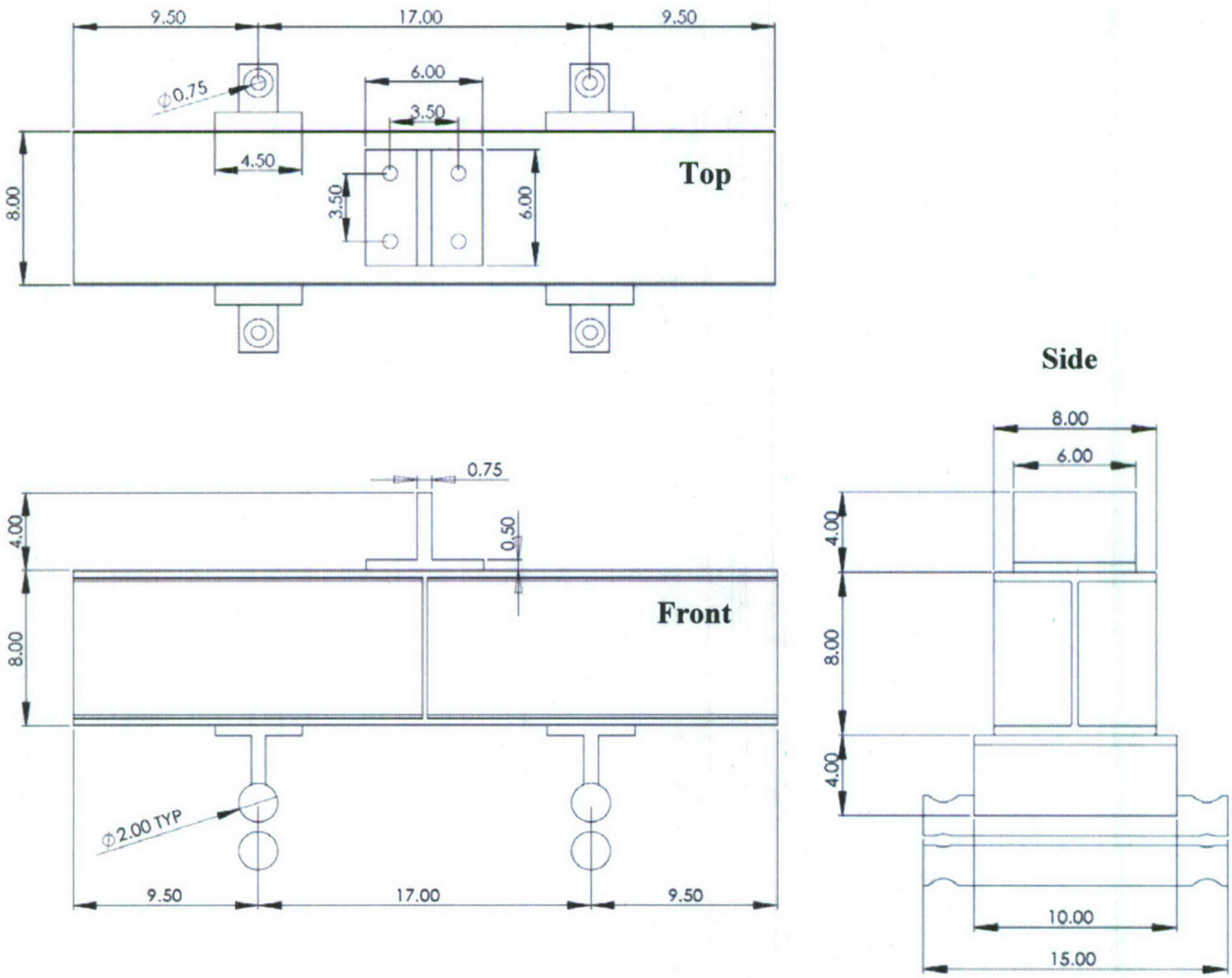

Figure 4.2 – Dimensions of Fixture Designed for Fatigue Tests (in)

The full test fixture design for the flexural fatigue testing is shown in Figures 4.3 and 4.4 and consists of a steel wide flange section, a clamping mechanism for the test article, and an actuator mount. The connection testing was conducted at the Hybrid Structures Laboratory, located in the Advanced Manufacturing Center at the University of Maine. The test setup consisted of a 165-kip, ± 3-inch MTS actuator, mounted on a 300-kip capacity modular reaction frame. The load was transferred to the test article by an hydraulic grip. The steel tee support was mounted on the reaction frame by eight 0.875in grade 5 steel bolts. The composite panels were joined to the steel substructure by various connection schemes as mentioned previously. The ends of the composite panels were then secured between two grippers which were clamped together with 0.75in grade 8 bolts. The insertion procedure is found in section 4.3.2.

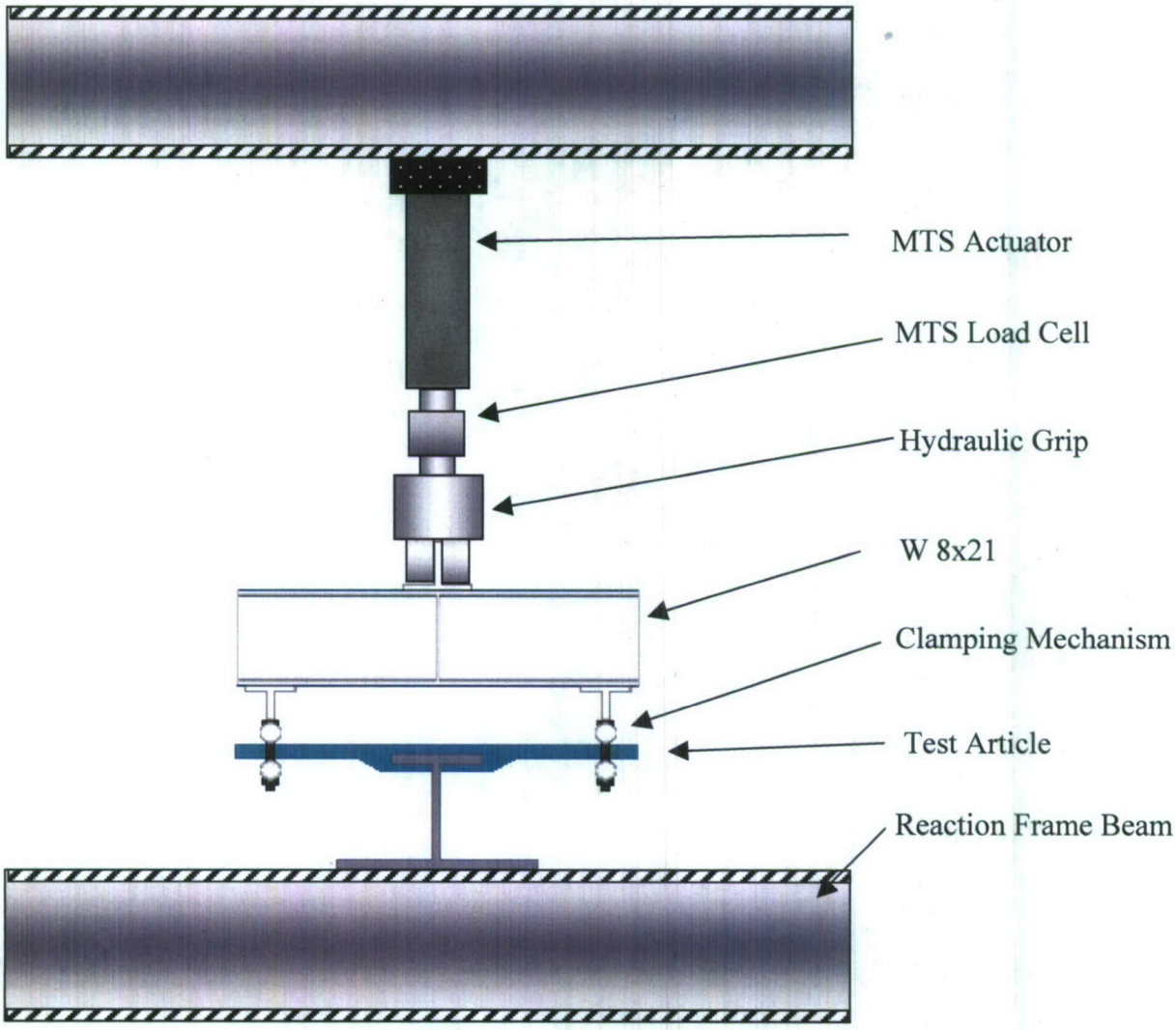

Figure 4.3 – Front View of Actuator, Fixture, and Joint Assembly

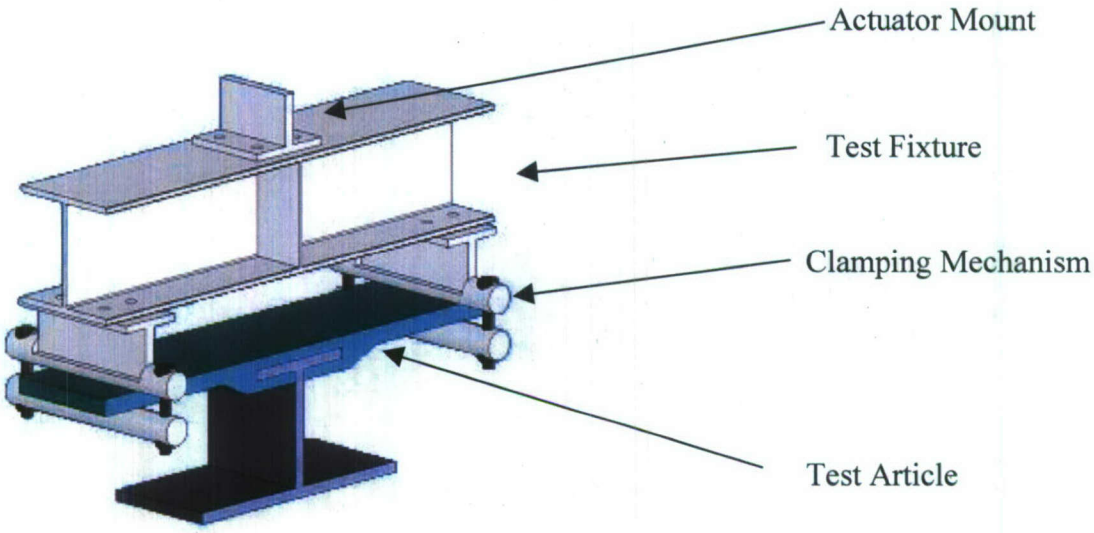

Figure 4.4 – Isometric View of Fixture and Joint Assembly

Figure 4.5 shows several photographs of the testing fixture gripping some clamped test articles.

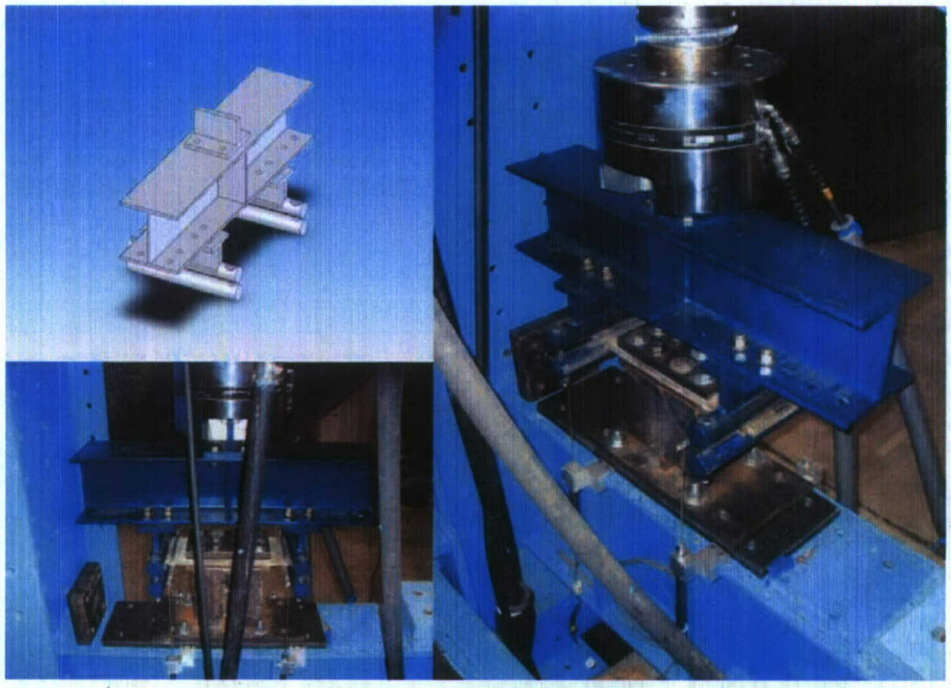

Figure 4.5 – Isometric View and Photographs of Fixture Gripping Test Article

4.2 Testing Controls

All testing for this research was done with an MTS universal test control system. A computer with DAQFI software written to run the tests communicated with the MTS in order to output the desired analog signals to the actuator, as well as to record the load and displacement values that load cell and transducer on the actuator output. Tests were controlled and data was collected for the tests using an IOTech data acquisition system with a Daqboard 2000, 16-bit resolution A/D card and a computer code called DAQFI. The DAQFI program was created at UMaine and was capable of both data acquisition and output of a control signal for the fatigue tests. A module was written specifically to run the fatigue testing. A schematic of the MTS can be seen in Figures 4.6-9. Figure 4.6 shows the overall setup with all components included. The computer sends and receives data from the first DAQ board, DAQ 1. The signal from the computer is converted from a digital signal to analog, which proceeds from DAQ 1 to the analog output board. A cable from this board then goes to MTS, which modifies the signal based on what the span is set to and sends it to the actuator. The load and displacement data from the actuator (analog) is then sent back to the MTS, which transmits the signal through a cable to the MTS Output board. The Analog input board also sends data to the MTS output board, and this is where any LVDT's, strain gages, or similar instrumentation would be connected. The data from the MTS and instrumentation is sent from the MTS output board to DAQ 1, which converts it to a digital signal and sends the information to the computer. Figure 4.7 shows the rear of the MTS, and where various cables are connected. It can be seen where the cable to the MTS output board is connected, as well as the cables from the actuator. Depending on whether control mode of the test being run is load control or displacement control, the cable from the computer is placed in the 9^{th} or 11^{th} "From Computer" port. Figure 4.8 depicts the MTS output and analog input boards. It can be seen that the MTS output cable with the load and displacement signals comes from the MTS and connects to the MTS output board. Channels 3-16 on the analog input board are where the peripheral instrumentation is connected. A cable then communicates from the MTS output board to DAQ 1. Figure 4.8 outlines the communications from the computer to and from DAQ 1. The computer sends its signal to the lower part DAQ 1, which then relays it to the analog output board. The Actuator, LVDT, and any other

signals come into the upper part of DAQ 1, which then sends that information to the computer.

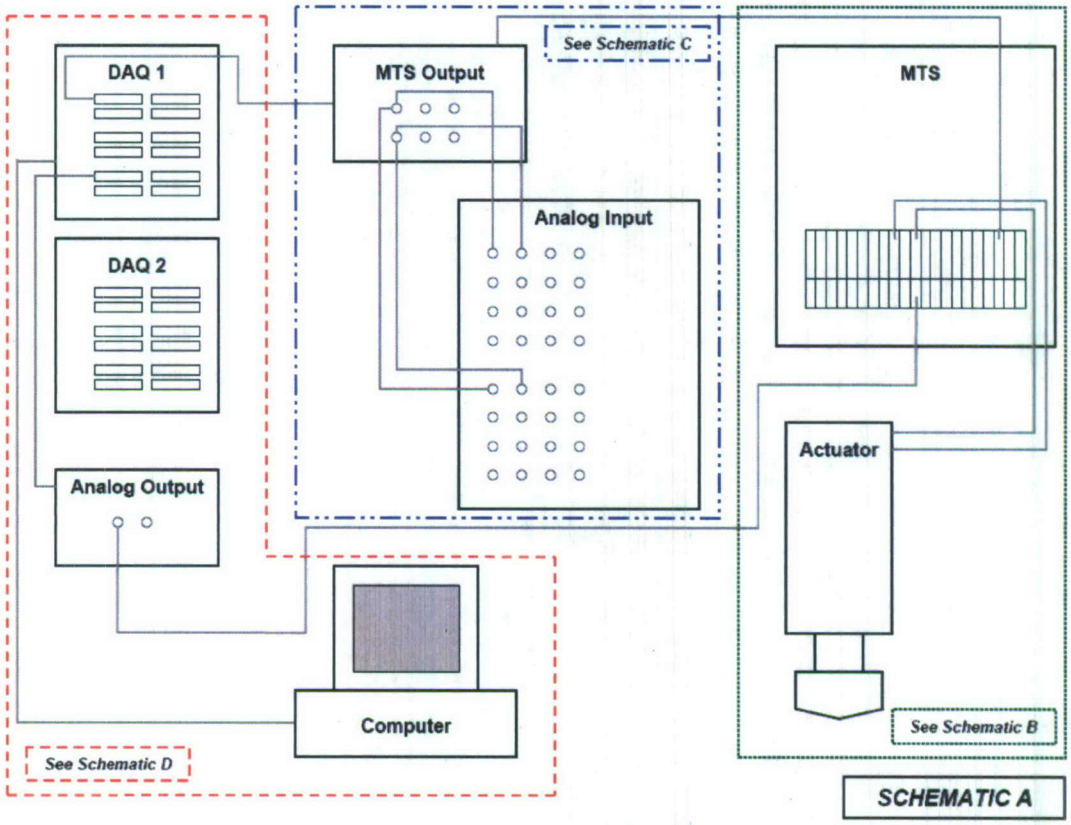

Figure 4.6 – Schematic A: Full Testing System

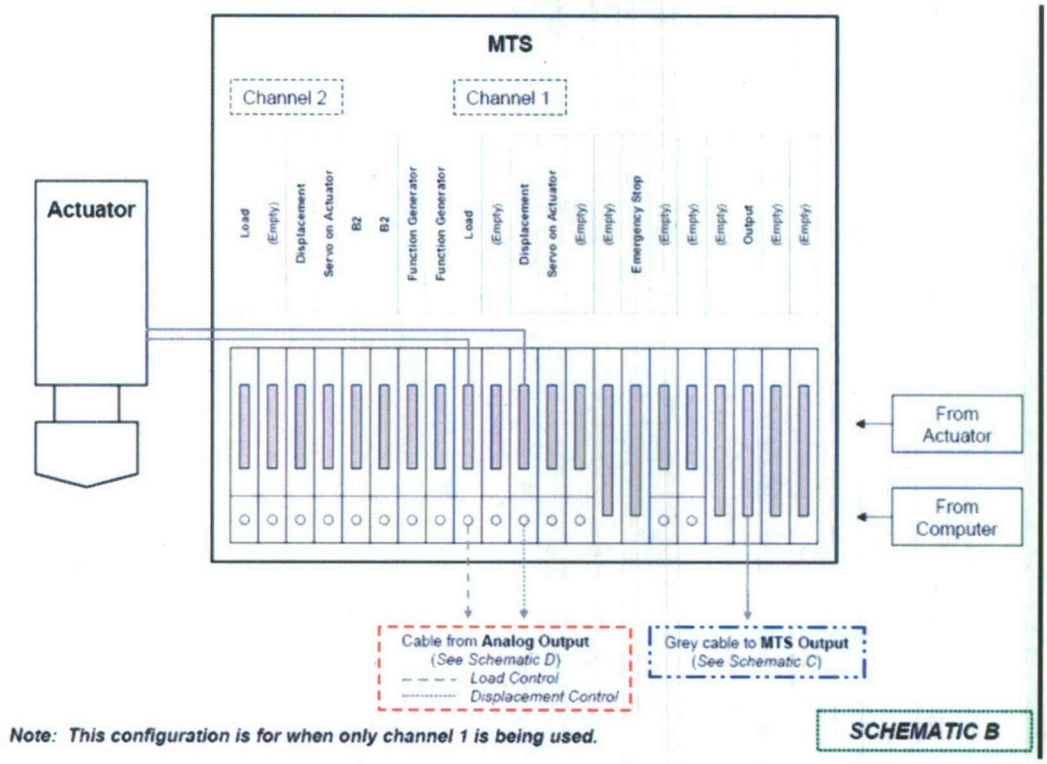

Figure 4.7 – Schematic B: Actuator and MTS

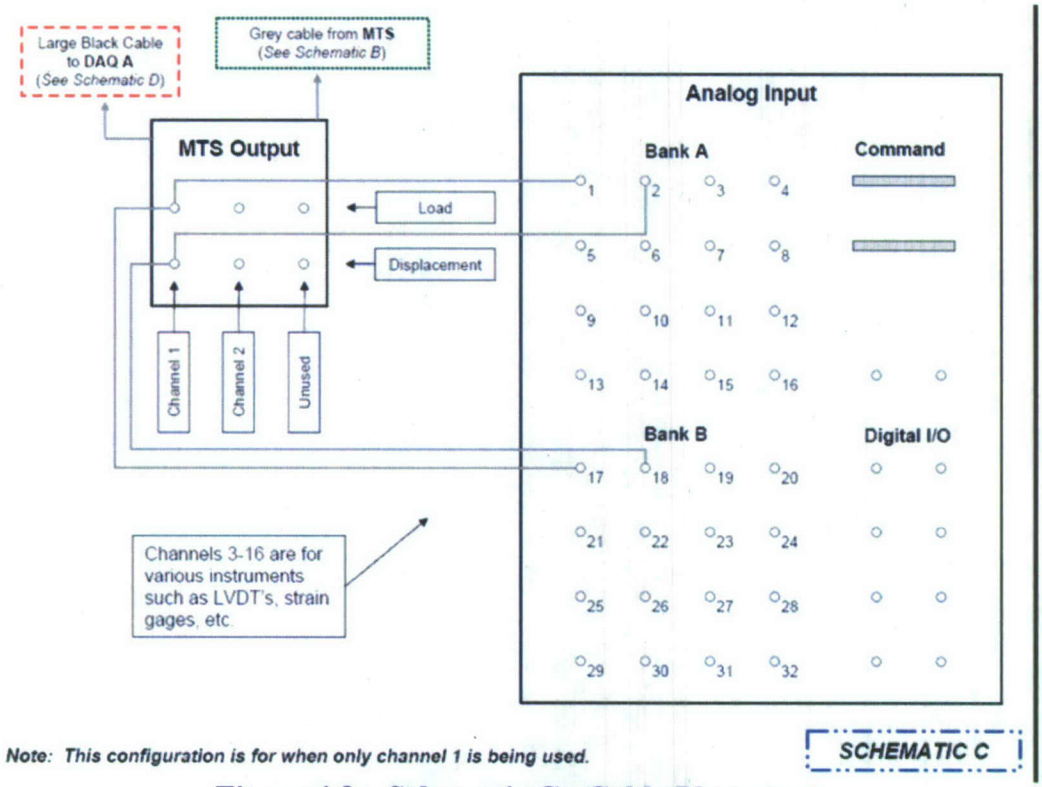

Figure 4.8 – Schematic C: Cable Placement

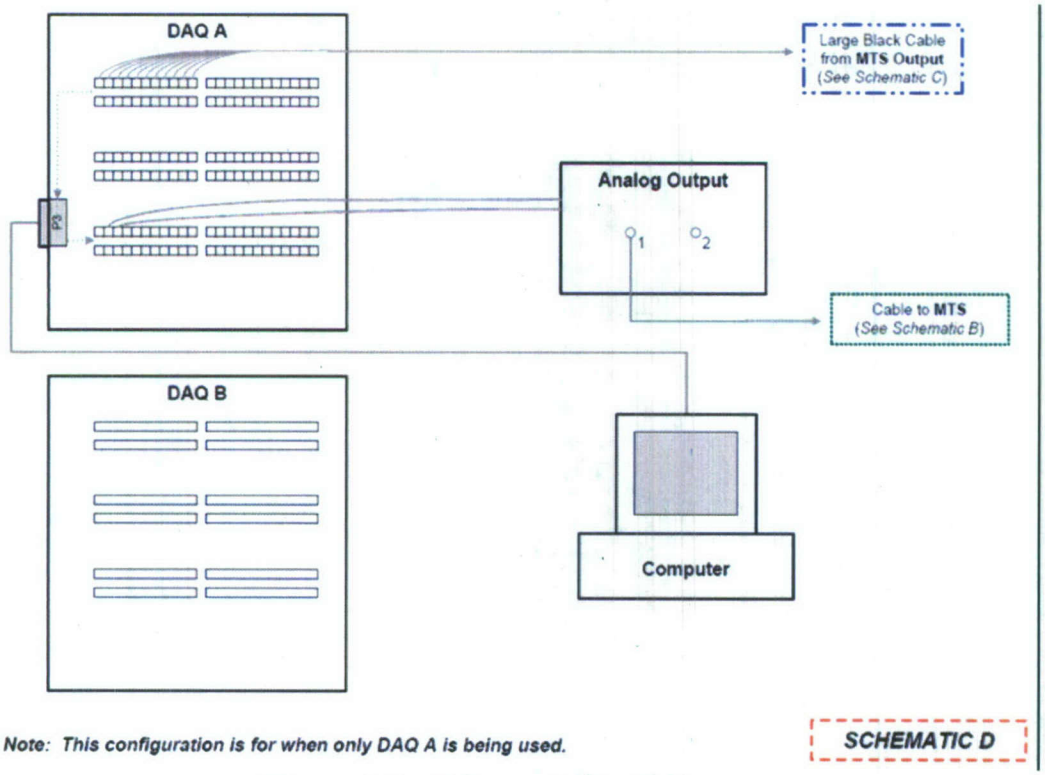

Figure 4.9 – Schematic D: Computer

4.3 Testing

Before any testing could begin, the location of the clamping mechanism, which controls the moment lever arm, had to be decided. This was a critical task, as the moment arm of the joint was a very important aspect of the tests. As previously discussed, the FEA data for target load, moment, and moment arm was consulted and a value of 8.5" chosen for the moment arm. With the clamping mechanism placed in the correct location, testing could proceed.

Four different joint styles would ideally be tested in the scope of this project: a clamped joint and a standard bolted joint for a baseline, as well as a bolted joint using thinner, high-strength steel tee and weldable embedded steel joint to investigate more novel joint styles. For each joint, four different tests would potentially be applied:

1) Cyclic Test to Failure: This is done once per joint style to determine the maximum load values the style can withstand. Once the maximum is determined, values at which the fatigue tests should be run can be determined based on desired percentages of the maximum load.
2) Fatigue Tests: As the main purpose of the research, these tests are done multiple times for each joint style, varying the load. Procedures for the flexure fatigue tests are adopted from previous fatigue studies performed for ONR and the US Navy at the University of Maine.
3) Intermediate Cyclic Tests: These are performed periodically throughout the life of the fatigue tests to track the degradation of the test articles as the test progresses.
4) Residual Strength Tests: These are performed in the occasion that a run-out cycle value is reached. The amount of cycles designated for a run-out is $2x10^6$ cycles.

4.3.1 Joint Styles

Due to the preliminary analytical and manufacturing work done for this research, the scope of testing in this thesis covers the two baseline joint styles, the more novel styles being left as future work under the project.

Standard Bolted Joint

The first joint style tested was a standard bolted joint. The bolted joints consisted of two 10inx6.75inx0.75in E-glass composite test articles fabricated as discussed in section 3.3. They were drilled with six 0.5in holes in the hole pattern seen in figure 4.10. The structural steel part of the joint was a DH-36 steel tee, which can be seen with di\mensions in see Figures 4.11 and 4.12. The composite test articles were bolted to the steel tee with 0.5"-13 x 3" grade 8 bolts, as seen in figure 4.13, and washers were placed between the bolts and the composite.

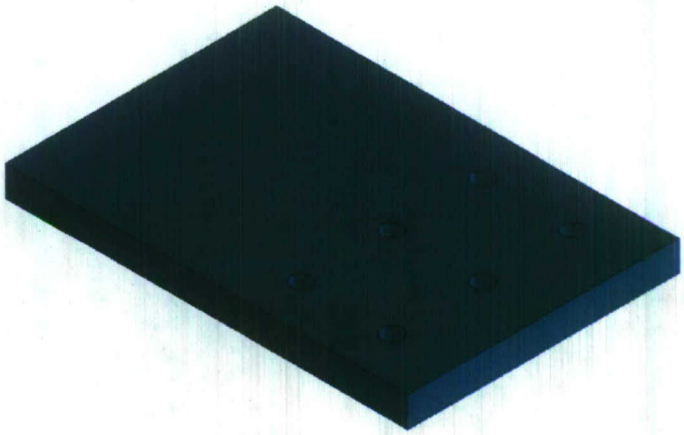

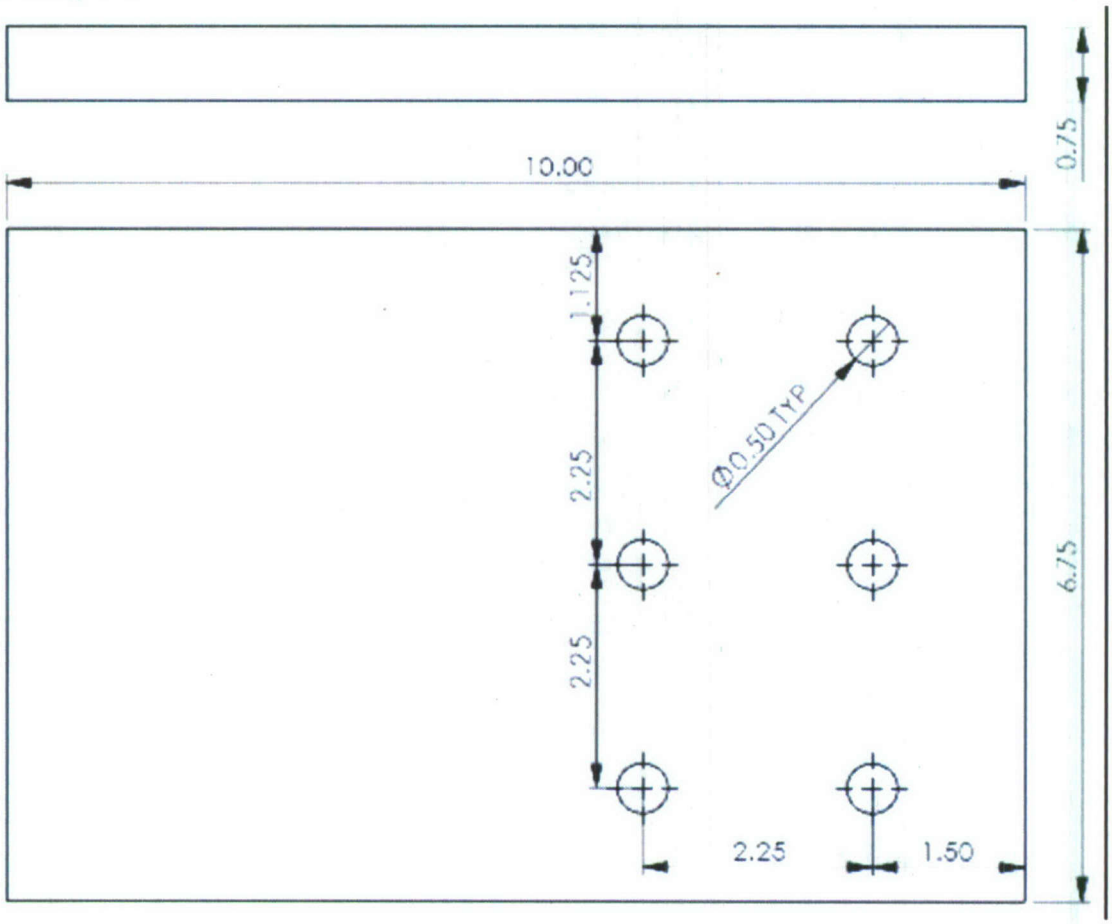

Figure 4.10 – Bolted Joint Hole Pattern

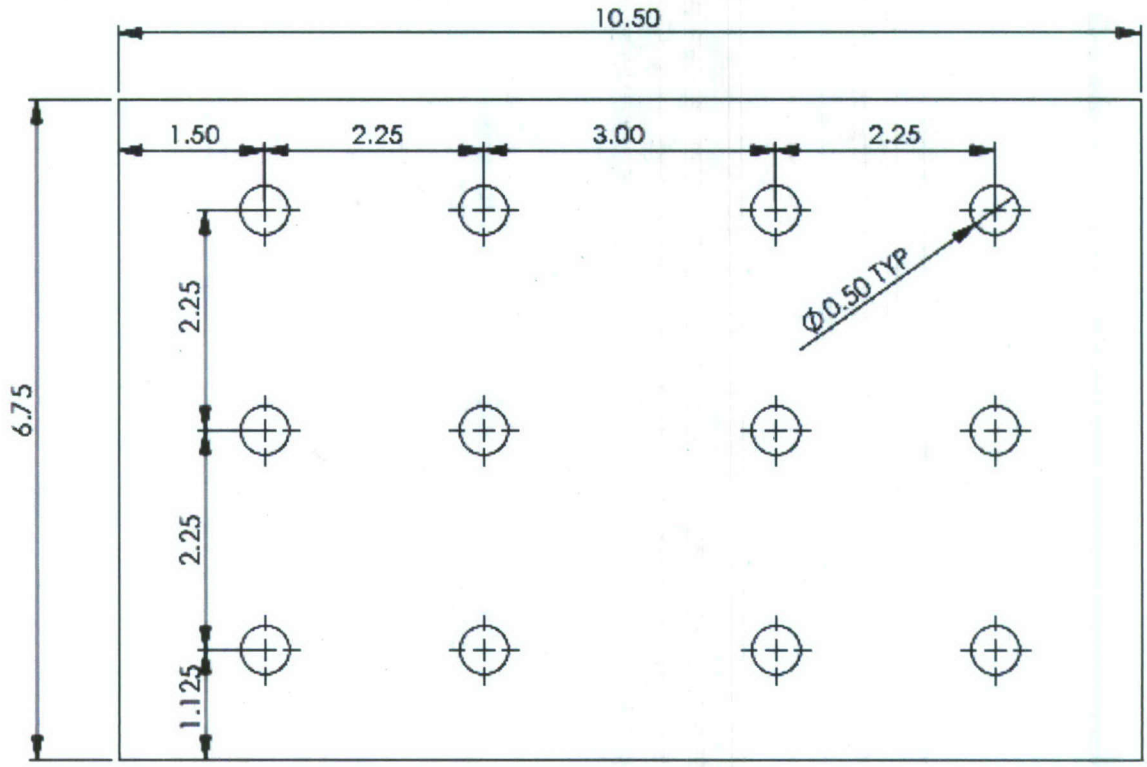

Figure 4.11 – Top Hole Pattern Dimensions for Standard Bolted Joint Tee (in)

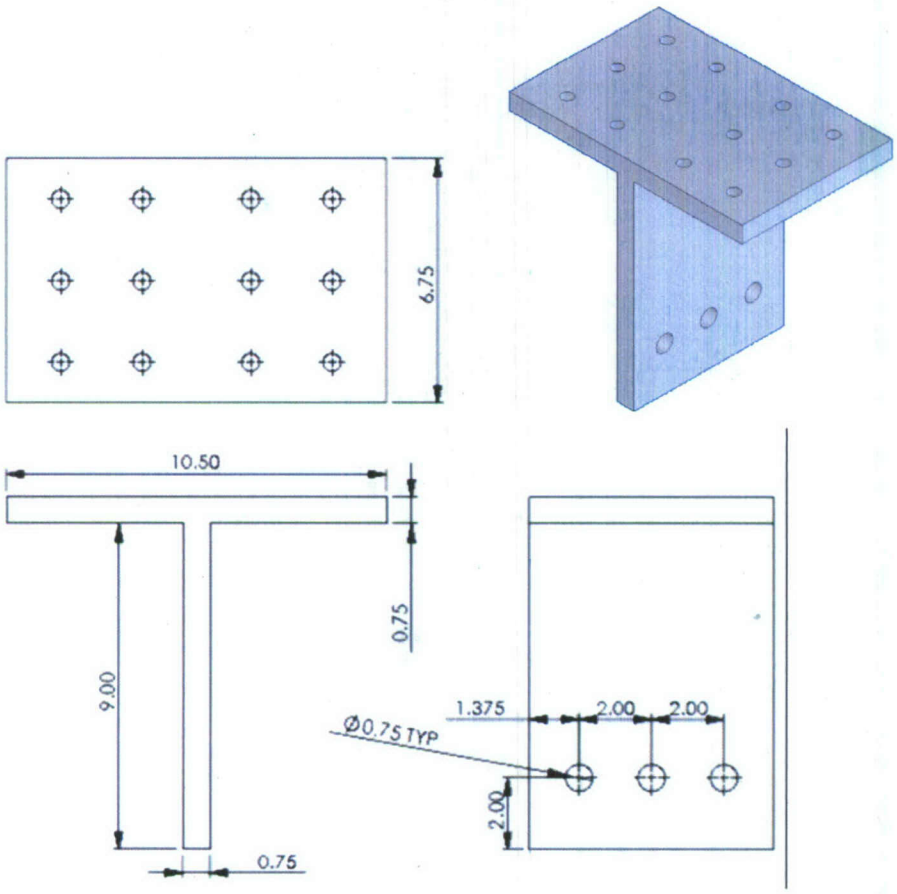

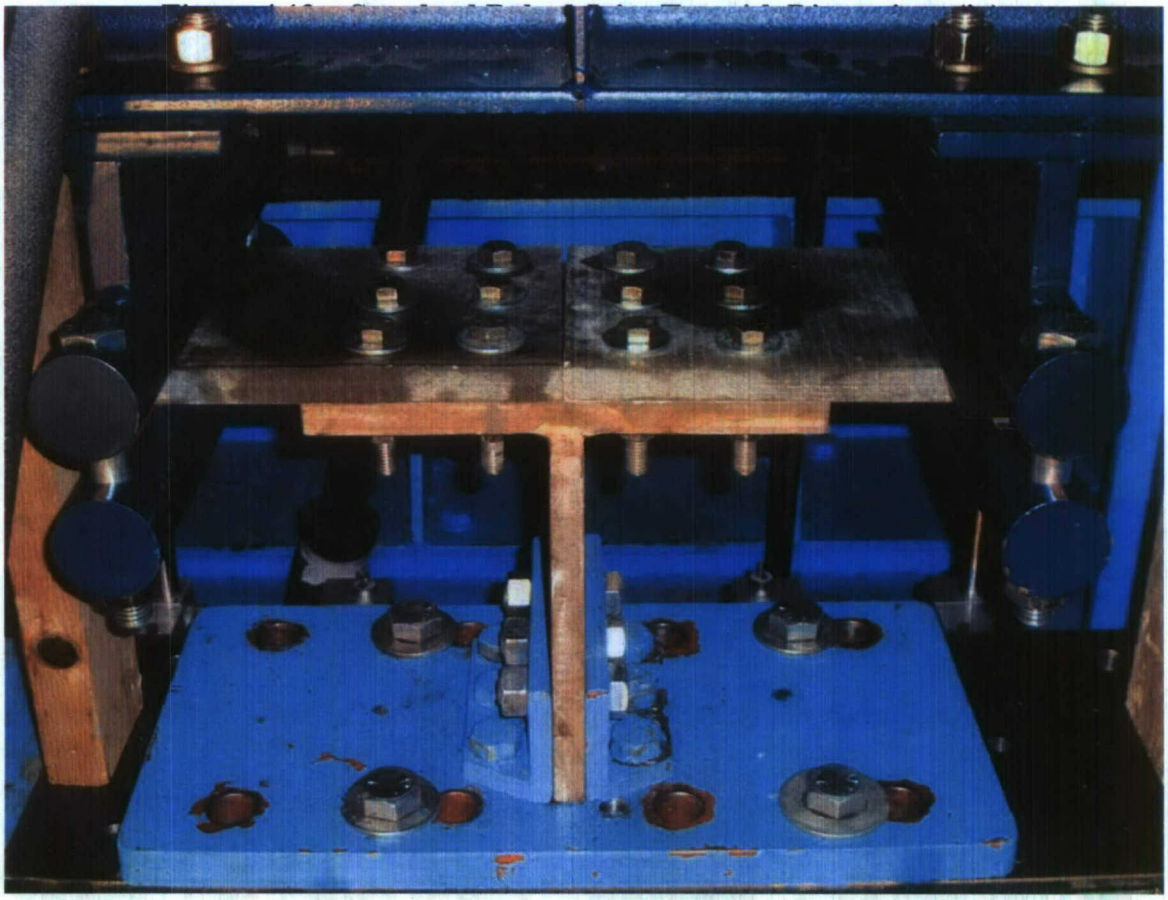

Figure 4.13 – Standard Bolted Joint in Test Fixture

Clamped Joints

The clamped joints consisted of two 10inx6.5inx0.75in E-glass composite test articles drilled with six 0.75in holes in the hole pattern seen in Figure 4.14. The tee used in the clamped tests (seen in Figure 4.15) was similar to that used in the bolted tests as far as material specifications are concerned. However, the holes were 0.75in in diameter to accommodate the larger bolts, and it was stiffened with a 0.25in plate stiffener on either side. The reason the clamped joints were tested was that they eliminated the effect of the steel tee on the test, effectively isolating the composite articles being tested. A steel plate with the same hole pattern as the tee was then placed on top of the two test articles and bolted to the tee, clamping the composite in place, as seen in Figure 4.16.

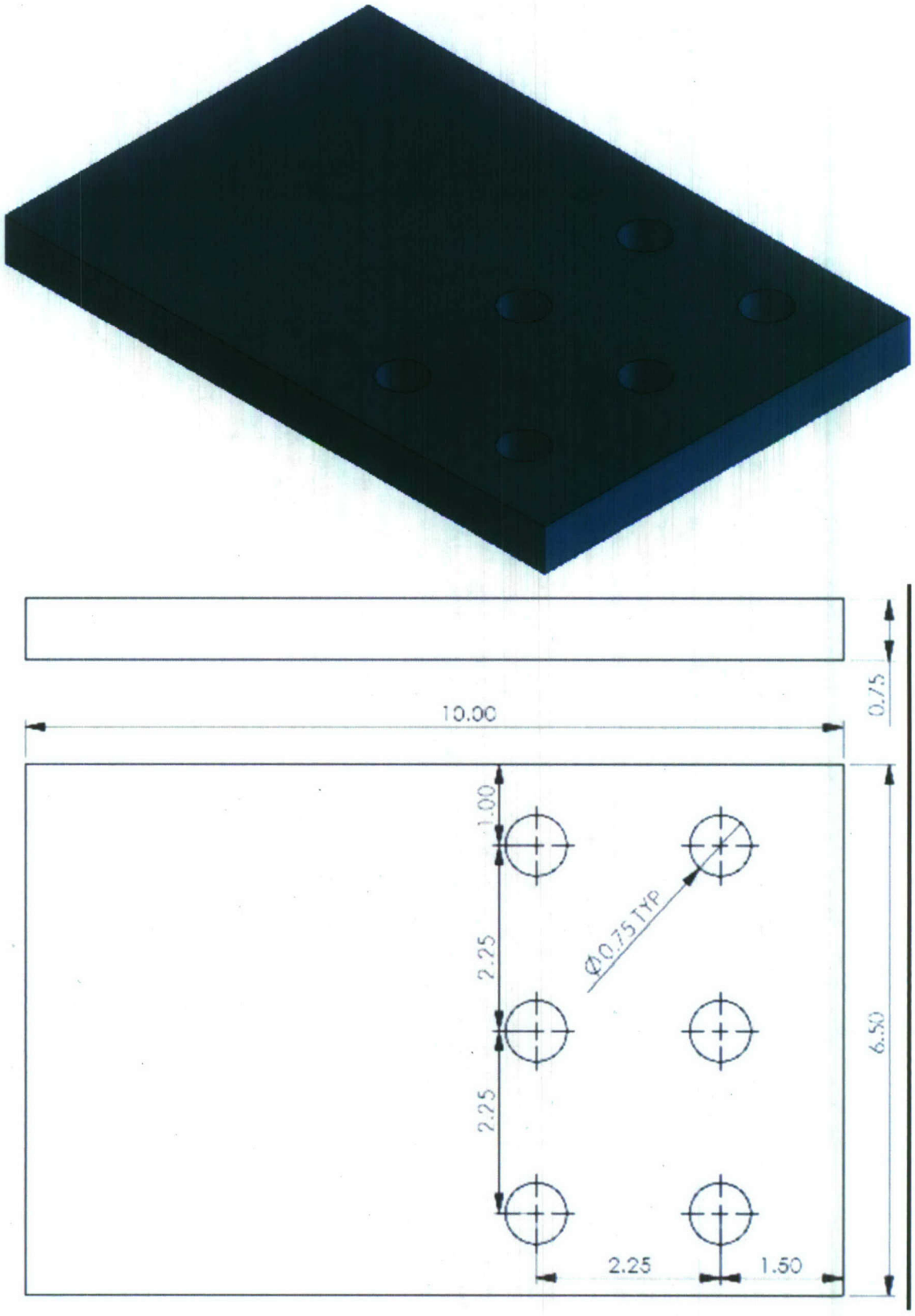

Figure 4.14 – Clamped Joint Hole Pattern

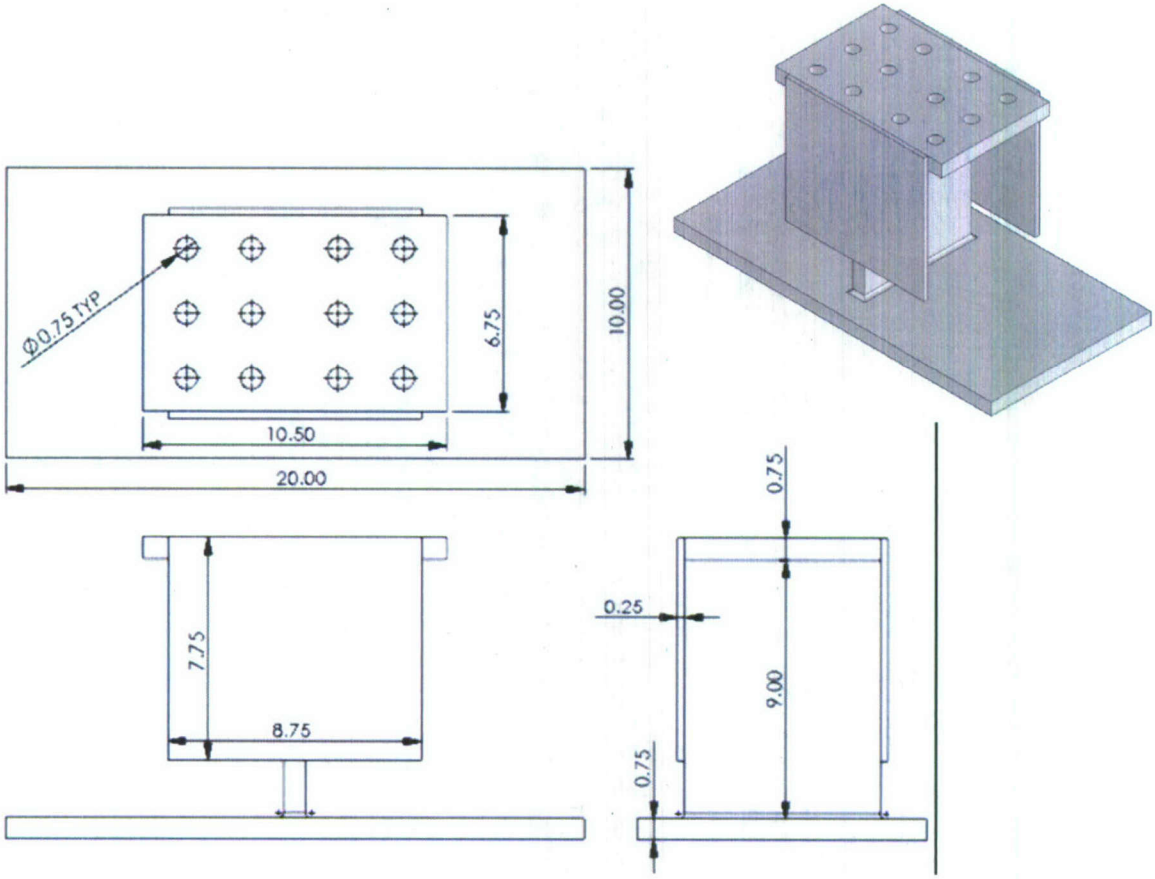

Figure 4.15 – Clamped Joint Tee with Dimensions (in)

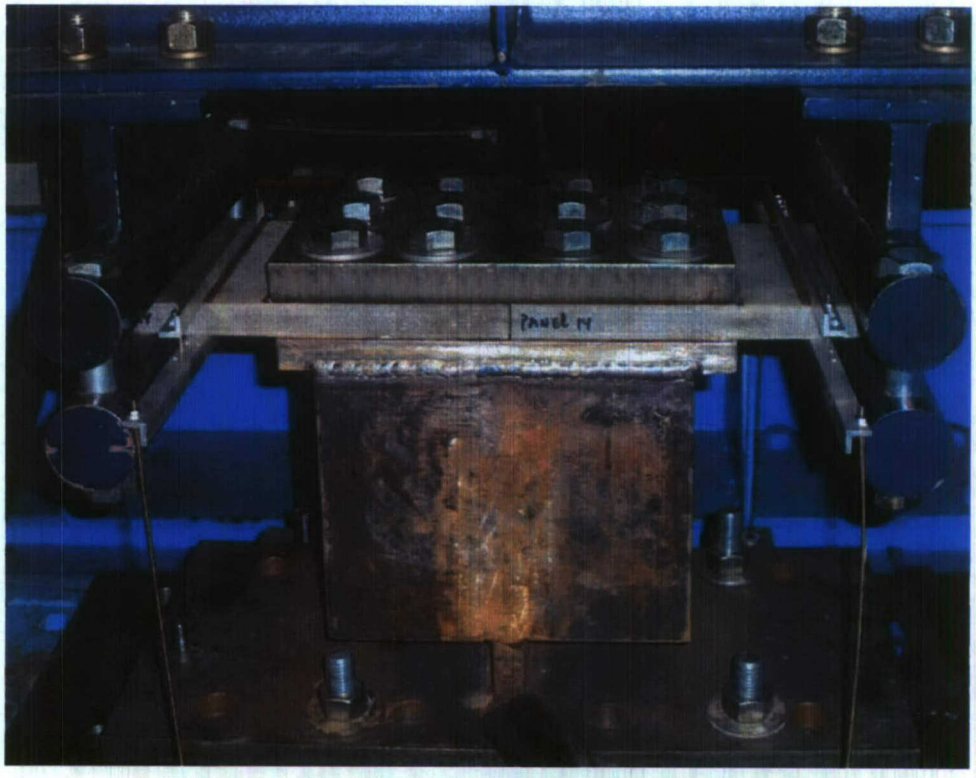

Figure 4.16 – Clamped Joint in Test Fixture

4.3.2 Specimen Insertion Procedure

Before tests of any kind could be carried out, there was a certain procedure that had to be followed to insert the joint being tested into the fixture. Once the joint itself was bolted into place, the MTS was used to set the actuator in the correct location to grip the specimen. The load and displacement being recorded by the MTS also needed to be correctly zeroed out before a test could successfully be run. The following is an outline of this procedure.

Step 1 – Check Settings: Before the hydraulics for the actuator can be turned on, certain precautions must be taken to ensure that there is not a large DC error between where the actuator is at rest and where the MTS controls will tell it to be when the hydraulics are initiated. The following steps must be followed, as small mistakes can result in catastrophic damage to a test setup or equipment.

a) Set the span to zero (***SPAN knob***). Otherwise, there may be a residual signal from the computer that makes the actuator jump.
b) Make sure the MTS is in displacement control (***CONTROL light on displacement channel***)
c) Check D.C. Error and set it to zero (***SETPOINT knob***)

Step 2 – Turn Hydraulics On: (***OFF → LOW → HIGH buttons***)

Step 3 – Raise/Lower Actuator: The top rollers of the gripping mechanism should be just above the test article, but not touching it. Move the actuator (***SETPOINT knob***) so that this is the case. Turning the knob clockwise lowers the actuator.

Step 4 – Attach Bottom Rollers: Bolt the bottom rollers of the gripping mechanism to the top rollers so that they are hanging underneath the test article but not touching it. This ensures that the entire load supported by the actuator other than that applied to the panel is accounted for.

Step 5 – Zero Load: While still in displacement control, switch to load display (***DISPLAY button on load channel***). Check the load value and set it to zero (***ZERO***

knob). View the DC Error and set it to zero (***SETPOINT knob***). The load is now zeroed appropriately.

Step 6 – Clamp Test Article: Lower the actuator until it touches the specimen (***SETPOINT knob***). Tighten the grippers so that the specimen is securely held.

Step 7 – Re-Zero Load: Return to the MTS and move the actuator down (or up) until the load reads zero again (***SETPOINT knob***). Check DC error for load, set to zero (***SETPOINT knob***). The load is now zeroed and the specimen correctly clamped by the gripping mechanism.

Step 8 – Zero Displacement: Switch to load control (***press CONTROL button on load channel and CONTROL TRANSFER ENABLE button simultaneously***). The load Setpoint knob may need to be moved very slightly for load control to engage. Switch to displacement display (***DISPLAY button on displacement channel***). Zero out the displacement (***ZERO knob***). Check DC Error for displacement, set to zero (***SETPOINT knob***). The displacement and load are now zeroed appropriately, and the test article correctly gripped by the test fixture.

4.3.3 Cyclic Test to Failure Procedure

Before beginning the load-controlled fatigue testing, a displacement-controlled cyclic test to failure is performed to determine the compliance and strength of the joint. Once the procedure for gripping the test article described in the previous section is followed, this and all other kinds of tests can be performed. Two cyclic tests to failure were conducted, one for each joint style analyzed. The procedure for running a cyclic test to failure is as follows:

Step 1 – Open Software: DAQFI software is used to run all the tests for this research. Once the software has been opened, the *Fatigue001.cfg* file is opened as within the program. Cyclic tests to failure are performed by the *"MTS Control"* module, which can be selected from the *"Test Control"* Menu.

Step 2 – Enter "MTS Control" Module Settings: With the *"MTS Control"* module open (see Figure 4.17), the following settings must be correct:

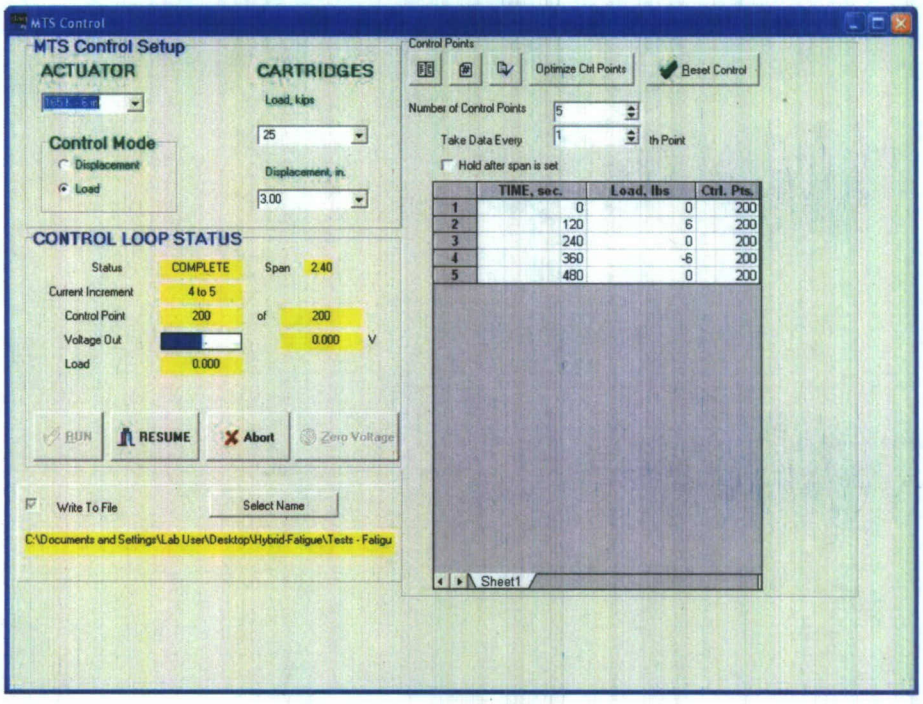

Figure 4.17 – MTS Control Module

a) Actuator: Set to *"165k – 6in."*

b) Load and Displacement Cartridges: Set load cartridge to *"25kip"* and displacement cartridge to *"3in"*.

c) Control Mode: Set to *"Displacement"*, since these tests load the test articles to failure.

d) Number of Control Points: Set to *5*.

e) Take Data Every: Set to *1*

f) Critical Points: For cyclic tests to failure, the specimen undergoes 3 cycles of positive and negative displacement before the displacement increment is

increased. This data can be imported from MS Excel, and Figure 4.18 shows the

Time (s)	Disp (in)
0.00	0.000
1.57	0.079
3.15	0.000
4.72	-0.079
6.29	0.000
7.87	0.079
9.44	0.000
11.01	-0.079
12.59	0.000
14.16	0.079
15.73	0.000
17.31	-0.079
18.88	0.000
22.03	0.157
25.17	0.000
28.32	-0.157
31.46	0.000
34.61	0.157
37.76	0.000
40.90	-0.157
44.05	0.000
47.20	0.157
50.34	0.000
53.49	-0.157
56.64	0.000
61.36	0.236
66.08	0.000
70.80	-0.236
75.51	0.000
80.23	0.236
84.95	0.000
89.67	-0.236
94.39	0.000
99.11	0.236
103.83	0.000
108.55	-0.236
113.27	0.000

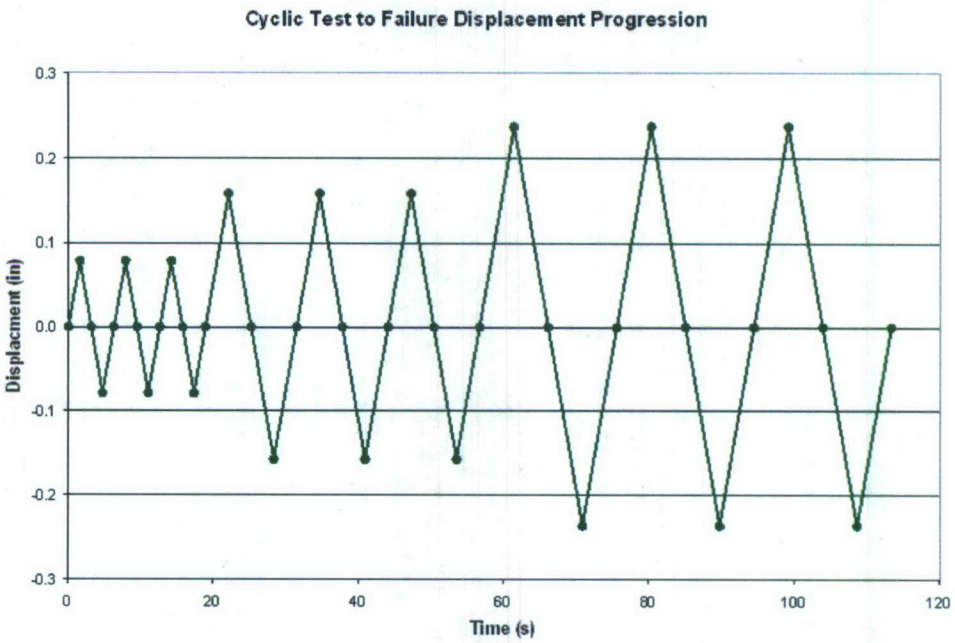

Figure 4.18 – Beginning of Critical Points for a Cyclic Test to Failure

Step 3 – Select File Name: Select the file name that the program will write the data to as the test is performed.

Step 4 – Set the Span: Click "Run". This will not start the test. The MTS Control Module uses the span of the MTS to control the maximum amplitude of the actual displacement output. A span of 10 on the MTS sends 100% of the signal output from the computer (10V), whereas a span of 0 sends 0%. Rather than controlling the amplitude of the signal from the computer, the module always outputs a full 10V signal, but calculates value the span must be set at to obtain the desired amplitude from the MTS. Once *"Run"* is clicked, this value is displayed. The span on the displacement channel of the MTS must then be set before clicking *"OK,"* because *"OK"* begins the test.

Step 5 – Begin Test: Click *"OK"*.

Once these steps have been followed, the cyclic test to failure begins. Data is collected, and the test article will eventually fail. This failure provides the ultimate strength of the joint. Cyclic tests to failure have been carried out on both the clamped and standard bolted joint configurations. The results are discussed in section 5.1.

4.3.4 Intermediate Cyclic Test Procedure

Before and throughout the fatigue testing, single-cycle load-controlled cyclic tests were performed at the test load amplitude. This was done to observe changes in the compliance of the specimen due to progressive damage. In cases of high stress levels, joint fatigue tests ended too quickly to perform intermediate cyclic tests, and the values from their initial cyclic tests resembled those from the cyclic tests to failure at their respective load values.

The procedure for running intermediate cyclic tests closely resembles that for the cyclic tests to failure described in the previous section. The only differences were that the control mode was set to *"Load,"* and that there were only 5 control points (0 load, + test load, 0 load, - test load, 0 load). With those two changes, the same procedure could be followed as previously described. Section 5.2 provides the results of the intermediate cyclic tests.

4.3.5 Fatigue Test Procedure

Once the data from a cyclic test to failure had been obtained, and the 0K cycle count intermediate cyclic test had been performed, fatigue testing of the joints could begin. The process followed to run fatigue tests was as follows:

Step 1 – Open Software: First, open the DAQFI software, being sure to open the *Fatigue001.cfg* from the DAQFI program once it is open. Fatigue are performed by the *"Fatigue"* module, which can be selected from the *"Test Control"* Menu. Figure 4.19 is an example of what the module typically looks like.

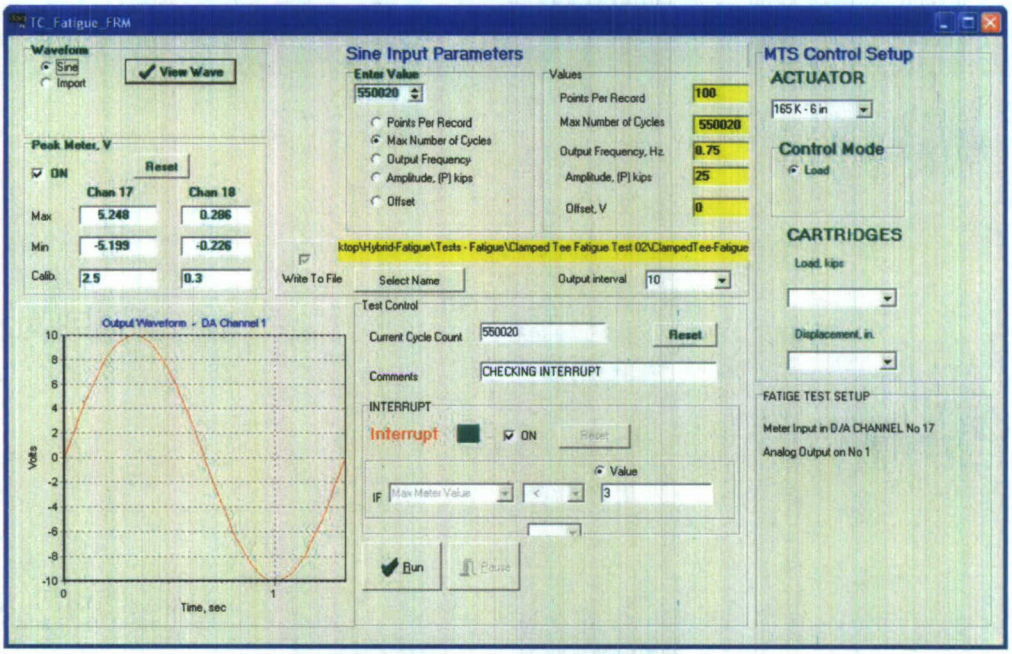

Figure 4.19 – Fatigue Module

Step 2 – Check Settings: With the *"Fatigue"* module open, the following settings must be correct:

a) Waveform: Set to *"Sine."*

b) Points Per Record: Set to 100.

c) Max Number of Cycles: This changes as the fatigue test progresses. This number is set to the cycle count at which the next intermediate cyclic test will be run. At the start of the fatigue test, this is set to 10000. The test will then proceed to 10000 cycles before pausing to run the intermediate cyclic test. After this has been performed, the Max Number of Cycles is set to 25000 and the fatigue test is started again.

d) Output Frequency: This value should reflect the best possible balance between efficiency and the capabilities of the MTS. The value should be set at the highest value that the MTS can run the test without having to compensate too much with the span. For example, in one test, the actuator would output a load of 6 kips at a span of 2.4 for the preliminary cyclic test. However, the span would have to be increased in order for the actuator to output that same load level at the frequencies typical of fatigue tests. Not wanting to exceed a span of about 2.5, the output

frequency was set to .75 Hz. Some experimentation may be necessary to determine the best frequency. (**NOTE**: The ability for the actuator to keep up will decrease as the displacement corresponding to the desired load increases due to specimen degradation. Therefore, the span will most likely need to be increased during the test run, and this should be taken into account when selecting the appropriate output frequency.)

e) Amplitude, (P) kips: Set to the full value (25 kips). This is done because the actual amplitude of the test is controlled by the span on the MTS. Setting the amplitude to 25 for a 25 kip card will output voltage in the same manner as the cyclic tests already described.

f) Offset: Set to 0.

g) Output Interval: Set to 10. This sets the program to record the load and displacement data every 10^{th} cycle. This can be increased for longer tests.

h) Actuator: Set to *"165k – 6in."*

i) Load and Displacement Cartridges: Set load cartridge to *"25kip"* and displacement cartridge to *"3in"*.

j) Interrupt: The interrupt is typically set so that it will terminate the test if the compliance doubles. To do this, select "Max Meter Value", "<", and set the value to half the load that the fatigue test is being run at. For a 6 kip test, the interrupt setting will read: "If [Max Meter Value] [<] [3]". This value can be increased if it is desirable to watch the test more closely. If the fatigue of test hardware (bolts, etc.) is an issue, this can be set higher to stop the test at a potential failure.

Step 3 – Select File Name: Select the file name that the program will write the data to as the test is performed.

Step 4 – Set the Span: The span calculated for the intermediate cyclic test performed previous to the start of the fatigue test must be remembered, as the *"Fatigue"* module does not calculate it in the same way the *"MTS Control"* module does. Before the fatigue test is started, the span should be set to the value used in the cyclic test. After the test has begun, the span is adjusted as needed to reach the desired load level.

Step 5 – Begin Test: The test should now be ready to run. Double check to make sure everything is set appropriately in the setup and in the software. There is not a second window in which *"OK"* must be clicked as with the Cyclic Tests. Click *"Run"* to start the test.

Step 6 – Observe Test and Perform Intermediate Cyclic Tests: The test will terminate if the interrupt is tripped or if the Max Cycle Count value is reached. If the test stops because it reaches the set value for cycle count, perform another single-cycle cyclic test (see previous section). After this is complete, set "Max Cycle Count" to the value designated for the next cyclic test and begin the fatigue test again by clicking "Run". If the test has terminated due to the interrupt being tripped, investigate whether the joint or fixture hardware has failed.

Fatigue tests were performed on both the bolted and clamped joint configurations. A presentation and discussion of the results of these tests can be found in section 5.3

4.3.6 Residual Strength Test Procedure

Residual strength tests were essentially cyclic tests to failure that were performed when a joint had successfully withstood fatigue loading for the prescribed amount of cycles. Their purpose was to determine the strength remaining in the joint. This was referred to as a run-out, and the cycle count chosen for the run-out cutoff was 2 million. The only joint to reach the run-out point was the clamped joint tested at a ±5kip load level. The procedure for running a residual strength tests is identical to that used for running the cyclic tests to failure. The data for the single residual strength test performed can be found in section 5.4

4.3.7 Test Dimensions

The critical dimensions for the tests are tabulated, with Figure 4.20 illustrating the dimension references in Table 4.1. The distances from the center of the rollers on the clamping mechanism to the edge of the steel tee (dimensions A-D) are recorded at the front and back for both the right and left sides of the test specimen. Similarly, the distance from the LVDT's to the edge of the steel tee closest to them (dimensions E-H) is

recorded. Table 4.2 lists the dimensions of the composite test articles themselves, with width and thickness given for both the right and left sides. The lengths of the test articles were approximately 10.5in, but these are excluded because they are not as important as dimensions A-D.

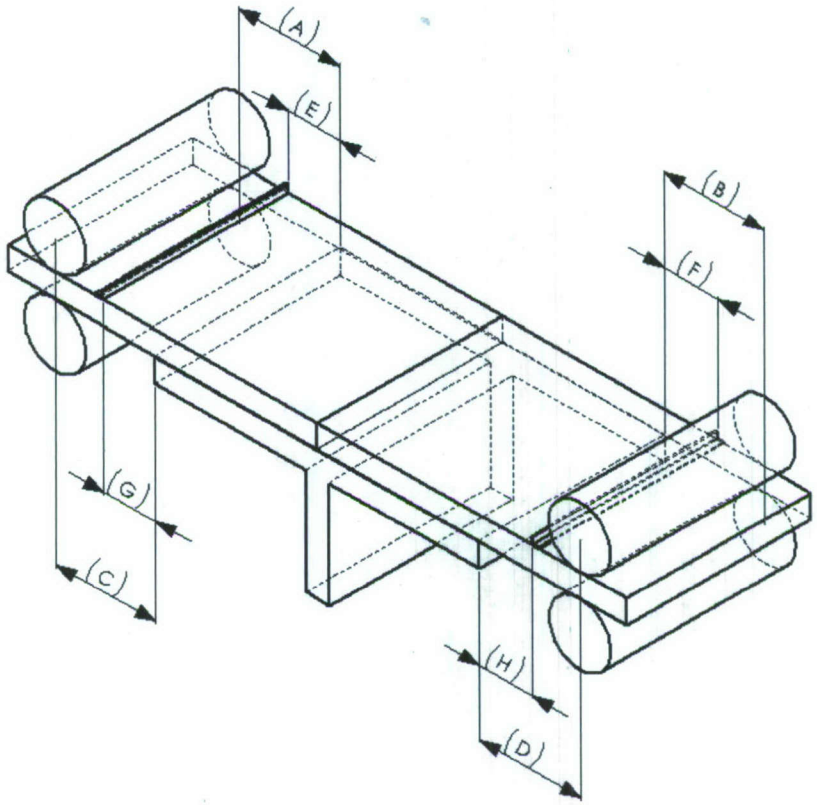

Figure 4.20 – Test Dimensioning Information

Table 4.1 – Test Dimensions (in)

Test Name/Type	A	B	C	D	E	F	G	H
Bolted Joint Cyclic Test to Failure	3.25	3.25	3.25	3.25	1.81	1.81	1.81	1.81
Clamped Joint Cyclic Test to Failure	3.25	3.25	3.25	3.25	1.81	1.81	1.81	1.81
8kip Bolted Joint	3.25	3.25	3.25	3.25	1.81	1.81	1.78	1.78
7kip Bolted Joint	3.25	3.19	3.25	3.19	2.00	2.00	2.00	2.00
6kip Bolted Joint	3.13	3.25	3.13	3.13	2.00	2.00	2.00	2.00
5kip Bolted Joint	3.16	3.16	3.06	3.16	2.00	2.00	2.00	2.00
4kip Bolted Joint	3.16	3.16	3.13	3.13	2.00	2.00	2.00	2.00
8kip Clamped Joint	3.25	3.25	3.25	3.25	2.00	2.00	2.00	2.00
7kip Clamped Joint	3.25	3.25	3.25	3.25	2.00	2.00	2.00	2.00
6.5kip Clamped Joint	3.19	3.25	3.22	3.19	2.00	2.00	2.00	2.00
6kip Clamped Joint	3.25	3.25	3.25	3.25	2.00	2.00	2.00	2.00
5kip Clamped Joint	3.25	3.19	3.22	3.13	2.00	2.00	2.00	2.00

Table 4.2 – Test Article Dimensions (in)

	Left Side		Right Side		Steel	
Test Name/Type	Thickness	Width	Thickness	Width	Thickness	Width
Bolted Cyclic Test to Failure	0.75	6.84	0.78	6.91	0.741	6.75
Clamped Cyclic Test to Failure	0.82	6.44	0.82	6.50	N/A	N/A
8kip Bolted Joint	0.78	6.83	0.78	6.81	0.735	6.75
7kip Bolted Joint	0.78	6.81	0.77	6.78	0.745	6.75
6kip Bolted Joint	0.77	6.72	0.78	6.75	0.743	6.75
5kip Bolted Joint	0.77	6.75	0.77	6.75	0.741	6.75
4kip Bolted Joint	0.77	6.78	0.77	6.78	0.745	6.75
8kip Clamped Joint	0.78	6.44	0.78	6.50	N/A	N/A
7kip Clamped Joint	0.81	6.50	0.79	6.47	N/A	N/A
6.5kip Clamped Joint	0.82	6.47	0.82	6.45	N/A	N/A
6kip Clamped Joint	0.81	6.47	0.83	6.47	N/A	N/A
5kip Clamped Joint	0.79	6.44	0.79	6.47	N/A	N/A

4.3. 8 Stress Calculations

Section 1.4 of this report discusses numerous methods of determining stress levels for fatigue analysis in connections. With regard to fatigue in metal connections, connection geometries give rise to stress concentrations that can control the fatigue response. Several methods were presented for dealing with these geometric influences including the hot spot stress approach, structural stress approach and fatigue life estimates base on joint details. With regard to laminated composite material, stress estimates are further complicated due to the non-linear variation in stress through the thickness caused by the laminations.

Nominal stress, σ_{nom}, in the laminated composite can be defined in much the same manner as done in a linear-isotropic material if the composite in not highly orthotropic. This definition assumes that the stress and strains through the cross-section of the material are linear. For example, in quantifying the flexural strength of laminated composites, ASTM D-790 uses the classic definition for isotropic materials in determining the flexural strength of laminated plastic beams. Accordingly, the nominal stress level, σ_{nom}, for the fatigue tests was calculated using the dimensions listed in Section 4.3.7. The variables used in the equations are presented in Table 4.3 where subscripts of *r* and *l* will denote the right hand side test article or left hand side test article, respectively.

In determining the nominal stress, the load applied to the side is assumed to be half of the total load applied by the actuator because of the symmetry of the test (see Figure 4.21):

$$P_s = \frac{P}{2} \qquad \text{(Eq. 4.1)}$$

The moment per unit width over the side of the test article is then calculated at the point of interest (this is in units of kip-in/in). For the clamped joints, this is at the edge of the clamped boundary. For the standard bolted joints, this is at the bolt line for the stress in the composite, and at the weld for the stress in the steel tee. The stress in the composite for the standard bolted joints is calculated in two different ways. The first way (referred to as the Gross Method) uses the gross width of the composite for *w*. The second way

(referred to as the Net Method) uses the net width (i.e. the total width minus the diameters of the bolt holes). As far as the actual stress in the composite is concerned, the gross width method is the more accurate of the two. The assumption is that the bolts are bearing as much load per unit width as the composite does. The net width method ignores the load-bearing effect of the bolts. Since the width is taken as the total width minus the bolt-hole diameters, it effectively treats the test article as if the bolts were not there at all. This obviously makes the composite appear to bear more load than it actually is. The results for the net width method are included since net area is sometimes employed to categorize bolted joints. The moment per unit width is calculated using the respective widths as follows:

$$M_o = \frac{P_s \cdot d}{w} \qquad \text{(Eq. 4.2)}$$

For simplicity, a section of unit width b (1in) is then taken (see Figure 4.21), and the moment calculated for that section.

$$M_b = M_o \cdot b \qquad \text{(Eq. 4.3)}$$

The nominal stress, σ_{nom}, is then found as follows:

$$\sigma_{nom} = \frac{6 \cdot M_o}{t^2} \qquad \text{(Eq. 4.4)}$$

An average value of the nominal stress, σ_{nomA}, can then be found by averaging the nominal stress values from each side of the test article.

Table 4.3 – Variables Used in Stress Calculations

Variable	Description
w	Width of the test article (in)
t	Thickness of the test article (in)
d	Average of the front and rear moment arms (center of roller to point of interest) (in)
P	Load applied by the actuator (kip)
P_s	Load applied to a side (kip)
M_o	Moment per unit width (kip-in/in)
M_b	Moment for a unit-width section (kip-in)
I	Moment of Inertia for unit-width section (in^4)
σ_{nom}	Nominal stress level for a side (ksi)
σ_{nomA}	Average nominal stress level for the Test (avg. of the stress for the two sides) (ksi)

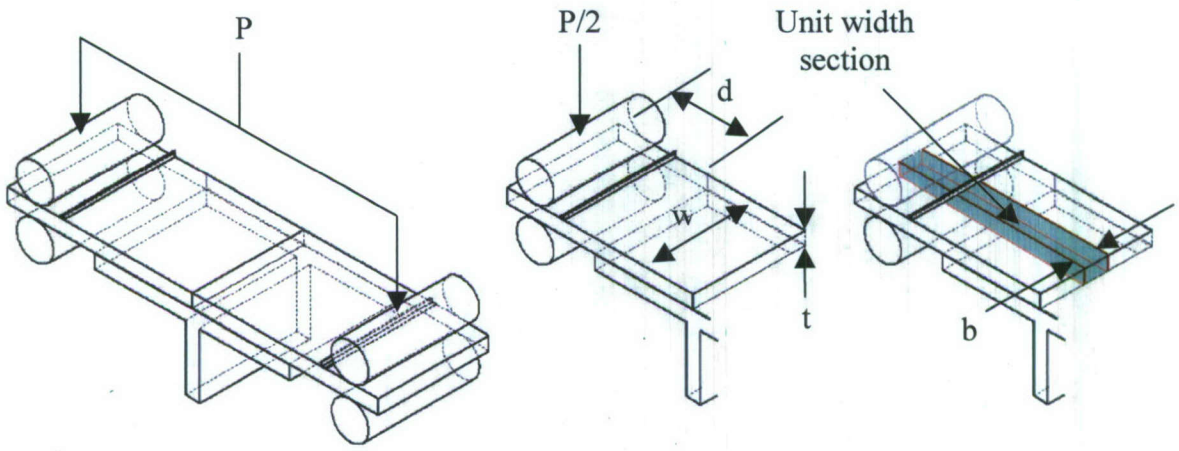

Figure 4.21 – Diagram of Stress Calculation Variables

A comparison of the layer by layer stress to the nominal stress is performed using composite laminate theory. The example presented is based upon the case of the clamped laminate setup with a 42-layer composite laminate as previously described. A laminate of 6.5 inches in width is subject to a nominal longitudinal bending moment of 1000 in-kips per inch of width. Figure 4.22 shows the laminate longitudinal direction stress verses position through the thickness. A peak stress of 20.4 ksi is observed in the outer 0-degree layers. The nominal stress computed from Equation 4.4 is also shown on this Figure. The peak nominal stress of 10.7 ksi is observed for this case which is about one-half of the peak laminate stress. A failure analysis using the maximum strain criteria predicts a first ply failure at a total load P of 6.78 kips, which is a resin tension failure in the outer 90-degree ply. The failure analysis assumes that a material resin normal stress failure causes the 99 percent reduction in modulus and a resin shear failure causes a 10 percent reduction in modulus. The analysis predicts a peak load of 12.5 kips when these parameters are used. If it is assumed that a shear failure causes no reduction in modulus then a failure load of 15 kips is predicted.

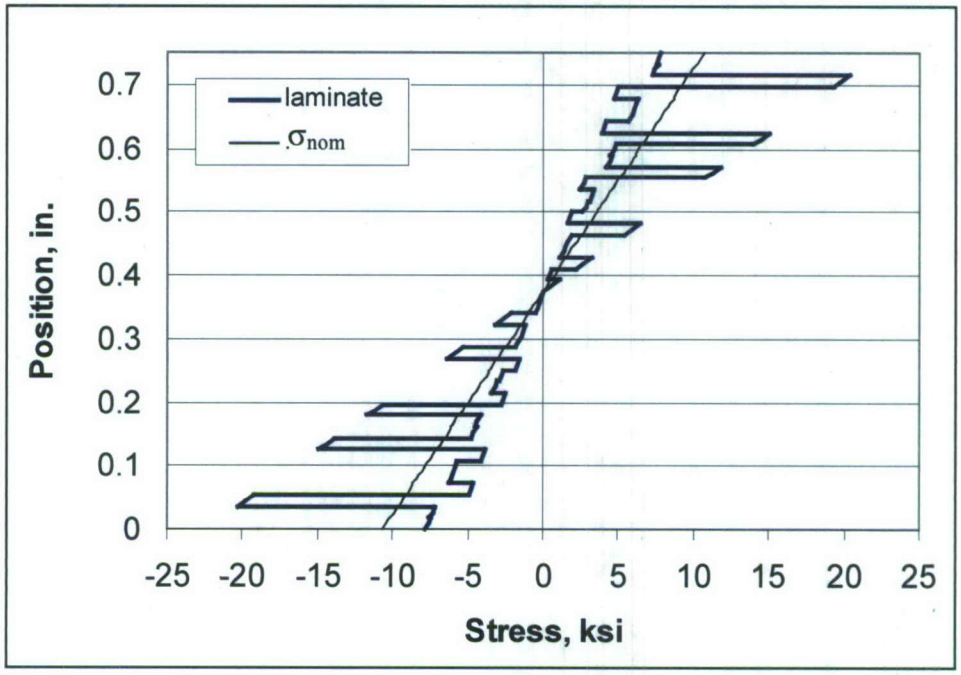

Figure 4.22 – Laminate Stress Distribution Compared to Nominal Stress

5. Discussion of Results

5.1 Cyclic Tests to Failure Results

Cyclic tests to failure have been carried out on both the clamped and standard bolted joint configurations. The results from these tests can be seen in Figures 5.1 and 5.2. Pictures of progressive failure can be seen in Figures 5.3 and 5.4, and close up pictures of failure in Figures 5.5 and 5.6. Peak load and displacement at peak load for both tests are summarized in Table 5.1.

It can be seen in the graph of the standard bolted joint cyclic test to failure that, as expected, the displacement in the negative (physically upward) direction is greater throughout the test than it is in the positive (physically downward) direction. When displacing upward, the bolts alone prevent the upward movement of the test article, whereas downward movement is prevented by the bolts as well as the steel tee. The clamped test, on the other hand, has virtually identical displacement in both directions because the bottom is constrained by the tee and the top by the clamping plate. Loading in both directions in the clamped case is more similar to downward loading in the bolted joint case. It is also observed that the case of the clamped plate shows much less accumulated damage prior to failure than in the bolted joint case.

Peak load observed for the clamped case is 17.83kip, compared to 16.2kip for the bolted joint case. This is due to the different stress state and forces induced because of the test geometry. The moment arm at the point of failure in the clamped case is 3.25in compared to 4.50in in the bolted case.

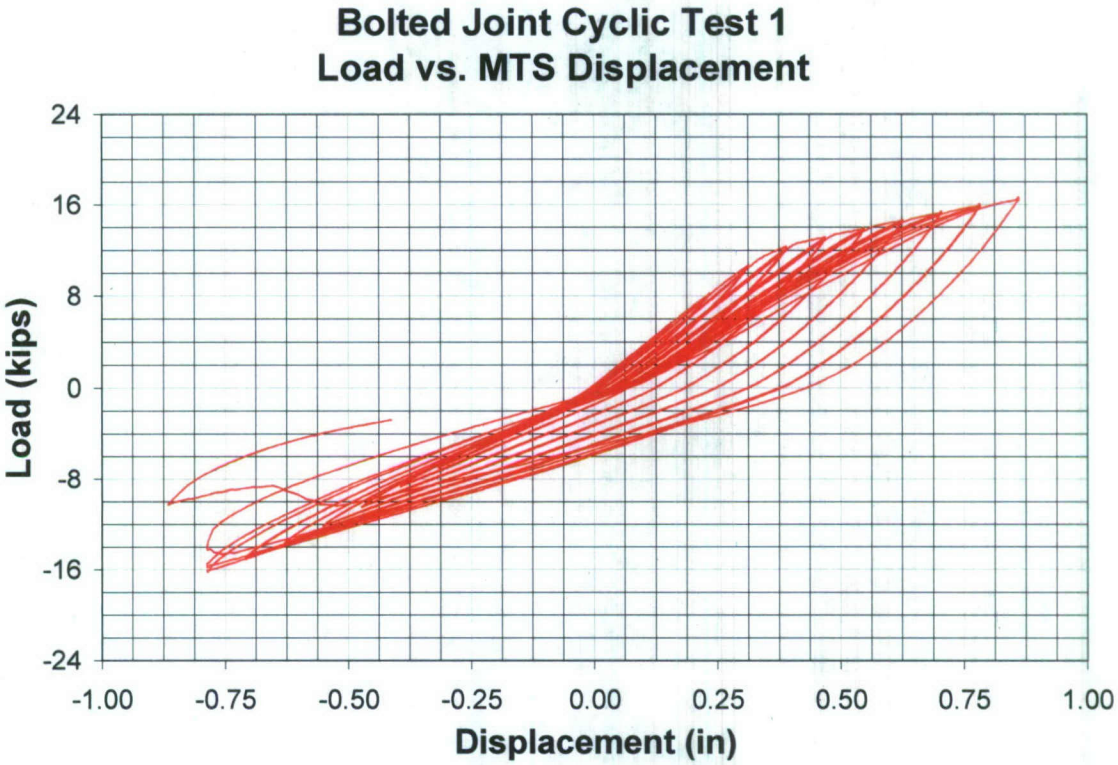

Figure 5.1 – Load vs. Displacement Data for Bolted Joint Cyclic Test to Failure

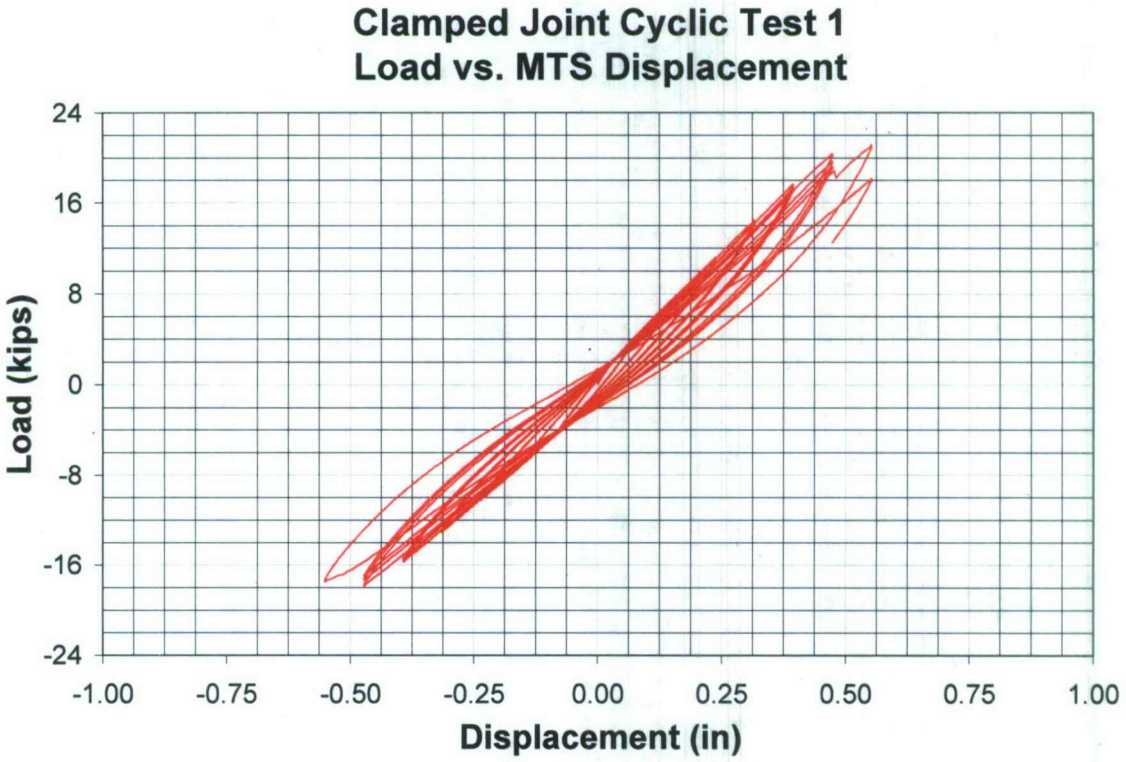

Figure 5.2 – Load vs. Displacement Data for Clamped Joint Cyclic Test to Failure

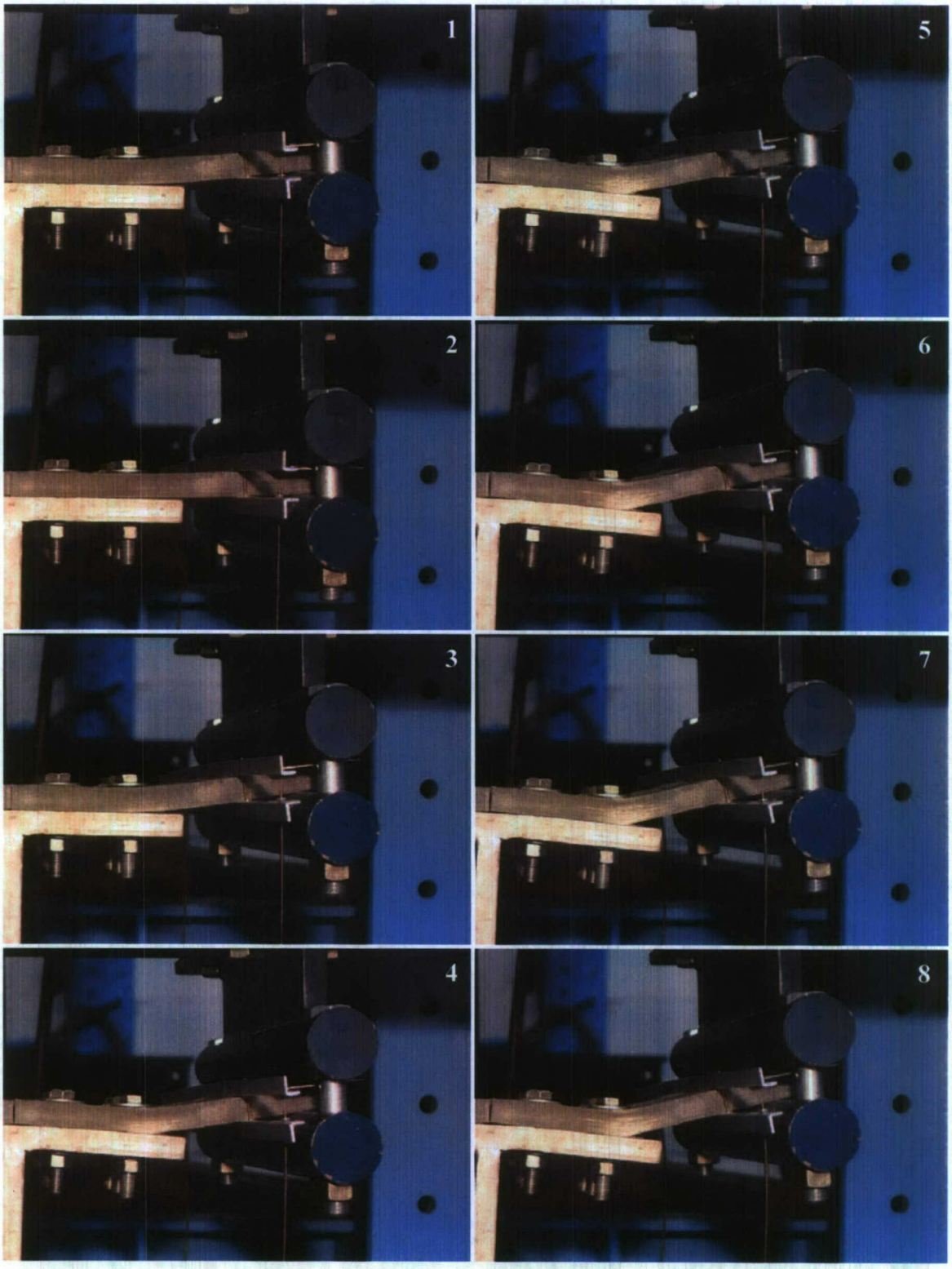

Figure 5.3 – Standard Bolted Joint Cyclic Test Progressive Failure

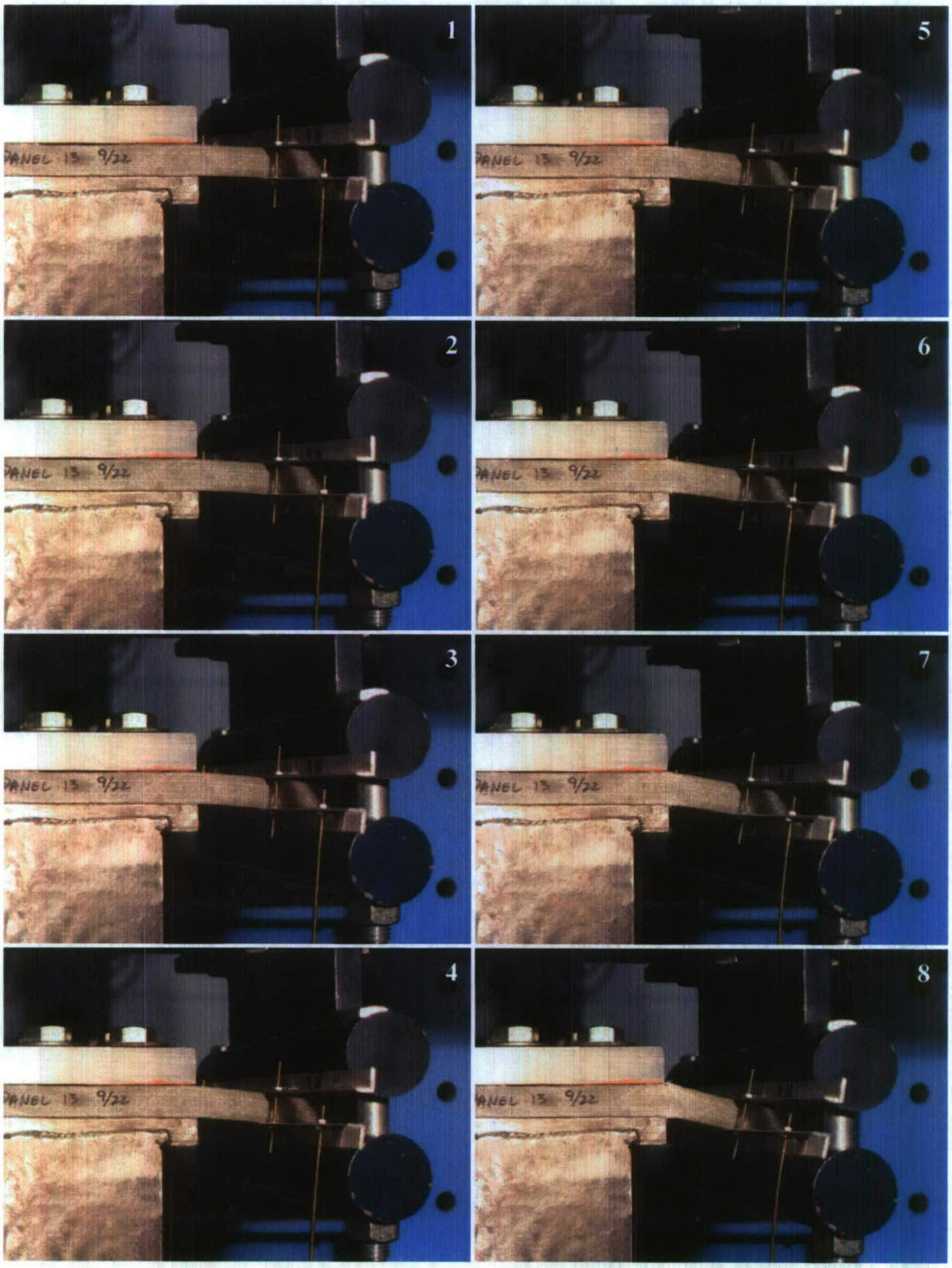

Figure 5.4 – Clamped Joint Cyclic Test Progressive Failure

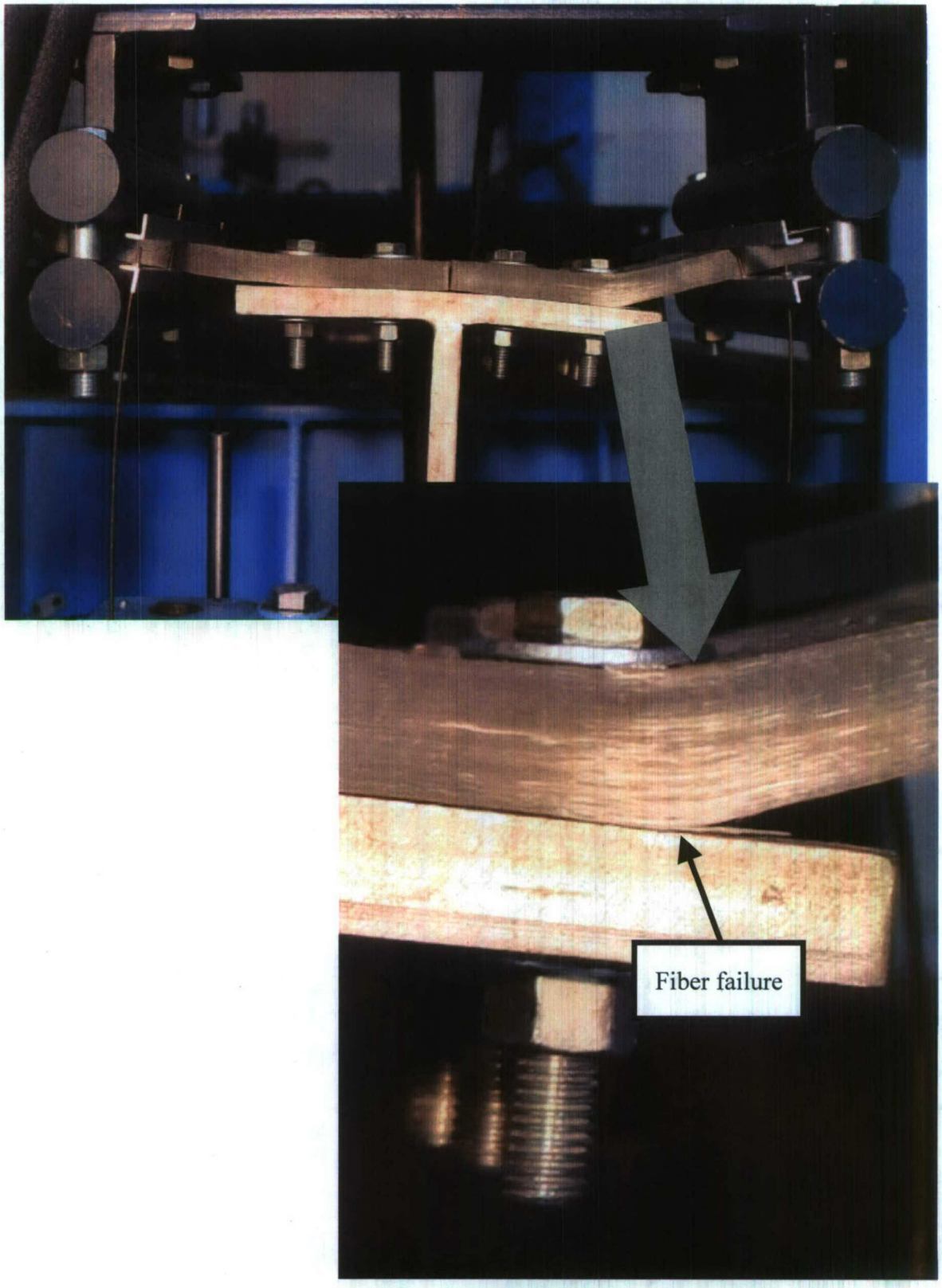

Figure 5.5 – Failure in the Standard Bolted Joint Cyclic Test

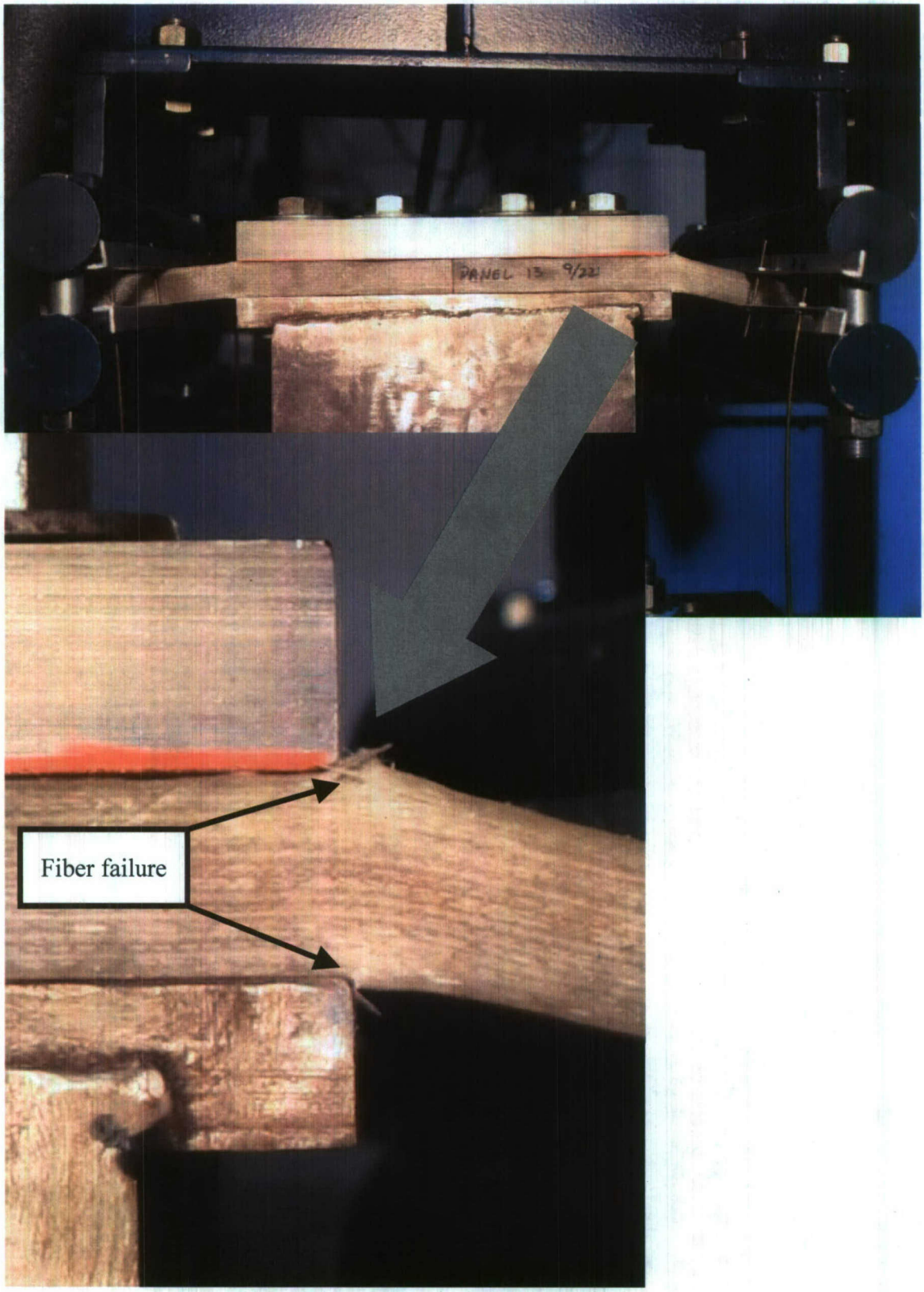

Figure 5.6 – Failure in the Clamped Joint Cyclic Test

Table 5.1 – Peak Load and Displacement at Peak Load Observed in the Cyclic Tests

Test Designation	Peak Load Up (kip)	Peak Load Down (kip)	Displ. @ Peak Up (in)	Displ. @ Peak Down (in)
C-S1-BP-050-75-001	-16.20	16.60	-0.786	0.860
C-S1-CL-000-75-001	-17.83	20.38	-0.472	0.472

The type of failure that occurred in cyclic tests to failure is classified as sudden. There was some minimal material degradation that occurred progressively, but for the most part the main failure of the test article occurred quickly. This is evidenced by the sudden load drops and displacement jumps in the two graphs at the ends of the tests. The primary reason for this is that the load increased steadily. The material remained relatively intact until the article's ultimate strength was reached. This is in contrast to the fatigue tests, where the load remains the same and the test articles experienced many more cycles before they failed. As will be seen later, there is a definite difference in the way failure occurs in the two cases, especially where the fatigue case consists of a lower test load.

In the bolted test, the article failed along the bolt line. Fiber failure began on the bottom layer and the failure moved up through the layers relatively quickly once the initial failure had begun. This was clearly seen in the previous Figures 5.3 and 5.5. In the clamped test, fiber failure initiated at the outer layers (top and bottom) of the test article at the clamped boundary, and worked its way inward. This was seen in the previous Figures 5.4 and 5.6.

The cyclic tests to failure provide the practical information necessary to begin the fatigue testing of a joint style. Whereas the FEA analysis provided the moment arm information and stiffness prediction for the different cases, the cyclic tests demonstrate and quantify the actual ultimate load. With this, load levels in the fatigue tests can be chosen at desired percentage of capacity. As seen previously in Table 5.1, the lower ultimate loads were 16.2kips for the bolted joint, and17.83 for the clamped joint. From this data, it was decided that an appropriate test to begin with would be an 8kip fatigue test for the bolted joints; approximately 50% of the ultimate load. The tests following the initial fatigue tests were then chosen based on the performance of the initial tests. The fatigue test

schedule with the percentages of ultimate load at which the tests were run is seen in Table 5.2 .

Table 5.2 – Fatigue Test Schedule with Percentage of Ultimate Load

Test Designation	Joint Style	Load Freq. (Hz)	Peak Load (kips)	% of Ultimate Load
FC-S1-BP-050-75-001	Bolted	0.50	± 8	49%
FC-S1-BP-050-75-002	Bolted	0.55	± 7	43%
FC-S1-BP-050-75-003	Bolted	0.61	± 6	37%
FC-S1-BP-050-75-004	Bolted	0.67	± 5	31%
FC-S1-BP-050-75-005	Bolted	0.71	± 4	25%
FC-S1-CL-000-75-001	Clamped	0.75	± 8	45%
FC-S1-CL-000-75-002	Clamped	0.75	± 7	39%
FC-S1-CL-000-75-003	Clamped	0.65	± 6.5	36%
FC-S1-CL-000-75-004	Clamped	0.75	± 6	34%
FC-S1-CL-000-75-005	Clamped	0.80	± 5	28%

5.2 Intermediate Cyclic Tests Results

Single-cycle cyclic tests at test level were performed in load control at the start of and throughout each fatigue test. The progression of cyclic tests can be seen in Figures 5.7a-e for the standard bolted joint test series and 5.8a-e for the clamped. The progression of the last clamped joint test (Figure 5.8e) is difficult to see due to the amount of tests performed. For this reason, Figure 5.9 has also been included. It tracks the progression of the displacements of the intermediate cyclic tests when they reached a value of ±4.9kips. As indicated, there is an initial increase in compliance that can be attributed to a crack in the stiffener weld. This will be discussed further in the next section. Once the crack was noticed, the tests were halted so that the weld could be repaired.

In a similar manner to the cyclic tests to failure, the clear difference between the bolted and clamped tests when operating in force control is that the displacement in the upward direction is significantly increased for the bolted cases.

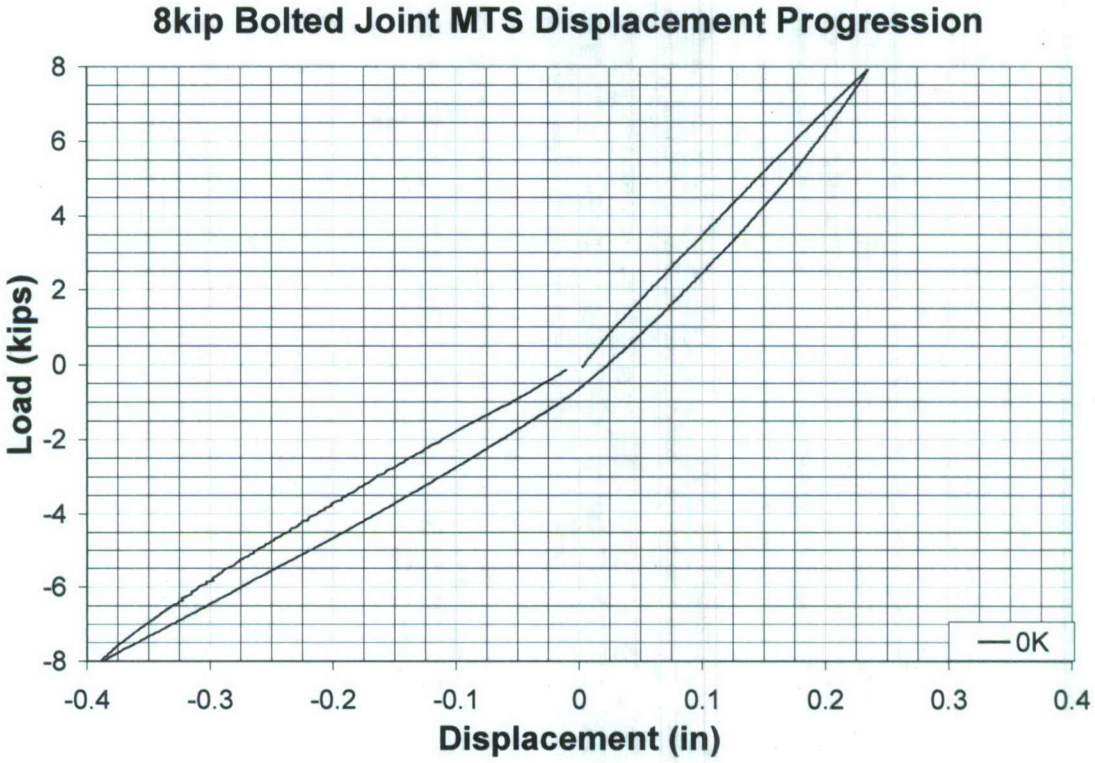

Figure 5.7a – 8kip Bolted Joint Cyclic Test MTS Displacement Progression

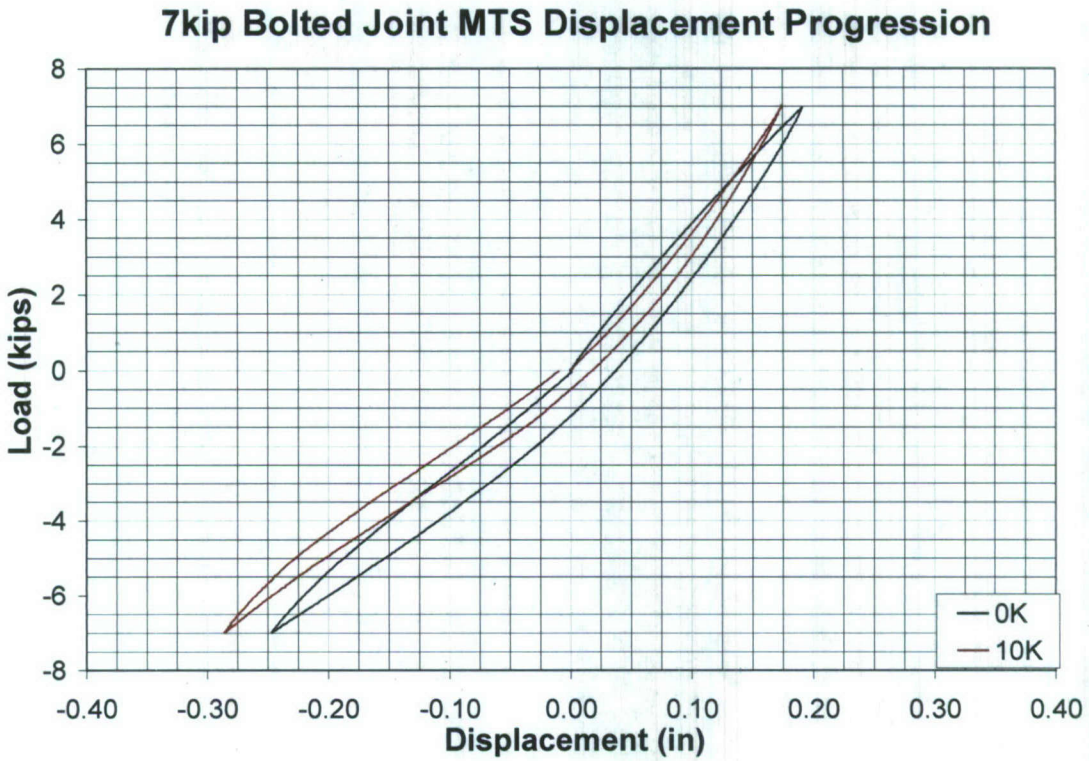

Figure 5.7b – 7kip Bolted Joint Cyclic Test MTS Displacement Progression

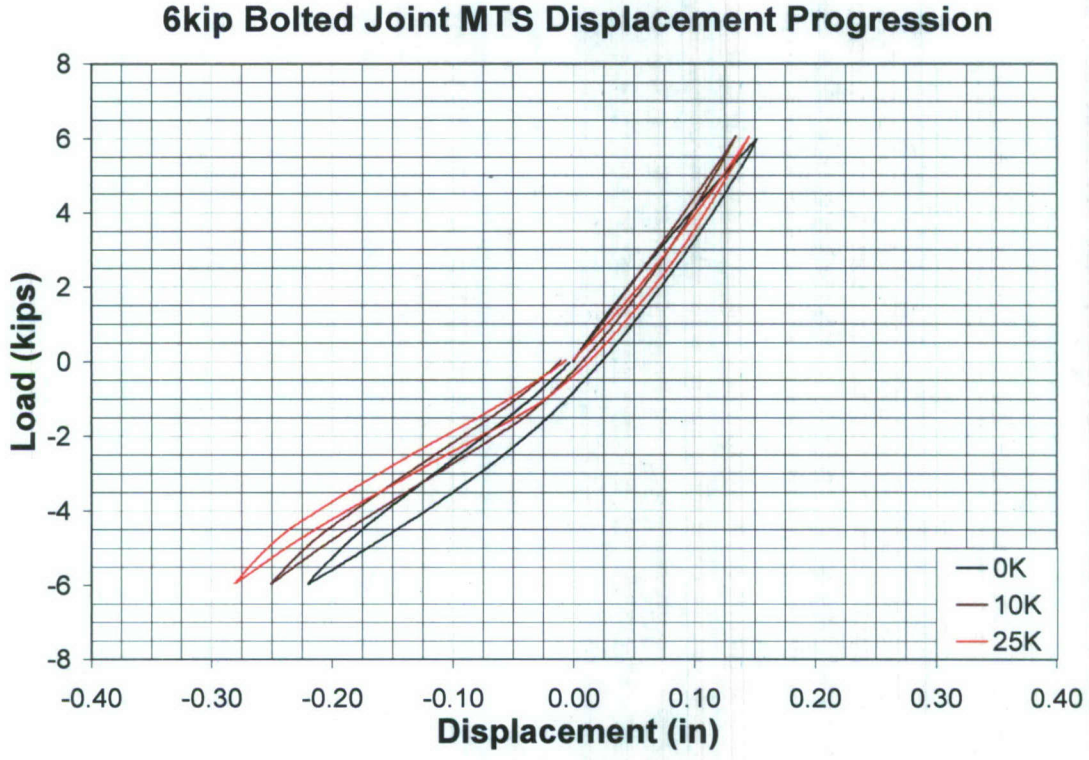

Figure 5.7c – 6kip Bolted Joint Cyclic Test MTS Displacement Progression

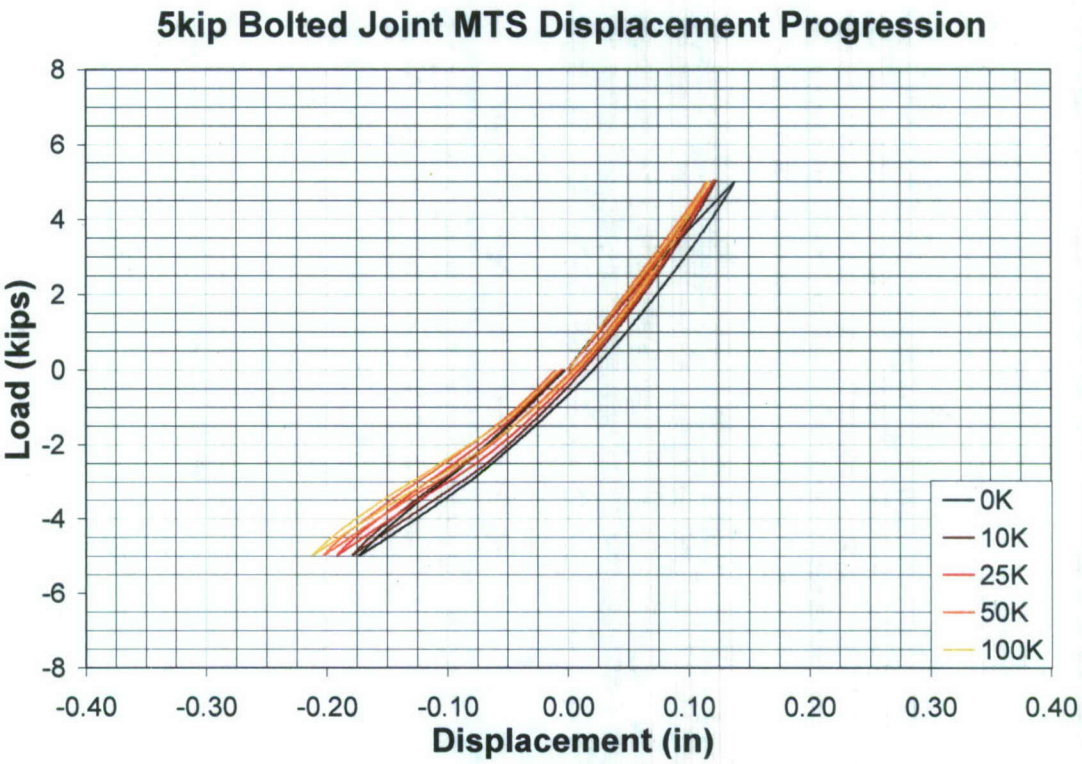

Figure 5.7d – 5kip Bolted Joint Cyclic Test MTS Displacement Progression

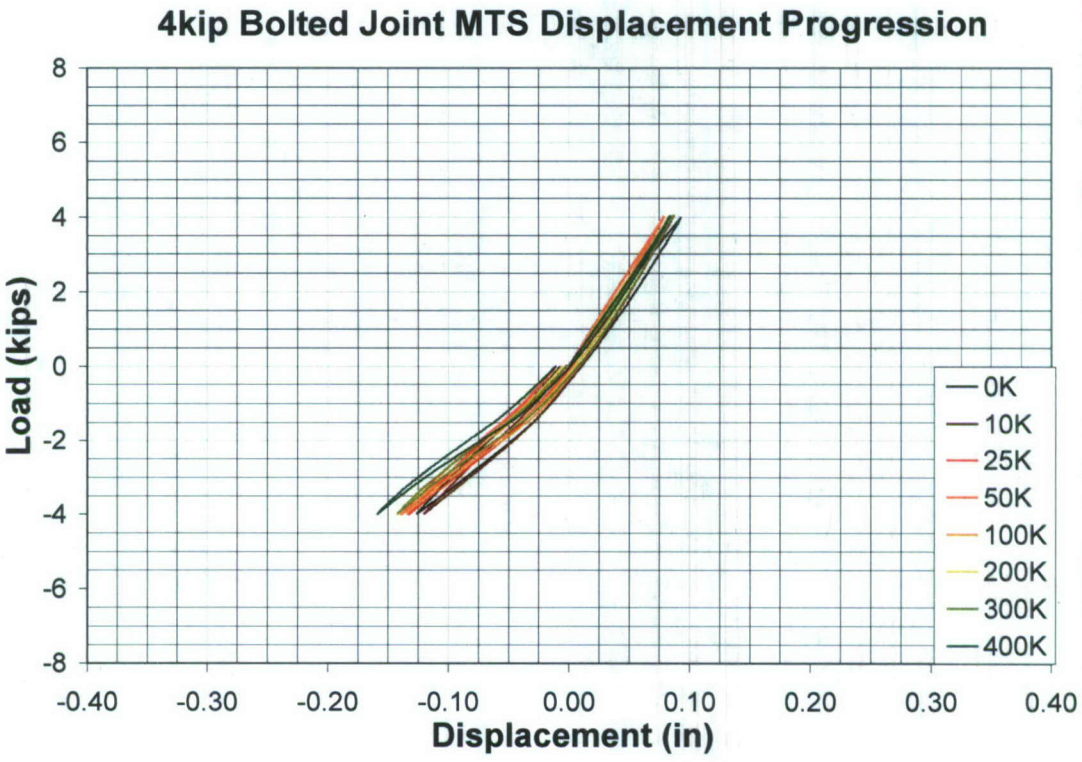

Figure 5.7e – 4kip Bolted Joint Cyclic Test MTS Displacement Progression

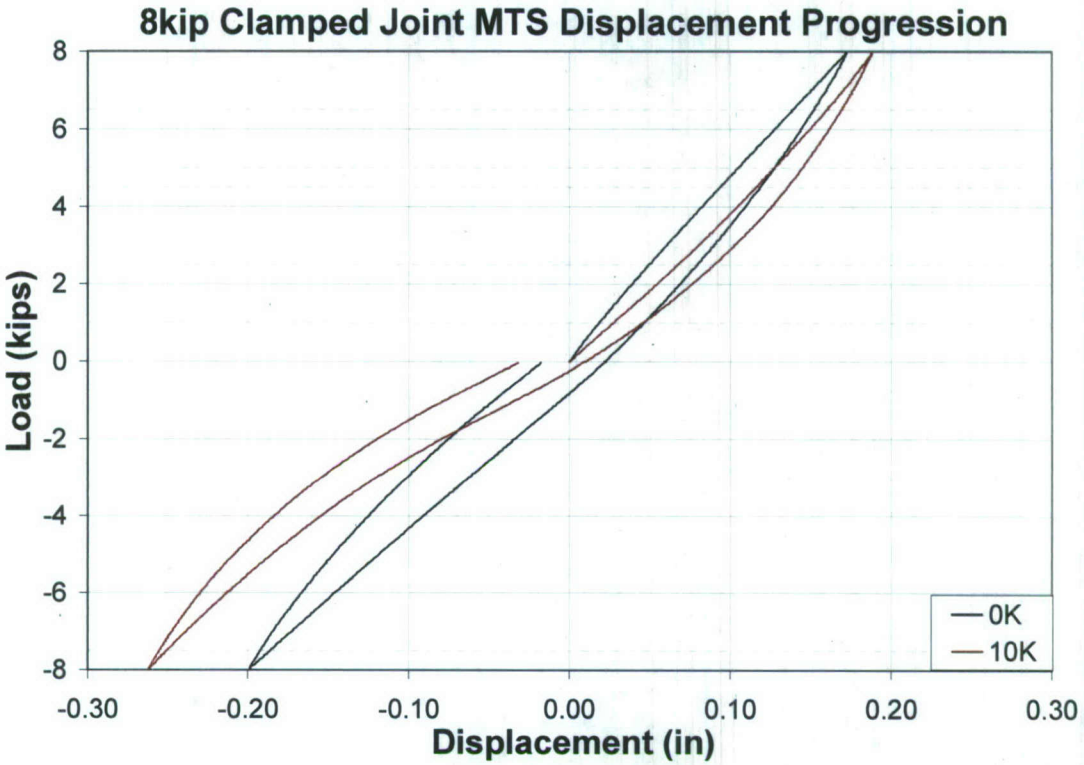

Figure 5.8a – 8kip Clamped Joint Cyclic Test MTS Displacement Progression

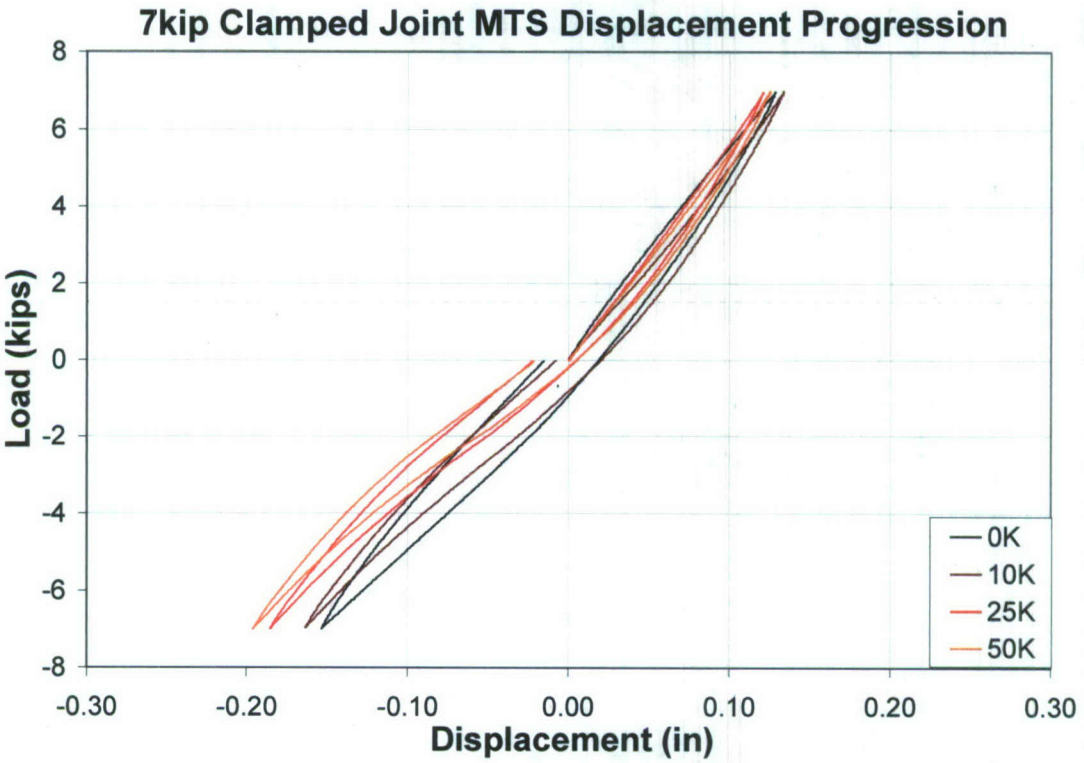

Figure 5.8b – 7kip Clamped Joint Cyclic Test MTS Displacement Progression

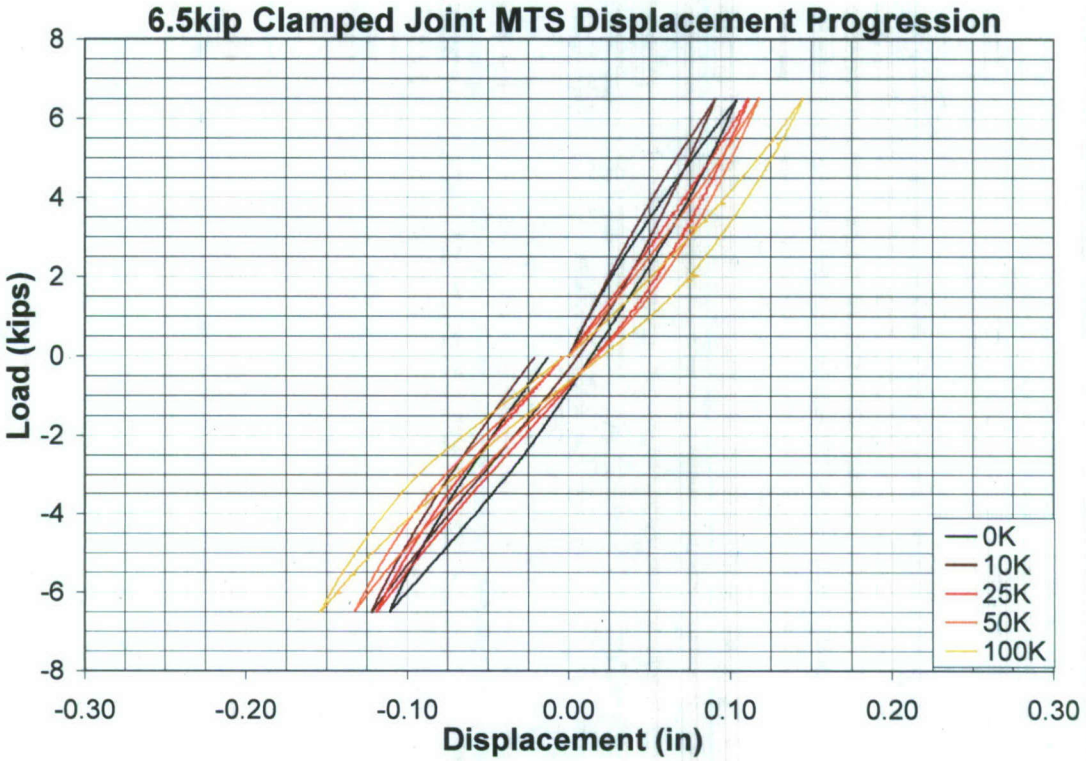

Figure 5.8c – 6.5kip Clamped Joint Cyclic Test MTS Displacement Progression

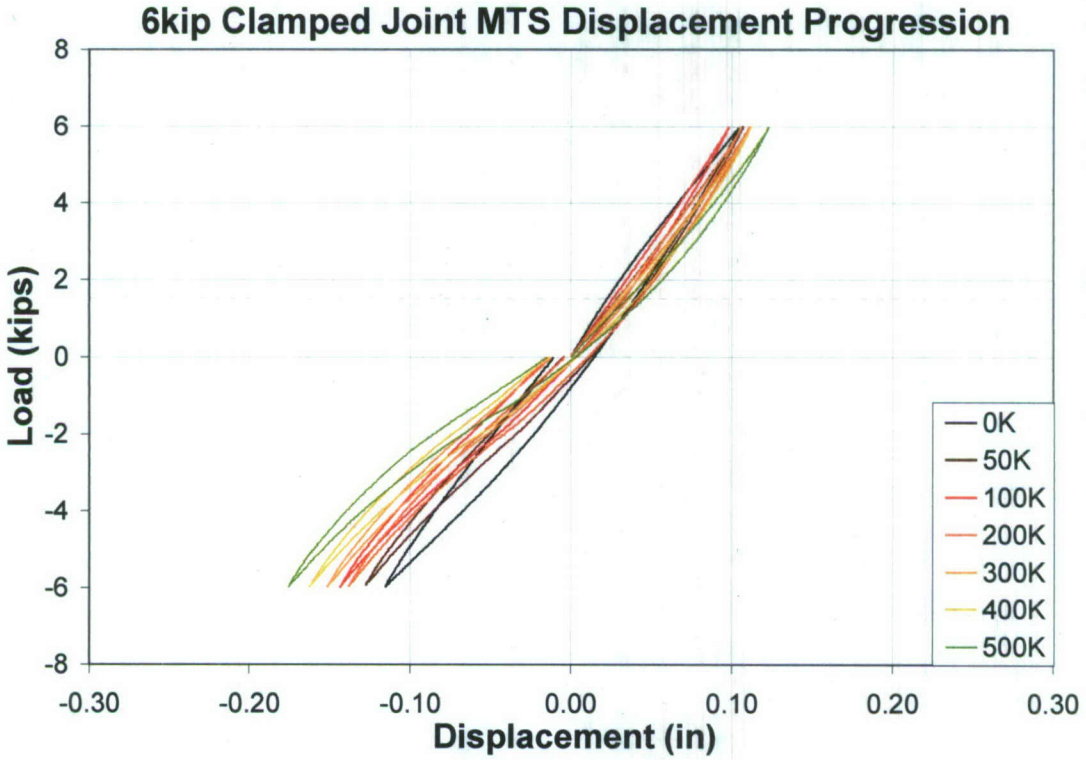

Figure 5.8d – 6kip Clamped Joint Cyclic Test MTS Displacement Progression

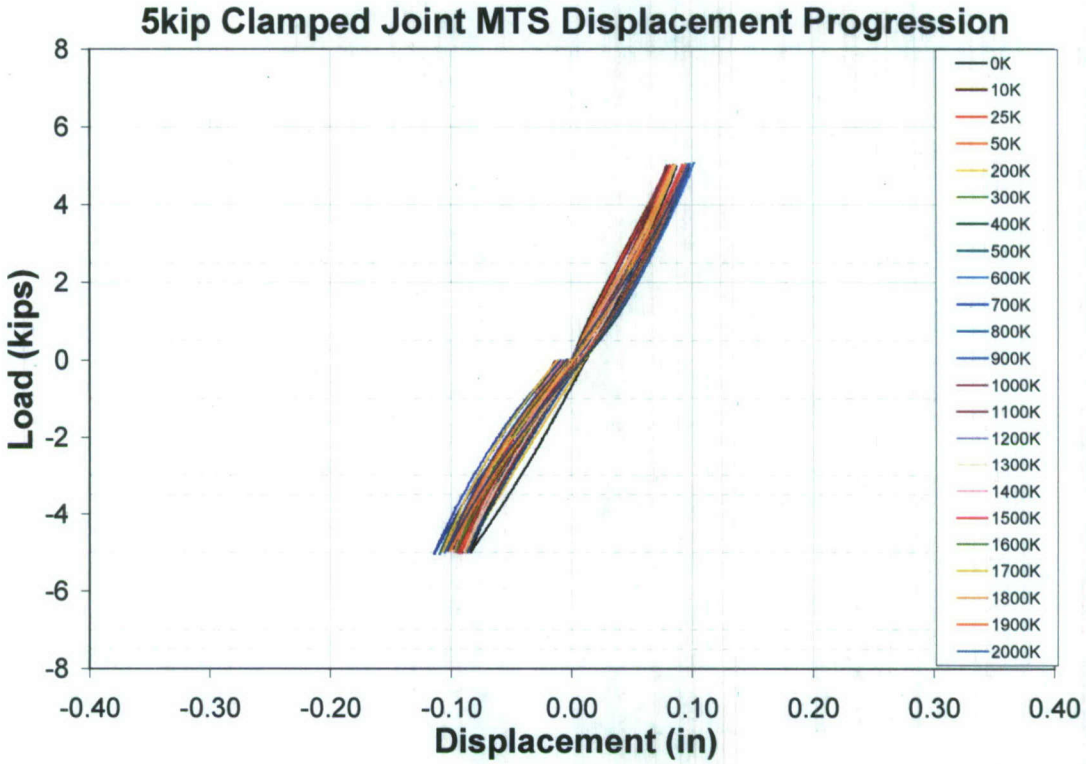

Figure 5.8e – 5kip Clamped Joint Cyclic Test MTS Displacement Progression

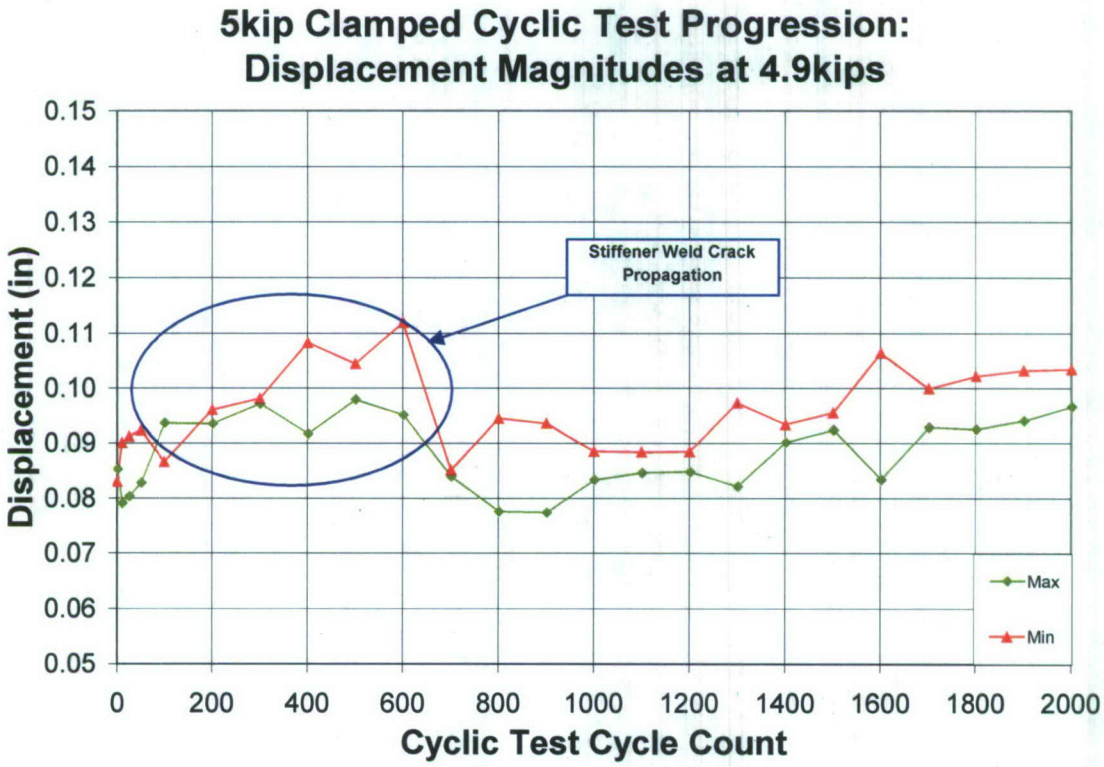

Figure 5.9 – 5kip Clamped Cyclic Test Displacements at ±4.9kips

5.3 Fatigue Tests Results

As already mentioned, the load levels at which to run the tests were determined by evaluating the cyclic test to failure data. The first test series was the standard bolted joint series. The cyclic test to failure had withstood at load of just over 16kips. A load level of approximately 50% of the maximum load level (8kips) was chosen for the first fatigue test. This test failed at the bolt line after 7,200 cycles. This indicated that 8kip would be the absolute upper end for the fatigue tests for this joint series, and so the following tests were run at 7, 6, 5, and 4 kip load levels. The data for the standard bolted tests is depicted in Figures 5.10a-e.

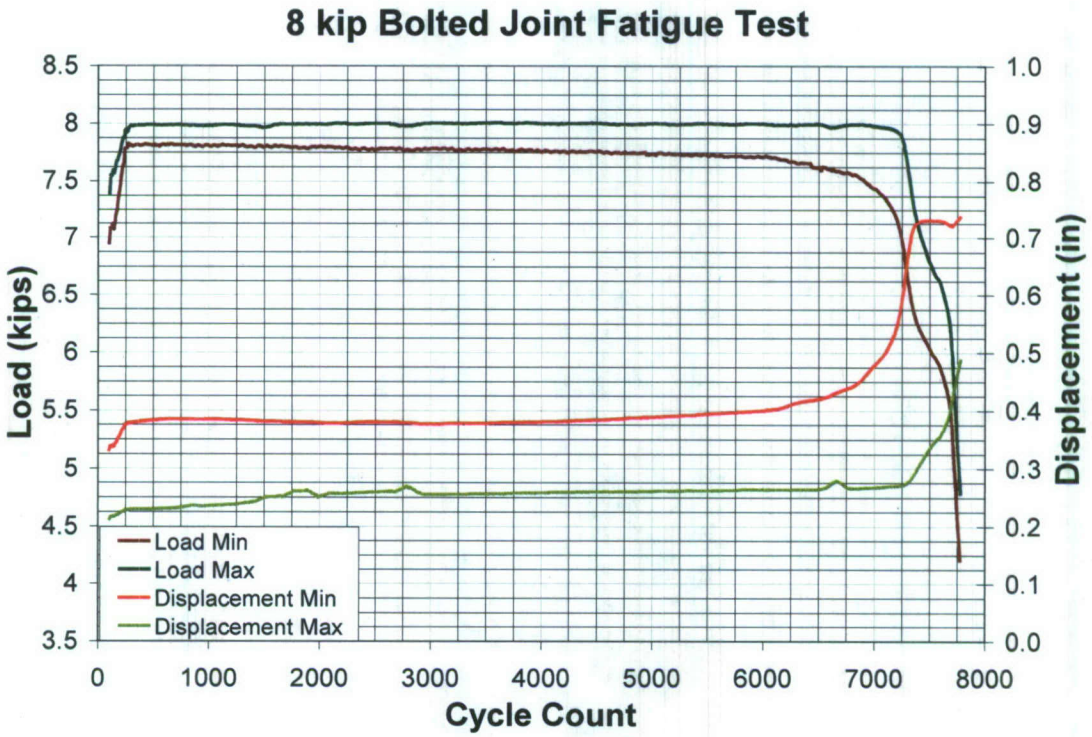

Figure 5.10a – 8kip Bolted Joint Fatigue Test Graph

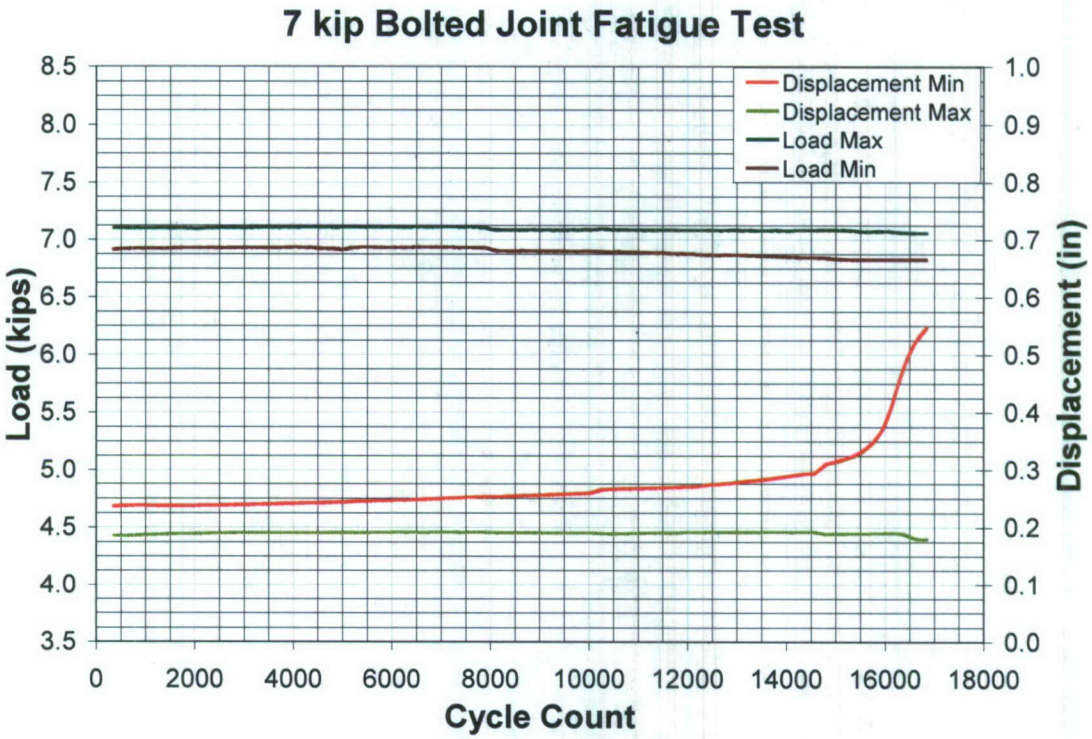

Figure 5.10b – 7kip Bolted Joint Fatigue Test Graph

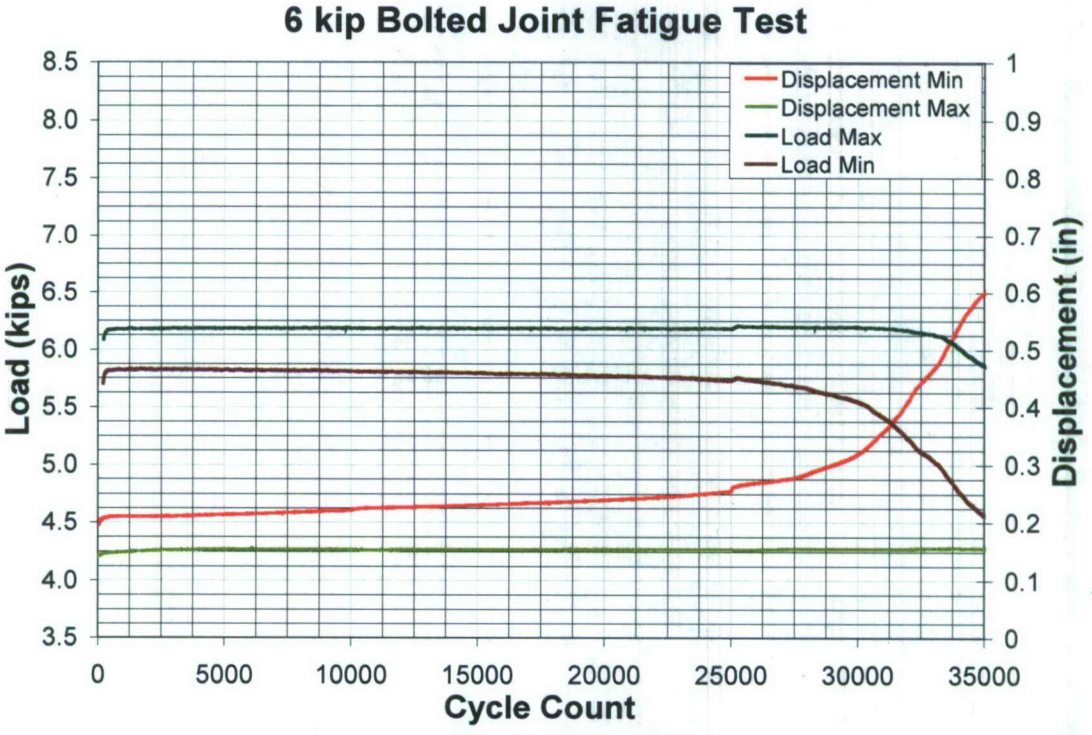

Figure 5.10c – 6kip Bolted Joint Fatigue Test Graph

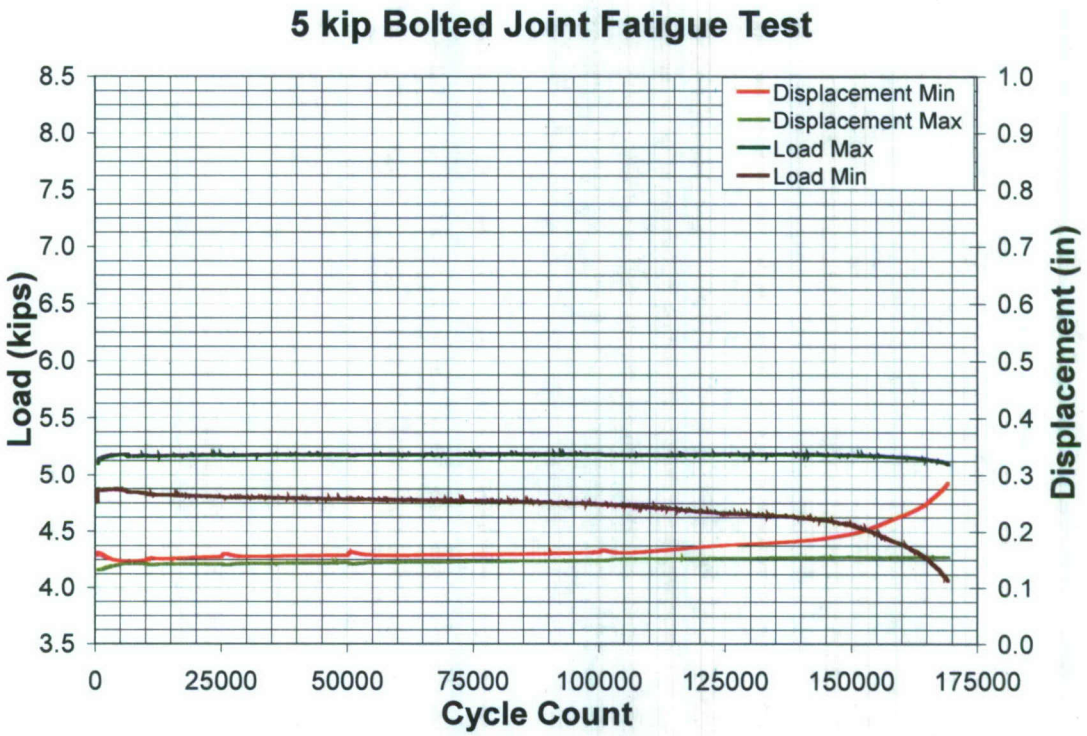

Figure 5.10d – 5kip Bolted Joint Fatigue Test Graph

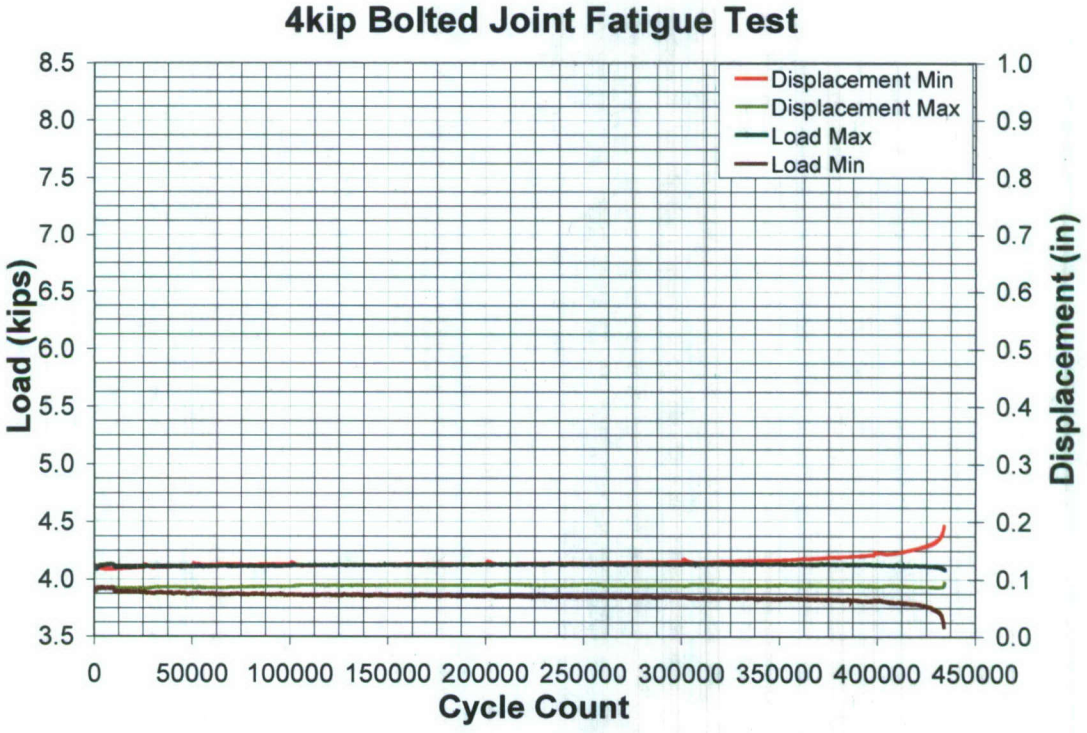

Figure 5.10e – 4kip Bolted Joint Fatigue Test Graph

With the completion of the standard bolted joint fatigue tests, it was deemed appropriate to begin the clamped joint tests at the same load level. The cycles to failure 13,125 resulting from this 8kip loading level was low enough to set 8kip as the ceiling for the clamped joints as well. As expected, the clamped joints proved more resilient to the loads applied than the standard bolted joints, and this resulted in a slightly different set of loading levels. Rather than 8, 7, 6, 5, and 4kips as with the standard bolted joints, the clamped joint fatigue tests were run at 8, 7, 6.5, 6, and 5kips with the 5kip test reaching the pre-determined run-out value of 2 million cycles. Data for the clamped tests is depicted in Figures 5.11a-e.

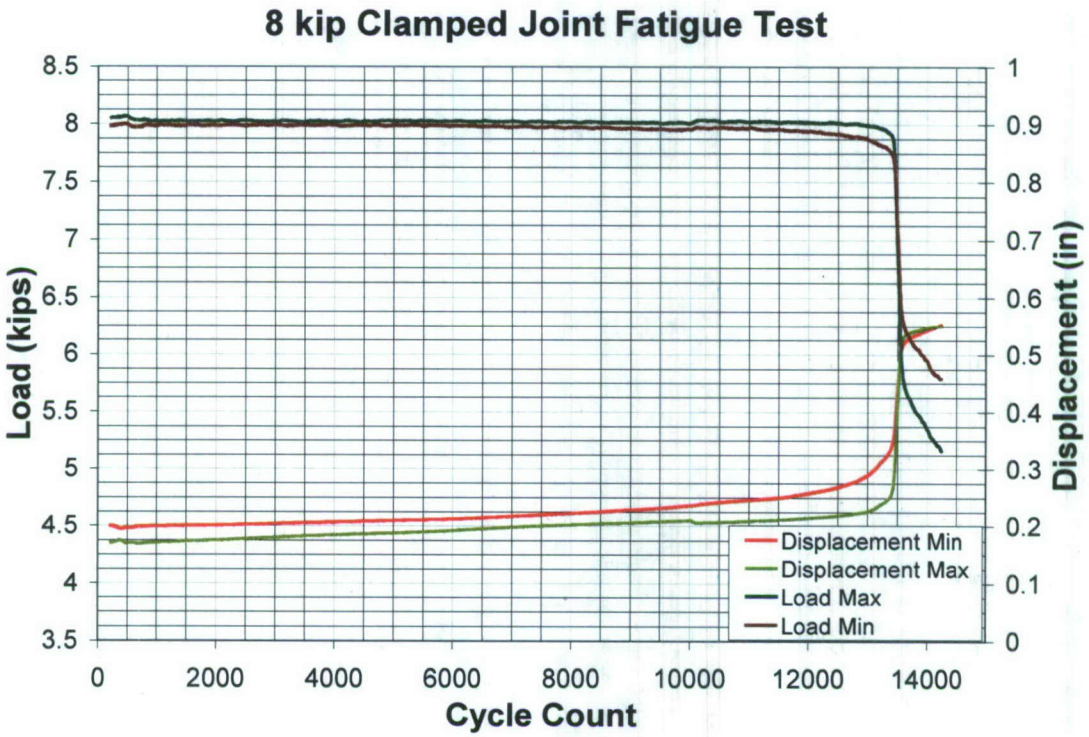

Figure 5.11a – 8kip Clamped Joint Fatigue Test Graph

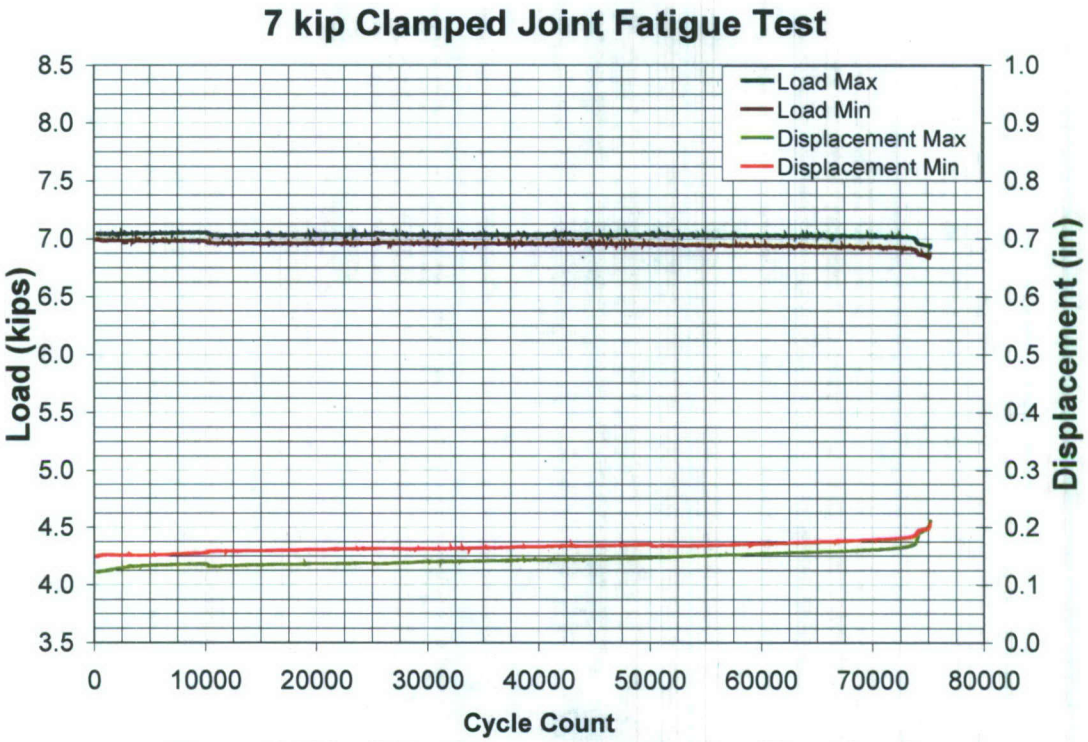

Figure 5.11b – 7kip Clamped Joint Fatigue Test Graph

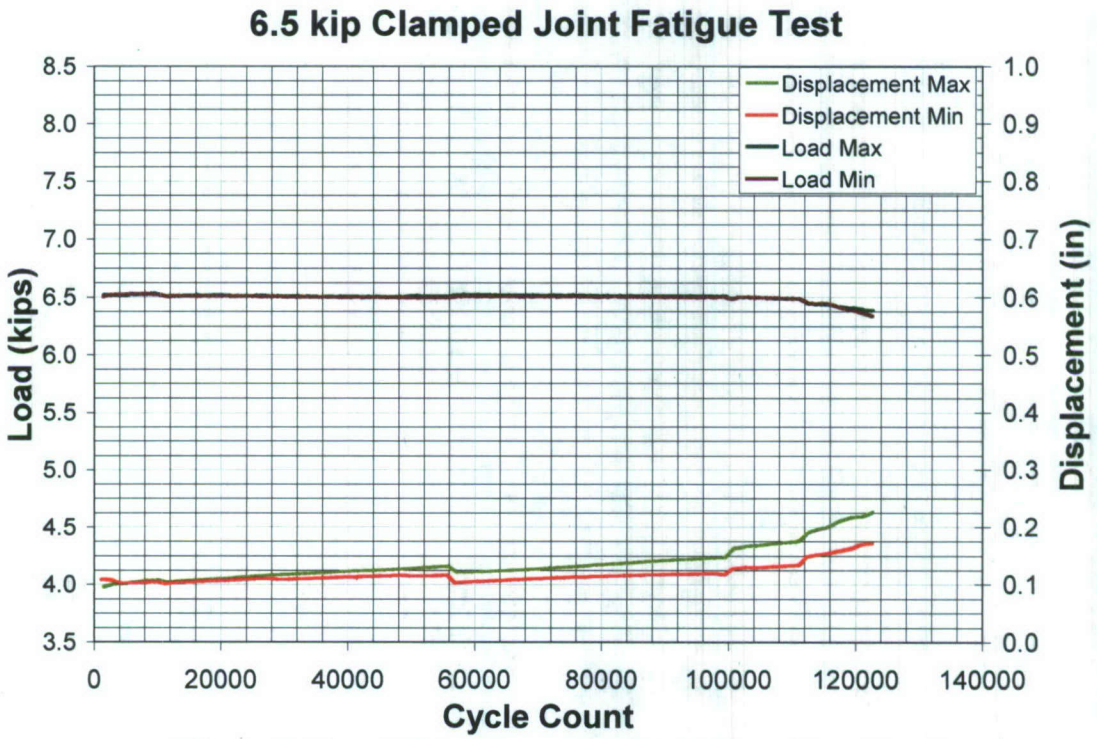

Figure 5.11c – 6.5kip Clamped Joint Fatigue Test Graph

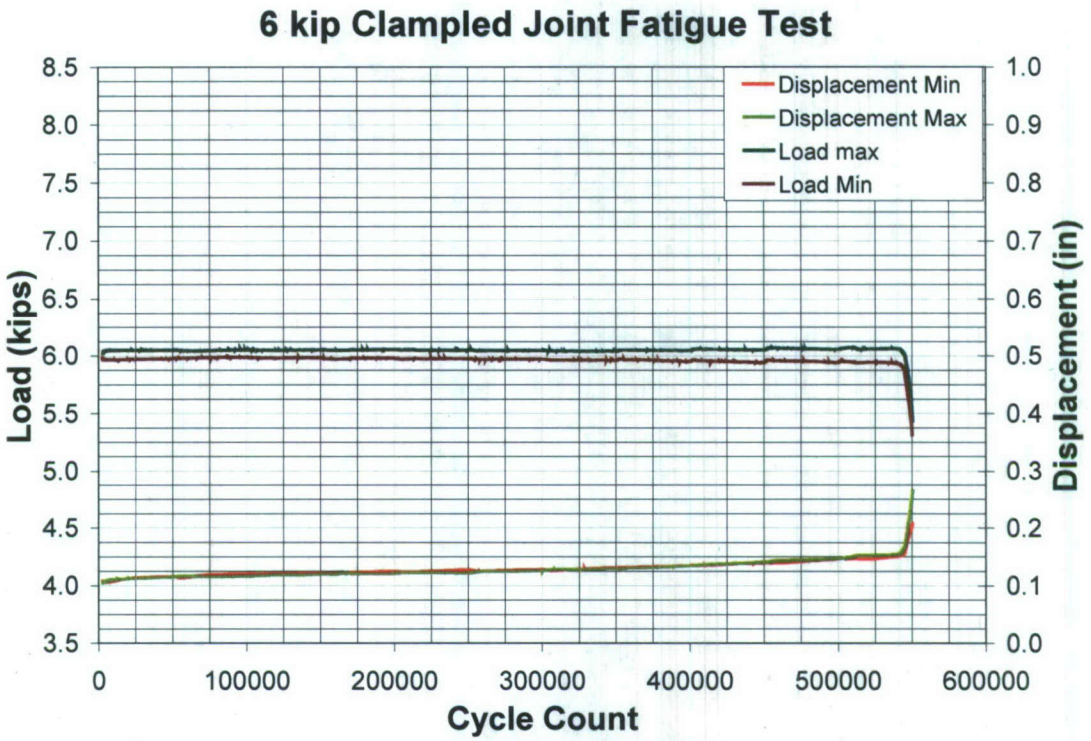

Figure 5.11d – 6kip Clamped Joint Fatigue Test Graph

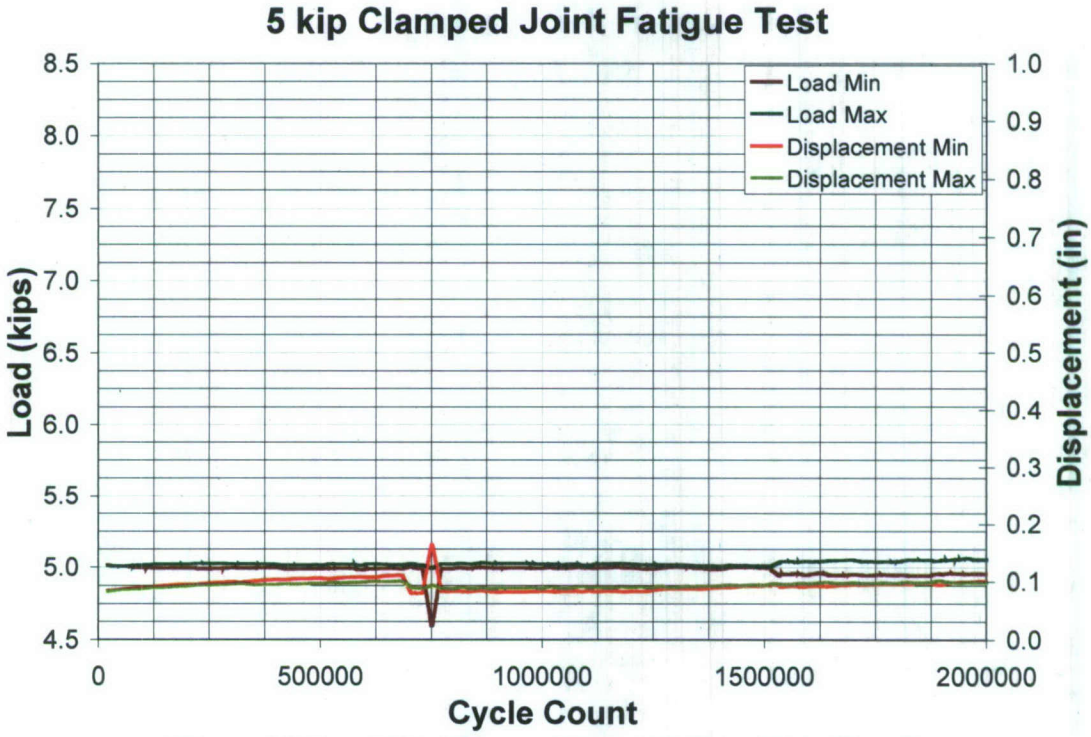

Figure 5.11e – 5kip Clamped Joint Fatigue Test Graph

Failure at the bolt line proved to be the rule for the higher load level standard bolted tests, and this is depicted in Figure 5.12. However, as the load levels decreased, the failure ended up moving from the composite to the steel tee at the weld toe. The final, lowest load level standard bolted joint tested failed in this fashion (see Figure 5.13). Another difference that was apparent in the graphs between the various tests is that the lower load levels resulted in much more progressive failure. While the failure the higher load levels tended to proceed quite quickly once it had initiated, the failure at the lower load levels was less catastrophic in nature. In other words, the compliance of the joint crept upwards more slowly in the lower load cases, making it more difficult to define the actual point of failure. With the lowest load level (4kips), the obvious reason for this would seem to be that the failure was in the steel as opposed to the composite. Though this is most likely the main reason for the more progressive failure, the same trend can also be seen in the next level up (5 kips) and the failure seems to become progressively more sudden as the loads increase. There tended not to be a great deal of delamination in the standard bolted joints. As with the bolted cyclic test to failure, fiber failure initiated at the bottom layers and worked its way upward until the joints failed (in the cases of composite failure.)

The clamped joint fatigue tests behaved differently than the standard bolted joints for obvious reasons. With no bolt line to fail at, the clamped joints typically failed at the clamped boundary. Failure for the clamped joints usually started at the outer (top and bottom) layers of the composite and worked its way inward until joint failure. Delamination played more of a role in the clamped joint tests than in the standard bolted joint tests. Figures 5.14 and 5.15 depict the failure of two clamped joint tests. Figure 5.14 is a case in which the fiber failure at the boundary was the dominant type of failure.

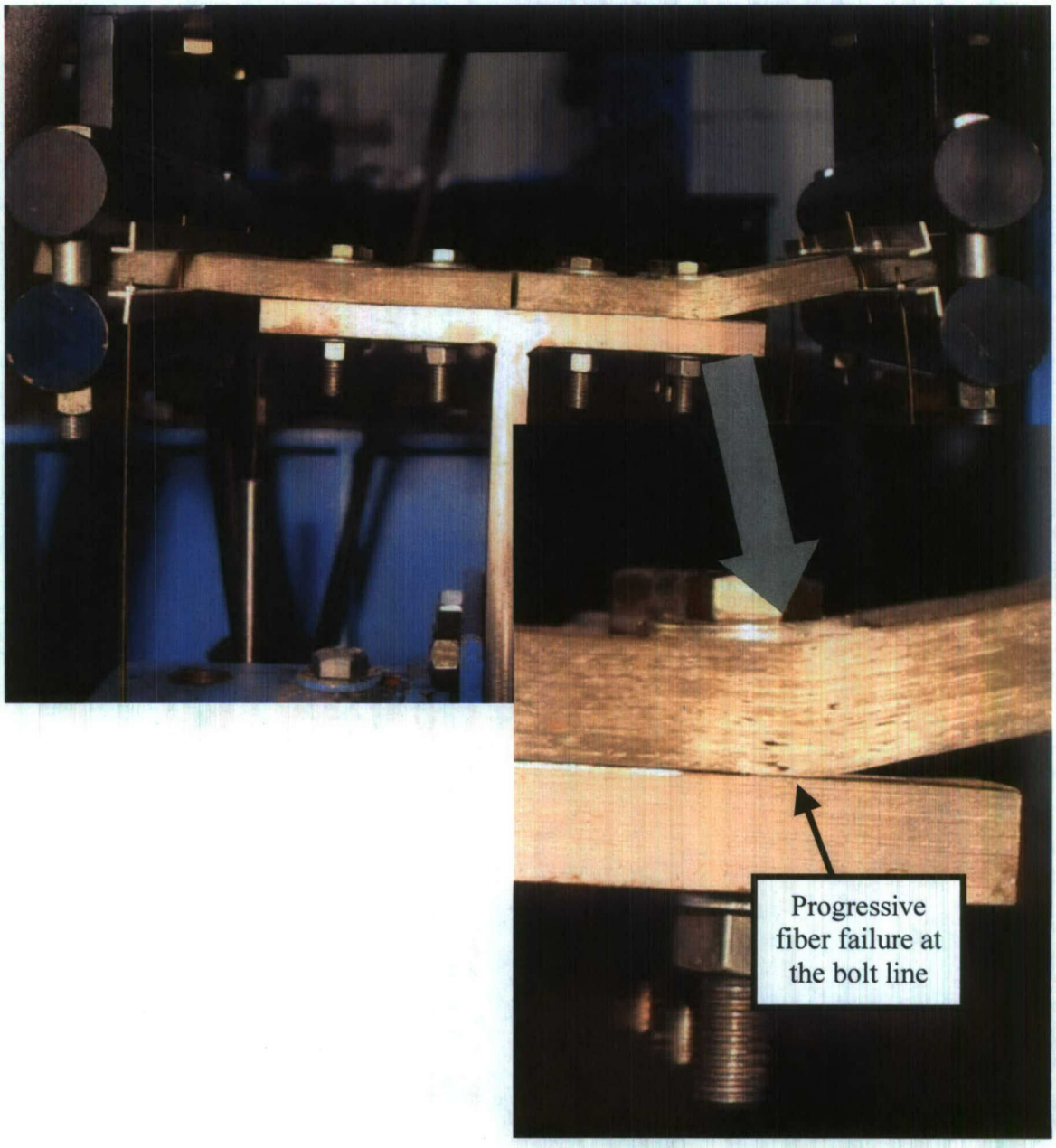

Figure 5.12 – Typical Fatigue Failure in a Standard Bolted Joint (from 8kip Test)

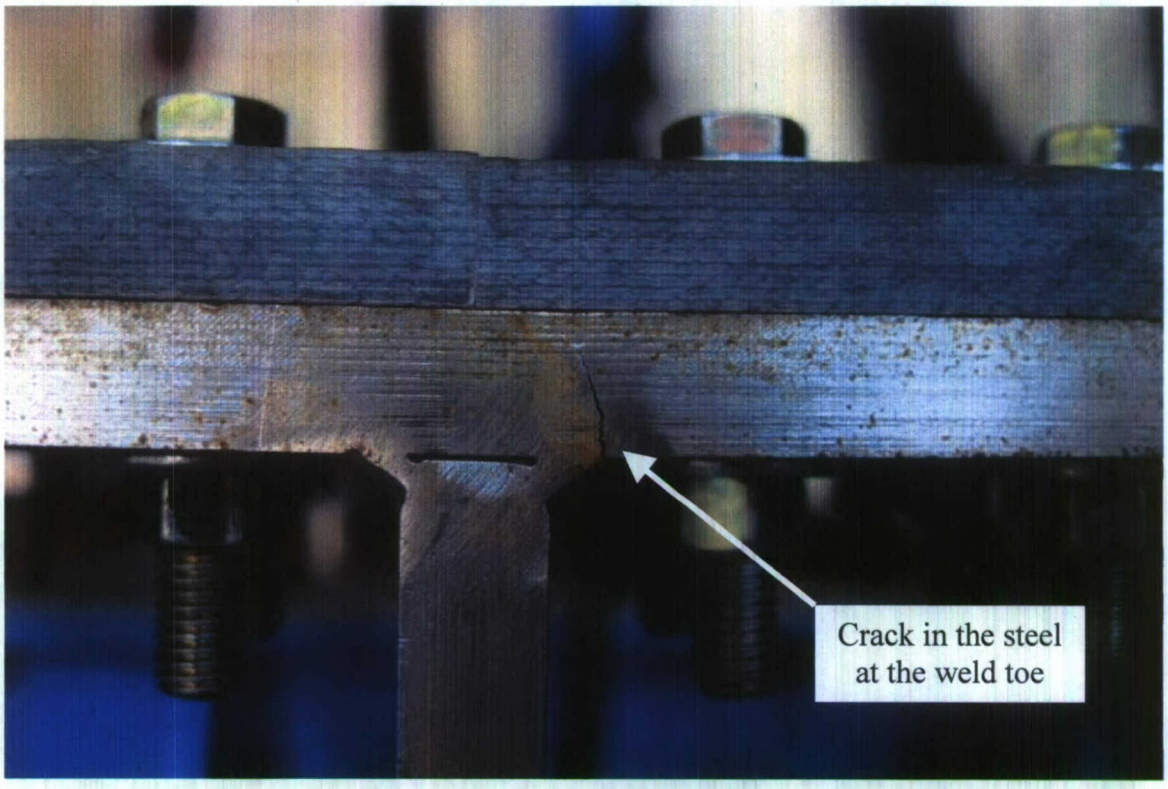

Figure 5.13 – Fatigue Failure in Steel Tee (from 4kip Standard Bolted Test)

Delamination is present, but this mostly occurred after the main failure. Figure 5.15, on the other hand, depicts how both fiber failure at the boundary (evidenced by the damage zones) and delamination contributed to the main failure. There was also one instance (the 6.5kip test) where delamination was the dominant failure type. This test article is shown with the major delamination in figure 5.16. This variation in types of failure can be expected, as the imperfections that lead to failure in composite materials vary as well. In the case of the 6.5kip clamped joint, the determining imperfection was between the layers that delaminated. This joint failed sooner than the trend created by failures predominantly due to fiber failure would have predicted, and this may indicate that delamination will lead to more rapid failure in the cases where it is the dominant source.

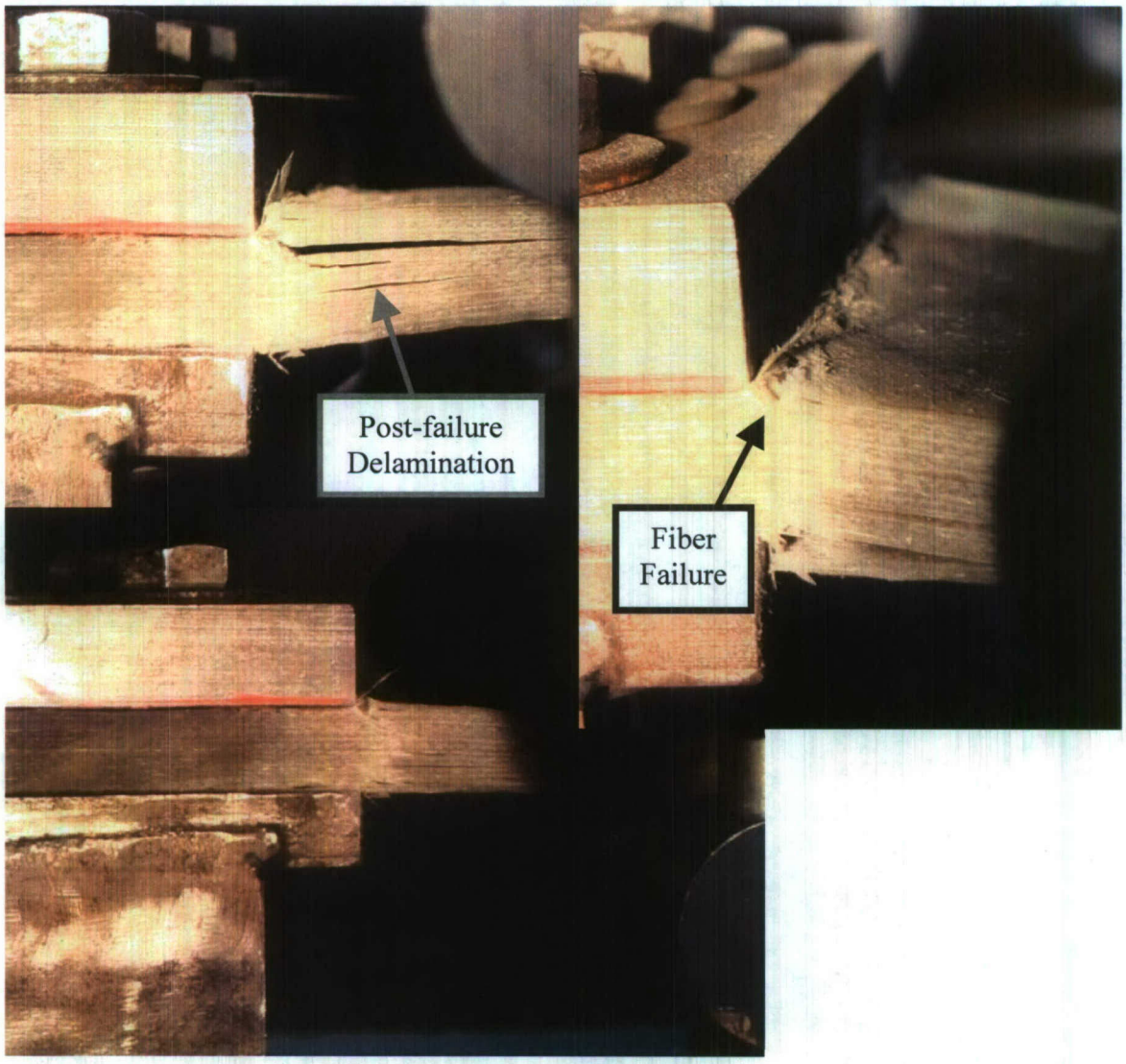

Figure 5.14 – Fatigue Failure in a Clamped Joint (from 8kip Test)

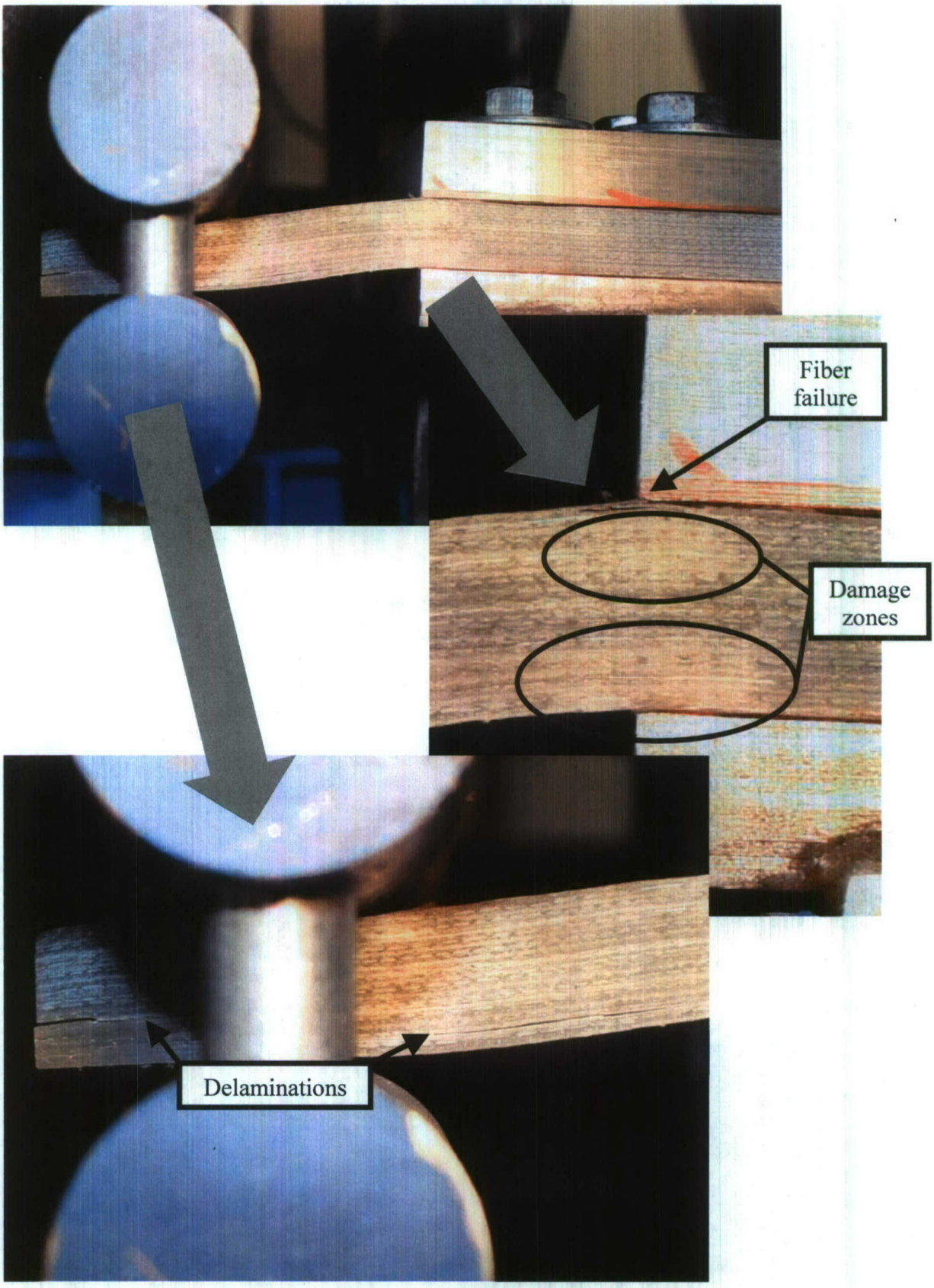

Figure 5.15 – Fatigue Failure in a Clamped Joint (from 6kip Test)

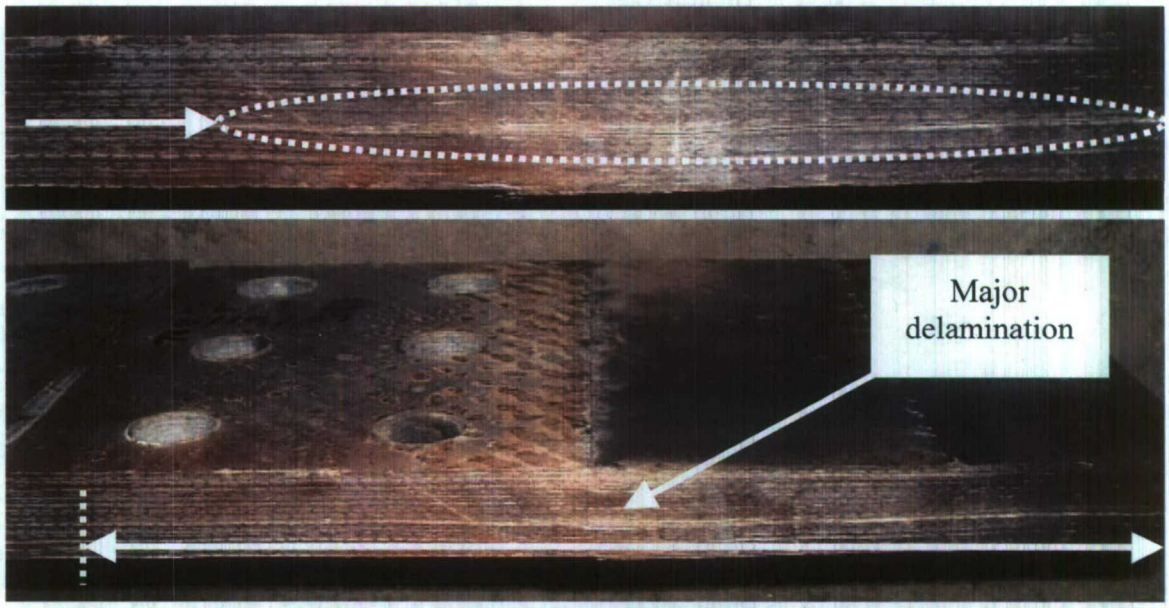

Figure 5.16 – Delamination in the 6.5kip Clamped Joint Fatigue Test

Another difference between the delamination and fiber failure as dominant failure types is that delamination, while causing failure to occur earlier, was less catastrophic. This closely resembles the difference previously described resulting from the differing load levels in the standard bolted joints. While the failure starting in the individual outer layers and working its way inward tended to fail quite quickly once failure had begun, the delamination failure was more gradual.

Of the clamped joint fatigue tests, there was one that reached the run-out cycle count of 2 million. This was the 5kip clamped joint. Due to the wear and tear on test equipment, this test encountered several setbacks. As mentioned in the previous section, one of these setbacks was a crack that initiated between the steel tee and plate stiffener. This can be seen in Figure 5.17. The weld was repaired, but shortly thereafter, one of the bolts in the clamping mechanism fatigued as well. This resulted in the spike seen in the data for the 5kip clamped joint fatigue test (Figure 5.11e).

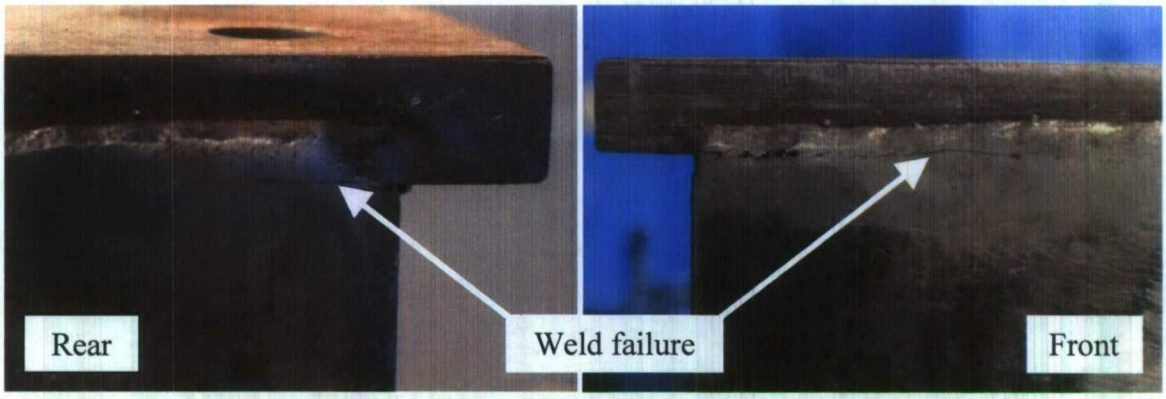

Figure 5.17 – Weld Fatigue Failure in the Clamped Joint Stiffened Tee

The determination of cycles to failure for the various tests proved to be less straightforward than anticipated for several reasons. One reason was a testing hardware limitation. The hydraulic actuator used would lose the ability to maintain the desired load level as the compliance of the test specimen increased. In theory, failure would be taken at the cycle count where the compliance of the test article doubled. However, since the load dropped as the test article was failing in many cases, the failure appeared less catastrophic and made the actual failure point more difficult to identify than if the load level were held constant. Another factor that complicated the process somewhat was that there were two separate parts to the test article. As seen in section 4, the test setup consisted of a symmetric tee joint. In most cases, one side of the tee joint would fail before the other. The data would therefore not appear to indicate that complete failure had occurred, while in actuality it had occurred in one side of the setup and the load was being maintained by the opposite side. The point of failure for these cases was determined by evaluating the data as well as observation of the joint itself. A list of the tests performed and the cycles to failure for each can be found in Table 5.3

Table 5.3 – Cycles to Failure for All Fatigue Tests

Test Designation	Joint Style	Load Freq. (Hz)	Peak Load (kips)	Cycles to Failure
FC-S1-BP-050-75-001	Bolted	0.50	± 8	7,200
FC-S1-BP-050-75-002	Bolted	0.55	± 7	16,500
FC-S1-BP-050-75-003	Bolted	0.61	± 6	32,500
FC-S1-BP-050-75-004	Bolted	0.67	± 5	170,000
FC-S1-BP-050-75-005	Bolted	0.71	± 4	425,000
FC-S1-CL-000-75-001	Clamped	0.75	± 8	13,500
FC-S1-CL-000-75-002	Clamped	0.75	± 7	75,000
FC-S1-CL-000-75-003	Clamped	0.65	± 6.5	112,000
FC-S1-CL-000-75-004	Clamped	0.75	± 6	550,000
FC-S1-CL-000-75-005	Clamped	0.80	± 5	N/A

5.4 Residual Strength Test Results

Residual strength tests are reserved for the test articles, which arrive at the pre-determined run-out cycle count of 2 million. The only joint to achieve this was the clamped joint tested at the 5-kip load level. As mentioned in Section 4.3.6, the residual strength test format is identical to that for the cyclic tests to failure other than the fact that it is run on a previously fatigue tested specimen. Pictures of failure of the residual strength test can be found in Figure 5.18. The test results can be seen in Figure 5.19. These results are divided into three parts in the graph: Part 1 includes the data until a major failure, Part 2 includes the major failures, and Part 3 includes the data of few cycles after failure. Peak load and displacement at peak load are summarized in Table 5.4. The graph shows that whereas the cyclic tests to failure essentially maintain the same properties until a more sudden catastrophic failure, the residual strength test gradually breaks down as damage progresses. The compliance steadily increases, causing a slight drop in the load level each time. Finally, failure does occur, but it is less severe than in the cyclic tests to failure. The joint surprisingly retained 92.5% of the ultimate strength for the clamped case, and there is not a great deal of difference between the values reached in the initial cyclic test to failure and those reached in the residual strength test.

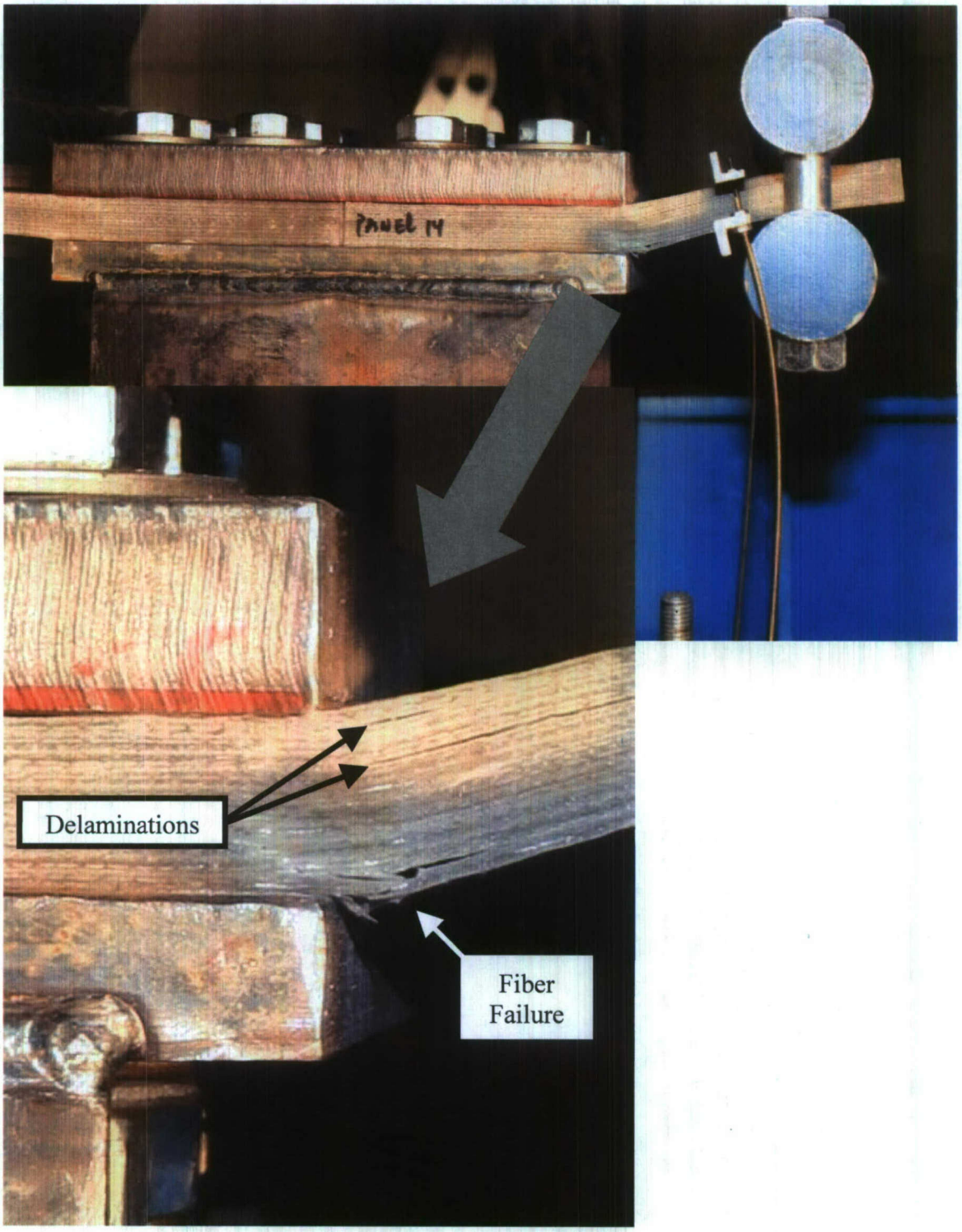

Figure 5.18 – Failure in the Residual Strength Test

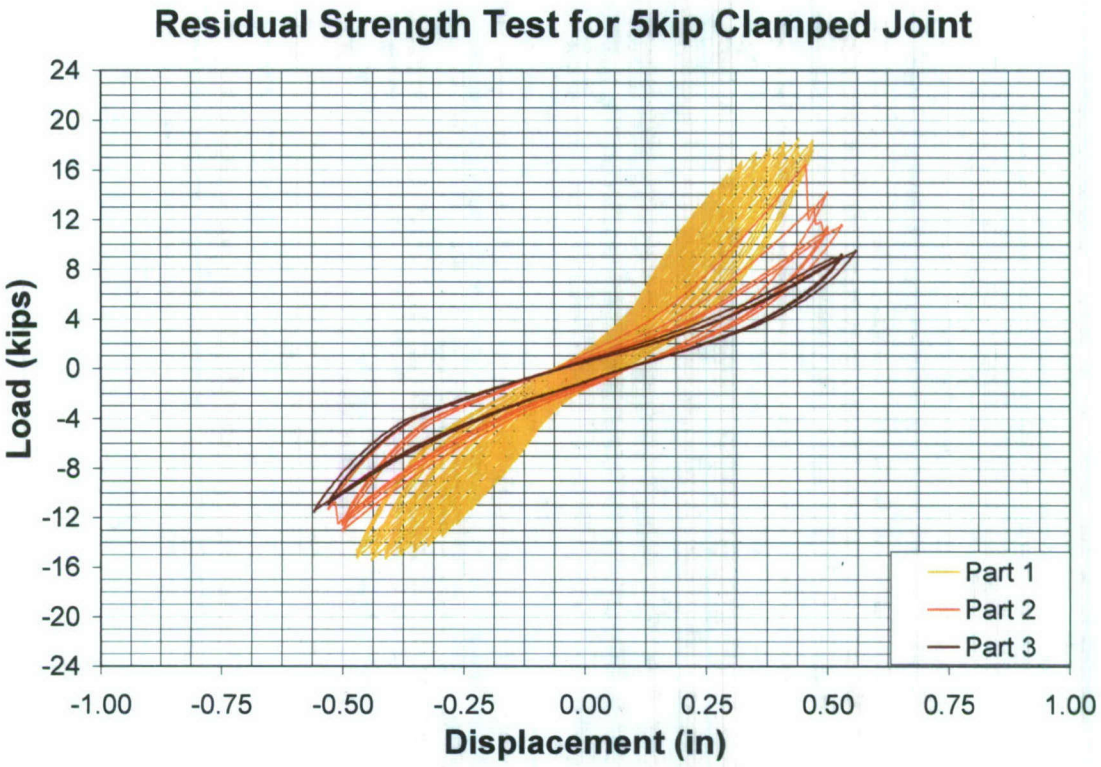

Figure 5.19 – Residual Strength Test for 5kip Clamped Joint

Table 5.4 – Peak Values for Residual Strength Test

	Peak Load (kip)	Peak Nominal Stress (ksi)	Displacement at Peak Load (in)
Up	-15.466	36.979	-0.4411
Down	18.498	44.227	0.4405

5.5 Nominal Stress Calculation Results

The nominal stress calculations described in Section 4.3.8 result in the data presented in Table 5.5. The nominal stresses presented for the cyclic tests are obtained by using the lower of the two peak load values from the cyclic tests to failure for each joint style as the load levels (this is the peak load in the upward direction in both cases). These are used as

the ultimate strengths (S_{ut} or σ_{ut}) for the joint styles. The net method of claculation uses the net area of the composite material across the bolt holes in the calcualtion of the nominal stress.

Table 5.5 –Summary of Stress Levels for Various Tests

Test Name/Type	Composite				Steel	
	Gross Method Nom. Stress Level		Net Method Nom. Stress Level		Stress Level	
	ksi	*N/mm²*	*ksi*	*N/mm²*	*ksi*	*N/mm²*
Bolted Joint Cyclic	54.413	375.180	69.602	479.908	106.601	735.012
Clamped Joint Cyclic	39.968	275.581	N/A	N/A	N/A	N/A
8kip Bolted Joint	26.034	179.503	33.376	230.126	53.525	369.055
7kip Bolted Joint	22.995	158.553	29.507	203.454	45.558	314.119
6kip Bolted Joint	19.882	137.086	25.580	176.371	39.265	270.730
5kip Bolted Joint	16.556	114.152	21.286	146.767	32.901	226.855
4kip Bolted Joint	13.186	90.917	16.931	116.739	26.033	179.497
8kip Clamped Joint	19.794	136.481	N/A	N/A	N/A	N/A
7kip Clamped Joint	16.554	114.142	N/A	N/A	N/A	N/A
6.5kip Clamped Joint	14.448	99.620	N/A	N/A	N/A	N/A
6kip Clamped Joint	13.503	93.105	N/A	N/A	N/A	N/A
5kip Clamped Joint	11.954	82.425	N/A	N/A	N/A	N/A

5.6 Nominal Stress Results with Steel Fatigue Curves

With the nominal stress level results from the fatigue tests, it is possible to begin a fatigue characterization of the two joint styles tested and compare them with existing data. Figure 5.20 is a graph of the failures of the joint styles studied. For the standard bolted joints, the stress in both the composite at the bolt line and the steel at the weld is recorded (as seen in Table 5.5). The results for the stress in the composite include those obtained by both the gross and net stress calculation methods as discussed in Section 4.3.8. Therefore, there are three data series for the standard bolted joints. It can be seen that in Figure 5.20, these three series have points that are solid, or filled in, and points that are empty. The solid data points indicate that the failure occurred in the material that the given series represent. For instance, at the highest stress level it can be seen that the data point in the steel series is empty and the data points in to composite series are solid. This means that failure occurred in the composite at this stress level. Similarly, at the lowest

stress level the data point in the steel series is solid while the points in the composite series are empty. This indicates that the failure occurred in the steel at this stress level. The reason that the empty data points are included is simply to indicate what the stress in the given material was when the other material failed. Empty points do not indicate failure in the material. For the clamped joint data series, the stress is calculated at the clamped boundary, where all the tests failed.

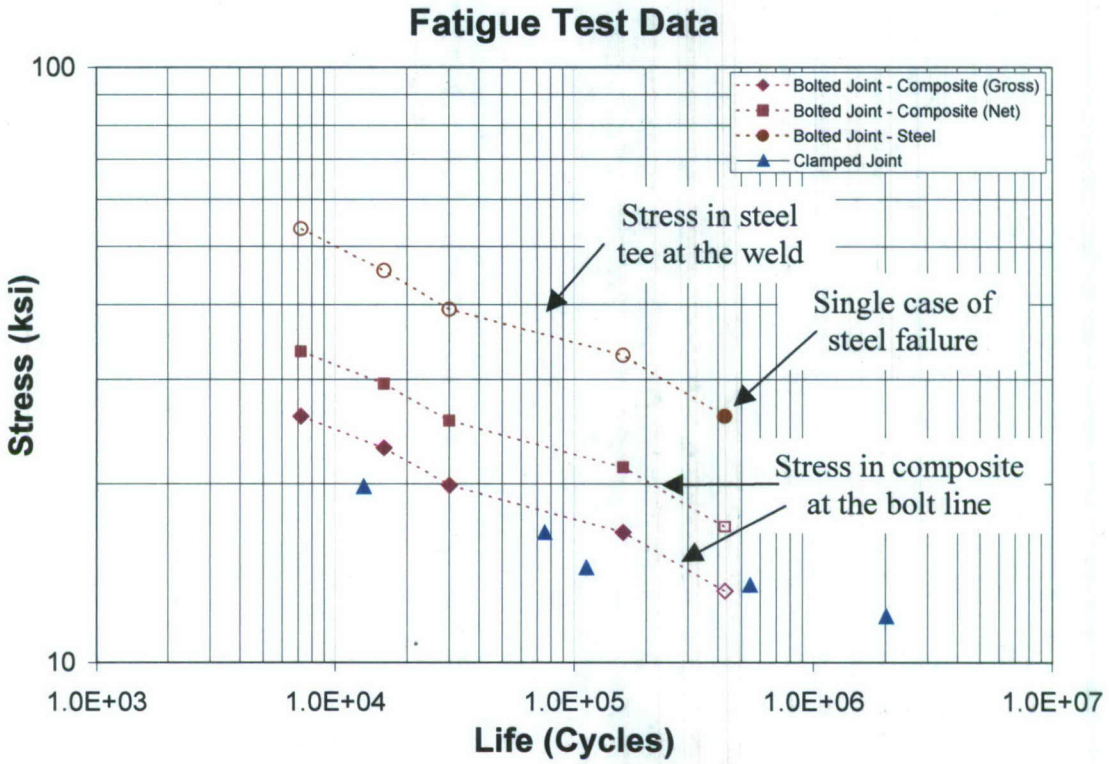

Figure 5.20 – Failure Data for All Tests

For comparison purposes, this data is then graphed in Figures 5.21 and 5.22 along with the data presented by Munse et al. and Mansour et al. discussed in the introduction. The steel tees used in the standard bolted joints most closely resemble detail 42 in the Munse et al. data. The failed steel tee fell below the curve for the 42 detail. This can probably be attributed to normal variation in fatigue test results and the fact that though they are the most similar, there are still some significant differences between the two configurations. For the style of characterization used by Munse et al., fatigue data can be expected to fall around the curve, as the curve is simply a fit of previously recorded data.

The British design curves employ a different kind of characterization. The experimental data is taken and the design curve is set so that it is below a given percentage, such as 99%, 99.9%, or 99.99%, for instance. This gives the design curves a built-in factor of safety, and data is not expected to fall beneath the design curve for a given joint. The steel tee used in the standard bolted joint tests would have fallen in F2 category of the British curves. As expected, it can be seen in Figure 5.22 that the steel failure occurred above this curve. As far as the stress level is concerned, the factor of safety for the failure is 1.8. For the cycles to failure, the curve gives a factor of safety of 5.7.

Observation of the data also reveals that the bolted joints seem to be more resilient as far as the stress that they withstood at the location of failure. As discussed in Section 4.3.8, the more accurate of the two methods of calculating the stress in the composite for the standard bolted joint tests is the Gross Method. The difference between the data for the clamped joints and the data for the standard bolted joints using this method is small, but present nonetheless. This is not intuitive, since it would most likely be expected that the stress concentrations from the bolt holes would cause just the opposite. However, it is probable that the clamping action of the bolts themselves actually reduced the peak stress levels in the composite, resulting in the better performance. It can also be seen the there was a transition in the failure medium in the bolted joint specimens. For the high-stress, low-cycle tests, the composite portion of the hybrid joint failed. However, when the load decreased and cycles increased, the failure moved to the steel. The purpose of this testing was to provide a baseline for comparison with the near-future testing of more novel embedded weldable hybrid joint configurations. However, also in question was whether fatigue characteristics of the materials composing the hybrid joints would be sufficient for prediction purposes. The interaction between the various components in these baseline tests indicates that the testing of a full joint is necessary to account for all of the intricacies specific to a particular joint. It is predicted that this will be especially true for the perforated embedded weldable joints.

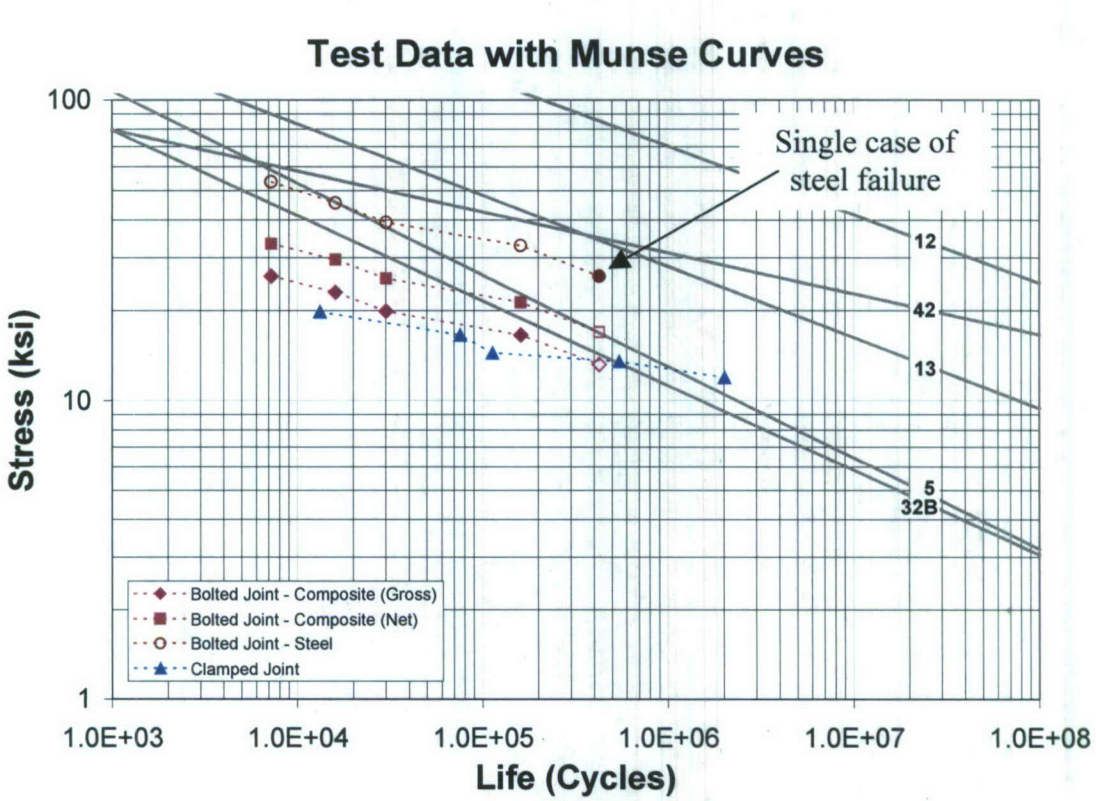

Figure 5.21 – *S-N* Data with Munse et al. (1983) Curves

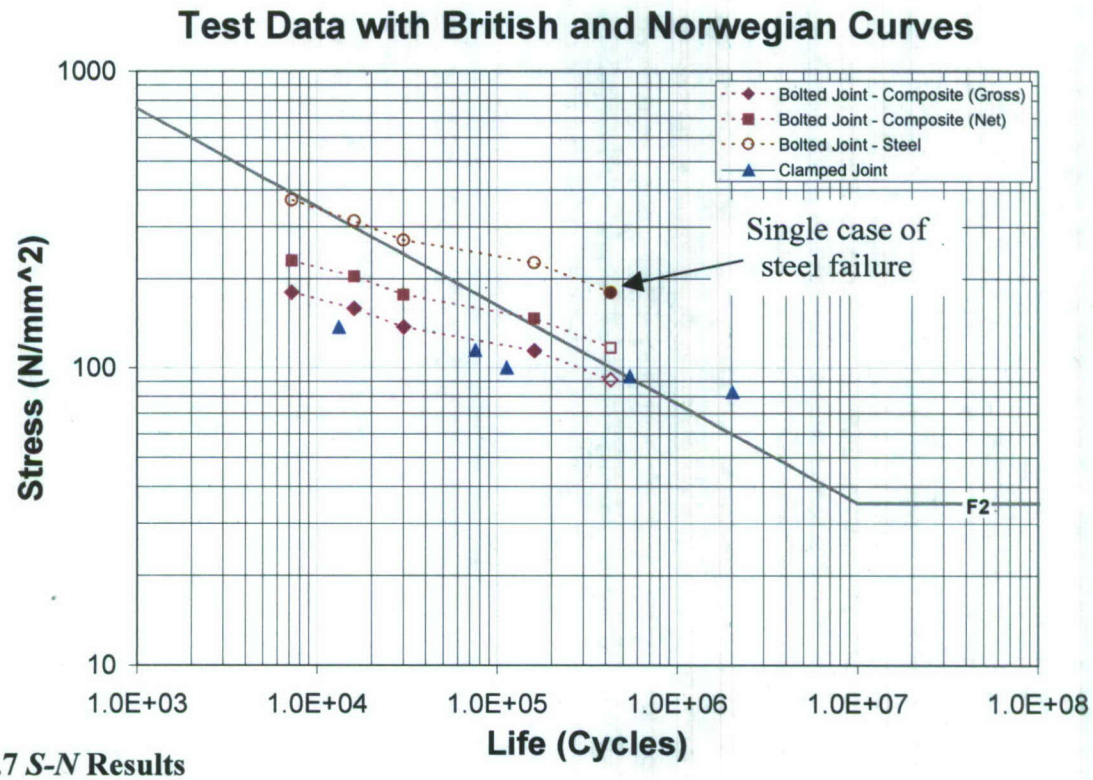

Figure 5.22 – *S-N* Data with British/Norwegian Curves

With the failure data available, the *S-N* parameters (namely, the values for m and A in Equation 1.1) are determined for the joint styles that have been tested. The S-N curves are determined by fitting Equation 1.1 to the data. This provides prediction curves, which characterize the different joint styles. These curves may then be compared to those of the more novel joint styles to evaluate their performance. While there would ideally be considerably more data to determine fatigue rules for the joint styles tested, the data that is available produces the m and A values found in Table 5.6. Again, nominal stress levels are used in this data analysis. The R^2 values are also included to indicate how closely the equations fit the data. The prediction curves generated by incorporating m and A for the different joint styles into Equation 1.1 are presented in Figure 5.23. The curve for the standard bolted joint test series is composed of the data points where failure occurred in the composite. Since the failure shifted from the composite to the steel for the last data point in this series, more data points where failure occurred in the steel would be needed for the last data point to be applicable. It is possible that the slope of the *S-N* curve for this series would change where the failure occurs in the steel at lower stress levels. Since the effect of this shift in failure on the *S-N* equation is currently unknown, the last data point where falilure occurred in the steel is not included in the calculations of m and A.

Table 5.6 – *S-N* Values for Fatigue Test Results

Joint Style	m	$Log_{10}A$ (ksi)	R^2 Value
Standard Bolted (Gross)	6.835	13.484	.977
Standard Bolted (Net)	6.878	14.285	.978
Clamped	10.173	17.186	.951

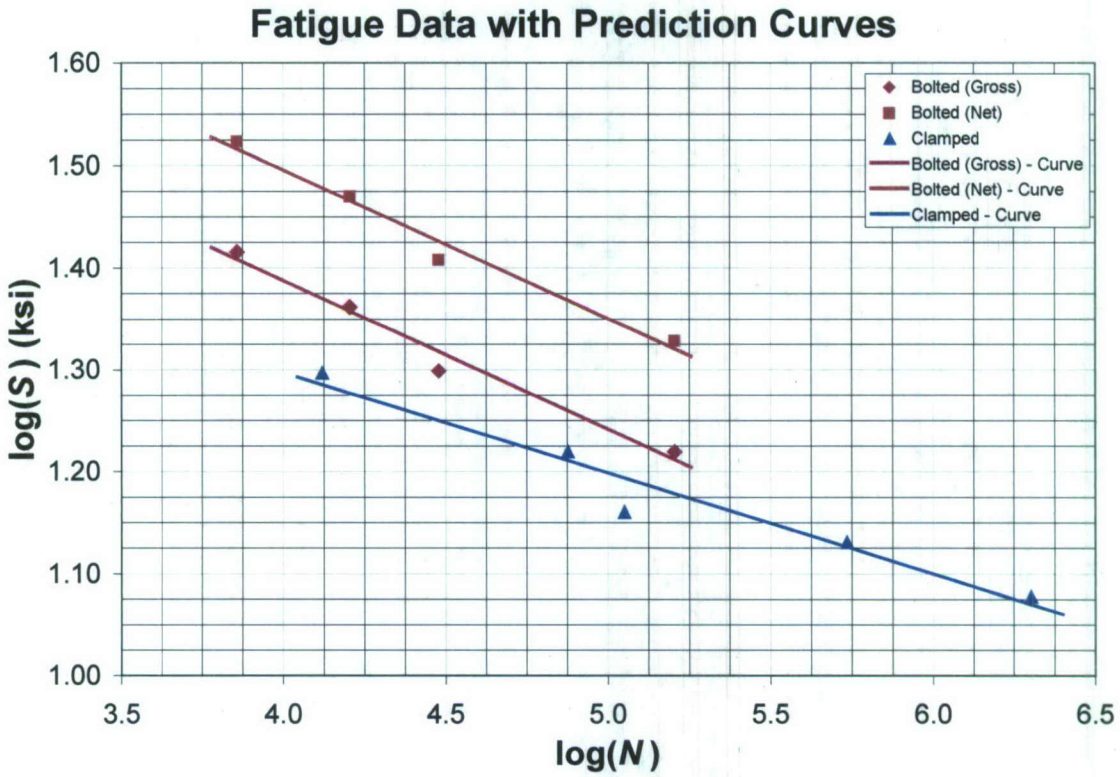

Figure 5.23 – *S-N* Prediction Curves with Fatigue Test Data

5.8 *S-N* Results with Composite Curves

With the *S-N* data from the fatigue testing available, it is beneficial to compare the results from the current research to some of the other studies of fatigue in composite materials discussed in section 1.4.6. The data on thick-section composites presented by Mahfuz et al. (2000), seen in Table 1.4 and Figure 1.17, is combined into one graph and plotted with the fatigue results and *S-N* curves developed in this study. Since the data in Table 1.4 is based on *percentages* of ultimate flexural strength ($\sigma_{applied}/\sigma_{ut}$), these percentages are multiplied by the ultimate flexural strengths that Mahfuz et al. provided to obtain the actual applied stresses. This makes it possible to compare the different data sets, since both now employ applied stress in the y-axis of the *S-N* plot. This plot can be seen in Figure 5.24.

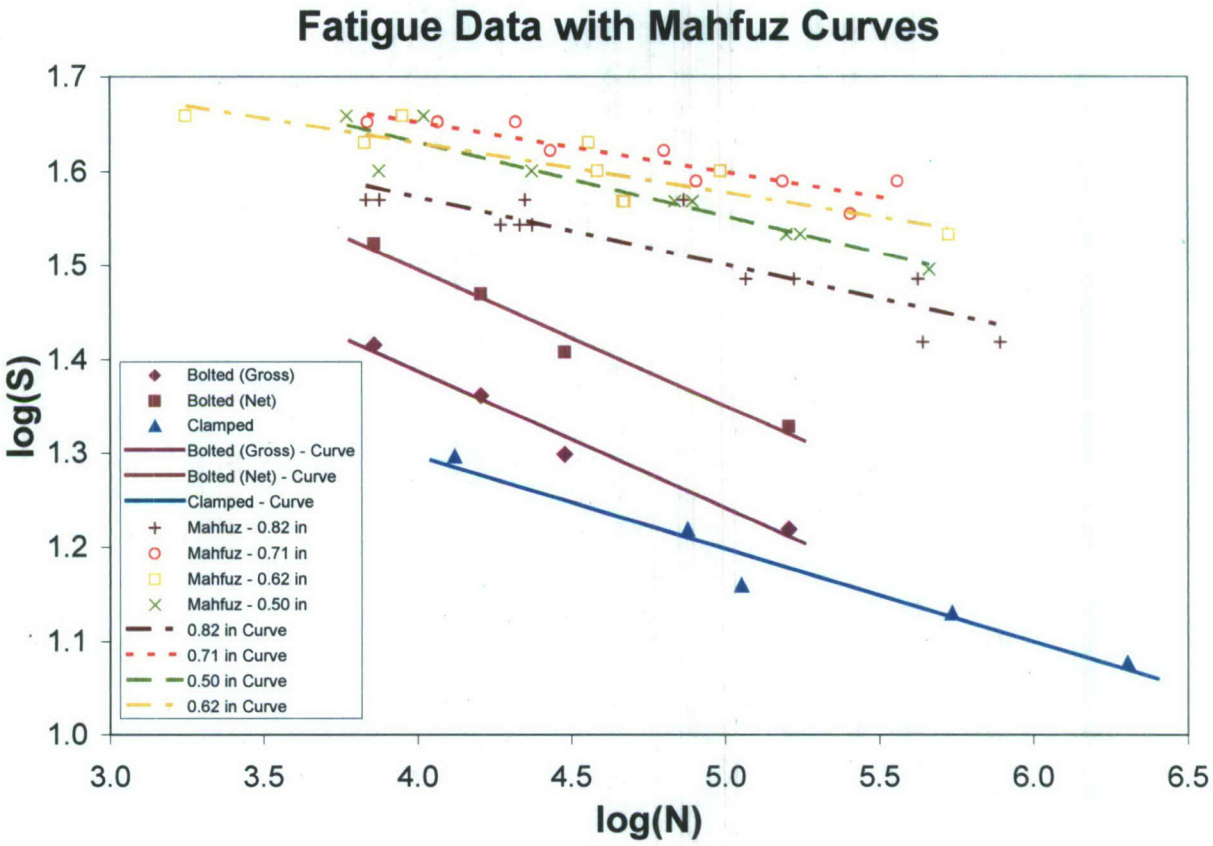

Figure 5.24 – *S-N* Data with Mahfuz et al. (2000) Data

While the fatigue resistance of the materials tested by Mahfuz et al. is significantly better than those used in the current study, this is to be expected. One reason for the better performance is that the materials tested by Mahfuz et al. had fiber volume fractions ranging from 55-60%, which is greater than the fiber volume fractions of approximately 48.5% for the materials tested in this study. Additionally, Mahfuz et al. used different materials. In that study, woven S2-glass fibers provided the reinforcement, whereas in this study, reinforcement consists of knit E-glass fibers. It is observed that although the materials studied by Mahfuz et al. displayed better fatigue performance, the slope of the fatigue life curves closely resembled that of the clamped joints in this study. This is expected because the Mahfuz et al. data is for composite materials. Clamped joints

isolate the composite, unlike the standard bolted joints where the effects of the steel tee, bolts, and bolt holes play a role in the fatigue life. All in all, the data presented by Mahfuz et al. verifies the legitimacy of the results and *S-N* curves procured by this research.

The frequency dependent fatigue model proposed by Tang et al. (2000) is also compared to the present research. The Tang et al. model was based on tension-tension rather than flexural fatigue loading, but used the same materials as those used in the current study, namely E-glass/vinyl ester composites. The Tang et al. model (seen in Equation 1.15) employs normalized maximum strength, $S_{\max} = \frac{\sigma_{\max}}{\sigma_{ult}}$. The data from the current research is appropriated for this model simply by dividing the stress level of the tests by the ultimate strength, which was discussed in section 5.5. Since the model is also frequency dependent, the frequencies of the tests are also necessarily taken into account. The tests were all run at slightly different frequencies, so the frequency, *f*, in the model is set to the average frequency of the tests in the series being evaluated. The Tang et al. model is then compared to the *S-N* curves developed in the current study. This comparison is found in Figure 5.25. It can be seen that the current data fits the model proposed by Tang et al. (2000) very well. This is especially the case for the clamped joint data. As with the previous example, the reason for this is that the Tang et al. (2000) model is for composite specimens, and the clamped tests isolate the composite. The fiber volume fractions of the materials tested by Tang et al. (2000) ranged from 36-37%. This should cause the fatigue performance to be worse than that of the materials tested here, and this proves to be the case. The layup of the E-glass layers, however, was unidirectional unlike the essentially quasi-isotropic layup used in the current research. This most likely somewhat counters the effects of the lower fiber volume fraction.

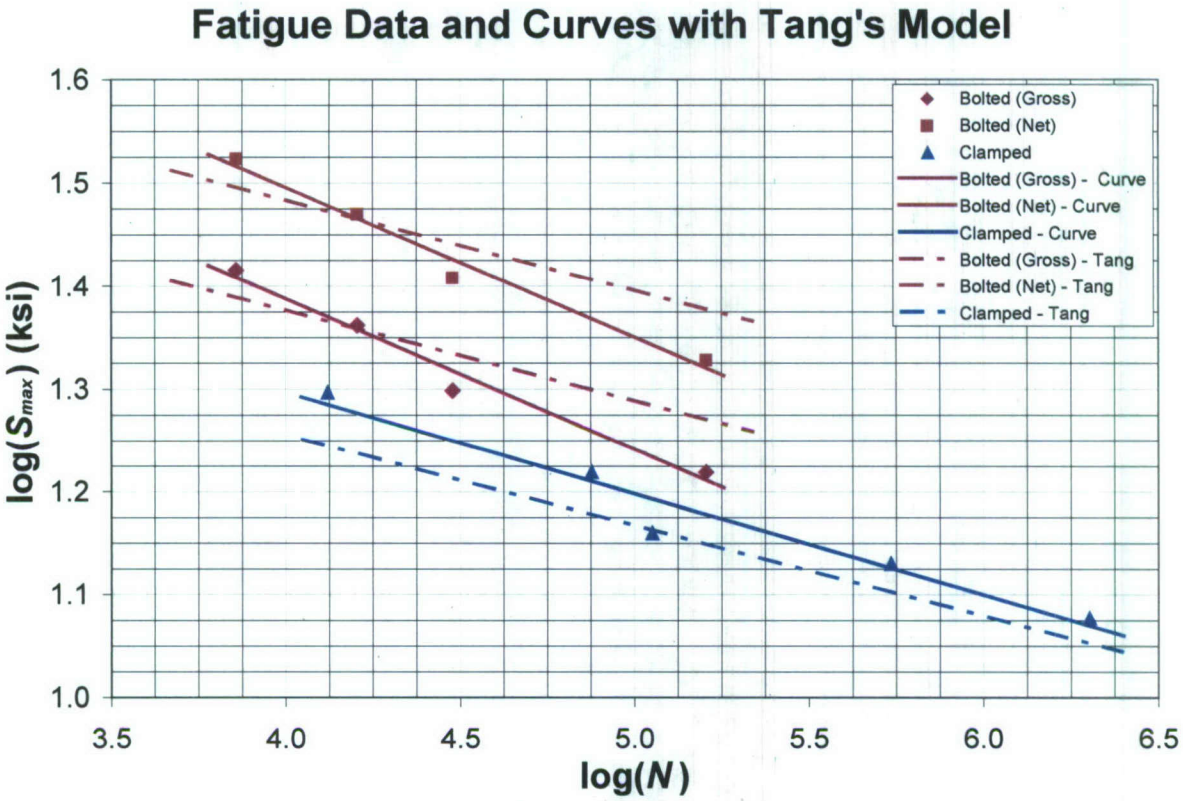

Figure 5.25 – *S-N* Data with Tang et al. (2000) Model

5.9 Summary, Conclusions, and Recommendations

A baseline evaluation of hybrid joint configurations has been carried out. The first part of this process was a preliminary finite element analysis to simulate the panels the joints tested were designed for, and obtain appropriate values for the moment arm to apply to the joints during testing. These analyses provided moment arms ranging from 6.23 to 8.84 inches. A moment arm of 8.5 inches was selected, placing it at the upper end of the spectrum. This was for practical reasons and also because shear stresses are usually lower than axial and bending stresses, making it appropriate to study cases with larger moment arms. Specimen fabrication was also undertaken. E-glass/epoxy vinyl ester test articles were fabricated, including a successful panel with an embedded perforated steel insert. With the test articles and moment arm information available, flexure fatigue testing was carried out on two baseline joint configurations: standard bolted, and

clamped. Strictly in terms of stress levels in the composite at the point of failure, the standard bolted joints seemed to perform slightly better than the clamped joints. It is assumed that the reasons for this include interactions between the bolts and the composite, such as the clamping force that the bolts apply. The fatigue life of the steel in the tests fell in the range as expected from currently available data. The case of steel failure fell near the curve of the joint detail presented by Munse et al. (1983) that most resembling the standard bolted joints. When applying the British fatigue curves presented by Mansour et al., (1996) the steel failed with a factor of safety of 1.8. The composite material presented by Mahfuz et al. (2000) peforms better than the joints tested in the current research, most probably due to the different materials used and the higher fiber volume fractions of Mafuz's specimens. However, the slopes of the fatigue curves plotted are extremely similar to the slope of the fatigue curve for the clamped joints experimented on in this study. The model proposed by Tang et al. (2000) fits the data of the clamped joints very well. The reasons for this are that the materials used are the same in both studies, and the effects of the two differences between the Tang et al. study and the current one somewhat counteract each other. The similarity of the pre-existing composite fatigue models to the data and *S-N* curves obtained in the present study attest to the validity of the current results.

The future work recommended based on this study is the immediate continuation of testing of more novel joint configurations. More perforated embedded joints should be fabricated, and fatigue tests of the weldable joints using these specimens should be performed and compared to the baseline data that this research has provided. Furthermore, it would be of interest to perform testing on variations of the joints presented here. Bolted joints using a higher grade steel, for instance, would be particularly beneficial for the purposes of comparing the occurrence of any transition points for failure with those which occurred in the standard joint configurations tested here.

REFERENCES

Alm, F. (1983) "GRP versus steel in ship construction", Naval Forces; 4:5; 82-86

ASTM D 790-07 (2007), "Standard Test Methods for Flexural Properties of Unreinforced and Reinforced Plastics and Electrical Insulating Materials" ASTM International, 100 Barr Harbor Drive, PO Box C700, West Conshohocken, PA, 19428-2959 USA.

ASTM D 2651 – 01 (2008), "Standard Guide for Preparation of Metal Surfaces for Adhesive Bonding" ASTM International, 100 Barr Harbor Drive, PO Box C700, West Conshohocken, PA, 19428-2959 USA.

Barsoum, R.G.S. (2003) "Ships: Navy experts explain the newest materials and structural technologies", AMPTIAC 2003; 7:3; 52-61

Black, S. (2003) "Fighting ships augment combat readiness with advanced composites", High Performance Composites; pp. 30-33.

Bonanni, D.L., Caiazzo, A., Flanagan, G. (2000) "Design guide for joints in marine composite structures – Part 1, concept development", Report No. NSWCCD-65-TR-2000/01, NSWC Carderock, January 2000, 84 pp.

Boone, M.J., Caccese, V., Bragg, R., Berube, K.A. (2003) "Mechanical testing of epoxy adhesives for naval applications", Univ. of Maine Department of Mechanical Engineering, Report No., UM-MACH-RPT-01-03

Boyd, S.W., Blake, J.I.R., Shenoi, R.A., Mawella, J. (2004a) "Fatigue life and residual strength analysis of steel composite ships", Applied Mechanics and Materials, Trans Tech Publications, Switzerland, 1-2; 81-86.

Boyd, S.W., Blake, J.I.R., Shenoi, R.A., and Kapadia, A. (2004b) "Integrity of hybrid steel-to-composite joints for marine application", Proceedings of the Institution of Mechanical Engineers: Part M - Journal of Engineering for the Maritime Environment; 218; 4; 235-246

Caccese, V., Blomquist, P.A., Berube, K.A., Webber, S.R., Orozco, N.J. (2006) "Effect of weld geometric profile on fatigue life of cruciform welds made by laser/GMAW processes", Marine Structures; 19; 1-22

Cao, J., Grenestedt, J.L. (2003) "Test of a redesigned glass-fiber reinforced vinyl ester to steel joint for use between a naval GRP superstructure and a steel hull", Composite Structures; 60; 439-445

Chen, H., Shivakumar, K., Abali, F. (2006) "A comparison of total fatigue life models for composite laminates", Fatigue Fract Engng Mater Struct; 29; 31-39

Clifford, S.M., Manger, C.I.C., Clyne, T.W. (2002) "Characterisation of a glass-fiber reinforced vinylester to steel joint for use between a naval GRP superstructure and a steel hull", Composite Structures; 57; 59-66

Davies, P., Choqueuse, D., Bigourdan, B., Gauthier, C., Joannic, R., Parneix, P., L'Hostis, J. (2004) "Design, manufacture and testing of stiffened panels for marine structures using adhesively bonded pultruded sections", Proceedings of the Institution of Mechanical Engineers: Part M - Journal of Engineering for the Maritime Environment; 218; 4; 227-234

Dong, P. (2003) "A robust structural stress method for fatigue analysis of ship structures", Proceedings of the 22nd International Conference on offshore mechanics and arctic Engineering, Cancun, Mexico. June 2003.

Fricke, W. (2002) "Evaluation of hot spot stresses in complex welded structures", Proceedings of The IIW fatigue seminar, Commission XIII, International Institute of Welding, Tokyo.

Fricke, W., Kahl, A. (2005) "Comparison of different structural stress approaches for fatigue assessment of welded ship structures", Marine Structures; 18; 473-488

Hashim, S.A., Knox, E.M. (2004) "Aspects of joint design and evaluation in thick adherend applications", The Journal of Adhesion; 80; 569-583

Herszberg I., Li H.C.H., Dharmawan F., Mouritz A.P., Nguyen, M., Bayandor, J. (2005) "Damage assessment and monitoring of composite ship joints", Composite Structures; 67; 205-216

Kabche, J.P., Caccese, V., Berube, K.A., Bragg, R. (2007a) "Experimental characterization of hybrid composite-to-metal bolted joints under flexural loading", Composites: Part B - Engineering; 38; 66-78

Kabche, J.P., Caccese, V., Berube, K.A., Thompson, L., Walls, J. (2007b) "Structural response of a hybrid composite-to-metal bolted connection under uniform pressure loading", Composite Structures; 78; 2; 207-221

Kabche, J.P., Caccese, V., Berube, K.A. (2006) "Testing and analysis of hybrid composite/metal connections and hull section for the MACH project", Univ. of Maine Department of Mechanical Engineering, Report No. UM-MACH-RPT-01-01, 348 p.p. April, 2006.

Kendrick, A. (2005) "Effect of fabrication tolerance on fatigue life of welded joints", Ship Structure Committee, SSC-436, NTIS, Springfield, VA 22161

Kim, H.S., Zhang, J. (2001) "Fatigue damage and life prediction of glass/vinyl ester composites", Journal of Reinforced Plastics and Composites; 20; 10; 834-848

Maddox, S.J. (2000) "Fatigue design rules for welded structures", Prog. Struct. Engng Mater.; 2; 102-109

Mahfuz, H., Zaman, K., Haque, A., Foy, C., Mohamed, H., Jeelani, S. (2000) "Fatigue life prediction of thick-section S2-glass/vinyl-ester composites under flexural loading", Journal of Engineering Materials and Technology; 122; 402-408

Makinen, K., Hellbratt, S.E., Olsson, K.A. (1988) "The development of sandwich structures for naval vessels," Mechanics of Sandwich Structures, Kluwer Academic Publishers, Netherlands, pp. 13-28.

Mansour, A., Wirsching, P., White, G., and Ayyub, B., (1996), "Probability Based Ship Design Implementation of Design Guidelines for Ships: A Demonstration", Ship Structure Committee, SSC-392, NTIS, Springfiled, VA 22161, 164 pp.

Melograna, J.D., Grenestedt, J.L. (2002a) "Adhesion of stainless steel to fiber reinforced vinyl ester composite", Journal of Composites Technology & Research; 24; 4; 254-260

Melograna, J.D., Grenestedt, J.L. (2002b) "Improving joints between composites and steel using perforations", Composites: Part A – Applied Science and Manufacturing; 33; 9; 1253-1261

Mouritz, A.P. (2006) "A simple fatigue life model for three-dimensional fiber–polymer composites", Journal of composite materials; 40; 5; 455-469

Munse, W.H., Wilbur, T.W., Tellalian, M.L., Nicoll, K., and Wilson, K. (1983), "Fatigue Characterization of Fabricated Ship Details for Design", Ship Structure Committee, SSC-318, NTIS, Springfiled, VA 22161, 207pp.

Shah Khan, M.Z., Mouritz, A.P. (1996) "Fatigue behaviour of stitched GRP laminates", Composites Science and Technology; 56; 695-701

Shivakumar, K., Chen, H., Abali, F., Le, D., Davis, C. (2005) "A total fatigue life model for mode I delaminated composite laminates", International Journal of Fatigue; 28; 33-42

Tang, H.C., Nguyen, T., Chuang, T., Chin, J., Lesko, J., Wu, H.F. (2000) "Fatigue model for fiber-reinforced polymeric composites", Journal of Materials in Civil Engineering; 12; 2; 97-104

Thompson, L., Walls J. (2003) "Preliminary design/analysis of hybrid hullforms for dual use in Maritime applications", Applied Thermal Sciences, Inc., Sanford, Maine, 31 May 2003.

Unden, H., Ridder, S.O. (1985) "Load introducing armature as a component part of a laminated structural element", US Patent 4,673,606; 13 February 1985

Van Paepegem, W., Degrieck, J. (2001) "Tensile and compressive damage coupling for fully reversed bending fatigue of fibre-reinforced composites", Fatigue and Fracture of Engineering Materials and Structures; 25; 547-561

Van Paepegem, W., Degrieck, J. (2004) "Simulating in-plane fatigue damage in woven glass fibre-reinforced composites subject to fully reversed cyclic loading", Fatigue and Fracture of Engineering Materials and Structures; 27; 1197-1208

Wacker, G., Brugge, D., Fach, K., Franzelius, W. (2004) "Theory and practice: requirements for adhesive bonding in marine structures", Proceedings of the Institution of Mechanical Engineers: Part M - Journal of Engineering for the Maritime Environment; 218; 4; 217-226

Wright, P.N.H., Wu, Y., Gibson, A.G. (2000) "Fibre reinforced composite-steel connections for transverse ship bulkheads", Plastics, Rubber and Composites; 29; 10; 549-557.

REPORT DOCUMENTATION PAGE

Form Approved
OMB No. 0704-0188

PLEASE DO NOT RETURN YOUR FORM TO THE ABOVE ADDRESS.

1. REPORT DATE *(DD-MM-YYYY)*	2. REPORT TYPE	3. DATES COVERED *(From - To)*
1-Jun-2008	Project Report	1-Jun-2005 to 31-May-2008

4. TITLE AND SUBTITLE

EXPERIMENTAL INVESTIGATION INTO THE FATIGUE LIFE OF HYBRID JOINTS UNDER FULLY REVERSED FLEXURE LOADING

5a. CONTRACT NUMBER

5b. GRANT NUMBER

N00014-05-1-0735

5c. PROGRAM ELEMENT NUMBER

6. AUTHOR(S)

Corriveau, Dominique
Caccese, Vincent
Vel, Senthil S.

5d. PROJECT NUMBER

5e. TASK NUMBER

5f. WORK UNIT NUMBER

7. PERFORMING ORGANIZATION NAME(S) AND ADDRESS(ES)

University of Maine
Office of Research and Sponsored Programs
5717 Corbett Hall
Orono, ME 04469-5717

8. PERFORMING ORGANIZATION REPORT NUMBER

C-2004-015-RPT-01

9. SPONSORING/MONITORING AGENCY NAME(S) AND ADDRESS(ES)

Office of Naval Research
Ballston Center Tower One
800 North Quincy St.
Arlington, VA 22217-5660

10. SPONSOR/MONITOR'S ACRONYM(S)

ONR

11. SPONSORING/MONITORING AGENCY REPORT NUMBER

12. DISTRIBUTION AVAILABILITY STATEMENT

Approved for Public Release, Distribution is Unlimited

13. SUPPLEMENTARY NOTES

14. ABSTRACT

The overall objective of this research is to develop and demonstrate methods for fatigue testing various common and novel steel/composite hybrid connections and to evaluate their suitability for their desired applications. Fatigue of hybrid connections subject to out-of-plane loading is highly variable and there is a lack of data reported in the literature. The intention of this effort is to provide additional baseline data for this type of connection. Testing and analysis techniques were successfully developed and employed. It was determined that separate analyses of the individual components of a hybrid joint (e.g. the composite plate and the steel T-section) are insufficient to determine the effects of fatigue loading on a given joint due to the effects of joining methods on the strength. Fatigue testing of a full joint configuration is necessary to adequately evaluate its response to fatigue loading. Further testing beyond what is presented in this report is recommended.

15. SUBJECT TERMS

Hybrid Structures; Connection Fatigue; Bolted Connections; Composites; Finite Element Analysis; Contact Analysis

16. SECURITY CLASSIFICATION OF:			17. LIMITATION OF ABSTRACT	18. NUMBER OF PAGES	19a. NAME OF RESPONSIBLE PERSON
a. REPORT	b. ABSTRACT	c. THIS PAGE			Vincent Caccese
U	U	U	UU	151	19b. TELEPONE NUMBER *(Include area code)* (207) 581-2131

Standard Form 298 (Rev. 8-98)
Prescribed by ANSI-Std Z39-18